Computational Fluid Dynamic Analysis and Optimisation of Microfluidic Systems

Hazim Hamad

University of Leeds

School of Mechanical Engineering

Submitted in accordance with the requirements for the degree of

Doctor of Philosophy

31 March 2021

Declaration

The candidate confirms that the work submitted is his own, except where work formed jointly-authored publication has been included. The contribution of the candidate and the other authors to this work has been explicitly indicated overleaf. The candidate confirms that appropriate credit has been given within the thesis where reference has been made to the work of others. This copy has been supplied on the understanding that is copyrighted material and that no quotation from the thesis may be published without proper acknowledgement.

Work Formed from Jointly Authored Publications

The candidate has publications from work contained in this thesis, and these were submitted with the support of supervisors. The contribution of the candidate to these works is explicitly mentioned below.

1. The work in chapters 4 and 5 of the thesis has appeared in publication as follows: Hamad, H.S., Kapur, N., Khatir, Z., Querin, O.M., Thompson, H.M., Wang, Y. and Wilson, M.C.T., 2021. Computational fluid dynamics analysis and optimisation of polymerase chain reaction thermal flow systems. Applied Thermal Engineering, 183, p.116122.

This thesis is dedicated to... My beloved parents

My beloved brothers and sisters; My friends who encourage and support me.

Acknowledgements

All the praises be to Allah, the Most Beneficent, the Most Merciful. I would first like to thank sponsor of this project British Petroleum , Rumaila Oil filed , Midland Refineries and Ministry of Oil in Iraq. I would like to express my grateful to my supervisors: Professor Harvey Thompson, Professor Nikil Kapur, Dr Mark Wilson, Dr Zinedine Khatir and Professor Osvaldo Querin. Also I would like to express my grateful to Dr Yongxing Wang and Dr Gregory de Boer.

Abstract

A novel Computational Fluid Dynamics-enabled multi-objective optimisation methodology for Polymerase Chain Reaction flow systems is proposed and used to explore the effect of geometry, material and flow variables on the temperature uniformity, pressure drop and heating power requirements, in a prototype three-zone thermal flow system. A conjugate heat transfer model for the three-dimensional flow and heat transfer is developed and solved numerically using COMSOL Multiphysics® and the solutions obtained demonstrate how the design variables affect each of the three performance parameters. These show that choosing a substrate with high conductivity and small thickness, together with a small channel area, generally improves the temperature uniformity in each zone, while channel area and substrate conductivity have the key influences on pressure drop and heating power respectively. A multi-objective optimisation methodology, employing accurate surrogate modelling facilitated by Machine Learning via fully-connected Neural Networks, is used to create Pareto curves which demonstrate clearly the compromises that can be struck between temperature uniformity throughout the three zones and the pressure drop and heating power required. Besides the deterministic optimisation discussed above in which the input variables are assumed to be deterministic. A robust optimisation is conducted, considering the uncertainties in design parameters of the PCR device due to uncertain tolerances from the manufacturing process of PCR system. Monte Carlo simulations (MCS) are carried out to propagate and quantify the uncertainties, then the mean and standard deviation of the output obtained. The robust design is formulated based on the output of probabilistic solutions from MCS and solved to find optimal objective values (greatest temperature uniformity throughout the three zones and the smallest pressure drop) that exhibit minimum change as a result of variations in the design parameters. The robust optimisation results demonstrate how the uncertainty in the

design variables affect the objectives and that single optimum objective points are different from the deterministic optimum points. The robust optimum value depends on the design requirements, such as whether minimising variation in performance due to uncertainties is more important than optimising the objective function, and illustrative examples are provided. The Pareto front of multi-objective solutions demonstrate that the robust optimisation Pareto front is slightly shifted from that of the deterministic solution, and this shift increases with increasing uncertainty in the input design variables. Hence in the presence of uncertainty the deterministic Pareto front is not useful and its solution is restricted.

Abbreviations

k_B	Boltzmann's constant
k_BT	Thermal energy
A	area (m^2)
Bi	biot number
C_p	constant-pressure specific heat
D_h	hydraulic diameter (mm)
H	microchannel height (mm)
h	Heat transfer coefficient [$W/m^2.K$]
k	thermal conductivity ($W/m.K$)
L	length (mm)
$\dot{m}$	mass flow rate (kg/s)
N_u	Nusselt number
P	microchannel perimeter (mm)
Δp	pressure drop (Pa)
Pe	Peclet number , $V_{ch}D_h/\alpha$
Pr	Prandtl number
q	wall heat flux (W/m^2)
Q	total power generated by PCR chip (W)
R_{th}	conduction thermal resistance (K/W)
Re	Reynolds number , $Re = \rho V_{ch}D_h/\mu$
S	spacing between heaters (mm)
T	temperature (K)
V	velocity (mm/s)
$\dot{V}$	volumetric flow rate (m^3/s)
W	width
avg	average
b	substrate
c	channel
CFD	computational fluid dynamics
dev	deviation
FEM	finite element method
f	fluid
h	heater
in	inlet
max	maximum
min	minimum
out	outlet
$RMSE$	root-mean-square error
s	solid
w	wall

Greek symbols

α	thermal diffusivity
Δp	drop
ρ	density (kg/m^3)
μ	dynamic viscosity ($Pa.s$)
ν	kinematic viscosity (m^2/s)

Contents

List of Figures

Chapter 1

Introduction

This thesis explores and develops computational techniques to design polymerase chain reaction (PCR) systems with precise thermal control. The goal of this initial chapter is to provide an introduction to microfluidic systems and describe a number of microfluidic thermal management applications including heat sinks and existing PCR devices for diagnostic analysis. The current chapter concludes with aim and objectives of this thesis.

1.1 Background and motivation

Microfluidics refers to devices consisting of a set of micrometre channels (He et al., 2010) relatively small (∼10 mm) etched into glass, polymer or silicon to form the desired features for controlling and manipulating small amounts of fluids (10^{-9} to 10^{-18} litres) (Whitesides, 2006). Recently, Microfluidics science has developed rapidly (Cui and Wang, 2019) and it has received considerable attention in research and technology due to its promise of rapid, inexpensive, efficient, and portable diagnostic devices (Sonker et al., 2017). This potential is reflected in the rapidly rising numbers of publications about Microfluidics as shown in Figure 1.1. Precise thermal control during the processing of small volumes of liquid in arrays of fluidic channels is a key enabling technology for numerous important applications. These include chemical reactors, fuel and solar cells, pharmaceuticals and droplet freezing systems to determine environmental pollution levels (Stroock et al., 2002; Tarn et al., 2018).

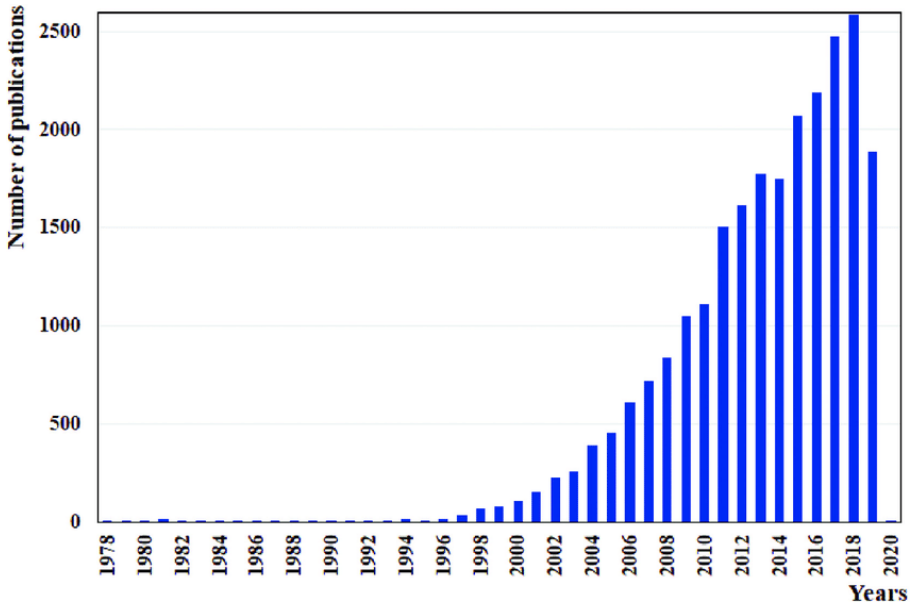

(a)

Figure 1.1: Number of articles published per year on the use microfluidic devices (Vicente et al., 2020).

1.2 Heat sink

In the context of electronics cooling the heat sink is one of the significant application of microfluidic devices used for cooling of the electronic devices that are required to operate under a specified temperature level. It has been used to remove the heat generated from electronic components or devices. Heat can be absorbed by conduction between the electronic system and the base plate of the heat sink and transferred to the fluid flowing by convection through the heat sink channels and it can be rejected either passively using natural convection or actively by forced convection. The first microchannel heat sink design was developed by (Tuckerman and Pease, 1981). They investigated the dissipation of heat from electronic chips by using a silicon microchannel with water as working fluid. They obtained heat dissipation up to $790 W/cm^2$ while the chip temperature was maintained at $110 \deg C$. The increasing densities of integrated circuits (up to $10 kW/cm^2$ by 2020 (Karayiannis and Mahmoud, 2017)) have inspired significant recent research interest in single-phase liquid flows in fluidic channels as a viable and practical method for cooling high heat flux densities encountered e.g. in Radio Frequency and microwave applications (Agarwal et al., 2017). However, the heat generated by the electronic chip is mostly non-uniform thus hot spots can be generated and the temperature of the cooled surface is not uniform even in the case of constant heat flux (Hetsroni et al., 2001). Thus, peak temperature can be generated due to the effect of the hot spot which has a negative impact on the device reliability and may cause its failure. However, there is continued interest in controlling and regulating the temperature of microfluidic electronic devices and the trend lies in decreasing the size of these devices.

Serpentine fluidic channels see Figure 1.2 are particularly useful due to the serpentine fluidic channels in the heat sink lead to break up the thermal boundary layer and improve the heat transfer. In addition to being capable of providing uniform processor temperatures for high-density electronics cooling applications, (Al–Neama et al., 2017). (Zhang and Jiang, 2016) have found widespread application in the Polymerase Chain Reaction (PCR) systems that have revolutionised biological research. PCR systems are described next.

1.3 Polymerase chain Reaction (PCR)

PCR systems perform a thermal cycling procedure in a fluidic channel, where each straight component incorporates three distinct stages of denaturation (melting of the double-stranded DNA at $\sim 95°C$), annealing (binding of the specific primers of the thermostable DNA polymerase between $40°C \sim 50°C$) and extension (extending the primers within the thermo-stable DNA at $60°C \sim 70°C$) (Park and Park, 2017).

The present thesis is motivated by the thermo-flow design and optimisation of fluidic channels used in PCR systems. They are used widely in rapid diagnostic systems for bacterial species leading to e.g. infectious diseases, or for the rapid and accurate detection of bacterial species causing micro-biologically induced corrosion in oil and gas production systems (Zhu et al., 2006; Agrawal and Lal, 2009).

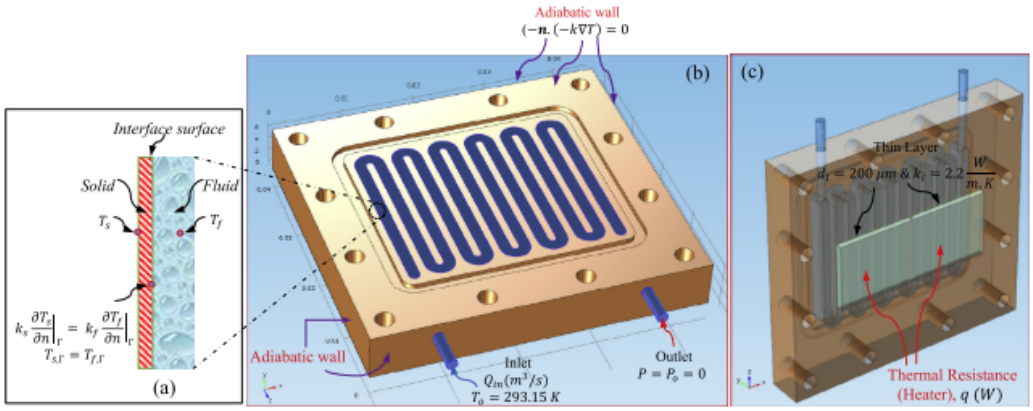

(a)

Figure 1.2: Serpentine microchannel used for cooling of electronic systems (Al–Neama et al., 2017).

1.4 Conventional PCR (macro-PCR)

In this type, the PCR process can be performed by injecting PCR samples into a set of tubes, see Figure 1.3, where they are thermally cycled through various temperatures. In fact to achieve the thermal cycle process of macro PCR that has a large thermal mass requires high power consumption and a considerable amount of time: approximately 1-2 hours for 30 cycles. Additionally, fabricating a design to be portable and integrated is difficult using this type of PCR (Chunsun et al., 2006; Ahrberg et al., 2016).

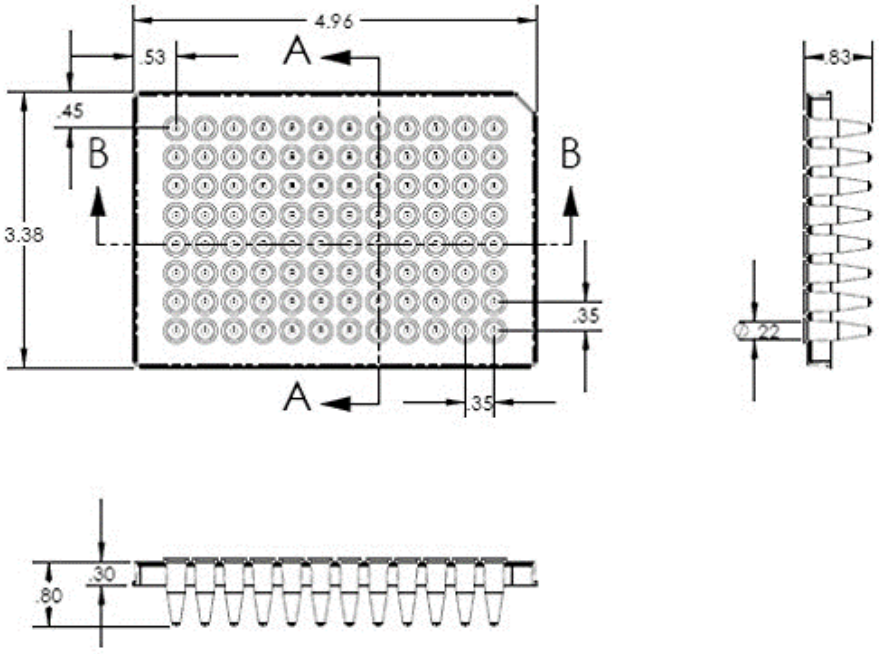

(a)

Figure 1.3: Simplified 96 tubes based PCR (Belgrader et al., 1996).

The drawbacks of Conventional PCR have motivated the researchers to find alternative PCR devices to minimize the reaction time. Microfluidic PCR devices have several desirable features. First, the total reaction time is significantly reduced due to micro-PCR devices requiring smaller sample volumes. Second, the

overall cost of raw materials is reduced as manufacturing micro-PCR devices require less material. Third, micro-PCR devices require fewer reagents to complete the same process as macro-PCR devices, significantly reducing the overall cost of the process. It is then possible to reduce the reaction volume and enhance the reaction efficiency by employing microfluidic theories, and that has led to the design of continuous flow PCR (CFPCR) with high performance and easy integration and miniaturization (O'connor and Dantsker, 2002).

1.5 Continuous-flow PCR microfluidic (CFPCR)

Continuous-flow micro PCR devices have dramatically shortened a lengthy PCR process that is caused by high thermal inertia,(Chen et al., 2011) In such type, the PCR process can be achieved by cycling the PCR sample through three different zones as described in Figure 1.4. These three temperature levels are essential in the PCR reaction, and this process is considered to have failed in the absence of one of these cycles. For instance, the first step involves heating the DNA samples to $95°C$ in order to duplicate stranded DNA or split into two single strands. While the second step involves cooling to $55°C$ where the primers allow attaching the single-strand of DNA. The third step involves heating to $72°C$ and the actual copying of the DNA is achieved during this cycle by the DNA polymerase. The DNA polymerase attaches to the primer site and copies DNA by using the nucleotides that are in the solution as building blocks, and this cycle is repeated about 30 times as shown in Figure 1.4.

Although CFPCR is used as an alternative to macro-PCR there have been some issues associated with CFPCR such as it has the same issue of surface-molecule interactions found in well-based approaches (Zhang et al., 2006; Zhang and Ozdemir, 2009). CFPCR is also disadvantaged to some extent by the concern of the velocity distribution (due to parabolic flow profiles) of the fluid when the PCR mixture is pumped through the microchannel(Zhang and Ozdemir, 2009; Zhang and Jiang, 2016). Since the velocity distribution is a parabolic shape, the sample moves more slowly near the wall because of the effect of fluid viscosity and shear stress than the sample in the middle. As a result, PCR samples experience a range of different residence times at different temperatures.

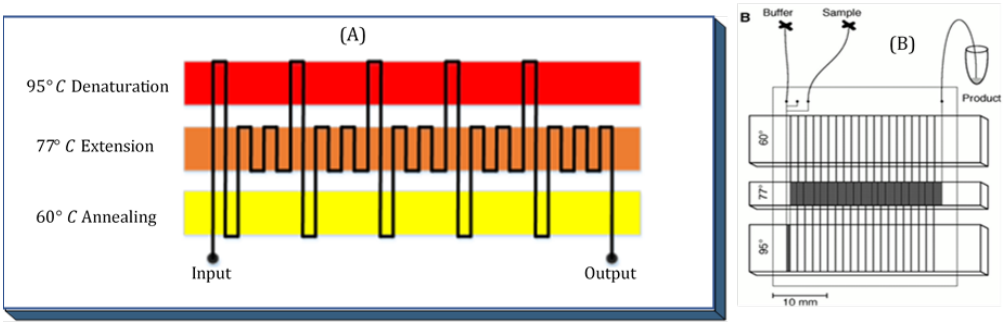

(a)

Figure 1.4: : (A) Schematic diagram of CF-PCR device (B) Show the device layout. Three temperatures regions associated with denaturation or melting, extension, and annealing. It can be noted that the extension step is longer than other steps because of the reaction in this step need a long time to complete the process and moving on (Kopp et al., 1998).

1.6 Droplet-based PCR

Droplet-based systems can be used to address many of the problems associated with single-phase PCR techniques, including adsorption, cross-contamination, and diffusional dilution of the sample (Mohr et al., 2007). Droplet-based PCR provides the potential to eliminate the undesired contact between the PCR sample and the flow channel, hence, the chemical reaction will occur in an isolated environment (Nisisako et al., 2002). The droplet-based PCR design includes a continuous-flow loop which is fabricated from a polymer material. This flow loop is performed by etching serpentine microchannels on the polymer substrate. The PCR mixture samples are confined in small aqueous droplets and continuously moved by using an oil carrier fluid through the desired temperature zones, see Figure 1.5. Hence, any local temperature variation will be small so each droplet can achieve the desired uniform temperature and the thermal mass is further reduced while the thermal cycles time is shortened. In contrast, CFPCR uses a single-phase aqueous flow with a larger thermal mass in comparison with PCR based droplet. As the samples are contained in droplets they could be detected

and subsequently sorted on the chip itself, which is particularly important for an integrated lab-on-a-chip system (Mohr et al., 2007).

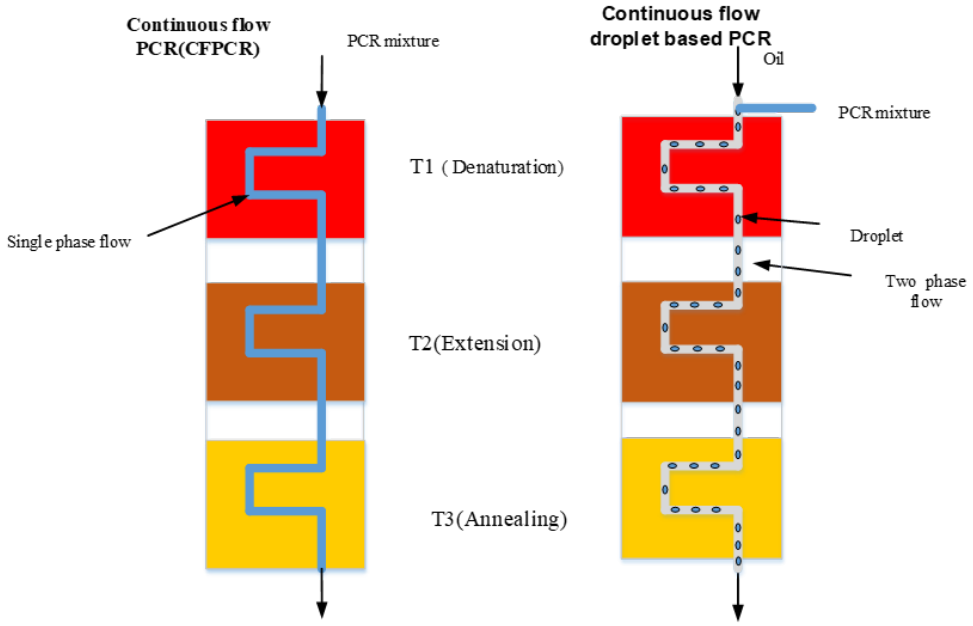

(a)

Figure 1.5: : A schematic highlighting the differences between segmented-flow and continuous-flow PCR. The droplet-based approach is carried out by pumping two immiscible phases into the microchannel to form water-in-oil droplets.

1.7 Challenges and Motivation of this research

This chapter discusses the importance of controlling the temperature in microfluidic systems in particular heat sinks and PCR. Microfluidic technologies offered different advantages, and it can be applied to different biological and chemical applications. For instance, the heat sink microchannel and PCR system. PCR remains one of the most significant devices in molecular biology and is primarily conducted using conventional PCR. As discussed in the previous section, these devices have several limitations based around their large thermal masses and

high consumption of reagent. Microfluidic technologies (continuous-flow PCR) offer a far better platform for PCR by reducing thermal masses and reagent consumption. Moreover, the droplet-flow approach combines the best features of well-based and continuous flow approaches. The droplet flow approach uses droplet for compartmentalization of the PCR reaction mixture and can handle multiple, isolated small volumes without the limitations of large thermal masses, surface interactions and flow dispersion (Demello, 2006).

However, the droplet-based PCR has several limitations such as it requires complex design in comparison with CFPCR, hence, it is more expensive and it is difficult to be integrated on-chip and portable due to the high fabrication cost and difficulties in controlling the sample in droplet aqueous flow. Also, it adds more complexity to control the particle with the interaction between the two-phase flow. For these systems to become commercialised they need to achieve several requirements, including low-cost, easy to use with fast analysis times. Therefore, in summary, CFPCR is more applicable and reliable. In contrast, droplet-based systems have several practical challenges and have not been commercialised yet.

1.8 Aims and Objectives

This thesis aims to investigate the effect of microfluidic geometry and operation conditions on the effectiveness of PCR design and establish computational techniques for optimising thermal control of such systems. This is achieved through the following five objectives:

1. **Use Computational Fluid Dynamics (CFD)** to develop high-fidelity flows models of CFPCR systems and explore the effects of design parameters on key performance metrics such as thermal uniformity, pressure drop and heating power.

2. **To formulate** a multi-objective design optimization problems for CFD-enabled deterministic optimisation of prototype PCR flows.

3. **To formulate practically-relevant** multi-objective design optimization problems for CFD enabled robust design optimisation of prototype PCR flows.

4. **To combine high fidelity CFD simulations of PCR systems** with design optimization techniques to determine the geometrical and operating parameters which optimize the thermal and flow field characteristics of prototype PCR flows subject to multi-objective criteria.

5. **Using high fidelity CFD simulations of PCR systems** with design optimisation tools to find the effect of uncertainty in geometrical and operating parameters on the output objectives the thermal and flow PCR systems. Find the robust optimum design points prototype PCR flows systems subject to multi-objective criteria.

6. **To carry out a complementary experimental investigation** of serpentine PCR systems in order to validate the CFD and optimisation methods for serpentine PCR systems.

1.9 Thesis outline

This thesis is divided into 7 chapters and the outline of this thesis can be summarised as:

The current chapter, Chapter 1, describes the background and objective of this thesis. An overview of the relevant literature is provided in Chapter 2. Chapter 3 presents the fundamental of heat transfer and fluid flow in microchannel PCR systems, while the methodology of CFD and optimisation is provided in Chapter 4. CFD analysis and optimisation of microfluidic PCR systems is conducted in Chapter 5 . Robust design optimisation of microfluidic PCR systems is carried out in Chapter 6. Finally, the conclusions and future work plan are presented in Chapter 7.

Chapter 2

Literature review

2.1 Introduction

This chapter provides a review of the literature on various PCR systems and their related microfluidic devices. The PCR process is described in Chapter one. Although it is usually carried out in conventional bench-top thermal cyclers, miniaturization of the process in continuous flow microfluidic devices makes it possible to reduce the cost and time needed to conduct DNA amplification (Ahrberg et al., 2016). Several studies have been conducted to investigate how different designs affect the PCR performance to achieve PCR chip designs that are more reliable and faster than conventional PCR. Moreover, different parameters have been employed in PCR research and PCR studies based on changing these parameters to investigate their effect on PCR performance. For example, substrate materials, drive mechanisms, and heating/cooling mechanisms, mass flow rate (injected fluid velocity), reaction time and a number of cycles.

2.2 Microchannel PCR systems

Early PCR systems used time-consuming devices involving wells where the whole chip is heated up and cooled down during each thermal stage (Khandurina et al., 2000; Lee et al., 2017). Over the last two decades, the trend has been changed from conventional to micro-PCR due to the progressive development

of PCR. Miniaturized PCR devices involve two categories: stationary PCR and continuous-flow PCR.

In the stationary type, the mode of thermal cycling is similar to that generally employed in conventional benchtop PCR machines. The PCR solution is kept stationary in a microwell or microchamber, and then the whole device is heated and cooled to make the repetitive cycle of the three temperatures for denaturation, annealing, and extension

2.2.1 Static PCR based microchannel

In the stationary type, thermal cycling is similar to that generally employed in conventional benchtop PCR machines. PCR solution is kept static in a microwell or chamber while the temperature of the system is cycled between different temperatures. The PCR based chamber can be divided into two types, the single-chamber PCR and the multi-chamber PCR as described in Figure 2.1. In 1993'

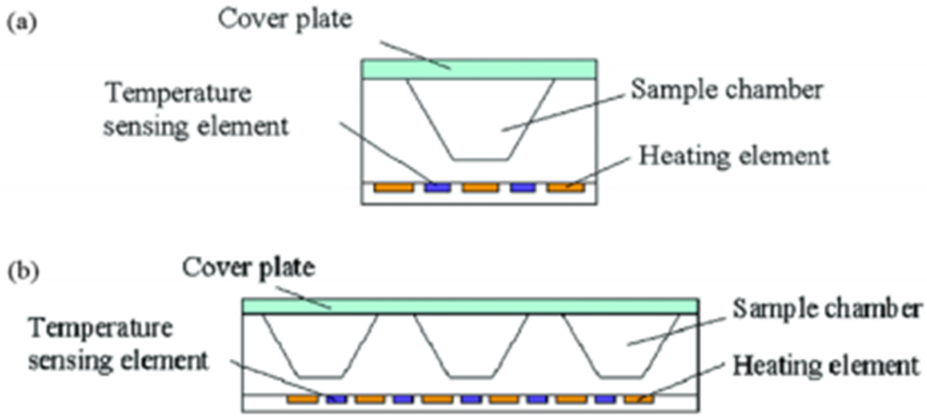

(a)

Figure 2.1: Chamber stationary PCR chips: (a) Single chamber PCR chip.(.b) Multi-chamber PCR chip (Zhang and Xing, 2007)

the miniaturised PCR in a chip was developed, by Northrup (1993) who fabricated a stationary reaction chamber by anisotropic wet etching silicon. This design was the first experimental stationary based PCR chamber in a chip that demonstrated

that a fast and efficient PCR can be obtained by reducing the thermal mass between the sample and the heater. Subsequently, this design has been replicated and improved to form a micro-electro-mechanical system (MEMS) technology which is used to create several different PCR devices. Singh and Ekaputri (2006) presented a simulation of the PCR process on a lab on a chip (LOC) using ANSYS to study the thermal management issues. They also analyse a theoretical model of the PCR chamber by using an electrical analogy of thermal heat flow as shown in Figure 2.2 where the temperature was replaced by voltage, thermal power was replaced by the current, thermal resistance was replaced by electrical resistance, and thermal capacity was replaced by electrical capacity. They demonstrated that the relative temperature deviation in the reaction chamber can be expressed as :

$$\frac{\Delta T}{T} = \frac{R_{th}}{(2(R_{th} + R_{ch}))} \tag{2.1}$$

where R_{ch} represents the resistance of the chamber and R_{th} represents the resistances of the links on both sides of the chip . The PCR chamber was placed in two independent places: the first was in the centre of the chip (symmetry) and the second in the corner (asymmetry) of a chip. Their simulation was aimed at studying the influence of operative parameters such as the chamber shape, chamber location, the placement of heaters, the symmetry of the thermal power supply and thermal power loss through thermal resistive links. It was found that the influence of asymmetries in the heater (heat supply)and the thermal resistive link to the sink was very significant for achieving temperature uniformity. They also observed that small thermal loss through thermal isolation materials such as glass can cause significant temperature variation of more than 1°C. They used four more heaters to ensure a more uniform thermal power supply to the chip and this resulted in a reduction in temperature variation to less than 0.3°C.

Qiu et al. (2010) used a novel PCR technique with a plastic disposable microfluidic reactor with volumes between 10 to 100 μL. They created a portable thermal cycler and a compact diagnostic PCR device which can quantify the quantity of amplified DNA during an experiment. The experimental system consists of a double-sided heater which includes a master thermoelectric element and a thermal plate connected to a second thermoelectric element in order to

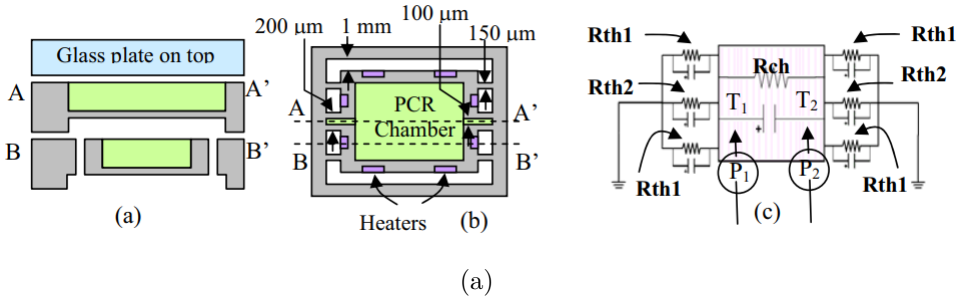

(a)

Figure 2.2: A typical symmetrical PCR, (a) cross section, (b) top view, and (c) equivalent circuit(Singh and Ekaputri, 2006).

maintain temperature homogeneity and a reasonably fast temperature ramping rate. They demonstrated that in this system the fluidic and thermal control can be achieved very precisely and it can accomplish a temperature ramp rate of approximately $\sim 6°C/s$ for cooling and $\sim 4°C/s$ for heating. In addition, the fluid temperature achieved uniformity with only a small deviation from the set point of approximately $\pm\ 0.1°C$ up to a temperature of $\sim 94°C$. However, there was an issue with using the single-chamber since it was not appropriate for some sequential PCR tests for a number of DNA samples. In addition, chamber based PCR devices have high thermal inertia and have long thermal-cycling times (Daniel et al., 1998; Zhang and Xing, 2007; Chen et al., 2011). Then a significant progress was employment in well or chamber based PCR allowing a generation to use a multi-chamber to reduce the analysis time and to reduce the reaction volume. The multi-chamber stationary PCR chips were also employed to increase the PCR throughput because they can perform different sequential PCR tests concurrently. However, it is essential to ensure temperature uniformity between chambers and special care must be taken to achieve the thermal optimization of the multi-chamber to achieve a uniform temperature between chambers. Woolley et al. (1996) successfully fabricated a stationary array of PCR chambers to form an integrated and rapid PCR analysis system. The reaction chamber was constructed from a double-sided polished silicon wafer and equipped with a miniaturized heater instead of a large heating/cooling block. They obtained high-speed DNA amplification and detection because their model achieved the

whole process in 45 minutes. However, the model was made using an expensive technology and using the chip is likely to enhance cross-contamination, because it is not disposable and has to be well-cleaned between samples. Daniel et al. (1998) fabricated an array of micro-chambers in silicon using bulk micro-machining by anisotropic wet etching. They achieved rapid temperature cycling and control at low power consumption using a novel thermal design of the chambers, integrated thin-film platinum resistors as temperature sensors and heaters. They demonstrated that the micro-chamber thermal characteristic can be improved by thermally isolating it from the wafer. However, the thermal cycle in a static chamber requires heated up and cool down the overall device which leads to a delay in the temperature response of the solution because of the large thermal mass of the device itself (Kim et al., 2016).

These were superseded by Continuous Flow PCR (CFPCR) devices.

2.2.2 Continuous Flow PCR (CFPCR)

Continuous Flow PCR (CFPCR) introduced first by Kopp et al. (1998),is based on single-phase flow in a serpentine fluidic channel of rectangular cross-section with three temperature stages in a glass substrate supported by three independent copper block heaters, see Figure 2.3.

Several studies show that, when used in a serpentine arrangement, CFPCR offers reduced reagent consumption and rapid heat transfer, enabling PCR processing times to be reduced dramatically compared to well-based systems.

In the design of Kopp et al. (1998) the PCR mixture was passed continuously along three different regions to achieve the desired temperature instead of heating and cooling the entire chip as in conventional PCR. Only the PCR sample was cycled through the PCR zones. Therefore, they found the thermal mass was significantly reduced. The PCR cycle could be achieved faster than Conventional PCR.

However, Kopp et al. (1998) conducted their experiments bypassing the flow from the denaturation region to the extension region before annealing takes place. That resulted in melted single strand of DNA samples directly from double-strand DAN without amplification. Therefore, the DNA sample would pass through the

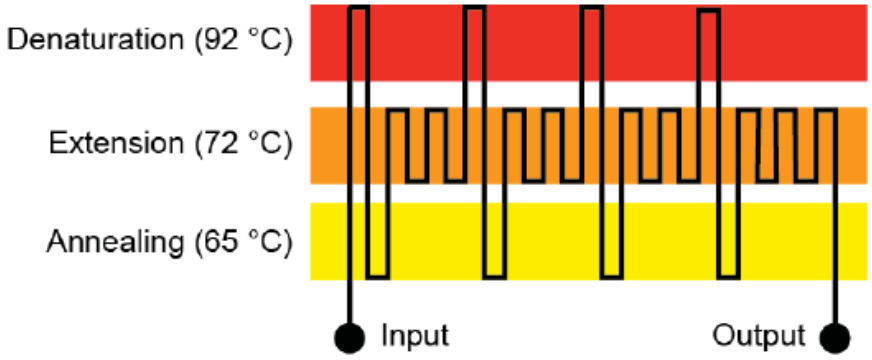

(a)

Figure 2.3: Schematic diagram of the serpentine microchannel PCR (Kopp et al., 1998).

extension zone without experiencing its temperature. To improve that, the channel should be fabricated to be very narrow at the extension zone to increase the PCR sample velocity. Furthermore, the second problem with the PCR serpentine design is the thermal crosstalk between the three thermal blocks used to create three temperature zones (Zhang and Xing, 2007; Mohammed et al., 2012). CFPCR devices using a steady-state temperature gradient have been employed to simplify the process of generating the desired temperature zones. This is in contrast with the CFPCR based on isothermal temperature zones where multiple isolated zones are required, Figure 2.4. Therefore, the PCR serpentine should be designed based on the temperature gradient. The two thermal zones of denaturation and annealing can be performed by thermal blocks that are placed at each ends of the chip. Therefore, based on these two thermal blocks the temperature gradient in the middle zone (extension zone $(65 - 72°C)$ can be achieved, and that results in eliminating the thermal block in the middle zone ,(Mohammed et al., 2012).

Crews et al. (2008) presented an experimental work based on the temperature gradient technique to investigate the pressure needed for PCR devices to carry out amplification. They fabricated 30 and 40 serpentine PCR cycles from glass chips $(25 \times 75 \times 2mm)$. The glass chip was heated and cooled by two thermal aluminium

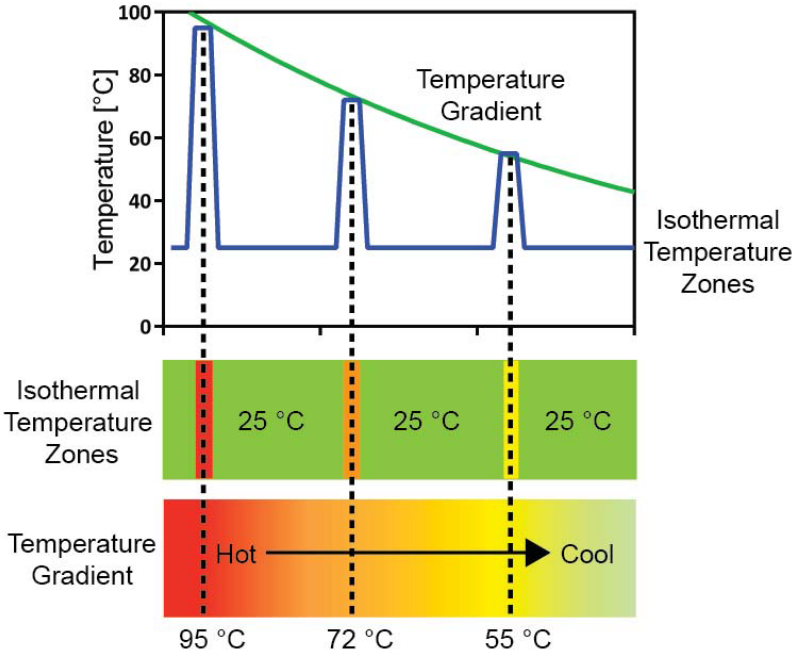

(a)

Figure 2.4: Two different approaches for generating the isothermal temperature zones needed for CFPCR.

strips placed underneath. A thermal gradient was achieved across the glass by heating one strip and the serpentine channel was placed in the area between the strips, where the temperature gradient is virtually linear. The channel was narrow where rapid temperature change is desired and wide where slow ramp rates are needed. They achieved amplification of control samples within 10 min for the 30-cycle PCR and 13 min for the 40-cycle PCR.

Mohammed et al. (2012) presented a study based on the PCR design of experimental work of Crews et al. (2008) using commercial software called ANSYS CFX to design a numerical model. This model was carried out to evaluate the temperature, pressure and velocity using CFPCR serpentine geometry. This geometry consists of 30 cycles of narrow and wide channels and only two block heaters were used for the denaturation and annealing, while the middle extension zone was achieved based on the temperature gradient. The results demonstrated that an increase in velocity was achieved at the narrow channel thus ensuring that the fluid at the narrow channel did not experience extension temperature. This can solve the problem faced in previous designs however, as a result, the pressure drop was 14.2 kPa for the 10 PCR cycle model and 42.6 kPa for a 30 cycle model. They demonstrated that this pressure drop is too high and can affect the full integration of this device, therefore they proposed using the approach of integrated pneumatic micropumps and valves with multi-chamber CFPCR for a better performing design of PCR. Moschou et al. (2014) presented design, fabrication and evaluation of a low cost and low power CFPCR device using polyimide as substrate material with three integrated resistive copper heaters as heating elements. Their device was designed to achieve 30 serpentine channels cycles of PCR with relative time ratios of 1:1:2 for denaturation, annealing, and extension respectively, as shown in Figure 2.5. They verified that the simulation results of the temperature uniformity and the power consumption of the chip device were in good agreement with the experimental work. They demonstrated that their design has a potential to be integrated into LOC systems and had the advantages of a small thermal mass which yielded low power consumption (2.4 W) and fast amplification rates. In addition, they achieved efficient DNA amplification within 5 min.

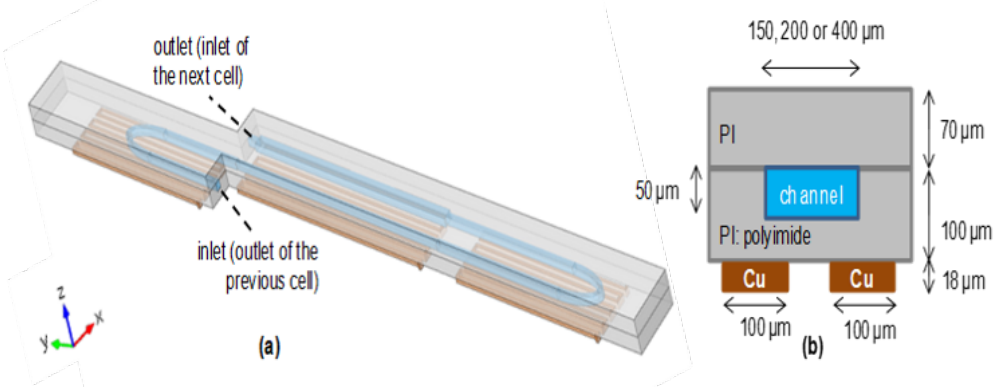

Figure 2.5: Schematic of the unit cell used for the calculations. The microfluidic channel as well as the three meander-shaped heaters, attached to the bottom of the cell, are shown. b) An XZ cross-section of the device, where the substrate layers and their thicknesses are depicted.

Schneegaß et al. (2001) constructed a 25 cycle PCR device from silicon and glass. The device consisted of reaction chambers etched into a glass chip and covered by a silicon chip and equipped with integrated heaters. Integrated chip (IC) manufacturing technology is used to fabricate the heater and temperature sensors on a PCR chip for temperature control. As illustrated in Figure 2.6. the channel at the inlet is placed horizontally for complete initial denaturation, then after the final cycle, an additional extension zone was combined for complete synthesis of PCR products. The extension region was arranged in the centre of the chip, the denaturation and the annealing zones at the opposite sides. They obtained an amplification time of approximately 1 min per temperature cycle. Hence, the residence time of a sample volume for the 25 cycle device was approximately 25 min. The energy consumption of the PCR chip for a 35 min PCR process was 0.012 kW/ h.

Yang et al. (2002) performed an experimental study to address the sensitivity aspect of the PCR chip. The study was performed by using a thin serpentine channel (0.75 mm) polycarbonate PCR microreactor device which was placed between two Peltier elements. They carried out experiments of 30 cycles in 30 min to amplify the K12-specific gene from 10 cells in the presence of 2 % blood.

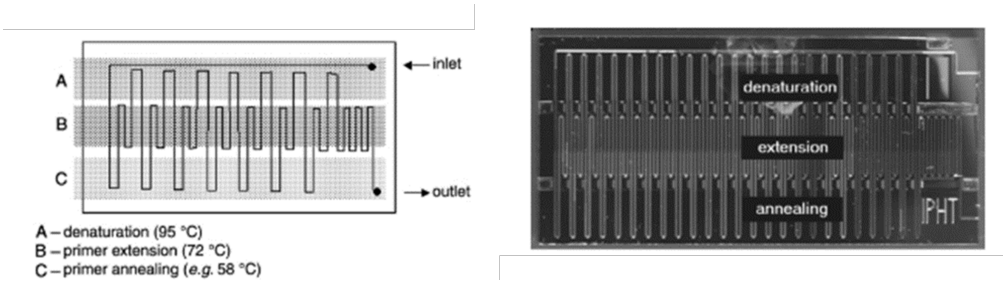

Figure 2.6: : Schematic sketch of the fluid channel through the individual temperature zones.

The authors demonstrated that their experiment was designed, fabricated and tested to detect the sensitivity and specify the amplification of Escherichia coli (E. coli) K12-specific gene fragment. In addition, they explored how to minimize the process operation time and enhance the PCR efficiency. Qiu et al. (2010) presented a novel technique to carry out PCR using a plastic microfluidic reactor with volumes between 10 to 100 μL. They developed a portable thermal cycler and a compact diagnostic PCR device. This device is a disposal thermal cycler and can quantify the amplified DNA during an experiment. The system of the experiment consists of a double-sided heater that includes a master thermoelectric element and a thermal plate connected to a second thermoelectric element in order to maintain temperature homogeneity. Fast temperature ramping rates of approximately 6 °C/s for cooling and 4 °C/s for heating was achieved and the liquid temperature of the reaction chamber follows the set-point temperature with an accuracy of ±0.1 °C up to a temperature of 94 °C.

Zhang and Xing (2009) studied the effect of the thermal convective gradient of PCR with different annealing temperatures on DNA samples amplifications. They found that PCR annealing can be achieved within a temperature range between $\sim 60°C$ to $\sim 68°C$. However, they demonstrated that with the increase in the annealing temperature the PCR does not yield sufficient amplification due to defects that have been occurred.

Due to their potential to provide an isolated environment with lower thermal mass than single-phase systems, there are now intensive efforts to create droplet-

based PCR systems, (Zhang and Jiang, 2016; Lee et al., 2017). For example Mohr et al. (2007) presented experiments and numerical work to couple a micro-droplet technology with a continuous-flow PCR chip. Their numerical simulation was extended from the previous studies of (Zhang et al., 2002) and (Sadler et al., 2003) While, Mohr et al. (2007) performed a droplet-based PCR as described in Figure 2.7 to investigate the effect of different parameters on droplet-based PCR design, including flow rate, thermal mass, and thermal resistance. A total of 32 serpentine cycles were performed on a PCR chip which was fabricated from polycarbonate. Mohr et al. (2007) focused in particular on the temperature profile of the fluid and substrate within the PCR chip and the droplet residence times in different temperature regions. They demonstrated that the temperature distribution within the carrier fluid was strongly affected by the flow rate. They also found the flow rate had a major impact on the droplet residence time. Moreover, the thermal resistance of the various layers in the chip substrate had a significant influence on the temperature distribution within the channel.

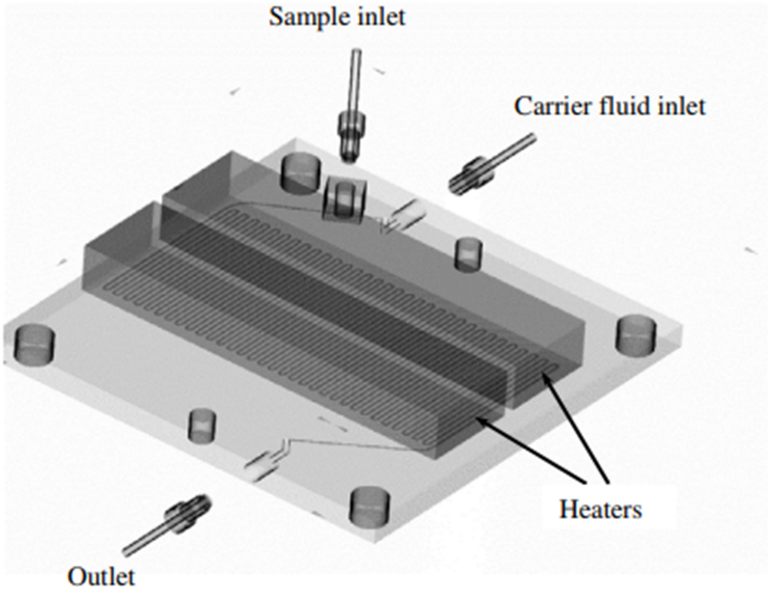

Figure 2.7: Schematic diagram of the PCR chip showing the overall layout and the inlets and outlet. (Mohr et al., 2007).

However, currently, most practical systems use CFPCR based on single-phase flow and these are the focus of the present thesis. Previous studies of these have shown that the most influential parameters include the substrate's thermal conductivity and the system's thermal resistance, and that fluidic channel sizes and spacing, carrier heat capacity and flow rate and, crucially, the heating arrangement chosen are also all very influential (Thomas et al., 2014). Controlling the residence times in the denaturation, annealing and extension zones is crucial since insufficient dwell times in each thermal state can seriously degrade DNA amplification efficiency (Chen et al., 2013). Residence times in each zone can be optimised by controlling the flow rate and channel geometry (Chen et al., 2012). Cao et al. (2011) explored the role of absolute and relative residence times on DNA amplification efficiency using a combined experimental and numerical approach. The latter employed a Lagrangian modelling approach to predict the temperature histories of individual DNA molecules flowing through CFPCR devices. Their methodology enabled design times for CFPCR devices to be reduced significantly. A number of other studies have shown that it is also important to control the interference and transition times between the thermal zones, which may require the use of active heating and cooling between the zones since ordering and interactions between the PCR thermal zones affects PCR yield significantly. These considerations complicate the drive towards CFPCR device miniaturisation, to develop portable devices for diagnostic and testing purposes, since minimising thermal interference between neighbouring serpentine channels tends to lead to wider fluidic devices (Chen et al., 2013). The geometry of the serpentine channels is very important and a number of studies have attempted to improve PCR yield by providing a more uniform thermo-flow environment within the PCR zones. Hashimoto et al. (2004), for example, used spiral microchannels depicted in Figure 2.8 to reduce reaction times and carried out a study to evaluate the effect of high velocity on thermal and biochemical characteristics in CFPCR. This CFPCR has a 20 cycle loop of the microchannel which was fabricated from polycarbonate in a spiral shape. They used Finite Element Analysis (FEA) techniques to predict the temperature distribution variation among different channel radii on a 20 cycle spiral CFPCR device and how the heat transfers to the fluid mixture at a single channel. One thermal cycle was simulated because the temperature

distribution in each thermal cycle was assumed to be the same. Furthermore, quantities such as the transition and residence times of the fluid in each temperature zone were determined to investigate the influence of increasing fluid flow rate and heat transfer characteristics on the product yield. Based on the finite element simulation results they demonstrated that the moving fluid was able to achieve the required temperatures with sufficient periods of thermo-cycling times. They demonstrated that the fluid temperature distribution along the channel is significantly changed with increasing velocity in particular for velocities above $6mm/s$. The fluid in the denaturation zone achieved the desired temperature for velocities less than $20mm/s$, while in the extension zone the fluid never achieved the target temperature for velocities above $10mm/s$. They found the optimum velocity was $2mm/s$.

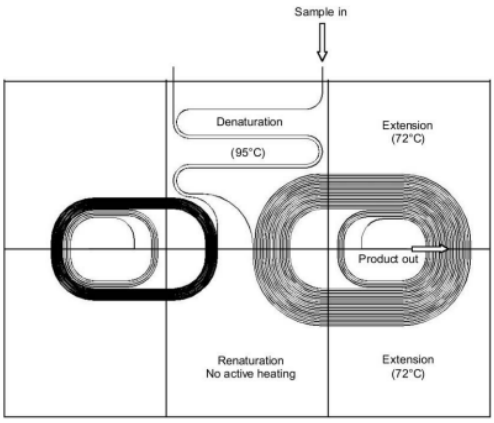

(a)

Figure 2.8: Schematic view of the spiral CFPCR device layout (Hashimoto et al., 2004)

Other studies have explored the benefits of employing a radial PCR device. (Schaerli et al., 2009) carried out an experiment using a 34 cycle continuous flow PCR device in a radial shape consisting of water-in-oil nano-litre droplets, see Figure 2.9. The droplets pass through different temperature zones in a radial pattern for denaturation, annealing and extension. The obtained measurements

proved that highly efficient amplification was achieved even at low template concentrations where most of the droplets either contain no or only one template.

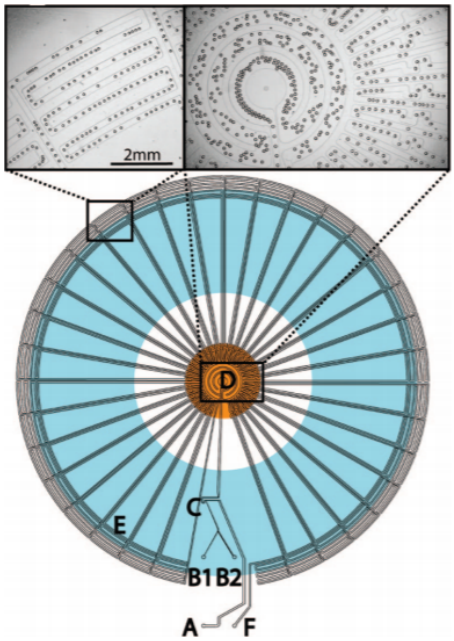

(a)

Figure 2.9: Design of the radial PCR device (Schaerli et al., 2009).

In addition to spiral and radial design presented above PCR based straight channels was presented by (Chiou et al., 2001; Frey et al., 2007), who suggested a capillary microchannel to control the flow of PCR instead of using a micro-pump for active CFPCR. Chiou et al. (2001) explored a novel capillary PCR machine. They tested and conducted thirty-cycle PCR. The obtained results demonstrated that the amplification efficiency was improved by about 78 % within 23 min compared to well-based PCR which takes time 1–2 hr to carry out the same task.

Also Frey et al. (2007) considered a prototype disposable polymer PCR unit consisting of PCR straight channels made of PDMS that is pneumatically connected to a chamber, which is used as an integrated pump as shown in Figure 2.10. They conclude that the amount of sample liquid required for microchannel based PCR was significantly reduced compared to well-based PCR. Consequently, the

reaction and processing time has been shortened. Using a pneumatic pump and external heating source for pumping a small amount of liquid between different temperature zones offers advantages. For instance fast sample manipulation for rapid cycling and low fabrication cost.

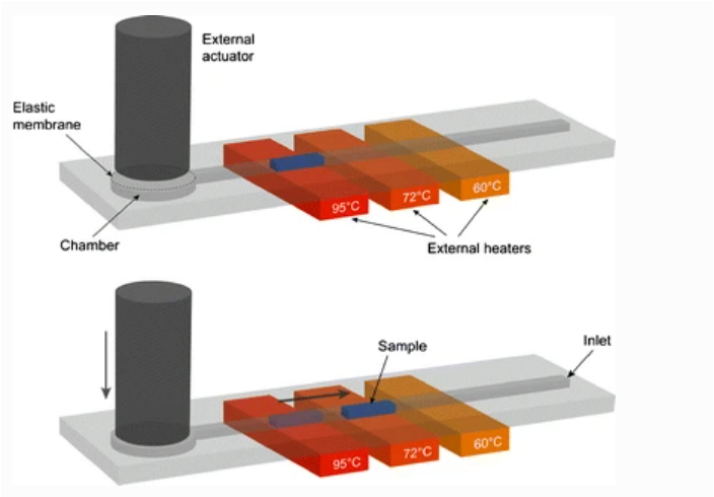

(a)

Figure 2.10: straight microchannel based PCR (Frey et al., 2007)

Tachibana et al. (2015) fabricated a microfluidic PCR device based on capillary forces to transport the sample through the PCR zones. They performed 50 cycles over a microchannel of 1600 mm length, 150 μm wide and 150 μm depth in 14 minutes.

Duryodhan et al. (2016) showed how diverging fluidic channels can create more uniform wall temperatures as a first step to improving the overall temperature uniformity of fluid flowing within the PCR zones. Improved flow uniformity was also achieved through the use of electro-kinetic flow to create a plug-like velocity profile to reduce sample dispersion and increase flow-rate control within PCR channels, (Gui and Ren, 2006).

Selecting appropriate thermal properties which are biologically compatible with the PCR liquid (Kodzius et al., 2012) is also very important for CFPCR device optimisation, (Zhang and Ozdemir, 2009), and the goal of minimising the

heating power required (Miralles et al., 2013). Tsuda et al. (2015) demonstrated the ability of 3D printing to produce bespoke fluidic reactors with complete control of the 3D fluidic network, a finding which motivated a recent exploration of the potential of using 3D printed serpentine fluidic channels for CFPCR, (Park and Park, 2017). The flexibility of 3D printing allowed them to explore a number of alternative heating arrangements with heaters located under each of the three temperature zones. They noted that the low thermal conductivity of the 3D printable materials is an important factor limiting their application in CFPCR devices that require rapid heating and cooling.

Studies on PCR indicated that the PCR reaction kinetics took place in the extension zone and the sample need only to experience the temperature in the denaturation and annealing zone hence, the time needed for extension will dominate each thermal cycle and the PCR process time can be considerably reduced (Innis et al., 1999; Zhang and Xing, 2009). However, to achieve an optimal temperature design for denaturation, annealing, and extension, it should be noted that the temperature in these zones is significantly affected by the fluid flow rate and it is also essential to examine the fluid flow velocity in detail. Thus, considerable optimization for the device design and operation is required to attain the desired temperature and to reduce the residence time in the denaturation and annealing zone. Finding optimal designs and operation for microfluidic PCR systems still mainly relies on the trial-and-error approach. However, the operating parameters and the geometry design can be optimised, and CFD can be employed for this purpose to provide the numerical results essential for optimization where the influence of various materials and layout, flow rate, and heating-cooling arrangements can be easily explored (Kumar et al., 2008; Chen and Li, 2018). Hashimoto et al. (2004) carried out a study to evaluate the effect of high velocity on thermal and biochemical characteristics in CFPCR. This CFPCR has a 20 cycle loop of the microchannel which was fabricated from polycarbonate in a spiral shape. They used Finite Element Analysis (FEA) to predict the temperature distribution variation among different channel radii on the 20 cycle spiral CFPCR device and how the heat transfers to the fluid mixture at a single channel. One thermal cycle was simulated because the temperature distribution in each thermal cycle was assumed to be the same. As mentioned above, such as the transition and

residence times of the fluid in each temperature zone were determined to investigate the influence design and operation influences on the product yield. The finite element results indicated that the moving fluid was able to achieve the required temperatures with sufficient periods of thermo-cycling times. The fluid temperature distribution along the channel changes significantly with increasing velocity, particularly for velocities above 6 mm/s. The fluid in the denaturation zone achieved the desired temperature for velocities less than 20 mm/s, but in the extension zone, the fluid never achieved the target temperature for velocities above 10 mm/s. The optimum velocity was 2 mm/s.

Zhang et al. (2002) used ANSYS Fluent to explore the effect of using different material on continuous–flow PCR chip design, focusing on the heat transfer and temperature distribution. For example, they used glass and silicon as substrate materials which have an extremely different thermal conductivity that is 130 $W/m.K$ for silicon, 0.65 $W/m.K$ for glass. They found that the temperature distribution is significantly affected by the type of material. Due to, the microchannel's small dimensions, the effect of velocity was neglected. They confirmed that it is most significant for a PCR thermal cycle the PCR sample to achieve optimal temperatures for PCR zones. In addition, they demonstrated the temperature distribution in the flow channel, which relies on fluid properties and flow rates, should be explored in more details. Chen et al. (2008) presented a numerical and experimental study to evaluate the temperature distribution along the microchannel of a CFPCR device. The numerical study was based on FEA to investigate the temperature distribution and the effect of different velocities (0 mm/s to 6 mm/s) on CFPCR performance. From their experimental and simulation results they suggested some points to ensure the temperature uniformity within PCR zones such as: (a) decreasing the thermal capacity by reducing the substrate chip thickness; (b) increasing the heat conductivity by using a heating element made from the copper plate; (c) increasing the thermal resistance to lateral heat conduction between temperature zones by making grooves between PCR zones. Their experiments also indicated that the increase of velocity leads to a decrease in the CFPCR amplification efficiency while time per cycle was decreased. This was because shortened residence times can be achieved by increasing the velocity in each temperature zone and the length of the thermal

transition zones can be increased by increasing velocity, and this was predicted by the simulation model of the simple microchannel flow.

2.3 Importance of residence time in PCR

As discussed in Chapter 1, most of the PCR is implemented on (conventional) thermal cycler devices that need more than one hour to complete the process due to the large thermal mass of commercial devices. However, since the 2000s, the miniaturisation of PCR systems have received much attention and accelerated the integration of sample preparation, the product detection, and the DNA amplification into amplification testing systems in order to reduce the processing time. The total analysis time can be significantly reduced by miniaturization. For example, in the CFPCR device, the PCR reaction mixture moves through different temperature zones in a thin channel. Therefore, the residence time can be defined as the duration of time required for moving a sample along thermal PCR steps and exposing them to each temperature region. The transition time is the time period required for the sample to travel between two adjacent temperature regions, for example, denaturation to annealing. Hence, the reaction time is the sum of the transition time and residence time (Ahrberg et al., 2016; Chen and Li, 2018). The microfluidic PCR amplification time can be reduced significantly by increasing the fluid flow velocity through the isothermal zones of the device; for flow velocities at the optimum design value, the PCR mixture achieves thermal equilibrium at each region quickly so that the ideal temperature profiles can be achieved. However, at high flow velocities, there are penalties for an increased pressure drop and a reduced residence time in each temperature zone for the DNA/reagent mixture, which potentially affect the amplification efficiency. Decreasing the sample residence time is significant for amplification efficiency because as described in 1 the amplification is 2^n where n is the number of the cycle. Therefore, decreasing the residence time means the sample will pass the cycle quickly and it can be achieved by increasing the fluid flow velocity in each isothermal zone.

As a result, the pressure drop will be increased by increasing of the velocity and the PCR amplification efficiency can be affected due to the reduced residence

time in each isothermal zone leading to a reduction in the expansion time in the extension zone (Hashimoto et al., 2004; Chen et al., 2015).

2.4 Multi-objective optimisation

The above brief review of PCR systems shows that their effective design presents a complex multi-objective optimisation problem with several competing objectives, constraints and design variables. Key objectives include the minimisation of total processing time and heating power requirements, and the maximisation of temperature uniformity and DNA amplification efficiency. There are also important structural constraints on the pressure drop that can be supported by a PCR chip, while the drive towards device miniaturisation constrains the spacing between fluidic channels. These are all influenced by design variables such as flow speeds, fluid and chip thermal properties, the heating arrangements used, fluidic channel and chip dimensions, their channel shape and the distances between the thermal zones, the latter determining the thermal 'cross-talk' between the zones.

Design optimisation using physics-based simulations is used routinely in the aerospace and automotive industries to solve complex design problems, and several recent advances, that have significantly reduced the time needed to optimise complex flows using CFD, have led to growth in several other applications areas too (Khatir and Thompson, 2019). The time needed for complex flow simulations, for example, can be reduced significantly by exploiting multi-scale wavelet methods, which provide efficient surrogates for transferring dynamic, microscale interactions into macroscopic flow simulations, (Gur et al., 2016), or by using multi-fidelity modelling which enables most of the computational work to be done on cheaper, lower fidelity models, (Serani et al., 2019). In addition, advances in design space exploration methods are making large-scale optimisation feasible within practical timescales. Haftka et al. (2016) noted that adjoint methods can now be used to solve large design problems, where the number of design variables is in the 1000s, whereas for problems with < 100 design variables (such as the design of PCR systems), gradient-free surrogate-assisted optimisation methods are very effective. Examples of the latter include Moving Least Squares, which is effective at minimising the deleterious effects of numerical noise, (González Niño

et al., 2019). Gaussian Process Emulators also provide very effective statistical surrogates, (Domingo et al., 2020), which can determine confidence intervals around predictions and deal effectively with mixed continuous/categorical design variables, (Garrido-Merchán and Hernández-Lobato, 2020). Supervised Machine Learning (ML) methods also provide powerful surrogate modelling methods with Neural Networks (NNs) and Support Vector Machines (SVMs) having been applied successfully to a range of complex flow systems, (Wang et al., 2017). After the surrogate models have been calibrated successfully, they can be implemented within an appropriate multi-objective optimisation algorithm, (Kotinis and Kulkarni, 2012).

Applying optimisation methods like the above to PCR systems is a key contribution of this thesis and these methods are discussed in much more detailed in Chapter 4.

2.5 The scope of present work

The scope of the present work is to explore how the geometry and operating parameters affect the temperature, fluid flow conditions and the residence time fields in serpentine PCR systems, and variations throughout each PCR zone. For example, substrate materials, drive mechanisms, and heating/cooling mechanisms, mass flow rate (injected fluid velocity), reaction time and number of cycles are considered.

Chapter 3

Heat Transfer and Fluid Flow Fundamental in PCR Microfluidic Systems

3.1 Introduction

The basic concepts of fluid flow and heat transfer in rectangular channels are described in this chapter. Firstly, the types of heat transfer and relevant non-dimensional parameters will be presented. Secondly, the flow features in channels, such as hydrodynamic and thermal entrance length, and the influence of thermal boundary conditions will be explained. Thirdly, useful correlation equations will be discussed. This chapter will be focused on theory and fundamental heat transfer and fluid flow in microfludic PCR systems.

3.2 Fluid dynamics

Fluid dynamics is a part of fluid mechanics that describe the fluid (liquid and gases) in motion and it can be subdivided to aerodynamics (the study of air and other gases in motion) and hydrodynamics (the study of liquids in motion), (Batchelor and Batchelor, 2000).

Fluid flow is categorized into two types: external flow and internal flow, depending on whether the fluid is forced to flow in a confined channel or over a surface, (Yunus, 2010). External fluid flow is the flow of fluid over surfaces. In contrast internal flow means the flow of liquid confined within surfaces such as flow inside channels, (White, 2009). The flow of fluid also can be classified based on the type of flow into natural and forced flow. The fluid flow can be forced by using pump or natural by buoyancy force.

Additionally, the flow can be classified to steady and unsteady flow. Steady state flow is defined as the condition of fluid flow of a specific domain in which the properties of the flow (pressure, velocity, temperature) at a point do not change with respect to time (time independent). While the unsteady flow refers to the condition of flow in which the fluid properties at a point in fluid domain change with respect to time (Cengel et al., 2004).

3.3 Microfluidic channels

Microfluidic channels are a set of micrometer channels that can be etched or moulded into a material such as glass, polymer or silicon to form the desired features of a microfluidic device. This device can be recognized by the fact that it has one or more channels with at least one dimension of less than 1 mm, (Whitesides, 2006). Additionally, the channel can be classified according to its dimensions to the conventional channel, mini-channel, and microchannel. Based on channel dimensions, (Mehendale et al., 1999) suggested a classification in terms of hydraulic diameter or the smallest dimension for other cross-sections, while, (Kandlikar et al., 2005) classified the channels based on fluid flow. The classifications pointed out by both these authors are listed in Table 3.1.

In next section the governing equations used to describe the three-dimensional flow and heat transfer in microchannel PCR systems will be presented.

Microchannel classification		
Channel type	(Mehendale et al., 1999)	(Kandlikar et al., 2005)
Conventional Channels	$D_h > 6mm$	$D_h > 3mm$
Compact passages	$1mm < D_h \leq 6mm$	-
Meso-channels	$100\mu m < D_h \leq 1mm$	-
Micro-channels	$1\mu m < D_h \leq 100\mu m$	$10\mu m < D_h \leq 200\mu m$
Mini- channels	-	$200\mu m < D_h \leq 3mm$
Transitional Microchannels	-	$1\mu m < D_h \leq 10\mu m$
Transitional Nanochannels	-	$0.1\mu m < D_h \leq 1\mu m$
Molecular Nanochannels	-	$D_h \leq 0.1\mu m$

Table 3.1: Classification of the Microchannel

3.4 Equations governing fluid flow and heat transfer

The flow and heat transfer of a laminar, Newtonian fluid in microchannel PCR systems depicted in Figure 3.1 is governed by the Navier-Stokes equations. The governing equations are described in the following subsections.

3.4.1 Continuity equation

The continuity equation, representing the conservation of mass, is given in a three-dimensional flow in terms of compressible flow:

$$\frac{\partial \rho}{\partial t} + \frac{\partial (\rho u)}{\partial x} + \frac{\partial (\rho v)}{\partial y} + \frac{\partial (\rho w)}{\partial z} = 0 \tag{3.1}$$

where u,v and w are respectively the velocity components of flow in the x , y and z directions. Equation 3.1 can be applied for the general case of three-dimensional unsteady compressible flow.

$$\nabla = \frac{\partial}{\partial x} i + \frac{\partial}{\partial y} j + \frac{\partial}{\partial z} k \tag{3.2}$$

This can be written in a vector form:

$$\frac{\partial \rho}{\partial t} + \nabla \cdot \rho \overrightarrow{V} = 0 \tag{3.3}$$

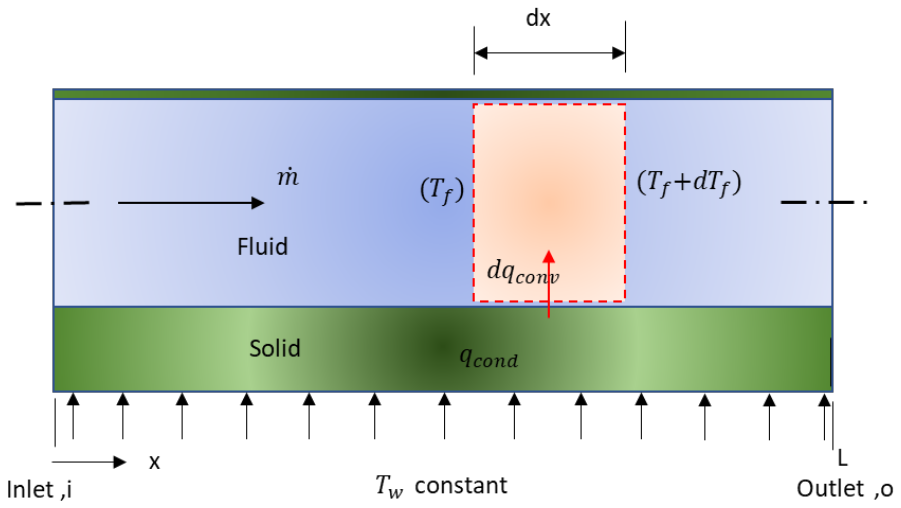

(a)

Figure 3.1: Control volume of fluid flowing in a fluidic channel heated at constant wall temperature.

where ρ is the density of liquid ($kg \cdot m^{-3}$), ∇, refers to the vector gradient operator and $\overrightarrow{V}$ is the fluid velocity vector defined.

Therefore, for steady state flow this equation can be reduced to:

$$\nabla \cdot \rho \overrightarrow{V} = 0 \tag{3.4}$$

3.4.2 Momentum equation

The Navier-Stokes equations denote the conservation of momentum. For single-phase laminar flow, a compressible Newtonian fluid including the effect of gravitational forces, under transient conditions, the general momentum equation in a three-dimensional Cartesian coordinate form is :

X- direction

$$\rho(\frac{\partial u}{\partial t} + u\frac{\partial u}{\partial x} + v\frac{\partial u}{\partial y} + w\frac{\partial u}{\partial z}) = -\frac{\partial p}{\partial x} + \rho g_x - (\frac{\partial \tau_{xx}}{\partial x} + \frac{\partial \tau_{yx}}{\partial y} + \frac{\partial \tau_{zx}}{\partial z}) \tag{3.5}$$

Y-direction

$$\rho(\frac{\partial u}{\partial t} + u\frac{\partial v}{\partial x} + v\frac{\partial v}{\partial y} + w\frac{\partial v}{\partial z}) = -\frac{\partial p}{\partial x} + \rho g_y - (\frac{\partial \tau_{xy}}{\partial x} + \frac{\partial \tau_{yy}}{\partial y} + \frac{\partial \tau_{zy}}{\partial z}) \tag{3.6}$$

Z-direction

$$\rho(\frac{\partial w}{\partial t} + u\frac{\partial w}{\partial x} + v\frac{\partial w}{\partial y} + w\frac{\partial w}{\partial z}) = -\frac{\partial p}{\partial x} + \rho g_z - (\frac{\partial \tau_{xz}}{\partial x} + \frac{\partial \tau_{yz}}{\partial y} + \frac{\partial \tau_{zz}}{\partial z}) \quad (3.7)$$

where :

$$\tau_{xx} = -\mu(2\frac{\partial u}{\partial x} - 2/3\nabla \cdot \overrightarrow{V}) \quad (3.8)$$

$$\tau_{yy} = -\mu(2\frac{\partial v}{\partial y} - 2/3\nabla \cdot \overrightarrow{V}) \quad (3.9)$$

$$\tau_{zz} = -\mu(2\frac{\partial w}{\partial y} - 2/3\nabla \cdot \overrightarrow{V}) \quad (3.10)$$

$$\tau_{xy} = \tau_{yx} = -\mu(\frac{\partial u}{\partial y} + \frac{\partial v}{\partial x}) \quad (3.11)$$

$$\tau_{xz} = \tau_{zx} = -\mu(\frac{\partial u}{\partial z} + \frac{\partial w}{\partial x}) \quad (3.12)$$

$$\tau_{yz} = \tau_{zy} = -\mu(\frac{\partial v}{\partial z} + \frac{\partial w}{\partial y}) \quad (3.13)$$

Therefore, for temperature dependent fluid properties this equation can be expressed in vector form :

$$\rho\frac{\partial \rho}{\partial t} + \overrightarrow{V}\nabla \cdot \overrightarrow{V} = -\nabla p + \nabla \cdot \mu(\nabla \cdot \overrightarrow{V} + (\nabla \cdot \overrightarrow{V})^T) - 2/3(\nabla \cdot \overrightarrow{V}))I + F \quad (3.14)$$

For steady state solution this equation can be reduced to:

$$\overrightarrow{V}\nabla \cdot \overrightarrow{V} = -\nabla p + \nabla \cdot \mu(\nabla \cdot \overrightarrow{V} + (\nabla \cdot \overrightarrow{V})^T) - 2/3(\nabla \cdot \overrightarrow{V}))I + F \quad (3.15)$$

Where $\overrightarrow{V}$ is the fluid velocity vector $\overrightarrow{V} = ui + vj + wk.$ which represent the velocity components [m/s] in the x,y,and z directions, F is the body force, p is the fluid pressure $[Pa]$, and ρ and μ are the density and viscosity of the fluid, respectively.

3.4.3 Energy equation

The energy equation describes the heat flow through the liquid phase and solid in the microchannel by considering convection terms in the equation as:

$$\rho_f C_p(u\frac{\partial T}{\partial x} + v\frac{\partial T}{\partial y} + w\frac{\partial T}{\partial y}) = k(\frac{\partial^2 T}{\partial x^2} + \frac{\partial^2 T}{\partial y^2} + \frac{\partial^2 T}{\partial z^2}) \tag{3.16}$$

where C_p $(J/kg.K)$ is the specific heat and k is the thermal conductivity of the liquid. The heat transfer (energy) equations for the liquid and the solid can be expressed in vector form respectively as:

$$\rho_f C_p \overrightarrow{V} \cdot \nabla T_f = \nabla \cdot (k_f \nabla T_f) \tag{3.17}$$

$$\nabla \cdot (k_s \nabla T_w) = 0 \tag{3.18}$$

where T_f, k_f are the temperature and thermal conductivity of the liquid, while T_w and k_s are the temperature, and thermal conductivity of the solids. Water has been chosen as the working fluid for numerical analysis in this project.

3.5 Dimensionless Parameters in Fluid Flow and Heat Transfer

3.5.1 Reynolds Number

Reynolds number (Re) is the ratio between inertial and viscous forces, as presented in Equation 3.19 it is a dimensionless number used to identify the characteristics of the fluid (laminar or turbulent).

$$Re = \frac{\rho_f V_{ch} D_h}{\mu_f}, \tag{3.19}$$

where ρ_f and μ_f are the density and viscosity of the fluid respectively, V_{ch} is the channel inlet velocity and D_h the channel hydraulic diameter defined by:

$$D_h = \frac{2W_c H_c}{W_c + H_c}. \tag{3.20}$$

For CFPCR flows, $V_{ch} \sim 1mm/s$, $D_h \sim 10^{-4}$ m and a water density of $10^3 kg/m^3$ and dynamic viscosity $10^{-3} Pa \cdot s$, leads to $Re \sim O(10^{-1})$, i.e. laminar flow conditions. In microfluidic systems the flow is typically laminar (Hardt and Schönfeld, 2007) and Reynolds number is low due to the slow flow type and small size in which the flow is dominated by viscous effect. In case of (Re≤1) creeping (Stokes) flow can be applied. In Stokes flows also called creeping flow where, the viscous forces are high in comparison with inertial forces. For example, paint flow and lubrication in mechanical systems.

In addition to Reynolds number there is another dimensionless number are used in Microfluidic systems such as:

3.5.2 Prandtl number

The Prandtl number (Pr) is a dimensionless number representing the relative ratio of momentum diffusivity to thermal diffusivity, (Rapp, 2016).

Prandtl number can be used to evaluate the relation between momentum transport and thermal transport of fluid.

$$Pr = \frac{\text{Molecular diffusivity of momentum}}{\text{Molecular diffusivity of heat}} \tag{3.21}$$

$$Pr = \frac{\nu}{\alpha} = \frac{\mu_f/\rho_f}{k_f/\rho_f C_{pf}} = \frac{\mu_f C_{pf}}{k_f} \tag{3.22}$$

where C_{pf} and k_f respectively represent the specific heat capacity (J/kg.K) and the thermal conductivity (W/m.K) of the fluid. The relative thickness of the velocity δ_u and the thermal δ_{th} boundary layers can be assessed by the Prandtl number as:

$$Pr = (\frac{\delta_u}{\delta_{th}})^{1/n} \tag{3.23}$$

where n is a positive exponent ($n > 0$). Figure 3.2 reveals the Pr as a function of temperature for different fluids at atmospheric pressure. For fluids with laminar flow and low Prandtl number ($P_r < 1$) (i.e., liquid metals such as Mercury), the thermal boundary layer is thicker than the velocity boundary layer; the fluid is low viscosity but very conductive (the fluid will transport thermal energy very

well but not momentum). While in the case of $P_r > 1$, such as engine oils, the thermal boundary layer is fully contained within the velocity boundary layer, as shown in Figure 3.3, and the fluid in this case is viscous and non-conductive (the fluid will transport momentum very well but not thermal energy).

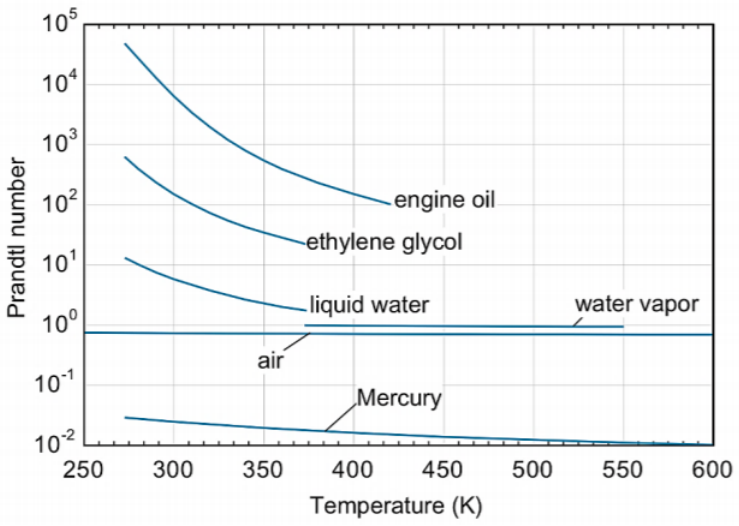

Figure 3.2: Prandtl number versus temperature for various fluids.

3.5.3 Peclet Number

The Peclet number (P_e) is the ratio of the rate of heat convection to heat diffusion. The Peclet number is related to the product of Prandtl number and Reynolds number. The Peclet number can be used to assess the importance of convection in comparison with thermal conduction. Thus, in the case of small Peclet number < 1 the axial thermal conduction should be considered. Also, the axial conduction effect is small for $P_e > 10$ and it can be neglected for $Pe > 100$.

The Peclet number is defined as:

$$P_e = ReP_r \tag{3.24}$$

$$P_e = \frac{V_{ch}L_c}{\alpha} \tag{3.25}$$

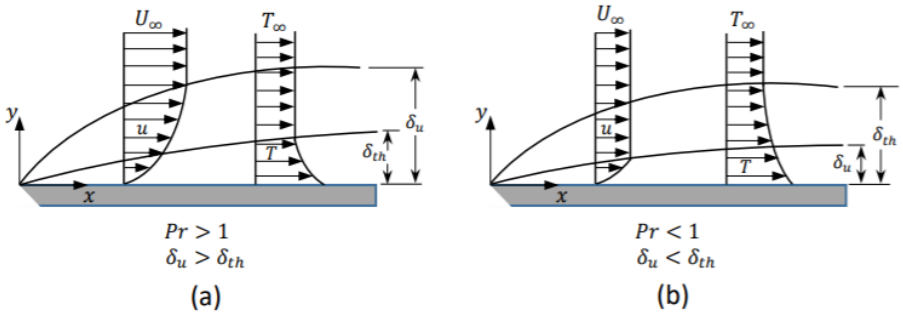

Figure 3.3: The hydrodynamic and thermal boundary layer thicknesses for (a) $P_r > 1$ and (b) $P_r < 1$.

where α is the thermal diffusivity of the liquid and L_c is the characteristic length and it represents D_h in channel flow. Thus Equation 3.25 can be rewritten as :

$$P_e = \frac{V_{ch}.D_h}{\alpha} \tag{3.26}$$

3.5.4 Nusselt number

The Nusselt number (Nu) is a dimensionless number represents the ratio of convective to conductive heat transfer rates across the boundary. It is first proposed by Wilhelm Nusselt. A small Nusselt number around 3 and 4, for which convection and conduction of similar magnitude, is characteristic of laminar flow. A larger Nusselt number corresponds to more active convection, with turbulent flow typically more than 85. The Nusselt number is defined as:

$$N_u = \frac{\text{Convective heat transfer}}{\text{Conductive heat transfer}} \tag{3.27}$$

$$N_u = \frac{h.D_h}{k_f} \tag{3.28}$$

where h is convective heat transfer coefficient and k_f is the thermal conductivity of the fluid.

The Nusselt number for fully developed laminar flow inside a channel heated at constant heat flux can be calculated based on the correlation proposed by (Shah, 1978)

$$Nu = 8.235(1 - 2.0421\epsilon 3.0853\epsilon^2 - 2.4765\epsilon^3 + 1.0578\epsilon^4 - 0.0.1861\epsilon^5) \quad (3.29)$$

The Nusselt number for fully developed laminar flow inside a channel heated at constant wall temperature can be calculated based on the following correlation also proposed by (Shah, 1978)

$$Nu = 7.541(1 - 2.61\epsilon + 4.97\epsilon^2 - 5.119\epsilon^3 + 2.702\epsilon^4 - 0.548\epsilon^5) \quad (3.30)$$

where $\epsilon = W_c/H_c$. h can then be found from:

$$Nu = hD_h/k_f \quad (3.31)$$

3.5.5 Biot number

Biot number(Bi) is the ratio of conduction to convection heat transfer.

$$Bi = \frac{h.D_h}{k_s} \quad (3.32)$$

where h refers to heat transfer coefficient, D_h is the channel hydraulic diameter and k is the material thermal conductivity. Bi number < 0.1 means that conduction dominate over convection.

3.5.6 Grashof number

Grashof number is the ratio of the buoyancy forces to the viscous forces acting on the fluid, its play role in free convection similar to the role of Reynolds number in forced convection. Grashof number is described as:

$$G_r = \frac{g\beta(T_w - T_\infty)L^3}{\nu^2} \quad (3.33)$$

where g is the gravitational constant , β is the thermal expansion coefficient which is $595.4 \times 10^{-6}/K$ at a temperature of $345K$.

Grashof number is used to identify the flow regime in free convection whether the fluid flow is laminar or turbulent. For example the flow on vertical flat plate is considered turbulent if Gr greater than 10^9. The Rayleigh number (R_a) is the

product of the Grashof number and the Prandtl number (Squires and Quake, 2005; Çengel et al., 2008):

$$R_a = G_r P_r \tag{3.34}$$

In microfluidic PCR systems the top and side walls of the PCR chip are exposed to natural convective. So natural convection boundary conditions should be involved in this study. The value of external heat transfer coefficient $\hat{h}$ can be obtained from the empirical correlation related Nusselt number and Rayleigh number

$$N_u = \frac{\hat{h} L_c}{k_{air}} \tag{3.35}$$

The empirical correlation equations need to find the free convection from surfaces are available in CFD packages such COMSOL and it is easy to be engaged with heat transfer and fluid flow model.

3.6 Viscous flow

Fluid flow in a confined channel or over a surface arises through motion of the fluid layers relative to each other in which the slower layer near the surface attempts to retard the faster layer due to internal resistance to flow that is quantified by the fluid viscosity . Such flow is named viscous flow in which the frictional effects are significant, typically all the fluid involve viscous effect to some degree.

However, in fluid flow there is a region not close to the surface called inviscid region in which the viscous forces are negligibly small compared to inertial or pressure forces. Figure 3.4 shows a flat plate inserting parallel into a fluid stream of uniform velocity, on both sides of flat plate the fluid is Stuck where there is no slip boundary condition. A thin boundary layer is developed near the plate surface in which the viscous effect is important. This figure also showed the region of flow on both sides away from the plate are not affected by the presence of plate that is called inviscid region.

At high Reynolds number, typically $Re > 4000$ for external flow and $Re > 2300$ for internal flow, the flow is inviscid flow in which the inertial force is dominantand and the effect of viscosity can be neglected. While at low Reynolds number, the flow is viscous flow and it is governed by viscous effects in which

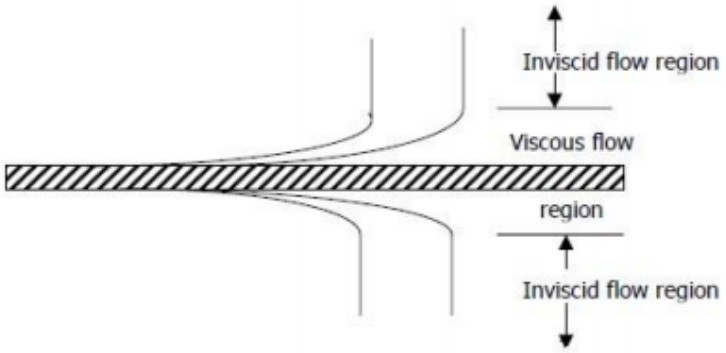

Figure 3.4: The flow of an originally uniform fluid stream over a flat plate, and the regions of viscous flow (next to the plate on both sides) and inviscid flow (away from the plate) (Yunus, 2010).

the effect of viscosity is significant due to internal friction resistance (Cengel and Ghajar, 2007). Also dominated by no slip condition at solid walls. The fluid flow regime in microfluidic systems is dominated by the viscous forces,as flows typically arise on a length scale that is a small order of magnitude, so the Reynolds number value is small.

In the case of motion of fluid inside a channel the viscosity effect takes place. This effect leads to friction forces between fluid particles and in the contact area between fluid and the bounded surface. This results in velocity gradients leading to a growing boundary layer. The conditions at which interfacial forces dominate over gravity, inertial and viscous forces corresponds to low velocities and small microchannel sizes

3.6.1 Hydrodynamic and Thermal Fluid Flow Entrance zone

The velocity profile of a fluid flowing through a channel develops at the entrance region of the channel and the flow profile is named hydrodynamically developing flow. After this region the flow is developed continuously, and the flow profile is changed from developing to fully developed region. At this region the flow become

hydrodynamically fully developed and the velocity profile shape becomes parabolic and does not change, see Figure 3.5. The hydrodynamic entrance length for single laminar flow in a rectangular channel can be calculated using the equation proposed by (Shah, 1978):

$$L_h = 0.05 Re D_h \tag{3.36}$$

The hydrodynamic entry length is about the size of the diameter for Re=10, (Cengel, 2014). For microchannel based PCR, where the hydraulic diameter is order of 10^{-3} and Re order of 1, the hydrodynamic entrance length is very small and the flow is fully developed from the entrance. In addition, the thermal boundary layer starts to develop from the channel entrance region in which the temperature profile shape is developing, and the flow is named thermally developing. After the entrance zone the flow become thermally fully developed. The thermal entrance length for laminar flow is estimated by (Holman, 2009) to be:

$$L_{th} = 0.05 Re Pr D_h \tag{3.37}$$

3.6.2 Flow Condition in Microchannel

In the case of long narrow channels with small values of heat flux, the flow in the channel quickly becomes fully developed. The velocity profile assumes parabolic shape, the average fluid velocity is constant, and the fluid temperature at the wall increases linearly along the length of the channel. In this fully developed regime, the local heat transfer coefficient is constant (neglecting the temperature dependence of fluid properties).

3.7 Heat transfer

Heat transfer is a form of energy transport which takes place in the presence of temperature differences. Heat transfer can be categorized into three modes: conduction, convection and radiation (Cengel and Heat, 2003) as shown in Figures 3.6 and 3.7. Heat conduction is the transfer of heat in one medium (solids, liquids, or gases) or in more than one medium through physical contact between them

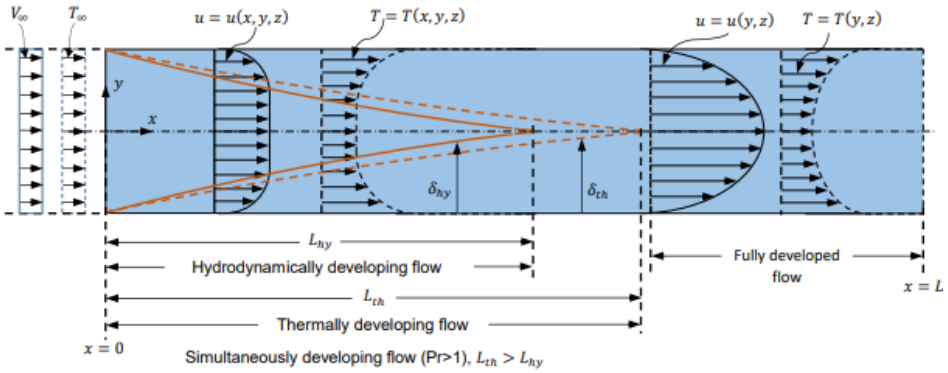

Figure 3.5: Thermal and hydrodynamics developing flow in channel.

(Arpaci, 1966). It is the microscopic transport of energy from higher energy particles to lower energy particles within the substance. The second mode of heat transfer is that between a solid surface and an adjacent moving fluid and is referred to convection. The third mode of heat transfer is the radiative heat transfer which can be defined as the emission of heat from a substance in the form of electromagnetic waves owing to change in electronic configuration of the atoms (Polder and Van Hove, 1971)

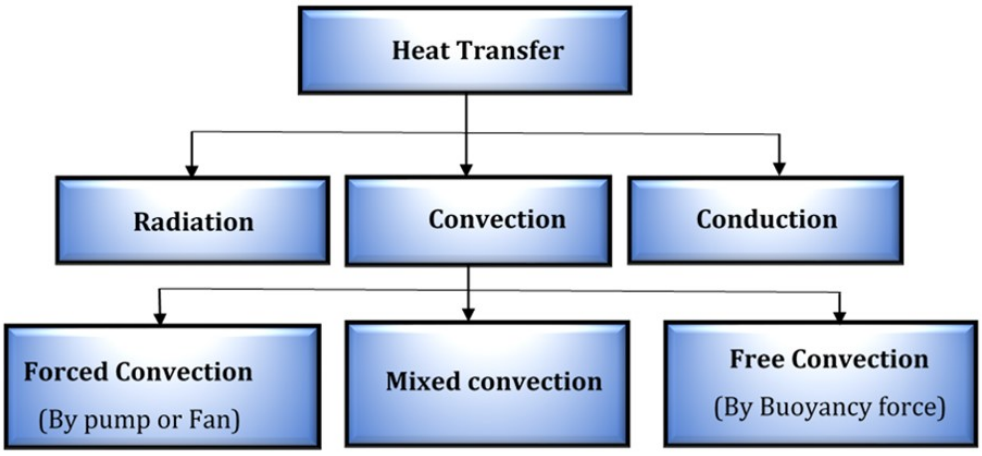

Figure 3.6: Simple flowchart for types of heat transfer modes.

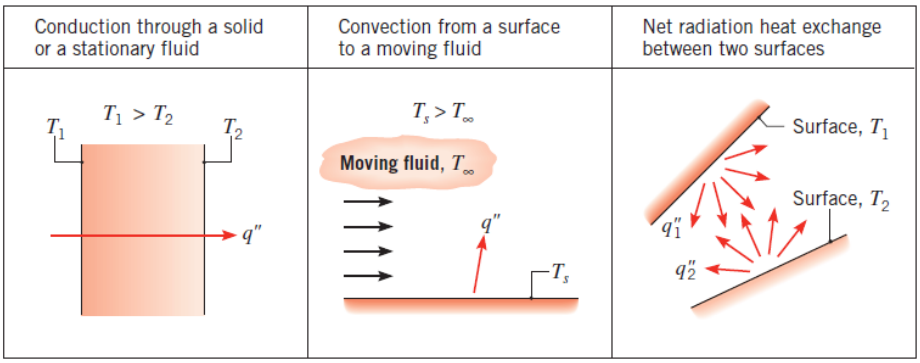

Figure 3.7: Conduction, convection, and radiation heat transfer modes (Bergman et al., 2011).

3.7.1 Physical mechanism of conduction heat transfer

The physical mechanism of heat conduction can be denoted as the exchange of kinetic energy between the molecules within the substance from the high temperature zone, which has more energetic particles, to a low temperature zone which has less energetic particles. Conduction can take place in fluid or solid. In a fluid (gases or liquids) conduction takes place due to the diffusion and collisions of the molecules during their random motion. In a solid it takes place due to the energy interactions caused by vibrations of the molecules in a lattice and the energy transport by free electrons (Holman, 2008; Ahsan, 2011). Thus, the high thermal conductivities of metals are primarily due to the electronic component, see Figure 3.8 which reveals the molecule collisions at the boundary surface between two bodies. The left side represents a region of high energy due to its high temperature compared with the right hand region of low energy due to its low temperature. Consequently, a molecule in the higher-temperature region has high energy before collision, however, the energy of this molecule will be decreased after collision with a molecule from low energy region at the contact surface. In contrast the molecule in the lower-temperature region has low energy before colliding and its energy is increased after colliding with a high-energy molecule at the contact surface.

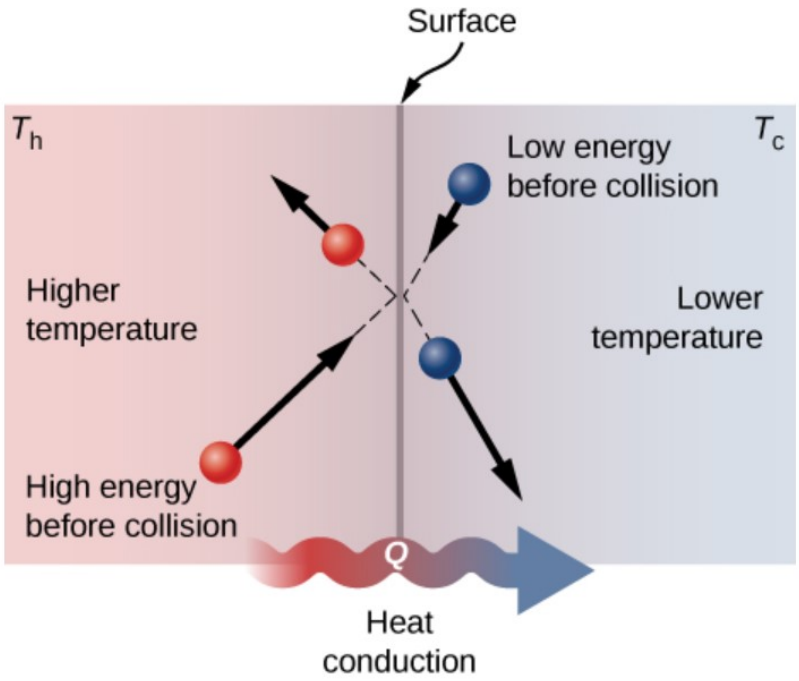

Figure 3.8: Schematic diagram of molecular collisions at different temperatures. (Afework et al., 2020)

Therefore, in microfluidic systems the heat transfer in the solid region is dominated by conduction and the fluid conveys the heat away from the surface by convection. At low Reynolds numbers and flow speeds, heat transfer can be dominated by heat conduction through the fluid layers. The rate of conductive heat transfer was firstly modelled by Joseph Fourier in 1822 who noticed that the rate of heat transfer by conduction through a medium depends on the negative gradient of the temperature within the substance, its thickness, and its material type. He proposed Fourier's law for one dimension as:

$$q = -k\frac{dT}{dX} \tag{3.38}$$

where q is the rate of heat conduction $(W/m^2 \cdot K)$, i.e heat flow rate per unit area. k is the (isotropic) material thermal conductivity. dT is the temperature difference between two points. dx is the distance between two points. Equation 3.38 can be rewritten by considering three-dimensional heat conduction as:

$$q = -(k\frac{dT}{dX} + k\frac{dT}{dY} + k\frac{dT}{dZ}) \tag{3.39}$$

Thermal conductivity is a physical property of a material which describes its ability to transfer heat by diffusion. Therefore, it can be noted that the thermal conductivity of metals is high compared to thermal conductivity of plastics. Therefore, the thermal conductivity of a substance is the rate of the conductive heat transfer through a unit thickness of the material per unit temperature difference. The thermal conductivity of materials is significant in microfluidic systems. Table 3.2 shows examples of thermal conductivity for different materials commonly used in microfluidic systems.

Material	**thermal conductivity k (W/m.K)**
Water	0.6
Silicon	130
Glass	1.4

Table 3.2: Typical values of thermal conductivities of selected materials.

3.7.2 Physical mechanism of radiation

In general, the radiation of heat can be defined as the thermal energy transport due to emission of electromagnetic radiation waves from the material. In contrast to conduction and convection, thermal radiation does not necessarily require a medium for the transport of energy. The heat energy can be radiated between bodies from the body with the higher temperature to the lower temperature one when these are not in direct physical contact, (Holman, 2009). Thermal radiation is the transfer of heat from the surface wall to the space or it can be transmitted from the heating source to the bodies such as the heat radiation from sun to the earth or from the sun to the solar plate.

At the microscopic level radiation can be described as the emission of electromagnetic radiation due to the radiation of particles. Accordingly, acting at a distance, the radiation is global, and is reversible when it happens through vacuum. The energy radiated from a surface depends on its temperature and its capability to emit energy, i.e. its emissivity. The amount of absorbed, transmitted or reflected energy from a surface due to incident radiation depends on the material properties of surface see Figure 3.9. The ideal thermal radiator is named a black-body, which is also the perfect absorber of incident radiation of all wavelengths. Also, the black-body can emit thermal energy at rate to the fourth power of the absolute temperature of the surface which ac be determined by Stefan-Boltzmann law of radiation:

$$Q/t = \sigma.\epsilon.A.T^4 \tag{3.40}$$

where σ=5.67$X10^{-8}$ $(J/(s.m^2.K^4$)) is the Stefan-Boltzmann constant, A is the surface area of the object, and T is its absolute temperature in Kelvin. The symbol ϵ stands for the emissivity of the object, which is a measure of how well it radiates. An ideal jet-black (or black body) radiator has $\epsilon = 1$, whereas a perfect reflector has $\epsilon = 0$.

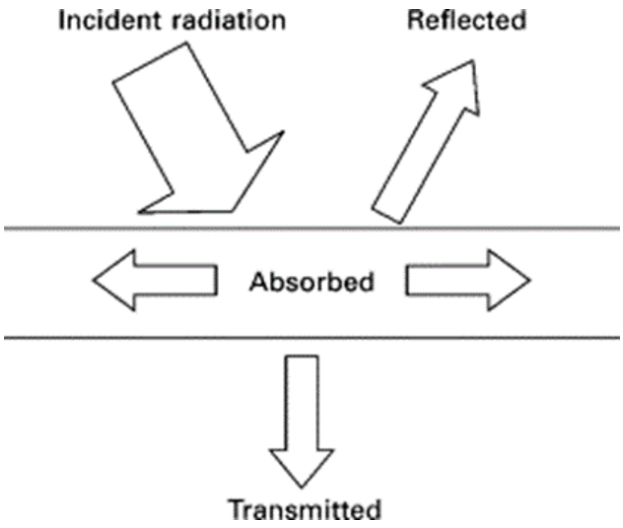

Figure 3.9: Absorption, reflection and transmission of incident thermal radiation by a material (Hall and Allinson, 2010).

3.7.3 Physical mechanism of convection heat transfer

A convection process is a heat transfer process whose rate is directly affected by the fluid motion. This process can be described by the flow of energy from high energy zone to low energy zone. The convection heat transfer refers to the heat transfer due to the energy exchange between a surface and an adjacent fluid in motion when the two are at different temperatures.

The convection heat transfer mode is divided into two mechanisms (Zhang et al., 2019):

1. Diffusion which refers to thermal energy transfer due to random molecular motion.

2. Advection which refers to thermal energy transfer due to the bulk or macroscopic motion of the fluid.

The convection heat transfer mode takes place by both diffusion and advection within the boundary layer. The diffusion dominates near the surface where the fluid velocity is low. In particular at the interface between fluid and solid where the velocity is zero, the heat transfer is only by diffusion. With the progress of

the flow the boundary layer grows in the flow direction, and the heat is conducted into the thermal boundary layer and swept downstream, then transferred to the fluid outside this layer. The relative growth of the hydrodynamic and thermal boundary layers in laminar flow is governed by the Prandtl number. The convection can be classified to internal or external convection based on the fluid flow types, internal or external see section 3.2. Also for both types of convection and based on whether the flow is forced or free, the convection can be subdivided into two types: forced and natural convection.

Forced convection can take place under the effect of an external force such as a fan or pump, see Figure 3.10(a) which reveals a fan used to provide air for cooling of hot surface by forced convection. In the natural convection the flow is induced by buoyancy forces, which are due to density differences caused by temperature variations in the fluid, see Figure 3.10 (b) which shows the transfer of heat from a hot surface due to the increases of air temperature in contact with the surface. This leads to a reduction in air density; then it becomes lighter and goes up due to buoyancy forces and it exchanges heat with air layers and cools then it goes down. This process is called external natural convection.

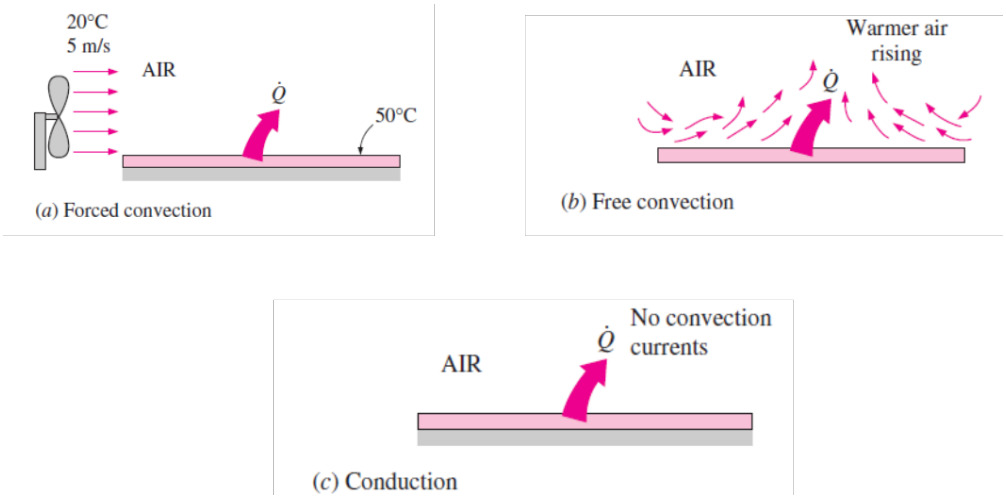

Figure 3.10: Physical mechanism of heat transfer from a hot surface to cool surrounding air by convection and conduction (Cengel, 2014)

3.8 Application of natural convection in PCR systems

Flow driven by convection can be produced due the temperature gradients by applying heat from the bottom boundary or from one side of vertical boundaries, see Figure 3.11. This concept can be applied to design PCR thermal systems by generating a temperature gradient across a closed loop geometry. For example the rectangular enclosure geometry shown in Figure 3.12 illustrates the thermal cycle closed loop to create the three steps of PCR process by using two Peltier heaters one fixed in the bottom fixed at $(95°C)$ (denaturation) and one fixed on the top side at $(56°C)$(annealing) the annealing zone can be attained by passive cooling (Allen et al., 2009). Also, the PCR thermal cycle closed loop can be obtained by using a prototype of a triangular flow geometry to replicate the three steps of PCR process (denaturation, annealing and extension). Two independent Peltier heaters were fixed on opposite sides of a triangular aluminum geometry as depicted in Figure 3.13. The first heater is fixed at $(94°C)$ in denaturation zone and the second one is fixed at $(72°C)$ in extension zone while the annealing zone can be attained by passive cooling to obtain $(55°C)$ or $(60°C)$. This design offers appropriate driving force to initiate circulation flow through the loop, (Agrawal and Ugaz, 2007).

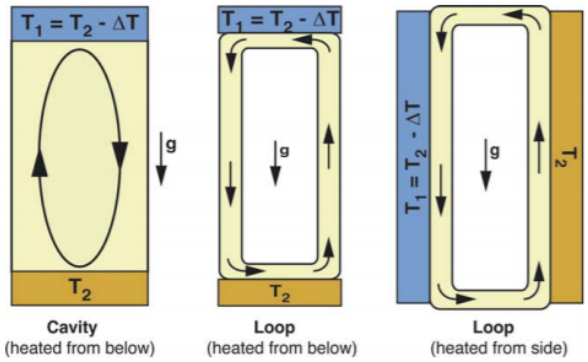

Figure 3.11: Buoyancy-driven convective flows in a cavity and closed loop geometries (Agrawal and Ugaz, 2007)

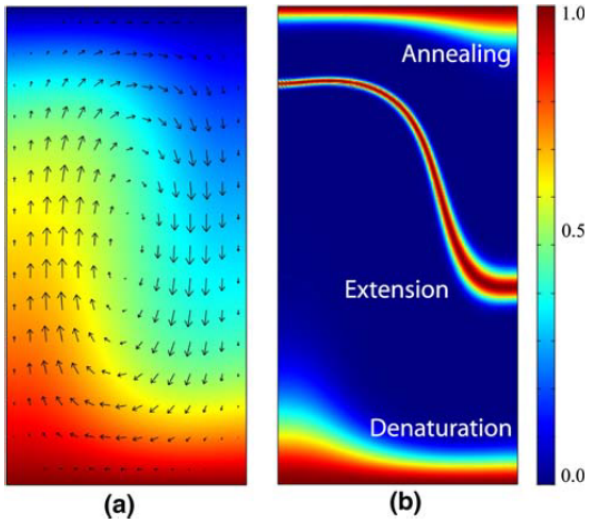

Figure 3.12: (a) Velocity and temperature contour at width to height ratio 0.5 and and a Rayleigh number Ra = 3,000. (b) Kinetic rates (Allen et al., 2009)

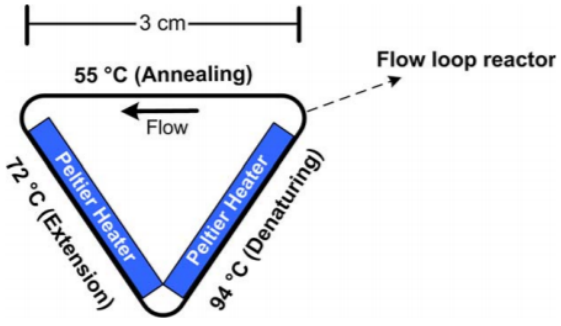

Figure 3.13: Schematic of the Thermal PCR device incorporating Peltier heaters on two sides of a triangular geometry(Agrawal and Ugaz, 2007)

3.9 Forced Convection in PCR systems

The geometry of the serpentine channels is proposed, to improve the thermal performance of the PCR device as shown in Figure 3.14, which reveals a fluidic channel passing through denaturation ($95°C$), annealing ($55°C$) and extension ($72°C$) zones used as a prototypical CFPCR thermal flow problem. Glass or silicon is used as the substrate material, which have high thermal conductivity compared with different microfluidic materials to reduce the conductive thermal resistance between the copper block and substrate material. This ensures the heat is transferred to the substrate instead of going in the axial direction. In addition, the cover material used needs to be material with low thermal conductivity to reduce the heat dissipated to the air by free convection. Thus, PDMS or PMMA are appropriate for the cover and can provide good thermal insulation. Individual copper or aluminum blocks can be used as a heat source with built-in cartridge heaters placed underneath the glass chip and separated by a distance between them in order to isolate the zones to reduce thermal cross between PCR zones. The continuous flow polymerase chain reaction (CFPCR) process is an example of forced convection heat transfer. The top and side walls of PDMS are imposed with natural convective boundary conditions.

The value of external heat transfer coefficient (h) can be computed by using empirical relation of Nusselt number and Rayleigh number as:

3.10 Heating method in microfluidic systems

In microfluidic PCR systems, the heat needs to be generated and transferred to the fluid zone to achieve the desired fluid temperatures in each PCR zone. Effective heating strategies are needed in order to achieve consistent CFPCR amplification and to avoid the temperature fluctuations that has a negative impact on PCR yield, (Miao et al., 2020). Several heating methods have been used in PCR systems to create the desired temperature distribution by using heating elements which are in contact with the PCR substrate and DC power supply. Consequently, the heat can be transferred to the PCR wall by conduction and it can be absorbed by the fluid by convection. Presently, PCR heating systems

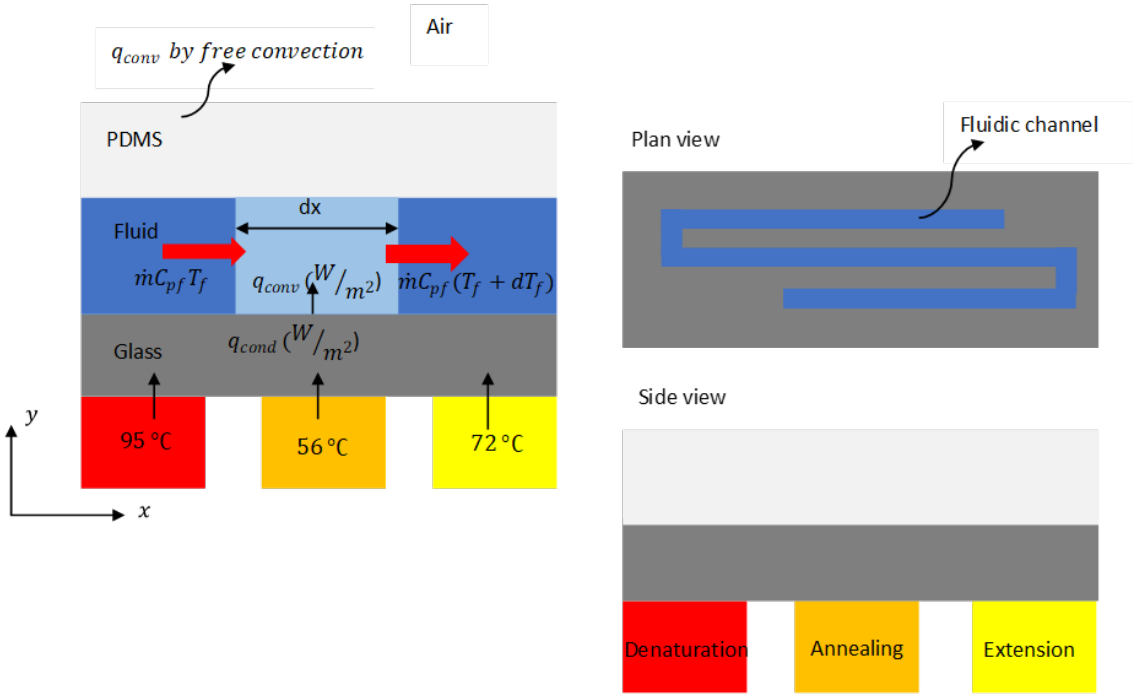

Figure 3.14: (a) simplified two-dimensional control volume analysis in the microchannel; (b) one-cycle computational model.

comprise contact and non-contact heating according to the relationship between heater and reactor. The contact heating process is based on converting the electro thermal power to heating power in order to heat up the PCR chip by conduction using heater in contact with the PCR chip, (Zhang et al., 2006). In this method the heating system being in contact with PCR chip, is often placed underneath of PCR channel substrate. An example of contact heating system is the thin film heater. A thin film heating element comprised of thin layers of platinum or of poly crystalline silicon can be used as heaters to achieve the desired temperature. Additionally, the contact heating method includes the heating block technique, (Miralles et al., 2013). In this method metal blocks with high thermal conductivity such as aluminium or copper are used. The heating system consists of the metal block heated by a cartridge heater or a Peltier heating element (Chen and Li, 2018). In contrast to the contact heating method is the non-contact heating method which is a suitable choice for achieving an appropriate temperature profile on PCR devices with fast heating and accurate temperature control. Heating is by infrared light as the sample can be heated directly without convection or conduction steps. For example, a tungsten lamp which is used for infrared heating cycle and a fan for forced convective cooling, indoor to achieve heating and cooling cycles which rates of about $(10°C/s)$. This method can be used for chip disposal since the heating system is separated from the PCR chip. Also, it does not add additional mass weight to the PCR chip design. This method can be achieved by using an infrared IR beam.

3.11 Temperature of fluid and solid in one dimensional model

In microfluidic the flow is laminar and for small channels with typically $Dh \sim 50\mu m$ the thermal and hydrodynamic entrance effect can be neglected. The thermal boundary at the surface used in heat transfer problems can be expressed either isothermal or isoflux boundary conditions. However, these two boundaries cannot be used together as they have different thermal behaviour and for flow inside microfluidic channels exposure to one of these boundaries results in variation

in temperature profile according to the thermal boundary as explained in Figure 3.15. The convective heat through the boundary control volume by applying energy balance as:

Rate of heat through wall + Rate of energy inflow=Rate of Energy outflow.

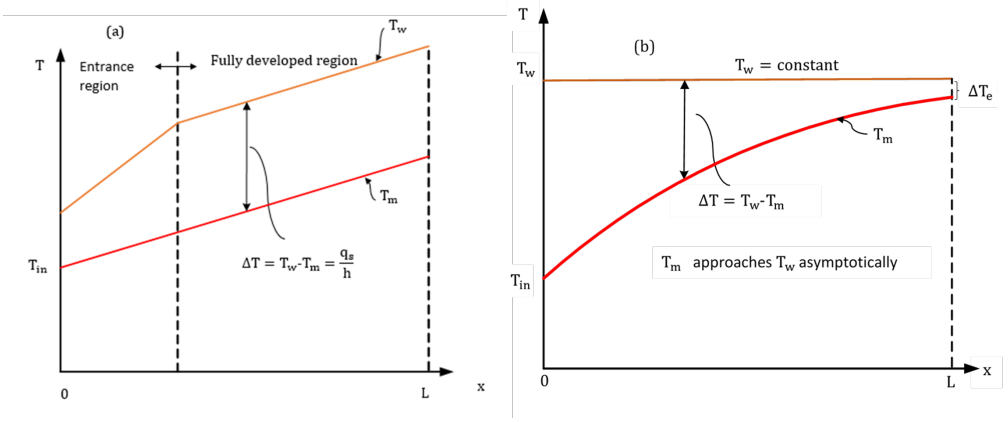

Figure 3.15: The variation of the mean fluid temperature along the channel for the case of (a) constant heat flux and (b) constant wall temperature.

.

3.11.1 Isoflux boundary condition

The isoflux boundary condition used for microfludic thermal analysis which means the heat flux at the surface is constant. Figure 3.15 (a) reveals the mean temperature T_m varies linearly along the channel length. It can be noted also that the temperatures difference between surface temperature T_w and mean fluid temperature T_m is initially small as heat transfer coefficient h is large then it increases with increasing of x due to the decreases in h because of the effect of developing of boundary layer. This difference become constant in fully develop region. Moreover, the mean fluid temperature T_m increases linearly in the flow direction with increases of (x) while, the surface temperature increases linearly just in the fully developed region where the local and average heat transfer coefficient h_x and h_{avg} is constant. The energy balance can be used over a unit volume (control volume) of fluidic channel as depicted in Figure 3.16 which revels that the net

energy supplied by the conduction heat source is equal to the convective energy carried by liquid. The heat applied through the control volume can be presented as:

$$q_s = h(T_w - T_m) \tag{3.41}$$

where q_s is the surface heat flux (W/m^2). For constant heat flux the rate of heat transfer can also be represented as:

$$Q = q_s A_s = \dot{m} C_p (T_e - T_{in}) \tag{3.42}$$

Thus:

$$T_e = T_{in} + \frac{Q A_s}{\dot{m} C_p} (T_e - T_{in}) \tag{3.43}$$

where T_e represents the mean fluid temperature at the channel exit. From Equation 3.41 T_w can be expressed as:

$$T_w = T_m + \frac{q_s}{h} \tag{3.44}$$

In case of constant heat flux and in the fully developed region the heat transfer coefficient h is constant,thus, the slop $T_m - T_w$ is constant see Figure 3.15(a) The slope of the mean fluid temperature T_m on a $(T\&x)$ diagram can be obtained by applying the steady-flow energy balance to a channel slice of thick dx

$$\dot{m} C_p dT_m = q_s (P dx) \tag{3.45}$$

where P is the perimeter of the channel.

$$\frac{dT_m}{dx} = \frac{q_s P}{\dot{m} C_{pf}} \tag{3.46}$$

Due to both q_s and h are constants the differentiation of Equation 3.41 gives:

$$\frac{dT_m}{dx} = \frac{dT_w}{dx} \tag{3.47}$$

Also in the fully developed region the dimensionless temperature profile remains unchanged that gives:

$$\frac{\partial}{\partial x} \left(\frac{T_w - T}{T_w - T_m} \right) = 0 \tag{3.48}$$

Consequently the equation above can be simplified as:

$$\frac{1}{T_w - T_m}\left(\frac{\partial T_w}{\partial x} - \frac{\partial T}{\partial x}\right) = 0 \tag{3.49}$$

Thus:

$$\frac{\partial T}{\partial x} = \frac{\partial T_w}{\partial x} \tag{3.50}$$

$T_w - T_m$=constant. Equations 3.46, 3.47 and 3.50 are combined to give:

$$\frac{\partial T}{\partial x} = \frac{\partial T_w}{\partial x} = \frac{\partial T_m}{\partial x} = \frac{q_s P}{\dot{m} C_{pf}} = constant \tag{3.51}$$

To determine the variation of mean temperature along the channel, Equation 3.51 can be integrated from $x = 0$ ($T_m = T_{in}$) to x:

$$T_m(x) = T_{in} + \frac{q_s P}{\dot{m} C_{pf}} x \tag{3.52}$$

where, T_{in} is the fluid inlet temperature, $\dot{m}$ is the mass flow rate, h is a heat transfer coefficient, P is the perimeter of the microchannel and C_{pf} is the fluid heat capacity.

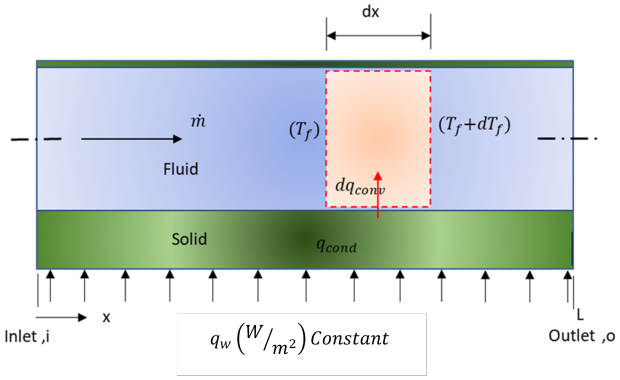

Figure 3.16: Control volume of fluid flowing in a fluidic channel heated at constant heat flux.

3.11.2 Isothermal Boundary condition

The isothermal boundary condition used in heat transfer problems which also can be applied in microfluidic thermal analysis which means the temperature at the boundary (surface) is constant. It can be noted from Figure 3.15(b) the temperature difference between the surface T_w and fluid T_m decays exponentially with increases of x (in the flow direction) and the rate of decay rely on the magnitude of the exponent $(hAs/m.C_{pf})$.

By using the Newton's law of cooling, the convective heat transfers from the channel wall to the fluid stream can be determined:

$$dq_{conv} = hA_s(T_w - T_m) \tag{3.53}$$

By applying energy balance on a differential control volume depicted in Figure 3.17 gives:

$$\dot{m}C_p dT_m = dq_{conv} = hA_s(T_w - T_m) \tag{3.54}$$

Here the differential surface area is $dA_s = Pdx$, P is the perimeter of the microchannel. Since T_w is constant, thus, $dT_m = -(T_w - T_m)$ Equation 3.54 can be rearranged as:

$$\frac{d(T_w - T_m)}{T_w - T_m} = -\frac{hP}{\dot{m}C_{pf}}dx \tag{3.55}$$

By integrating Equation 3.55 from $x = 0$ to x, gives:

$$ln\frac{(T_w - Tm)}{(T_s - T_i)} = -\frac{hPx}{\dot{m}C_{pf}} \tag{3.56}$$

The average flow temperature, T_m, for the constant wall temperature boundary condition can be obtained be taking the exponential of both sides of Equation 3.56 that gives:

$$T_m(x) = T_w - (T_s - T_{in}) \times \exp(-h.P.x/\dot{m}C_{pf}) \tag{3.57}$$

where x is the distance along the channel.

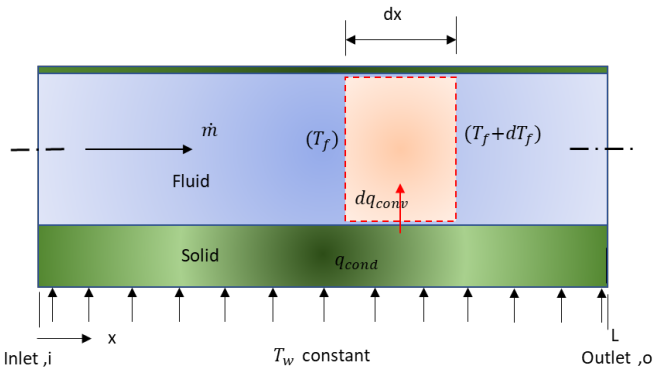

Figure 3.17: Control volume of fluid flowing in a fluidic channel heated at constant wall temperature.

Chapter 4

Computational Fluid Dynamics(CFD) and Optimisation methods for Microfluidic PCR Systems

4.1 Introduction

This Chapter provides a description of the mathematical and Computational Fluid Dynamics (CFD) modelling adopted for prototype PCR systems also optimisation methods being analysed in this thesis. An introduction to Computational Fluid Dynamics and the process of solving a simulation model is presented in this chapter. The boundary conditions for simulating the PCR model are described. The governing equations, boundary conditions, and assumptions are discussed. The examination of mesh element type and mesh verification are performed. The optimisation methods are presented.

4.2 Computational fluid domain

Analysis of the heat transfer between a solid and a fluid in microfluidic PCR channel depicted in Figure 4.1 involves solving a set of governing differential

equations, which include continuity, momentum and energy equations presented in chapter 3.

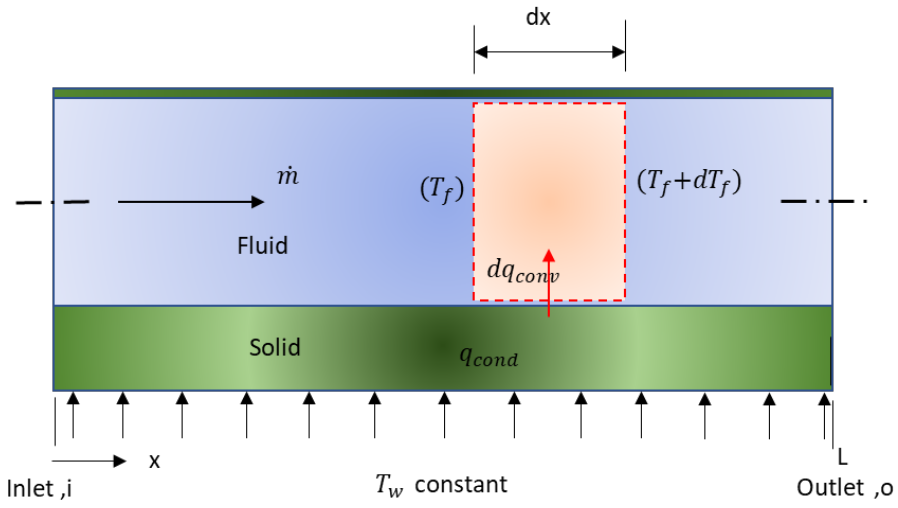

(a)

Figure 4.1: Microfluidic channel

In order to find a solution of problems involving coupled heat transfer and fluid flow Equations 3.14 and 4.37 need to be solved. However, it can be noted that 4.37, a scalar equation with the variables, v (fluid velocity) and T (temperature), and Equation 3.14, a vector equation with the variables v and p (pressure), which give together four equations with five unknowns - the three components of velocity (u, v, and w), pressure, and temperature. Thus, more information is required to help in finding solutions involving the dependent variables. Therefore, the principle of conservation of mass, can be used which leads us to the continuity equation as presented in Equation 3.3 which states that the rate of accumulation of mass is equal to the rate of net mass flowing in Equations 4.37 , 3.17 , 3.14 and 3.3 represent the fully formulated coupled problem of heat transfer and fluid flow described in Chapter 3.

4.3 Computational Fluid Dynamics (CFD)

Computational fluid dynamics (CFD) uses numerical analysis and computational methods to solve and analyse problems that involve fluid flow, heat transfer and relevant phenomena (Versteeg and Malalasekera, 2007; Hu, 2012; Pragati, Sharma et al., 2012). It plays a significant role in the improvement of the engineering design process that demands a comprehensive long-term, research objective strategy (Slotnick et al., 2014). In order to solve the governing equations analytically it is not possible without use major simplifications and assumptions such as one dimensional or two dimensional and laminar, thus to simulate a real fluid dynamics and heat transfer cases it is required to change the PDEs to a set of algebraic equations. This can be achieved by using the CFD discretisation process.

4.3.1 Discretisation approaches

The discretisation is a method used in CFD to convert partial differential equations (PDEs) into approximate algebraic equations (Shu et al., 2004; Date, 2005; Al–Hashmi et al., 2015). Three different approaches of discretisation are available which are Finite volume method (FVM), Finite difference method (FDM) and Finite element method (FEM). (Patera, 1984; Kurganov and Tadmor, 2000; Shu et al., 2004; Peiró and Sherwin, 2005; Salvi et al., 2010; Pepper and Heinrich, 2017) and can express the governing equations in either integral or differential form (Oh, 2012).

4.3.2 Finite difference

The FD approach was initially proposed in CFD to convert the set of PDEs to algebraic form using differential discretisation based on Taylor's series (Salvi et al., 2010; Pepper and Heinrich, 2017) or by using a piece-wise polynomial function. However, in this approach, it is required to describe the domain into a grid of points called nodes in which the approximate solution need to be obtained. This encounters approximation errors that can increase significantly with sharp corners or edges so this method is not effective for complex geometries while the

FVM and FEM are integral forms (Patankar, 1980; Pepper and Heinrich, 2017) that are more commonly used.

4.3.3 Finite volume

The FV is one of the discretisation methods used in numerical CFD in which the physical computational domain is divided into finite discrete elements called a control volume. Over each control volume, the system of governing equations are integrated and then solved in terms of independent variables (Patankar, 1980).

4.3.4 Finite element

In this section, the finite element method will be introduced and example implementation can be found in Appendix *A*. The Finite element method is a powerful numerical approach used to obtain approximate solutions to the PDEs arising in physics and engineering (Pepper and Heinrich, 2017). The FEM can handle complex geometries effectively due to its integral formulation and its capability to find an accurate solution of the PDEs using unstructured grids (Blazek, 2015). FE enables the dependent variables (temperature, pressure, velocity) to be approximated over each finite elements using known functions usually polynomial approximation functions (Patankar, 1980; Hirsch, 2007). The values of the dependent variables are obtained at any point inside the domain as a function of the distance from this point to the elements' nodes by interpolation using the polynomial. An algebraic set of equations for just the value of the variable at these nodes are obtained by substituting this polynomial function in PDE's. With this method, the approximation of PDE's can be obtained by replacing the dependent variable (solution) by a polynomial function rather than replacing the partial derivatives as finite differences. The PDEs such as governing equation that need to be solved in the finite element method are integrated over each finite element, then they are assembled over the entire domain. Consequently, a set of finite linear equations is determined in terms of the values of the unknown variables at the elements nodes. Linear algebra techniques can be used to obtain solutions of these equations.

The FE solution procedure can be summarised as (Nikishkov, 2004):

- **A- Discretize the domain** : In this step, the computational domain is subdivided into smaller non-overlapping elements that comprise a set of nodes see Figure 4.2, (Gnanavelu, 2010). The element can be formed by different types edge, triangle, quad, tetrahedron, or hexahedron. The number of nodes used to create an element depends on the type of element (or interpolation function).

- **B- Choose interpolation function**: The next step is to choose the type of interpolation functions which represents the relationship between the variable within each element (Lewis et al., 2004). The shape function is defined over each element in FE usually polynomial which can be either linear or quadratic based on model geometry (1D, 2D or 3D) and complexity see Figures 4.3 and 4.4. The nature and number of unknown variables at each node also affect the choice of shape function. Variations in field variables and the degree of freedom within an individual element and through the full system have to also be considered.

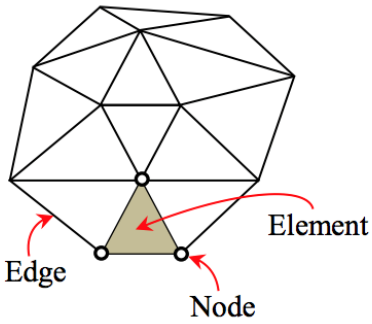

Figure 4.2: Typical finite element mesh (Al–Neama, 2018)

The accuracy of the numerical solution is usually improved by increasing the degree of the shape function (Pepper and Heinrich, 2017). However, this leads to an increase computational time and memory required due to the increase number of the degree of freedom. The chosen polynomial of approximate solutions has significant impact on convergence of the solution and the following properties are required to satisfy a monotonically convergent solution of the PDEs:

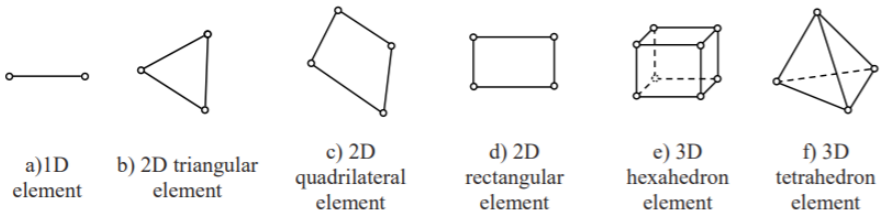

Figure 4.3: Types of linear element in one , two or three dimensional (Al-Waaly, 2015)

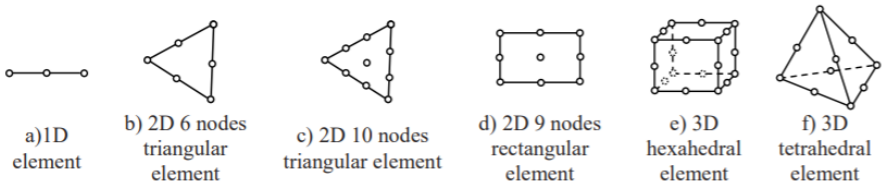

Figure 4.4: Types of quadratic element in one , two or three dimensional (Al-Waaly, 2015).

1. Non overlapping between elements.
2. The elements should have the same degree of freedom at the element boundaries to achieve compatibility of each element to its neighbors.
3. Continuous behavior of the shape function at the element boundaries and within all the elements of the model.
4. Isotropic element geometry: that means the shape function have the same properties in the transformation from one coordinate system to another.

To satisfy these requirements a complete polynomials is used. The general compact form of complete polynomial of order n in one dimension can be written as follows (Madenci and Guven, 2015)

$$P_n(x) = \sum_{k}^{n+1} \alpha x^{k-1} \tag{4.1}$$

where P is the polynomial shape function (temperature as an example), n is the polynomial degree, α is a constant, x is the coordinate along the element. Complete polynomials of 0th, 1st, and 2nd order (constant, linear, and quadratic) as can be written respectively as follows in one-dimensional system:

$$\begin{aligned} P_o(x) &= \alpha_1 \\ P_1(x) &= \alpha_1 + \alpha_2(x) \\ P_2(x) &= \alpha_1 + \alpha_2(x) + \alpha_3(x)^2 \end{aligned} \tag{4.2}$$

A higher degree of the shape function (for one- and two dimensional problems) can also be predicted from a Pascal's triangle, as shown in Figure 4.5

The approximation function over the element for the field variable, $\phi(x)$, is assumed as a polynomial of order $(m-1)$

$$\phi^e(x) = \alpha_1 + \alpha_1 x_2 + \alpha_3 x_3 + \alpha_4 + \ldots + \alpha_{m-1}^{m-2} + \alpha_m^{m-1} \tag{4.3}$$

Equation 4.3 can be expressed as :

$$\phi^e(x) = \mathbf{g}^{\mathbf{T}} \alpha \tag{4.4}$$

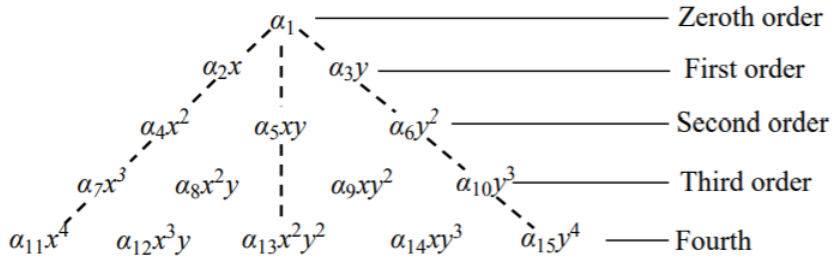

Figure 4.5: Pascal's triangle for higher order of shape function (Madenci and Guven, 2015)

where

$$\mathbf{g^T} = \{1, x, x^2, \ldots, x^{m-1}\} \tag{4.5}$$

and

$$\alpha^{\mathbf{T}} = \{\alpha_1 + \alpha_2 + \alpha_3 + \ldots + \alpha_m\} \tag{4.6}$$

where $\phi(x)$ is the field variable such as (T,P and v) The number of generalized coordinates $(\alpha_i, i = 1, 2, \ldots, m)$ is equal to the number of nodes within the element.

The field variable, $\phi(x)$, can also be expressed within the element through the use of its nodal values, $\phi(x)(i = 1, \ldots, m)$, in the form:

$$\phi^e(x) = N_1\alpha_1 + N_2\alpha_1 x_2 + N_3\alpha_3 x_3 + N_4\alpha_4 + \ldots + N_{m-1}\alpha_{m-1} + N_m\alpha_m \tag{4.7}$$

or it can be expressed as:

$$\phi^e(x) = \mathbf{N_T}\psi \tag{4.8}$$

Here

$$\mathbf{N_T} = \{N_1, N_2, N_3, \ldots, N_M\} \tag{4.9}$$

and

$$\psi^T = \{\phi_1 + \phi_2 + \phi_3 + \ldots, \phi_m\} \tag{4.10}$$

The shape functions are denoted by $N_i(i = 1, m)$ which are associated with node i and must have a unit value at node i and a zero value at all other nodes.

Also, they must have the same degree of polynomial variation as in the element approximation function. The explicit form of the shape functions can be obtained by solving for the global coordinates,α_i, in terms of the nodal coordinates, X_i, and nodal values, $\phi_i (i = 1, \ldots, m)$, using Equation 4.7, and the resulting expressions can be arranged according to Equation 4.8. The field variable $\phi^e(x)$ can be approximated at each node as:

$$\begin{aligned}
\phi_1 &= \alpha_1 + \alpha_2 x_1^1 + \alpha_3 x_1^2 + \alpha_4 x_1^3 + \ldots + \alpha_{m-1} x_1^{m-2} + \alpha_m x_1^{m-1} \\
\phi_2 &= \alpha_1 + \alpha_2 x_2^1 + \alpha_3 x_2^2 + \alpha_4 x_2^3 + \ldots + \alpha_{m-1} x_1^{m-2} + \alpha_m x_1^{m-1} \\
&\vdots \\
\phi_m &= \alpha_1 + \alpha_2 x_m^1 + \alpha_3 x_m^2 + \alpha_4 x_m^3 + \ldots + \alpha_{m-1} x_1^{m-2} + \alpha_m x_1^{m-1}
\end{aligned} \tag{4.11}$$

Equation 4.11can be expressed in matrix form as:

$$\begin{pmatrix} \phi_1 \\ \phi_2 \\ \phi_3 \\ \vdots \\ \phi_m \end{pmatrix} = \begin{bmatrix} 1 & x_1 & x_1^2 & \ldots & x_1^{m-1} \\ 1 & x_2 & x_2^2 & \ldots & x_2^{m-1} \\ 1 & x_1 & x_2^2 & \ldots & x_2^{m-1} \\ \vdots & & & & \\ 1 & x_m & x_m^2 & \ldots & x_m^{m-1} \end{bmatrix} \begin{Bmatrix} \alpha_1 \\ \alpha_2 \\ \alpha_3 \\ \vdots \\ \alpha_m \end{Bmatrix} \tag{4.12}$$

or

$$\psi = \mathbf{A}\alpha \tag{4.13}$$

By solving the global coordinates in terms of nodal coordinates and nodal values of the field variable result in :

$$\alpha = \mathbf{A}^{-1}\psi \tag{4.14}$$

Substituting for the generalized coordinates in Equation 4.4 yields:

$$\phi^e(x) = \mathbf{g^T A}^{-1}\psi \tag{4.15}$$

the explicit form of the shape functions N_i can be obtained by using equations 4.15 and 4.8 The properties of shape functions are:

1. $N_i = 1$ at node i and $N_i = 0$ at all other nodes.

2. $\sum_{i=1}^{m} N_i$

The field variable $\phi_e(x)$, refers to (p,T,v) can be approximated by a linear function in terms of the global coordinate x:

$$\phi_e(x) = \alpha_1 + \alpha_2 x \tag{4.16}$$

The shape function over each node can be represented by $N_i(x)$ and $N_i(x) = 1$ and $N_i(x) = 0\ if j \neq i$. The general form of basis function in terms of T is:

$$T_1 = \alpha_1 + \alpha_2 x_1 \tag{4.17}$$

and

$$T_2 = \alpha_1 + \alpha_2 x_2 \tag{4.18}$$

where T is the temperature at any location x and α_1 and α_2 are constants. Since there are two arbitrary constants in the linear representation, it requires only two nodes to determine the values of α_1 and α_2.

$$\begin{aligned} T_i &= \alpha_1 + \alpha_2 x_i \\ T_j &= \alpha_1 + \alpha_2 x_j \end{aligned} \tag{4.19}$$

From the above equations, we get

$$\begin{aligned} \alpha_1 &= \frac{T_i x_j - T_j x_i}{x_j - x_i} \\ \alpha_2 &= \frac{T_j - T_i}{x_j - x_i} \end{aligned} \tag{4.20}$$

α_1 and α_2 are substituted back into Equation 4.16(Lewis et al., 2004), then:

$$T(x) = \left[\frac{x_j - x}{x_j - x_i}\right] T_i + \left[\frac{x - x_i}{x_j - x_i}\right] T_j \tag{4.21}$$

or:

$$T(x) = N_i T_i + N_j T_j = [N_i N_j] \begin{bmatrix} T_i \\ T_j \end{bmatrix} \tag{4.22}$$

Here , N_i and N_j are the shape functions which is also called Interpolation functions or Basis functions written as:

$$N_i = \left[\frac{x_j - x}{x_j - x_i}\right], N_j = \left[\frac{x - x_i}{x_j - x_i}\right] \tag{4.23}$$

Equation 4.22 can be written in the matrix form:

$$T(x) = [\mathbf{N}][\mathbf{T}] \tag{4.24}$$

where

$$[\mathbf{N}] = [N_i \; N_j] \tag{4.25}$$

is the shape matrix and

$$\mathbf{T} = \begin{bmatrix} T_i \\ T_j \end{bmatrix} \tag{4.26}$$

is the matrix of a unknown variable (i.e temperature) at any location (x,y,z) that should be calculated using the shape functions Ni and Nj evaluated at x, y, z and represents degrees of freedom of the element. Degrees of freedom in the model are the total number of unknown variables on each node(s). Shape function(s) are equal to one at the specific node and zero at the other node(s). Moreover, the derivative is constant along the element, as depicted in Figure 4.6. The shape functions of different degrees and dimensions can be found in detail in (Madenci and Guven, 2015; Pepper and Heinrich, 2017).

Figure 4.6: Shape function properties (Lewis et al., 2004)

- **C- Find properties of element**: In this step, the Galerkin method is used to represent a matrix of equations of finite element which relates the unknown function of the dependent variable nodal value to other parameters.
- **D- Assemble the equations of the element**: The equations of each individual element of the grid needs to be combined in an appropriate way such that the resulting matrix represents the behaviour of the entire solution. The boundary conditions must be incorporated after the assemblage of the individual element contributions.
- **E-Solve the system of equations** The resulting set of algebraic equations, can be solved to determine the nodal values of the field variable, for example, temperature.
- **F-Post-processing** From the nodal values of the field variables, for example, temperatures, we can then calculate the secondary quantities such as heat fluxes and pressure.

Figure 4.7 shows flow chart that is simplified the process of finite element solution.

The governing differential equations for any system is as follows:

$$L(T) = 0 \qquad in\,\Omega \tag{4.27}$$

The approximate solution is performed as a linear combination of a set of basis functions:

$$T \approx \bar{T} = \sum_{i=1}^{n} a_i N_i(x) \tag{4.28}$$

$$L(\bar{T}) \neq 0 \tag{4.29}$$

or

$$L(\bar{T}) \neq R(residual) \tag{4.30}$$

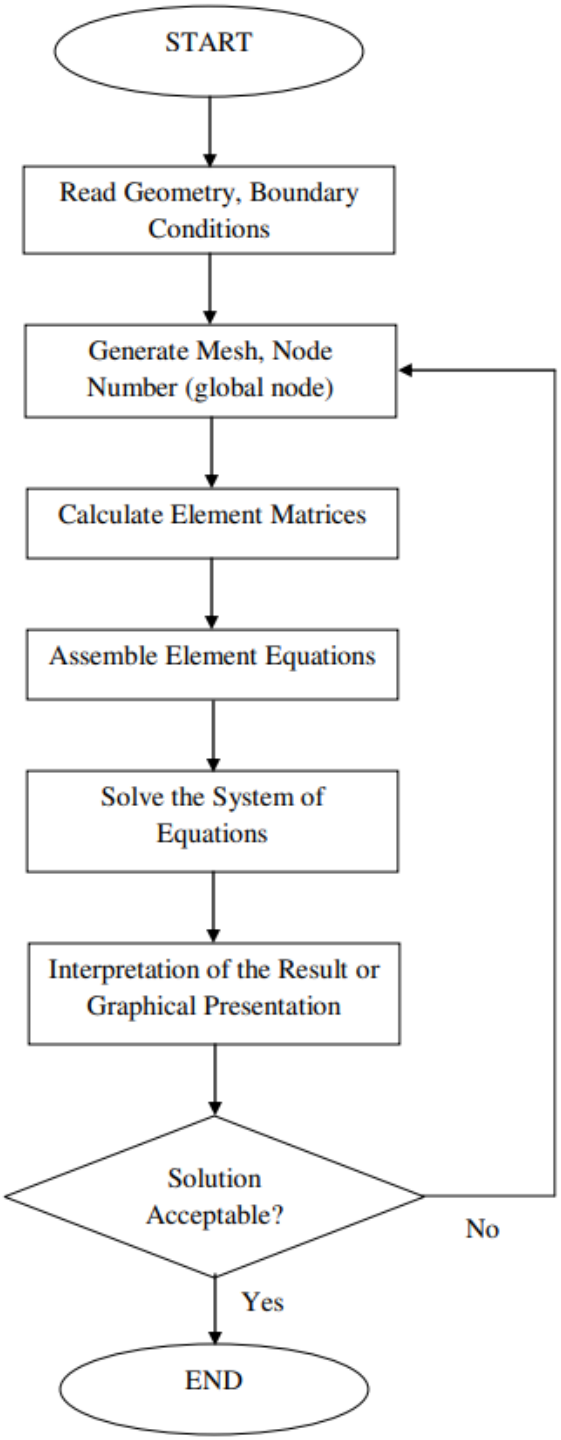

Figure 4.7: Flow Chart of Finite Element Method (Azmi, 2010)

The residual is multiplied by a proper function and integrated over the entire domain in order to specify the parameters $(\alpha_1, \alpha_2, \ldots \alpha_n)$. Then:

$$\int_{\Omega} w_i(x) R dx = 0 \tag{4.31}$$

where $w_i(x)$ is the weighting function. Galerkin approximation is used to determine the weighting function that can satisfy Equation 4.31.

According to Equation 4.31, a proper weighting function should be specified in order to convert the governing equations including the continuity, Navier-Stokes and energy equations described in section 3.4 into the FEM integral form as follows: First select the appropriate shape functions for velocity, pressure and temperature field as depicted in Equation 4.32

$$\begin{aligned} u &= \sum N_i(x,y,z) u_i \\ v &= \sum N_i(x,y,z) v_i \\ w &= \sum N_i(x,y,z) w_i \\ p &= \sum N_{pi}(x,y,z) P_i \\ T &= \sum N_i(x,y,z) T_i \end{aligned} \tag{4.32}$$

where N_i and N_{pi} are the shape functions.

As an example the continuity equation:

$$\left(\frac{\partial \rho}{\partial t} + \nabla \cdot (\rho \mathbf{u}) \right) = 0 \tag{4.33}$$

This equation represents the conservation of mass can be written in steady state form as:

$$\nabla \cdot (\rho \mathbf{u}) = 0 \tag{4.34}$$

The next step is to multiply both sides of Equation 4.34 by a test function N_{pi} and integrate over the domain Ω:

$$\int_{\Omega} \left(\frac{\partial \rho u}{\partial x} + \frac{\partial \rho v}{\partial y} + \frac{\partial \rho w}{\partial z} \right) N_{pi} d\Omega = 0 \tag{4.35}$$

Also multiply both sides of the Energy equation by a test function N_{pi} and integrate over the domain Ω:

Energy equation:

$$\int_{\Omega}\Big(\rho_f C_p(u\frac{\partial T}{\partial x}+v\frac{\partial T}{\partial y}+w\frac{\partial T}{\partial y})-k(\frac{\partial^2 T}{\partial x^2}+\frac{\partial^2 T}{\partial y^2}+\frac{\partial^2 T}{\partial z^2})\Big)N_{pi}d\Omega=0 \tag{4.36}$$

$$\int_{\Omega}N_i\Big(\rho_f C_p(u\frac{\partial T}{\partial x}+v\frac{\partial T}{\partial y}+w\frac{\partial T}{\partial y})\Big)d\Omega-\int_{\Omega}N_i k\Big((\frac{\partial^2 T}{\partial x^2}+\frac{\partial^2 T}{\partial y^2}+\frac{\partial^2 T}{\partial z^2})\Big)d\Omega=0 \tag{4.37}$$

The elements equations are combined then the boundary conditions of problem of interest are represented in Figure 4.8 need to be applied ; the results are written in matrix form [80] for both the velocity and temperature fields:

$$\begin{aligned}[K][U]&=[f]\\ [K][U]&=[f]\end{aligned} \tag{4.38}$$

where $[K]$, $[U]$, $[T]$, and $[f]$ are the stiffness matrix, the vector of unknown velocity, the unknown temperature, and the force vector respectively. Equation 4.38 represents a system of linear/non-linear equations which can be solved to determine the unknown variables. Fluid properties such as temperature independent, hydraulic and energy equations can be solved separately. Both fluid and thermal equations are solved simultaneously when temperature-dependent properties are considered. Generally, the finite element method can solve PDEs of the system of single, two or more materials systems. The density of the mesh elements should be increased if there is a sharp change/gradient in the variables through the boundaries. For example, if fluid flow in the microchannel experiences a sharp velocity change near the walls then the density of the elements must be increased to capture this change.

4.4 FEM results accuracy

The FEM is an approximate solution, thus it is crucial to outline the numerical errors and follow the correct quality to control and minimise them to ensure maximum accuracy. There are three types of error associated with finite element solution:

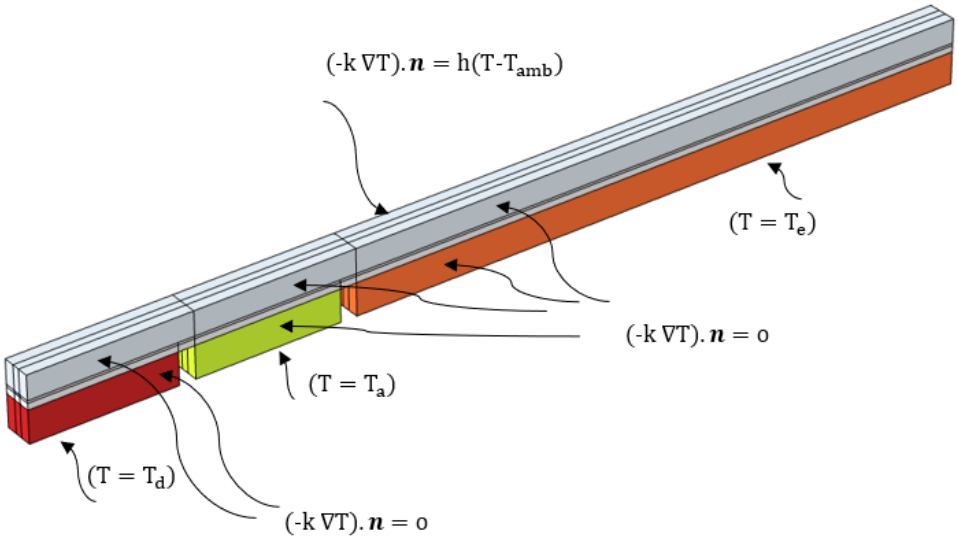

Figure 4.8: The domain equation and boundary conditions for a mathematical model of PCR microchannel

1. **Errors in physical data**: when solving numerical models these errors can occur due to human mistakes , for example,in defining the geometry dimension of the problem and material properties, boundary conditions these errors can be minimised with practice.

2. **discretisation errors**: The discretisation errors e arise due to the exact solution of PDEs is not obtained but numerically approximated. For instance, function u that may be the dependent variable in a PDEs (i.e., temperature, pressure, etc.). The function u can be approximated by a function u_h using linear combinations of basis functions according to the following expressions:

$$u_h = \sum_i u_i \psi_i \tag{4.39}$$

ψ_i represents the basis functions and u_i represents the coefficients of the functions that approximate u with u_h

$$u \approx u_h \tag{4.40}$$

Thus e represents the difference between the approximate numerical solution u and exact solution u_h to the model equations:

$$e = \|u - u_h\| \tag{4.41}$$

3. **Chosen appropriate order of polynomials** :

   The variation of the the dependent variable over the element is estimated by choosing the appropriate order of polynomials of the base functions see Figure 4.9 which reveals that increasing the order of the polynomial improves the convergence of the approximate solution u_h or (ϕ) to the exact solution u or(ϕ) monotonically. The most common finite element methods are second- to third-order accurate. Figure 4.10 shows a single quadrilateral element expresses a domain that is squared in shape with some curved sides. It can be noticed that the first-order element represents the curved sides as straight sides. While, the second-order element approximates these curved shapes boundaries accurately. This difference, is named a geometric discretization error.

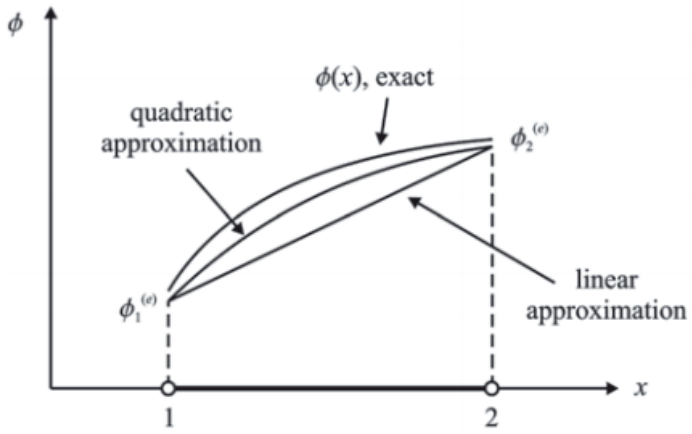

Figure 4.9: Element approximation functions (Madenci and Guven, 2015)

The discretization errors of the FEM can be mitigated by adopting an appropriate mesh for FEA simulations. Thus, mesh convergence test is crucial for

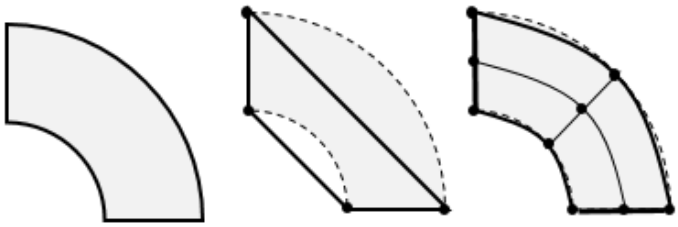

Figure 4.10: A domain with curved sides. Single first- and second-order quadrilateral elements are applied (Frei, 2016)

obtaining accurate results, which is a simple method that compares approximate solutions of successive meshes obtained for different meshes. Ideally, as mesh size decreases towards zero, the model solution close to exact solution. Consequently, choosing a very fine mesh leads to move the obtained approximation solution from FEM toward the actual solution. However, this process is limited by by finite computational resources and time, so there is a trade-off between mesh size and solution time. The goal of mesh convergence test is to minimise the error between approximate solution and the exact solution to some accepted tolerance level. The solution of mesh convergence process should start with coarse mesh which demands less computation time but it give inaccurate results. Then the process of mesh refinement starts by resolving the model with successively finer and finer meshes and comparing the obtained approximated results between these different meshes. This comparison can be done by analyzing the fields at one or more points in the model or by evaluating the integral of a field over some domains or boundaries. After comparing the solutions of a minimum of three successive meshes it is possible to judge the convergence of the solution with respect to mesh refinement. These meshes differ in terms of the element size and are compared in terms of the number of degrees of freedom (DOF) within the model. The DOF is related to the number of nodes, the computational points that define the shape of each finite element. The computational resources required to solve an FEA model are directly related to the number of DOF.

$$e = u_{h1} - u_h \tag{4.42}$$

where h refer to element size and h_1 refers to base element size (Very fine mesh). It is also possible to estimate the convergence from the change in the solution for each mesh refinement. The change in the solution should become smaller for each mesh refinement if the approximate solution is in a converging area, so that it moves closer and closer to the real solution.

FEM is the basis for the commercial CFD code, COMSOL which will be used in this thesis.

4.5 CFD solution methodology

The CFD model involves three main stages which are pre-processing, solver and CFD post-process see Figure 4.11. The pre-processing stage can be broken down into four steps including geometry design in which the geometry of problem of interest is defined and the mesh for domain is created. Then the material type of geometry needs to be assigned. Next, the boundary conditions need to be defined. In the second stage (solver), the CFD solving process starts after defining the boundary condition of the domain of interest. This process involves solving the matrix system of algebraic obtained from discretising the fluid flow and heat transfer PDEs. The flow solver can be either iterative or direct and it is important to monitor the convergence of the solution of the equations. The final stage in CFD is post-processing, in which numerical results analyses and full reports of the results can be obtained. Also, these results can be presented with colours, contour plots, and graphics. Thus the values of the flow properties can be obtained from these analyses of the results (Hughes et al., 1986; Gnanavelu, 2010).

4.5.1 Mesh generation and boundary conditions

After defining the geometry, the next step of the CFD modelling process is mesh or grid generation which requires the geometry domain to be subdivided into smaller sub-domains called elements in order the domain that comprises of a set of nodes (Gnanavelu, 2010) see Figure 4.2.

In general, A FE mesh is classified into three different types. The first element type is for a one-dimensional mesh, usually represented by lines and the second

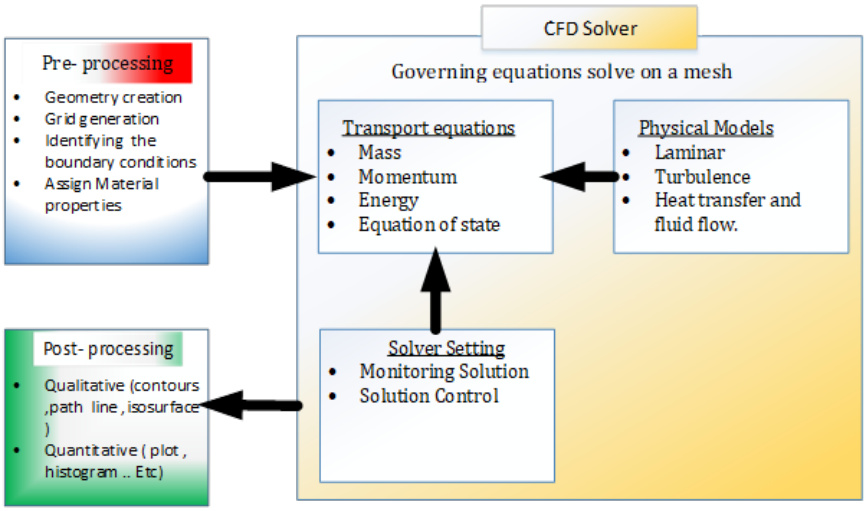

(a)

Figure 4.11: Main stages in a CFD simulation (Tu et al., 2018)

mesh type is two-dimensional, composed of triangular and quadrilateral elements. Three-dimensional meshes can be subdivided into four different element types, called tetrahedral, hexahedral cuboid(bricks), pyramids and triangular prisms (prisms). These four mesh types of elements are shown in Figure 4.12. These can be combined within a 3D mesh.

The element type and size of mesh generated have a strong impact on the mesh quality which influence the accuracy of the CFD results (Chen et al., 2020). Thus, adopting an appropriate mesh for the model of a particular case includes selecting the accurate element types and sizes necessary for accurate CFD results.

4.5.1.1 Mesh Quality

Ensuring sufficient quality of the mesh is important in CFD solutions due to poor quality causing the solution to diverge (Fabritius and Tabor, 2016). Also, it has a significant impact on the accuracy of CFD results. A number of criteria are considered in CFD to identify mesh quality. Typical quality criteria are: A- Aspect-ratio: ratio of the maximum and minimum edge length, per cell. B- Equiangle skew: a measure of cell distortion based on internal angles. C- Equisize

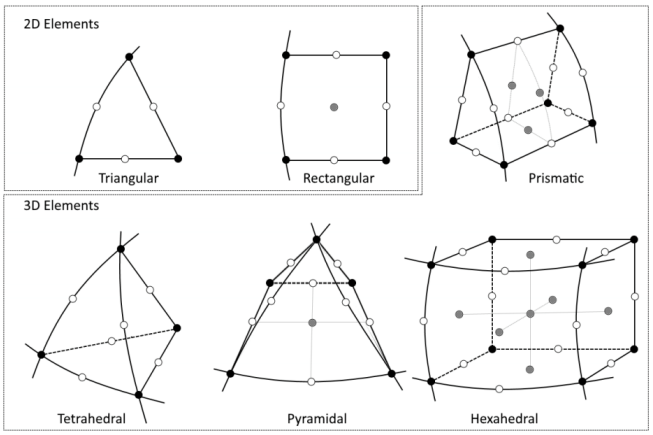

Figure 4.12: Types of elements

skew: assessment of distortion from cell edge lengths. D- Volume - compares cell volumes. In COMSOL the mesh quality can be checked automatically for both laminar and turbulent flow. COMSOL calculates the tetrahedral element quality by:

$$Q_{mesh} = 72\sqrt{3}V/(h_1^2 + h_2^2 + h_3^2 + h_5^2 + h_6^2)^{1.5} \tag{4.43}$$

Where V is the volume whereas h_1, h_2,h_3,h_4,h_5 and h_6 are the element's edge lengths. Good mesh quality corresponds to the Q_{mesh} value is greater than 0.1.

4.5.1.2 Structured and unstructured mesh

The mesh of the computational domain can be either structured or unstructured or in some cases it could be hybrid which is combined structure and unstructured. Adopting an appropriate mesh depends on the complexity of the geometry shape.

The particular structure of a structured mesh depends on the computational domain under consideration. The mesh is constructed and divided into sub-blocks and for each one, the mesh is created independently see Figure 4.16. Thus, this method is more flexible to control the mesh around the areas of interest that need to be locally finer.

An unstructured mesh comprises of elements which are not necessarily topologically consistent. The method is flexible and appropriate for complex geometries. The element sizes are changed automatically to fit with geometry change. This method generally demands less effort and time of execution as it is usually automated in available commercial packages such as ANSYS or COMSOL.

The construction of an unstructured mesh by COMSOL can be achieved by different methods; the first method is to use the densities (sizes). After defining one of these sizes, COMSOL automatically constructs the mesh. While the second method of constructing the mesh is user-defined along the edge and other associated parameters, this method provides more control and denser meshes can be constructed around the regions of interest.

4.5.2 Solution approach in COMSOL

After defining the boundary condition of the domain of interest the CFD (solver) stage is started. This process involves solving the matrix system of algebraic obtained from discretizing the fluid flow and heat transfer PDEs. The solver types available in COMSOL multiphysics ® can either be segregated or fully coupled. This means either all variables are solved together in one matrix or the variables are solved separately and iterated. The temperature dependence of a fluid will still be accounted for if the heat transfer and fluid physics are solved for within the same study step.This approach is used by default for most 1D, 2D, and 2D-axisymmetric models. With a segregated solver, this would mean the fluid properties are updated after each time the temperature profile is updated, and then used in the next iteration of the fluid physics. One way or two way coupling is different to Segregated/Fully Coupled solvers. One way coupling using two Study steps to first solve for the fluid physics and then using this solution as an input to solve for the heat transfer. This one-way coupling ignores the temperature dependence of any fluid properties, since the fluid flow is solved for once and prior to consideration of the heat transfer. A two way coupling would solve both physics (including material property temperature dependencies) in a single study step, and would use whichever solver type was most appropriate for the hardware/model size. In the present thesis simulations, the segregated solver

approach was used to solve the governing equations. To deal with the problem of velocity and pressure coupling, first-order discretisation type P1+P1 (first-order elements for velocity and pressure fields) was used with quadratic elements for temperature field. In the current simulations, the relative tolerance is set to 10^{-5}.

The convergence criteria can be found in the solver settings, while convergence is monitored through the graphics windows, showing relevant convergence plots dependent on the study and solver settings. Figure 4.13 shows the numerical error against iteration number which stopped at the specified tolerance level.

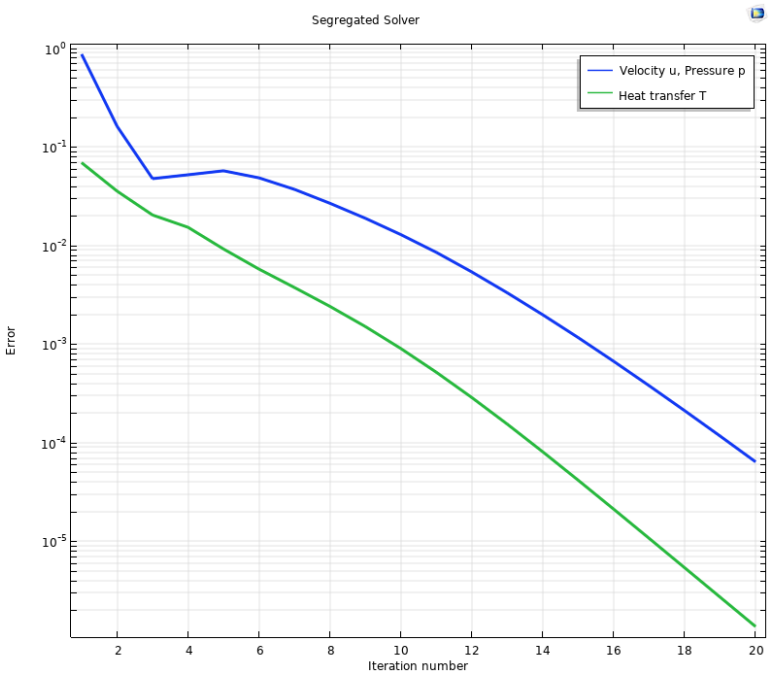

Figure 4.13: Numerical Error with iteration in COMSOL.

4.5.3 Post process of the results

Analyzing the results from a numerical solver involves investigating 3D plots of the modeled fields, cross-section plots (such as x-y plots), and also evaluating derived values, such as integrals over volumes, surfaces or edges, or values of expressions along edges or in a point.

An important task in post processing is to estimate the error in the numerical solution. As mentioned above, this can be achieved by solving the numerical model equations for different mesh sizes in order to estimate the convergence of the numerical solution.

Another important part of post-processing is to estimate the sensitivity of the model to the different data, such as material properties, initial conditions, boundary conditions, loads, constraints, and other input parameters required in the mathematical and numerical models.

4.6 Serpentine PCR microchannel modelling

The problem of the microfluidic channel and heating arrangements, together with modelling and numerical methods are described in this section.

4.6.1 Problem Description and Configuration

The serpentine microfluidic channel, shown in Figure 4.14, passing through denaturation ($95°C$), annealing ($56°C$) and extension ($72°C$) zones is used as a prototypical CFPCR thermal flow problem. This is based on those considered previously by (Hashimoto et al., 2004; Chen et al., 2008; Chen et al., 2013) but with glass, rather than a PDMS, substrate material to increase thermal conductivity and temperature uniformity. In addition, the cover material (H_p) used here is PMMA, which can provide good thermal insulation as well as the practical advantages of good optical access and a low cost. A schematic diagram of the microfluidic channel geometry is presented in Figure 4.15 where W_c, H_c, W_w, H_b and L are the microchannel width, height, wall thickness (the space between the channels), the bottom height and the total length respectively.

There are three individual copper blocks with cartridge heaters placed underneath the glass chip with a constant distance between them of $S = 1mm$, the length of the heaters being $9mm$ underneath the denaturation and annealing zones and $40mm$ underneath the extension zone. The height and length of each heater are $H_h = 2mm$ and L_h=$9mm$. The length of the denaturation, annealing

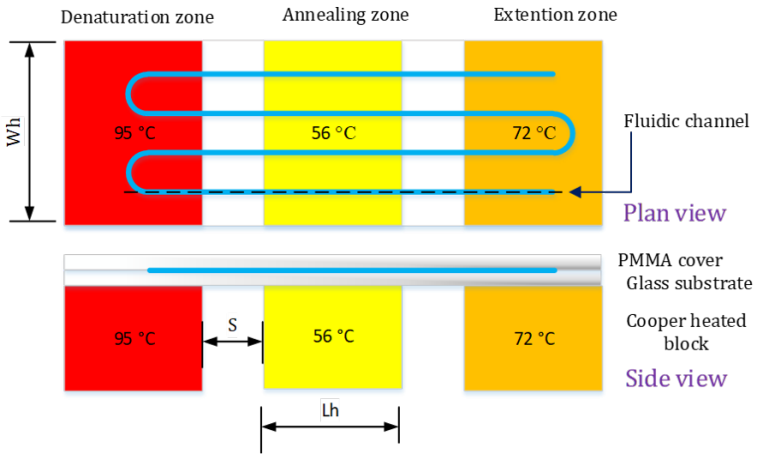

Figure 4.14: Serpentine PCR systems.

and extension zones are chosen to achieve the typical residence time ratios of $1:1:4$ respectively (Chen et al., 2008).

4.6.2 Conjugate Heat Transfer Model

A conjugate heat transfer model of the steady, single-phase, laminar flow problem shown in Figure 4.15 was developed using the following simplifying assumptions employed by previous studies (Chen et al., 2008; Moschou et al., 2014; Aziz et al., 2016; Chiu et al., 2017). The liquid is water, with temperature-dependent density, thermal conductivity and viscosity, and the effects of radiation and buoyancy are neglected within the computational domain. There is no internal heat generation.

The Reynolds number (Re), is given by:

$$Re = \frac{\rho_f V_{ch} D_h}{\mu_f}, \tag{4.44}$$

where ρ_f and μ_f are the density and viscosity of the fluid respectively, V_{ch} is the channel inlet velocity and D_h the channel hydraulic diameter defined by:

$$D_h = \frac{2W_c H_c}{W_c + H_c}. \tag{4.45}$$

For CFPCR flows, $Re \sim O(10^{-1})$, i.e. laminar flow conditions. This is explained in more details in chapter 3.

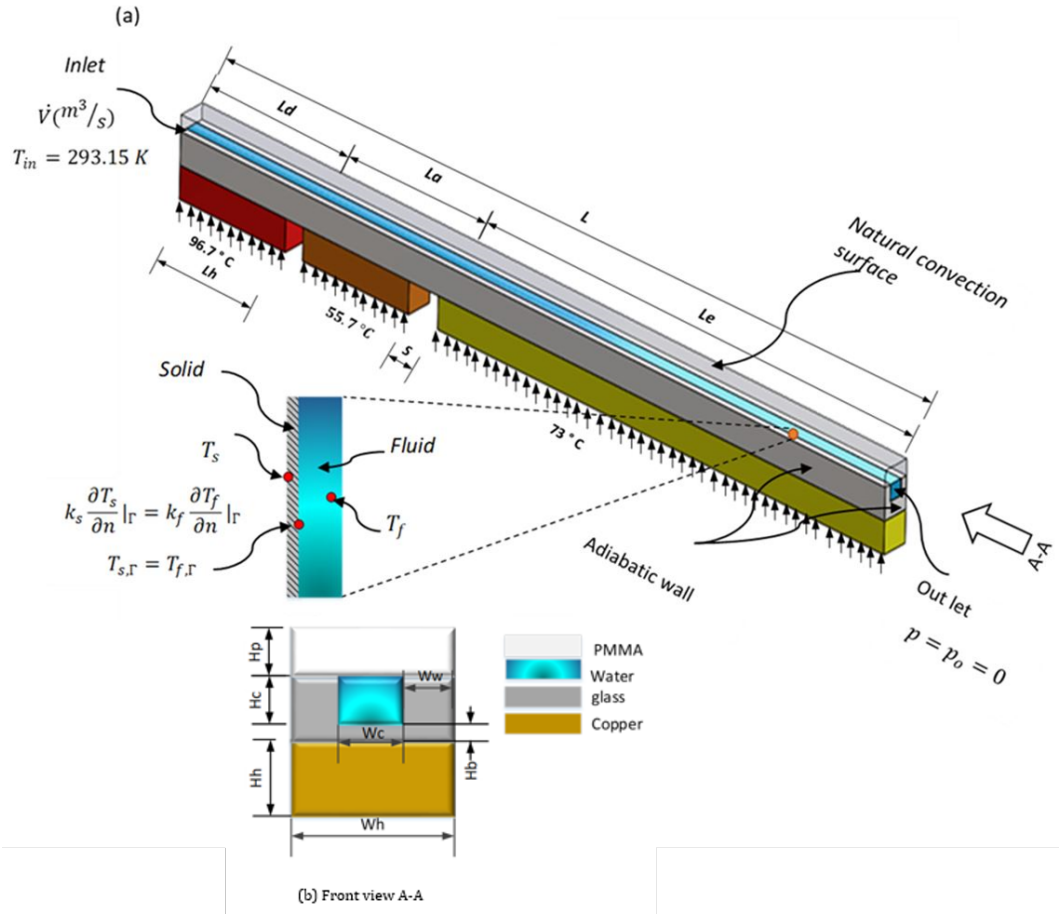

Figure 4.15: A schematic diagram of the microfluidic channel and heating arrangements in each of the CFPCR zones: a) the thermal boundary conditions applied in each zone and b) the cross-section of the microfluidic channel.

The flow is modelled using the governing continuity and Navier-Stokes equations, (White and Corfield, 2006) which are presented in chapter 3 described in section 3.4 include Equations 3.4 and 3.15

The heat transfer is a combination of conduction in the solid domain and convection in the fluid, coupled through conjugate heat transfer boundary conditions at the solid-fluid interface (Davaji, 2016).

The energy equation for the convective heat transfer in the fluid is given by Equation 3.17. While the energy equation for conductive heat transfer in the solid is described by Equation 3.18.

The thermophysical properties of the water (ρ_f, μ_f, C_{pf} and k_f) depend on the temperature and are given by (Bergman et al., 2011):

$$\rho_f = 838.466 + 1.4T - 0.003T^2 + 3.72 \times 10^{-7}T^3, \tag{4.46}$$

$$\begin{aligned}\mu_f =& 1.38 - 0.0212T - 1.36 \times 10^{-4}T^2 - 4.64 \times 10^{-7}T^3 \\ &+ 8.9 \times 10^{-10}T^4 - 9.08^{-13}T^5 + 3.846 \times 10^{-16}T^6,\end{aligned} \tag{4.47}$$

$$C_{pf} = 12010.147 - 80.407T + 0.3099T^2 - 5.382 \times 10^{-4}T^3 + 3.625 \times 10^{-7}T^4, \tag{4.48}$$

$$k_f = -0.869 + 0.00895T - 1.584 \times 10^{-4}T^2 - 7.975 \times 10^{-9}T^3, \tag{4.49}$$

where T is in Kelvin. The thermal conductivity of copper is $k_s = 400W/(m \cdot K)$.

4.6.3 Boundary Conditions

The computational domain and boundary conditions are shown in Figure 4.15. At the walls, no-slip velocity boundary conditions $\mathbf{u} = \mathbf{u}_s = 0$ are applied. The inlet velocity V_{ch} is set to achieve a typical Reynolds number of 0.7 and the inlet temperature is fixed at $T_{f,in} = 20°C$, with an ambient pressure condition, $p = p_0$, imposed at the outlet.

The conductive heat transfer in the solid is coupled to the convective heat transfer in the fluid through the following conjugate heat transfer boundary conditions at the solid-liquid interface (Davaji, 2016), Γ: (i) continuity in temperature, $T_{(s,\Gamma)}$=$T_{(f,\Gamma)}$ and (ii) continuity of heat flux given by Fourier's law (Qu and Mudawar, 2002):

$$-k_s \frac{\partial T_s}{\partial n}|_\Gamma = k_f \frac{\partial T_f}{\partial n}|_\Gamma \tag{4.50}$$

The upper surface of the domain includes the effect of natural convection via a heat transfer coefficient of $15W/(m^2 \cdot K)$ (Chen et al., 2008; Chen et al., 2015). All the outer surface boundary conditions are considered to be adiabatic except at the bottom of the copper heaters where temperatures are set to $96.7°C$, $73°C$ and $55.7°C$ respectively for the denaturation, extension and annealing zones.

The governing equations are solved subject to the boundary conditions using COMSOL Multiphysics 5.4 ® .

4.6.4 Performance Metrics

Three performance metrics are calculated for each flow. The temperature uniformity in the zones is calculated by quantifying deviations from the target temperature, T_{target}, via

$$T_{dev} = \sqrt{\frac{\iiint \left(T_{f_{i,j,k}} - T_{target}\right)^2 dV}{\iiint dV}}. \tag{4.51}$$

Where T_{target} refer to the target temperatures in the denaturation, annealing and extension zones are ($95°C$, $55°C$ and $72°C$) respectively.

The hydraulic performance is measured by calculating the pressure difference along the channel

$$\Delta p = p_{in} - p_{out}. \tag{4.52}$$

Heating power, Q, in each zone Q_d, Q_e and Q_a was obtained at the bottom of the heater surfaces using $\mathbf{n} \cdot (k\nabla T) = q/A_h$ where $\mathbf{n}$ denotes the outward normal vector of the domain and A_h is the surface area of the heater. The total heating power is calculated by:

$$Q_t = Q_d + Q_a + Q_e, \tag{4.53}$$

where Q_t, Q_d, Q_a and Q_e represent the total heat power in watts (W), heat transfer to denaturation zone, and heat extracted from annealing zone and heat transfer to the extension zone respectively.

4.6.5 Mesh generation

In the present study, the mesh tests were carried out by solving the model on a series of progressively refined meshes to identify suitable meshes for the study. The first created meshes were based on predefined unstructured tetrahedrons which are automatically constructed and adapted for the physics of the model. Structured meshes are also used. The QUAD mesh was selected per the faces and they swept to cover the domains, also different sizes are used see Figure 4.16.

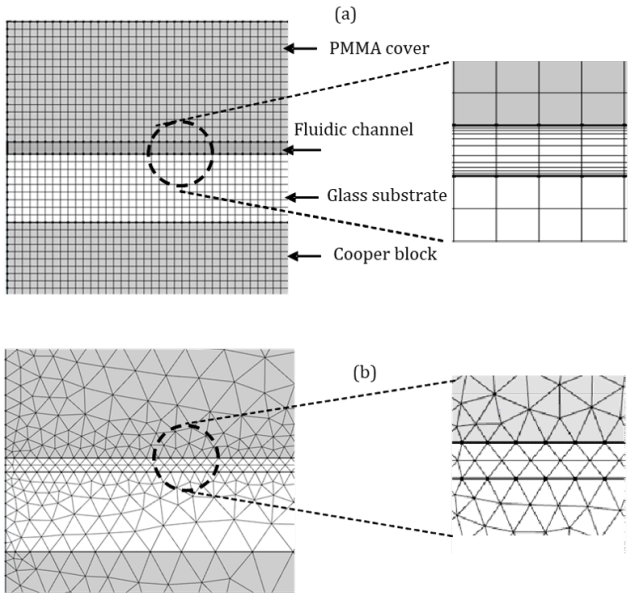

Figure 4.16: System meshing, using (a) structured, (b) unstructured meshes

4.6.6 Numerical Validation

The effect of grid density is examined by obtaining numerical solutions on a series of structured Finite Element grids of increasing refinement, on a desktop PC with Microsoft Windows 10 and 32GB physical RAM. Table 4.1 shows the number of degrees of freedom (DOF), physical memory (PM), Virtual Memory (VM), execution time and calculated T_{dev} and Δp for each grid. There is only a small change $< 0.2\%$ in the obtained results if the number of mesh elements is increased above 877552. Accordingly, numerical results presented below have been obtained on the mesh with 877552 elements as an appropriate compromise between computational expense and accuracy.

The numerical model is first compared with the experimental results (Duryodhan et al., 2016) for thermal flow in diverging channels. Figure 4.17 shows that the agreement between the experimental and numerical results is generally very good. The next comparison is with the numerical results of (Chen et al., 2008) where $H_c = 150\mu m$, $W_c = 50\mu m$, $S = 1mm$, $V_{ch} = 6mm/s$ and $T_{f,in} = 72°C$.

NO. of elements	DOF ($\times 10^5$)	PM (GB)	VM (GB)	Time	Δp(Pa)	T_{dev}(K)
93024	2.52	2.71	3.28	119	51.31	27.98
216096	5.1679	3.17	3.92	303	51.00	27.81
380480	8.3090	3.89	4.67	553	50.64	27.70
448686	14.485	4.47	5.26	677	50.58	27.58
877552	17.763	6.56	7.42	1839	50.48	27.57
1026602	20.373	8.23	9.52	3849	50.45	27.50
1171632	23.329	7.93	8.92	4050	50.43	27.52

Table 4.1: Effect of grid density for the case of $Re = 0.7$, $T_f = 20°C$, $H_c = 150\mu m$, $W_c = 500\mu m$, $W_w = 150\mu m$ and $H_b = 850\mu m$.

Once again the numerical predictions of the temperature profile along the three temperature zones, shown in Figure 4.18, are in very good agreement with the published results.

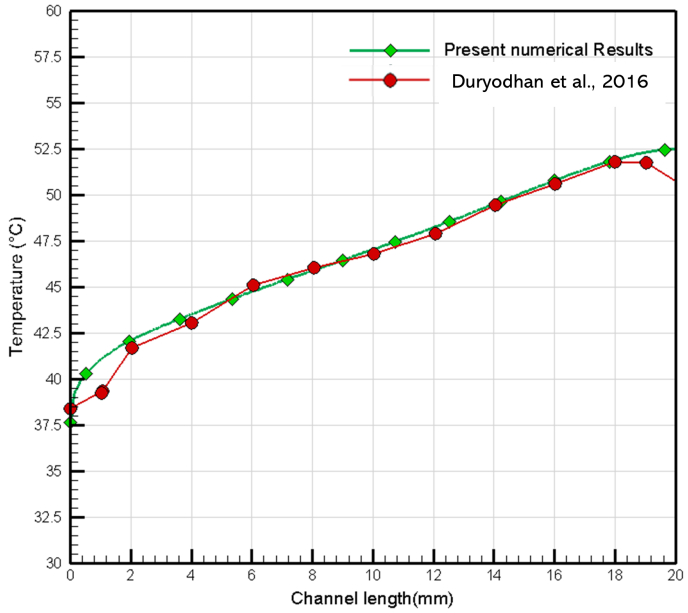

Figure 4.17: Comparison of surface temperature variation along flow direction in a diverging microchannel at $q = 4W$.

In the next section, a basic introduction to the optimization process will be

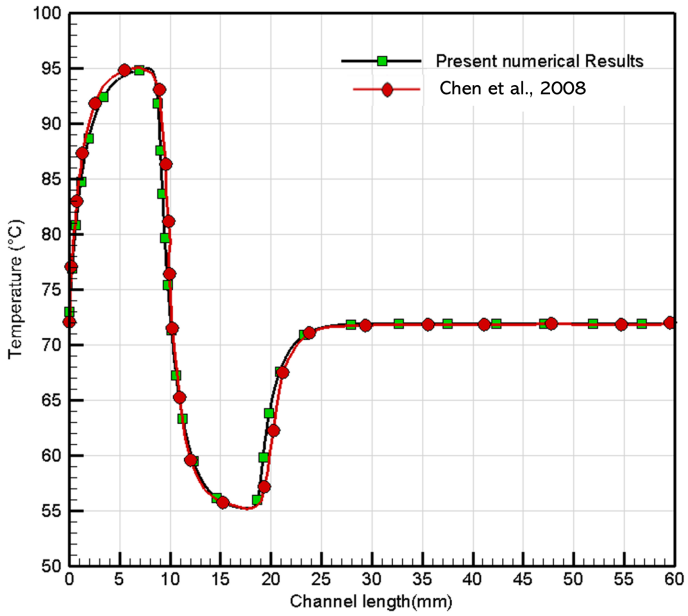

Figure 4.18: Comparison of fluid average temperature profile along the centreline of CFPCR zones.

presented and the primary aim of this section is to describe the optimisation procedure and algorithm methods used to find the optimal solution in chapter 5.

4.7 Design Optimisation

Optimisation aims to maximize or minimize a set of functions using a mathematical technique for searching the design domain and finding the design parameters that provide an optimal solution satisfying specified criteria, (Ibrahim and Alfa, 2017). This section is concerned with optimizing PCR systems using CFD-based optimization methods and describes the process of optimization from the stage of selection of design variables to the stage of obtaining the optimum design.

The optimisation procedures are shown in Figure 4.19 which reveals the steps of obtaining surrogate models that can be used to find solutions that are compromises between objectives. The first step is the formulation step used to identify

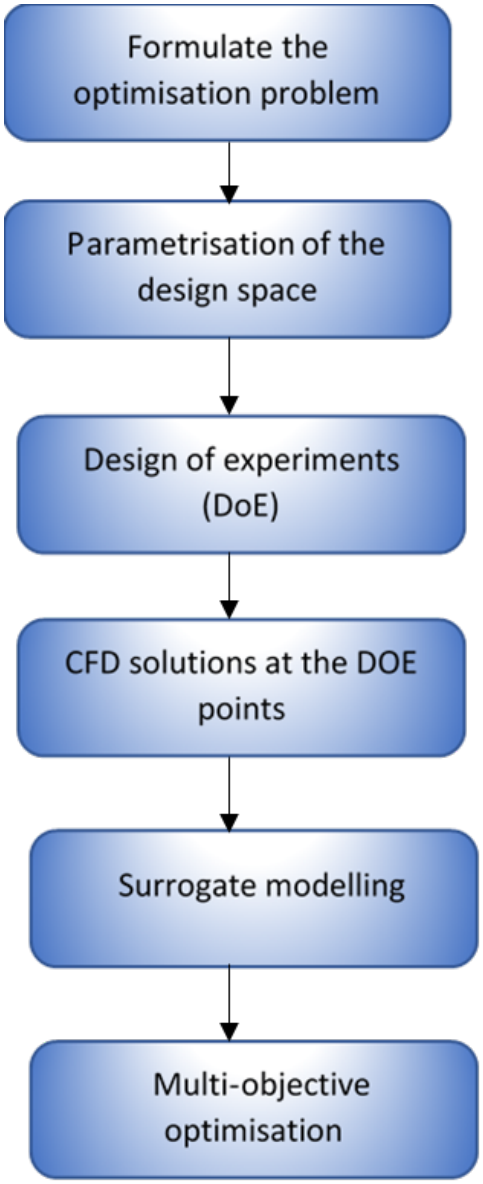

Figure 4.19: Flow chart of the optimisation process.

the objective functions and constraints. The second step is design space parameterisation which can be used to specify the design variables and design space. The third step is the design of experiments (DOE) generation in which a number of well-scattered design points are generated within the design space. The fourth step is to use the CFD simulations to find the CFD solution values of the object-

ive functions at each of the DoE points. The fifth step is to create the surrogate modelling used to build and validate accurate surrogate models for each objective function throughout the design space using an appropriate surrogate modelling method. The surrogate model is an approximate solution used as an alternative model to expensive CFD simulations which are computationally expensive and time-consuming. Also, a surrogate model is used to predict the values of unseen data (data in the DOE domain not educated by the CFD model). The sixth step is multi-objective optimisation: embedding the surrogate models within an appropriate multi-objective optimisation algorithm and generate Pareto surfaces showing optimal compromises between the objective functions and validate either accuracy against the CFD solutions at selected Pareto points or by using untested DOE points within the design space.

4.7.1 Formulation of optimization problems

This step of the optimization process is used to identify the objectives, parameters and constraints for a certain problem. The general form of problem that needs to be optimized can be written as follows:

min(f(x)) where the design space is governed by

$x_{lower} \leq x \leq x_{upper}$

where, x_{lower} and x_{upper} represent the lower and the upper limit for each of the design variables. It is also possible to have inequality constraints, $g(x)$, which effectively reduces the size of the design space, however, this is not used in the current work. The number of degrees of freedom in the design domain is equal to the number of design parameters. There is a need to minimise the number of these variables to avoid what is often termed the 'curse of dimensionality arising in the case of using a large number of design variables. Also, using a large number of design variables leads to the complexity of the design problem which increases exponentially with the number of design variables. As a result, a preliminary study needs to be carried out to identify those parameters which have a significant effect on the objective (Cavazzuti, 2013). The multi-objective optimisation problem considered in this thesis is the minimisation of each of $\{T_{dev}, \Delta p, Q_t\}$ within the design space:

$$150\mu m \leq W_c \leq 500\mu m, 50\mu m \leq H_c \leq 150\mu m, 400\mu m \leq H_b \leq 800\mu m, 70\mu m \leq W_w \leq 800\mu m.$$

After selecting the range and the number of design variables, the objective needs to be expressed as functions of these design variables to obtain a design model.

4.7.2 Design of experiments (DOE)

Design of experiments (DOE) are mathematical techniques used to generate random points and to combine and distribute them effectively within the design space in order to build the metamodel (Baco et al., 2019). The fitness accuracy of the surrogate model affects the accuracy and the quality of the results which are influenced by the number of DOE points and sampling strategy used (Baco et al., 2019). Various statistical methods are available to build up the DOE, among them factorial, Full Factorial, Latin Hypercube (LHC) and Optimal Latin Hypercube (OLHC) (Cavazzuti, 2013) which is used in this thesis. The key objective of the DoE is to generate sample points (sampling) for filling the design domain. The objectives of sampling methods can be summarized in the following points:

1. Explore the design space for a better understanding of the range in the outputs for a domain of interest.

2. Determine the parameters that have a significant impact on the output, and/ or explore the effect of deviations in the inputs on the output.

3. Create data to generate surrogate models by using the outputs at the DOE points from CFD simulations.

The DoE sampling methods can be categorized into classical and non-classical (stochastic) approaches. Classical sampling designs methods used to screen the design for exploratory targets in the initial stages of the design in order to minimise the size of design parameters by neglecting the insignificant parameters. Classical methods include full factorial and central composite designs as well as the less densely populated such as fractional factorial and Box-Behnken (BB).

These classic approaches tend to spread the sample points around the boundaries of the design space and leave a few at the centre of the design space. Stochastic approaches include orthogonal array sampling (Tissot and Prieur, 2015) and the Latin Hypercube (LH) methods,(Narayanan et al., 2007).

4.7.3 Sampling and Probability Distributions

Sampling is the process by which values are randomly drawn from input probability distributions (Etikan and Bala, 2017). Any probability distribution can be expressed in cumulative curve form. Probability distributions are mathematical functions that assign a probability to a random variable. They can be used to model experimental or historical data in order to generate prediction estimates or analyse a large number of outcomes such as in Monte Carlo simulations. For a specified parametric distribution, the parameters are estimated by fitting to data. Some common parametric distributions include:

- Normal (or Gaussian) distribution
- Weibull distribution

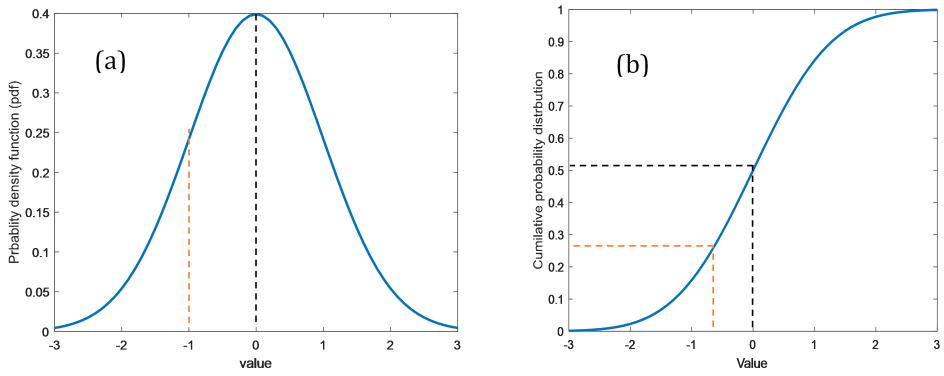

Figure 4.20: (a) probability distribution function (b) The same probability distribution function expressed in cumulative form

From Figures 4.20 shows an example of the probability distribution the computer will generate a random number between (0-1). Then the number will be assigned to a value using a cumulative probability distribution. For example, if we take x=0 in Figure 4.20(b) gives y=0.5 what does that is mean. From Figure

4.20(a) it can be noted 50 % below zero and 50 % above zero. Another example is x=-0.7 in Figure 4.20(b) gives y= 0.26 and Figure 4.20(a) shows about 26 % of the numbers is below -0.7 and 74 % is above -0.7.

The efficiency of a sampling method can be identified based on the number of iterations and simulation run time. Thus, if the sampling demands a long time and many iterations until sampled values approximate input distributions, it is not efficient. Monte Carlo sampling and Latin Hypercube sampling are the two common methods of sampling.

4.7.3.1 Monte Carlo Sampling

Monte Carlo sampling is a traditional method used for generating random samples from a probability distribution. This approach of sampling is widely applied for complex problems having a probabilistic behaviour (Shapiro, 2003). A wide variety of algorithms are available for generating random samples from different types of probability distributions. Monte Carlo sampling methods are entirely random; thus, the generated samples are randomly distributed within the range of the input distributions and these samples are more likely to be drawn in the regions of the distribution that have a higher chance of occurrence. In the cumulative distribution depicted in Figure 4.21, each Monte Carlo sample uses a new random number between 0 and 1. With enough iterations, Monte Carlo sampling "recreates" the input distributions through sampling. It can be noted from the Figure 4.21 that five samples drawn fall in the middle of the distribution and the values of samples are not represented in the outer ranges of the distribution leading to simulation results not represented in these ranges. It is significant to include the influences of these low probability outcomes which must be sampled. However, if their probability is low enough, a small number of Monte Carlo iterations might not sample sufficient quantities of these outcomes to accurately represent their probability.

Thus Monte Carlo Sampling method (MCSM) needs a large number of generated samples to follow the probability distribution and some issues have been raised when a small number of iterations are performed. Often, a Monte Carlo sampling set is not a good approximation of actual probability distribution. Also,

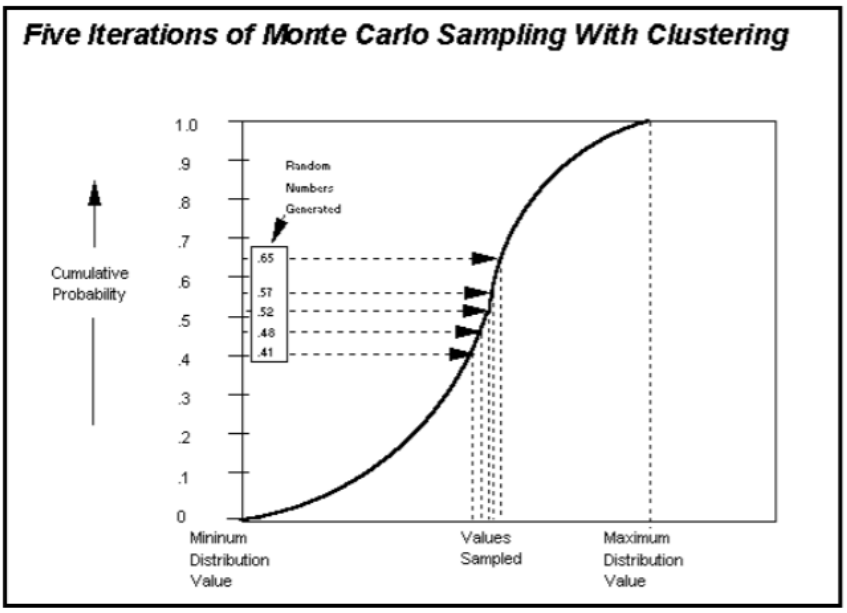

Figure 4.21: Five iterations of Monte Carlo sampling with clustering (Cavazzuti, 2012)

the MCSM has a memory-less system that means new sample points are generated without taking into account the previously generated sample points. As a result, a number of distribution methods are proposed to recreate the probability distribution with less sampling than Monte Carlo methods, one such example is Latin Hypercube sampling.

4.7.3.2 Latin Hypercube Sampling (LHS)

LHS was firstly used by (McKaya et al., 1979) to replace the Monte Carlo method to provide simple random and efficient sampling variables from their multivariate distributions (Minasny and McBratney, 2006) and it was further elaborated by (Iman and Conover, 1980). LHS could be nearly five times more effective in yield estimation than traditional sampling methods (Swidzinski et al., 1999). LHS uses a stratified sampling technique in order to reduce the number of simulations in computing response uncertainty. Stratification means dividing the vertical axis of the distribution function of random variables into equal non-overlapping segments and the number of these intervals is equal to the number of computer

runs to enhance the distribution of the input variables within the design space. The key to this method is to accurately recreate the input distribution in fewer iterations with less samples in comparison with the Monte Carlo method. The sampling procedure being used in Latin Hypercube is achieved without replacement, that means the sample is taken from one interval one time and the new sample is not drawn again the same segment but it is taken from a new segment which ensures accurate distribution. Figure 4.22 shows the samples generated by Latin Hypercube. Compared with the 5 clustered samples drawn by Monte Carlo method depicted in Figure 4.21, the samples of Latin Hypercube are more accurate in representing the input probability distribution with fewer iterations. In general, for the same accuracy in statistic LHS techniques demand fewer samples than the traditional Monte Carlo method (Helton and Davis, 2000).

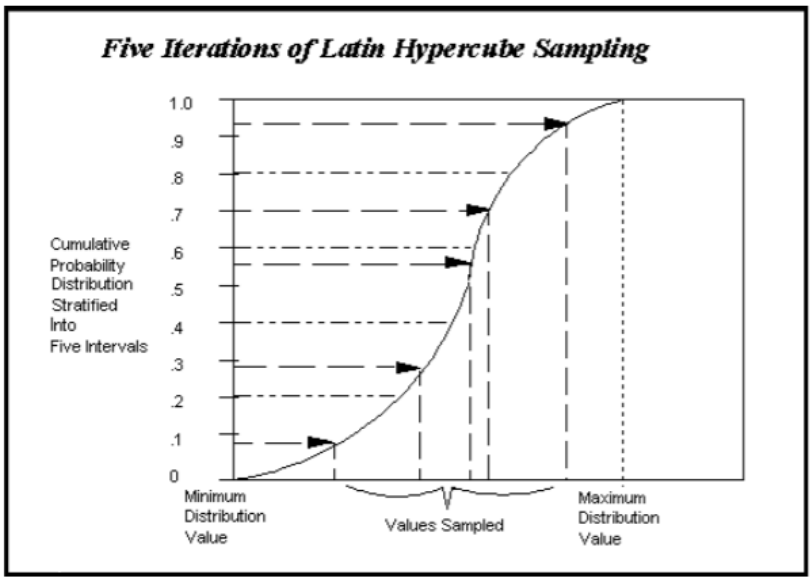

Figure 4.22: Five iterations of Latin Hypercube sampling (Cavazzuti, 2012)

4.7.3.3 Latin Hypercube Sampling in Two and multi Dimensions

Latin square sampling is a method used for generation of random samples of independent variables (x_1, x_2) in a squared grid by generating one sample in each row and each column. Generate one-dimensional LHS samples for each variable

x_1 and x_2 then randomly combine the LHS samples into two-dimensional pairs, see Figure 4.23(a) In Latin Hypercube the design domain is subdivided into an orthogonal grid with N elements of the same length per parameter if the variables have uniform distributions. LHS is a more advanced and efficient form of Monte Carlo analysis methods. With LHS, the points are randomly generated in a square grid across the design space, but no two points share input parameters of the same value. This means that no point shares a row or a column of the grid with any other point. Generally, LHS requires 20% to 40% fewer simulations loops than the Direct Monte Carlo technique to deliver the same results with the same accuracy. However, that number is largely problem-dependent. Similarly, Sub-volumes can be specified in the multi-dimensional grid N. Within the multi-dimensional grid N sub-volumes are specified so that along each row and column of the grid only one sub-volume is chosen. In Figure 4.23(b) the chosen sub-volumes are black and give a typical crossword-like graphical representation of Latin Hypercube designs. Inside each sub-volume, a sample is chosen randomly. It is important

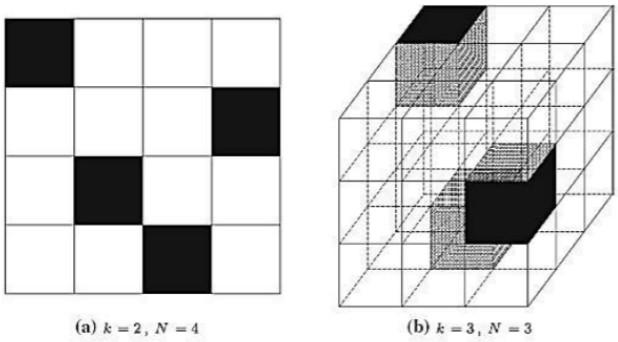

Figure 4.23: Latin Hypercube Sampling (Cavazzuti, 2012)

to choose the sub-volumes in order to have no spurious correlations between the dimensions or to spread the samples all over the design space. For example, a set of samples along a design space diagonal would satisfy the requirements of a Latin Hypercube DoE but would leave most of the design space unexplored. There are several techniques used to reduce the correlations in Latin Hypercube designs. Figure 4.24 shows an example of a correlation reduction between variable values in a Latin Hypercube DoE with $k = 2$ factors and $N = 10$.

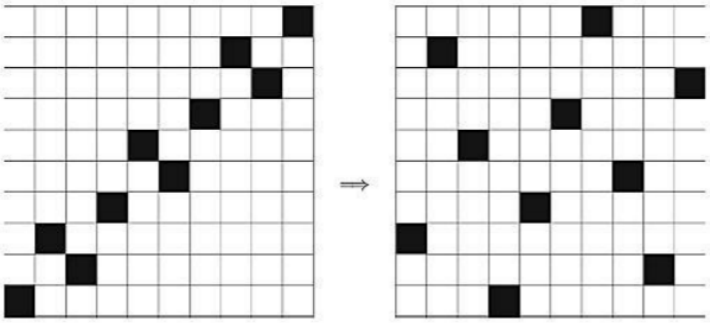

Figure 4.24: Correlation reduction in Latin Hypercube Sampling (Cavazzuti, 2012)

4.7.3.4 Optimum Latin Hypercube

As stated in the previous sections the Latin the LHS sampling approach divides each design parameter into N equally sized intervals where the same value of a parameter can only occur once. However, there are two different types of Latin Hypercube Sampling : Random Latin Hypercube (RLH) and Optimised Latin Hypercube (OLH). The distribution of DOE points is required to be uniform within the variable range to improve the quality of the surrogate model. Thus optimised LHS space filling design is desirable which is considered in the present thesis. The conventional LHS or random Latin Hyper cube design (RLH) requires that the input data only include the number of factors (parameters) N and the number of design experiments (number of DOE points). Figure 4.25 (a) shows 100 DOE points distributed randomly (non-uniform) using conventional random LHS leading clustering of samples which cause some areas of the design space to be less explored (Urquhart et al., 2020). The clustering of samples can be reduced by increasing the separation between design points which can be achieved by optimising the LHC using the Audze-Eglais objective function:

$$\sum_{p=1}^{P} \sum_{q=p+1}^{P} \frac{1}{(r_{pq})^2} \tag{4.54}$$

where $(r_{pq})^2$ is the distance between two sample points. The optimised LHC sample plan can be obtained by minimising Equation 4.54 using a permutation genetic algorithm (Bates et al., 2004).

The main desirable features of optimal Latin Hyper cube (OLH) are :-

1. the number of levels of factors (same for each factor) is equal to the number of experiments and for each level there is only one experiment;
2. the points of experiments are distributed as uniformly as possible in the domain of factors.

It can be noted from Figure 4.25(b) for a sample size N=100 and two design variables/factors(x_1 and x_2) that the Optimal Latin Hypercube sampling method is more effective at providing uniform sampling throughout the design space.

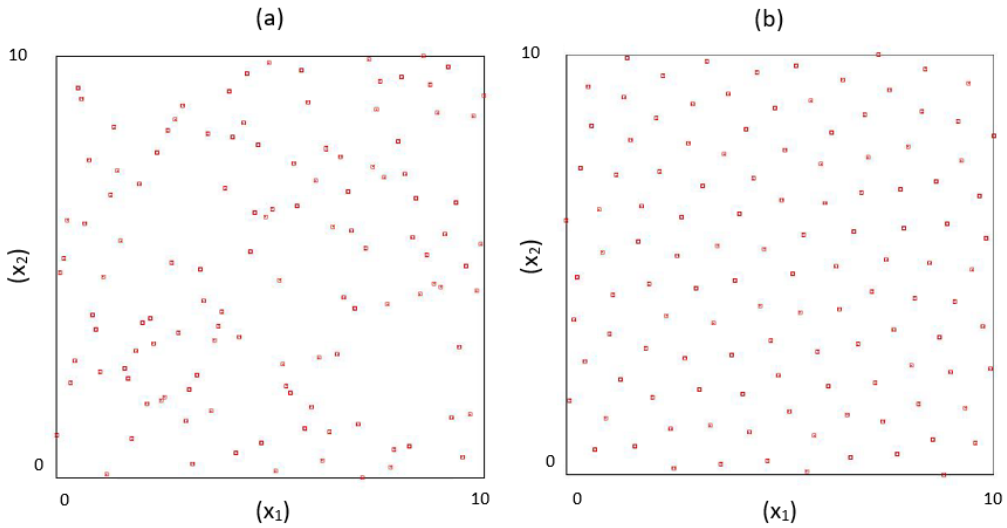

Figure 4.25: Comparison between LHS and OLHS for 100 design variables (Loweth et al., 2011)

The accuracy of optimization results depends on the number of DOE data and their distribution within design space. Thus; to reduce the computational cost an alternative solution can be used to address this issue such as using meta-modeling or surrogate modelling.

After validation of the CFD model it can be used to obtain an initial result based on set of data usually classical design DOE points in order to investigate the effect of the parameter on the objectives ,also it often used to obtain an initial

capture of the response surrogate model based on a number of DOE points also it can be used to validate a number of optimised points extracted from Pareto front.

4.7.4 Surrogate model enabled optimization

After obtaining the values of the objective function from the CFD model that has been solved at each of the DoE points, the surrogate model can be created. Surrogate models (also named response surface models or meta-models) (Razavi et al., 2012) are an alternative solutions for the CFD model used to describe the behaviour of the system and to predict the output values of an expensive CFD simulation codes (Viana et al., 2009). Surrogate models can also be used to evaluate the values of the objective function at new untested design points within design space. Thus; the surrogate model is often used in design optimisation to mimic the real system and create an approximate result to avoid doing CFD modelling in order to reduce the computational cost of CFD models. Also the surrogate models are used to reduce the effect of numerical noise or missing data (Forrester et al., 2008; Loweth et al., 2011). Once the surrogate model has been created, global optimization searching starts to determine the values of the design variables on the surrogate model surface corresponding to the global minimum value of the objective function. As noted in the previous section, building a surrogate model requires using a DoE approach where the design points are sufficiently distributed to ensure an accurate surrogate model that can be used to avoid running more CFD simulations (Forrester et al., 2008).

Different mathematical and statistical methods have been used to create the surrogate model and usually the criteria of these methods are based on two different schemes: approximation-based schemes and interpolation-based schemes. The approximation based methods include polynomial response surface, least square and moving least square methods. Polynomial approximation models are easy to implement, clear on parameter sensitivity, and cheap to work with but are usually less accurate than the interpolation models, particularly for non-linear system. Also, these methods do not interpolate the sample points and are limited by the chosen function type (Wang and Shan, 2006). The interpolation methods

include a radial basis, kriging functions and neural network (Dyn et al., 1986), require the surrogate model to pass directly through the DoE data points. The RBF and neural network methods are used in the present thesis to build up the surrogate model.

4.7.4.1 Radial Basis Functions (RBFs)

Radial basis functions (RBFs) are mathematical tools used to construct surrogate models to replace computationally expensive simulations (Gutmann, 2001). Recently RBFs have been widely used due to their attractive features involving their capabilities of predicting nonlinear and arbitrary behaviour functions and they can be used to deal with scattered points in multi-dimensional design space. Also, RBFs provide a convenient and easy method of creating a surrogate model from the DoE data based on an interpolation scheme (Acar, 2010). Thus RBFs can be used as a trade-off design between Kriging and polynomials (approximation) (Wang and Shan, 2006). The first step of the RBFs method is to define an estimate y at the design points which involves a number of design variables (ndv) and a total of n DoE points that can be described as:

$X_i = [x_{(i,1)}, x_{(i,2)}, ..., x_{(i,ndv)}]$

for $i = 1, ...n$ at which the response takes the values $Y_i = [y_{(i,1)}, y_{(i,2)}, ..., y_{(i,ndv)}]$ for $i = 1, ...n$. Then the RBF that can be used to predict y at any point $X_i = [x_{(i,1)}, x_{(i,2)}, ..., x_{(i,ndv)}]$ within the design space is given by the RBF approximation

$$\widehat{y}(x) = \sum_{i=1}^{n} \lambda_i \phi \left(r \left(x, x_i \right) \right) \tag{4.55}$$

where $\widehat{y}(x)$ is the prediction of a true response function, λ_i is the weighed coefficient for the $i-th$ basis function, n is the number of samples, $r(x, x_i) = |\mathbf{x} - \mathbf{x}_i\|$ denotes the Euclidean distance between the i_{th} sample x_i and a testing point x, and ϕ is a basis function

$$\widehat{y}(\mathbf{x}) = \sum_{i=1}^{N} \lambda_i \phi \left(\|\mathbf{x} - \mathbf{x}_i\| \right), \tag{4.56}$$

This can be written in matrix form:

$$\begin{bmatrix} \phi\left(\|\mathbf{x_1}-\mathbf{x_1}\|\right) & \phi\left(\|\mathbf{x_2}-\mathbf{x_1}\|\right) & \dots \phi\left(\|\mathbf{x_n}-\mathbf{x_1}\|\right) \\ \phi\left(\|\mathbf{x_1}-\mathbf{x}_2\|\right) & \phi\left(\|\mathbf{x_2}-\mathbf{x}_2\|\right) & \dots \phi\left(\|\mathbf{x_n}-\mathbf{x}_2\|\right) \\ \vdots & \vdots & \vdots \\ \phi\left(\|\mathbf{x_1}-\mathbf{x}_n\|\right) & \phi\left(\|\mathbf{x_2}-\mathbf{x}_n\|\right) & \dots \phi\left(\|\mathbf{x_n}-\mathbf{x}_n\|\right) \end{bmatrix} \begin{bmatrix} \lambda_1 \\ \lambda_2 \\ \vdots \\ \lambda_m \end{bmatrix} = \begin{bmatrix} \widehat{y}(\mathbf{x})_1 \\ \widehat{y}(\mathbf{x}_2) \\ \vdots \\ \widehat{y}(\mathbf{x})_n \end{bmatrix} \tag{4.57}$$

Matrix 4.57 can be written as:

$$\phi(r).\lambda = \widehat{y}(\mathbf{x}) \tag{4.58}$$

RBF are normally used in interpolating mode which means that the weights λ_i are chosen so that the RBF approximation is exact at each of the DoE points, i.e. $yrbf(x_i) = \widehat{y}(\mathbf{x_i})$ for $i = 1, \dots, n$. In this case the λ_i are obtained by solving the linear matrix equation:

$$\lambda = \phi(r)^{-1}\widehat{y}(\mathbf{x}) \tag{4.59}$$

where $\phi(r)$ is the Gram matrix defined such that $\phi(r)$=$\phi\left(\|\mathbf{x}-\mathbf{x}_i\|\right)$.

The RBF functions $\phi(r)$ can take several forms including Gaussian (G), multi-quadric (MQ), and inverse multi-quadratic (IMQ) functions and cubic radial basis function as summarized in Table 4.2.

Name	Form
Gaussian function	$\phi(r) = e^{-r^2/\beta^2}$
Multi-quadratic function	$\phi(r) = \sqrt{r^2+\beta^2}$
Inverse Multi-quadratic function	$\phi(r) = 1/(r^2+\beta^2)$
Cubic radial basis function	$\phi(r) = \beta r^3$

Table 4.2: Typical basis functions in RBF.

In the current thesis cubic radial basis function is considered so the basis function can be expressed : $\phi\left(\|\mathbf{x}-\mathbf{x}_i\|\right) = \beta\|\mathbf{x}-\mathbf{x}_i\|^3$, where β is a calibration parameter for the cubic RBF function. For each surrogate model, β is determined using a relatively simple Leave-One-Out (LOO) calibration, where each sample point is left out of the RBF function and then used to predict the value at the omitted DoE point. The Root Mean Square Error (RMSE) of the discrepancies between the predicted and actual DoE points is then minimised with respect to the β parameter over a suitable interval (González Niño et al., 2019).

$$RMSE = \sqrt{\frac{1}{N}\sum_{i=1}^{N}(y_i - \widehat{y}_i)^2} \tag{4.60}$$

where N is the number of DoE points, while $\widehat{y}_i$ and y_i respectively the predicted and the actual response values

4.7.4.2 Moving least squares Method (MLSM)

The moving least squares method (MLSM) is used to create a surrogate model for deterministic optimisation Thus, after identifying the lower and upper limit of design variables in the first step. The second step is to create 300 design points within the design space using the optimal Latin Hypercube. The next step is to run CFD simulations for all 300 DoE design points and to post-process the solutions to determine values for the two objective functions described above. Then, using these findings, a surrogate model can be created to be used as an alternative for a CFD solution that is capable to predict the objective (outputs) for any design points (input). The feature of MLSM is they are particularly useful to develop a surrogates model capturing a functional relationship between output and inputs (design variables) based on a limited number of CFD solutions. Also, the inherent capability of the surrogate model generated by MLSM in dealing with numerical noise resulting from CFD solutions (Gilkeson et al., 2014). Thus MLSM is widely used to handle the noise effect.

In the current thesis the number of design variables ndv is 4 which can be represented by vector $\mathbf{x}$ where :

$\mathbf{x} = (W_c, H_c, H_b, W_w)$ The design points are distributed within the design space as shown in the matrix 6.8.

The first step of the MLS method is to evaluate y at the design points which involve a number of design variables (ndv) and a total of n DoE points that can be described as:

$\mathbf{x_i} = [x_{(i,1)}, x_{(i,2)}, ..., x_{(i,ndv)}]$

for $i = 1, ...n$ at which the response takes the values $\mathbf{y_i} = [y_{(i,1)}, y_{(i,2)}, ..., y_{(i,ndv)}$for $i = 1, ...n$. Then the MLS can be used to predict y at any point $\mathbf{x_i} =$

$[x_{(i,1)}, x_{(i,2)}, ..., x_{(i,ndv)}]$ with the design space is given by the MLS approximation.

$$\widehat{y}(x) = \sum_{i=1}^{n} w_i \mathbf{y_i} \tag{4.61}$$

where $\widehat{y}(x)$ is the prediction of a true response function , w_i is the Gaussian weight decay function used to determine weighted coefficient for the $i-th$ basis function, n is the number of samples.

$$w = \exp\left(-\theta r_i^2\right) \tag{4.62}$$

$r(x, x_i) = \|\mathbf{x} - \mathbf{x}_i\|$ denotes the Euclidean distance between the i_{th} sample xi and a testing point x, and θ is is the closeness of fit parameter.

For a given data set the closeness of fit parameter θ has a significant influence on the surrogate model, and choosing an appropriate θ is necessary. Estimation θ manually leads to poor fit with numerical noise. θ can be tuned to reduce the effect of numerical noise. In the current thesis For each surrogate model, θ is determined using a relatively simple Leave-One-Out (LOO) calibration, where each sample point is left out of the MLS function and then used to predict the value at the omitted DoE point. The Root Mean Square Error (RMSE) of the discrepancies between the predicted and actual values at DoE points which is then minimised with respect to the θ parameter over a suitable interval (González Niño et al., 2019).

$$RMSE = \sqrt{\frac{1}{N}\sum_{i=1}^{N}\left(y_i - \widehat{y}_i\right)^2} \tag{4.63}$$

where N is the number of DoE points, while $\widehat{y}_i$ and y_i respectively the predicted and the actual response values.

4.7.4.3 Artificial Neural Network (ANN)

Another very significant technique of creating surrogate models is the Artificial Neural Network (ANN) method which is inspired by biological nervous systems. ANN structure typically comprises an input layer into which the input parameters (independent variables) are fed, the output layer that produces the predicted objectives (dependent variables) and one or more hidden layers (Makarynskyy

et al., 2015). The hidden layers connect the input and output layers together and allow for complex, nonlinear mapping from the input to the output. The mapping is not specified but is learned. An artificial neural network can be described in terms of the individual neurons, the network connectivity, the weights associated with the interconnections between neurons, and the activation function of each neuron.

4.7.4.4 Simple neuron

The process of training an Artificial Neural network ANN consisting of one neuron is depicted in Figure 4.26 which shows different important values composed of: inputs $[x_1, x_2, x_3...x_n]$, weight w, bias b, transfer function f and output y. The predicted values of output y need to be compared with target values of y (obtained from CFD) if the difference error is zero or very small the solution is satisfied if not the values of bias and weight need to be adjusted see Figure 4.27.

The process of training a network is the mathematical operations that taken place in the neuron to determine the suitable solution (output) of a number of input variables satisfying the provided target solution.

A vector to a scalar function named transfer function can be expressed based on adjusted weights of all input values through the processing element.

$$y = \sum_{i=1}^{n} [x_i.w_i] = [x_1.w_1 + x_2.w_2 + x_3.w_3...x_n.w_n] \tag{4.64}$$

In general, the neural network can contain one or more layers. Figure 4.28 shows a schematic artificial neural network (ANN) consisting of two hidden layers connecting the neurons. The neural network learning process can be broken down into the following steps:

1. Prepare a set of data for training and validation.
2. Prepare the input data which include a vector of input data and a vector of the target data.
3. Set network architecture.
4. Train neural network.

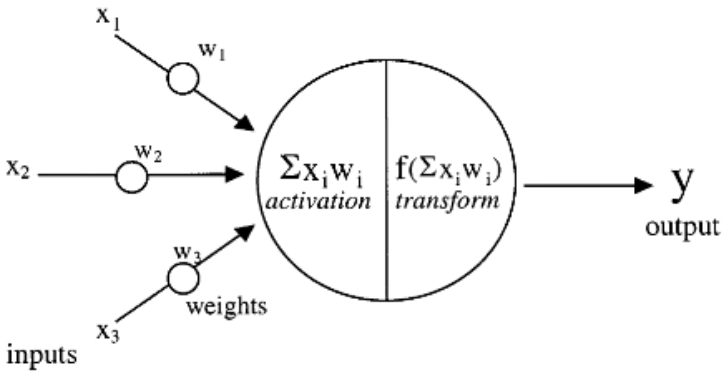

Figure 4.26: A schematic of a neuron(Holmgren et al., 2019)

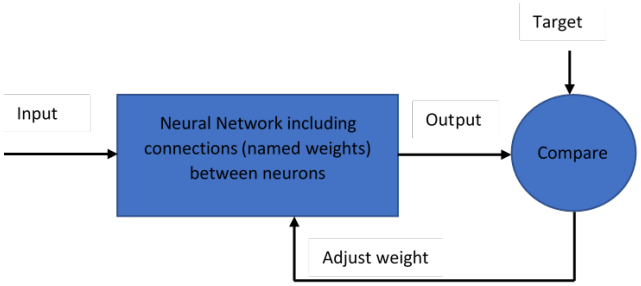

Figure 4.27: The control diagram of Artificial Neural network ANN (Holmgren et al., 2019)

Adjusting the connection weights between nodes by training the ANN can be carried out by different approaches such as supervised, unsupervised, and reinforcement learning. In the supervised learning method, the connecting weights are adjusted based on a direct comparison between the output of an ANN and the actual output of the training data (Walczak and Cerpa, 1999). The gradient descent-based optimisation algorithm such as back-propagation proposed by (Rumelhart et al., 1985) widely used a supervised learning algorithm to adjust connection weights in the ANN iteratively in order to minimise the error (Rumelhart et al., 1986; Petrini, 2012). The Stochastic Gradient Descent (SGD) algorithm adjusts the connection weights based on minimising the back-propagated error estimated between the target values and the estimated results (Gevrey et al., 2003).

In the current thesis a Stochastic Gradient Descent (SGD) method is used to

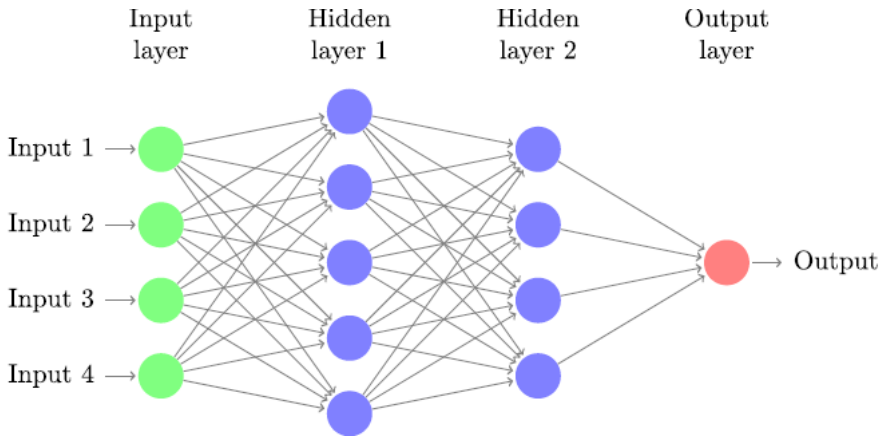

Figure 4.28: A schematic artificial neural network (ANN) with two hidden layers and a single neuron output(Holmgren et al., 2019)

minimise the cost function:

$$cost = \sum_{i=1}^{N_{train}} \|\mathbf{y}_i^{predict} - \bar{\mathbf{y}}_i^{train}\|/N_{train}. \tag{4.65}$$

The calculations are terminated after 5×10^4 iterations to avoid over-fitting when the error

$$err = \sum_{i=1}^{N_{train}} \|\mathbf{y}_i^{predict} - \bar{\mathbf{y}}_i^{test}\|/N_{test} \tag{4.66}$$

where N is the number of tested functions.

4.7.5 Global Optimization

In this step of optimization process is to examine the surrogate model to find the global minimum point. Genetic algorithms (GAs) is used to solve optimization problems based on a natural selection process that mimics biological evolution. Genetic algorithms are tools used to search the whole domain in order to find a global optimum for both constrained and unconstrained optimisation problems (Mardle, Pascoe et al., 1999). The process of GAs is a random population-based optimisation and it can be performed to determine an optimal solution through applying random changes to the current solutions to generate new ones (Sivanandam and Deepa, 2008). The genetic algorithm methods can be applied to solve a

variety of optimization problems that are not well suited for standard optimisation algorithms, particularly optimisation problems in which the objective function is stochastic, highly nonlinear discontinuous or non-differentiable (Almeida et al., 2015). GAs method can be effectively used to search the whole design domain to find the minimum candidate(s). However, although the GAs is a powerful method, for a particular problem where the local minimum GAs is appropriate only to determine the approximate zone of the global minimum and not necessarily the absolute optimum value. Thus, local search methods such as fmincon method need to be used that aspire the optimisation design to find global optima. These methods demand an initial 'good' guess of the solution, so the GAs result is used as a starting location. At this point, the local (and hopefully global) optimum will have been found. The design variables (inputs) for this candidate can then be validated using CFD to see if the final result matches the surrogate model prediction. A new surrogate needs to be created from the extra data point(s) and only when the CFD and surrogate model predictions are very close, will the optimum result have been found. The GAs are embedded within the MATLAB Optimisation Toolbox, which is used later in this study.

4.7.6 Genetic Algorithms GAs

The genetic algorithm process starts from the first step of randomly generating a population of individual solutions which are repeatedly modified (Sivanandam and Deepa, 2008). From the current population, the GAs randomly select solutions named individuals which are candidates to be parents that can be used to produce the children for the next generation. The populations need to be evolved (changed) over successive generations towards the optimal solution. The standard Genetic Algorithms process is shown in Figure 4.29 which involves the following stages:

1. Initial Population.
2. Creating the next Generation (selection, crossover and mutation).
3. Termination

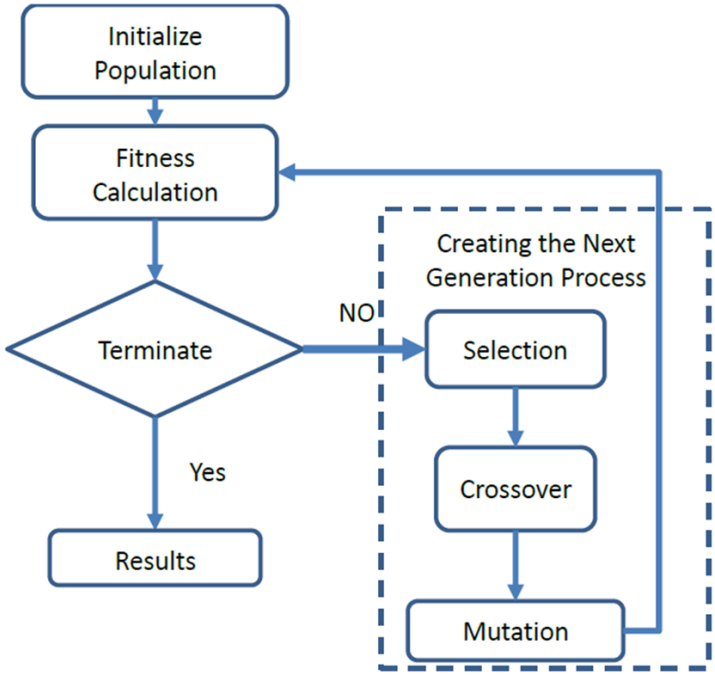

Figure 4.29: Overview of the Genetic Algorithm process(Jung et al., 2020)

The initial population is the first stage in the GAs which involves generating a set of potential solutions P. The first population is usually generated randomly, and each solution is named individual.

$P = (p_1, p_2, ..., p_{(\text{population size})})$

$P_i = (p_{i,1}, p_{i,2}, ...p_{i,j}, p_{i,novar})$

$i = 1, 2, \ldots, \text{pop size.}$

$j = 1, 2, \ldots, \text{no. of variables}$

$para^j_{min} \leq p_{i,j} \leq para^j_{max}$

where pop_{size} represents the population size; no_{var} represents the number of design parameters (variables).

$para^j_{min}$ and $para^j_{max}$ are the lower and upper limit of the design variables values.

At this stage of GAs each created chromosome in the population stage needs to be assessed by a defined fitness function (the fitness function is the function that need to be optimized) to measure the performance of an individual chromosome.

The better chromosomes will return higher values in this process. The fitness function to evaluate a chromosome in the population can be written as:

Fitness function = $f(pi)$. And if the problem of interest consists of four design variables $x_1, \ldots, x_4$. The Fitness function can be written as:

$$\textbf{Fitness function} = f(x_1), \ldots, f(x_4) \tag{4.67}$$

In more details, each individual consists of a fitness value and due to the random nature of GAs, the fitness function evaluates the entire initial population (from stage 1) in order to determine the best solutions from them to select a suitable group of individuals, called parents, who contribute their genes to children. The result of the fitness function is the fitness value indicating the quality of the solution where the higher the fitness value has the higher quality of the solution. The algorithm usually chooses individuals that have the best fitness values as parents. The next stage is stage 3 which is performed to create the next new generation using the initial population from stage 1 to determine a new solution, made up from (child) chromosomes, to produce an improved new generation. A fitness calculation is made on the initial population to identify candidate (parent) chromosomes. There are three different sub-steps related to stage 3 which need to be examined to classify the next generation: a) Selection: choosing the candidate chromosomes in the current generation which have high-quality fitness values to perform the next generation. b) Crossover: creating new child chromosomes by combining a pair of best parent chromosomes. c) Mutation process: introducing small random changes, or mutations, to a single gene. After determined the fitness for every individual (step 2), all the fitness of the population will be assessed by the criterion satisfied function (step3). Step 4 is the last step in the GA process which is called termination and involves criteria to stop searching. The searching is stopped when a maximum number of generations or a maximum time limit is reached. It is also stopped if there is any acceptable solution see Figure 4.29 which demonstrates the loop of GAs. It can be noted from Figure 4.29 if the criteria condition is satisfied (If 'Yes'), the loop will be finished (results), otherwise (If 'No') GAs will improve the population through repetitive application of parent selection (step 4) and reproduction (including copying, crossover, mutation in

step3). The population in the new generation comprises two parts: the high-quality fitness individuals in the last generation and new offspring produced by crossover and mutation.

After several generations, the algorithm converges to the best individual, which hopefully represents an optimal solution to the problem, (Gen and Cheng, 1999)

4.7.7 Single objective optimisation

The obtained surrogate models are examined to find the optimal solution of each of the objectives individually. Figure 4.30: shows examples of surrogate model surfaces for T_{dev} and $\Delta p(Pa)$, which demonstrate that minimising T_{dev} requires the smallest W_c and H_c values. While minimising $\Delta p(Pa)$ requires the highest W_c and H_c values. Similar insights can be noted from Figure 4.30 the minimum value of T_{dev} corresponds to comparatively large values of Δp, whereas the minimum Δp corresponds to comparatively large T_{dev} which reveals it is not possible to move along the design points on the meta-surface to minimize any of the objective functions without increasing the other objective function. Note that the minimum value of T_{dev} corresponds to comparatively large values of Δp and Q_t, whereas the minimum Δp corresponds to comparatively large T_{dev} and Q_t. This indicates that it is interesting to explore the trade-off between the objective functions through a multi-objective analysis.

4.7.8 Multi-Objective Pareto Analysis

In a multi-objective optimisation step, the surrogate models are explored to find the most suitable compromise solution between the competing objectives. These have been distinguished and for which the goal is to minimise the objective functions. The optimum multi-objective solutions in the current thesis were obtained using surrogate models RBF and NN. The RBF and NN methods were used to create Pareto curves of non-dominated solutions for Δp vs T_{dev}, Δp vs Q_t and T_{dev} vs Q_t. The RBF method uses the Multi-Objective Genetic Algorithm (MOGA) solver in MATLAB, whereas the NN methods use the SciPy.optimization module in Python based on a simple weighting between the competing objectives. In a

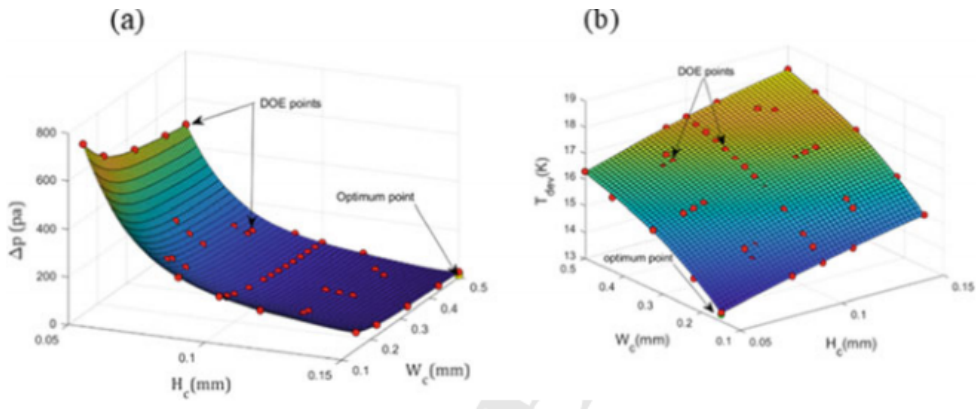

Figure 4.30: Response surfaces of $p(Pa)$ and $T_{dev(K)}$ in terms of W_c and H_c for the PCR (Hamad et al., 2021).

multi-objective optimisation problem, a Pareto front can be used by designers to select the most suitable compromise between the various objective functions that have been distinguished and for which the goal is to minimise the objective functions.

The final designs determined by deterministic optimisation described above is unable for accounting uncertainty effect lead to infeasible when the uncertainty in the system parameters is considered. The next section outlines an overview of the uncertainty quantification and the optimization formulation that takes account of this uncertainty

4.8 Optimisation Under Uncertainty (OUU)

Optimisation Under Uncertainty is a combination of optimization techniques, numerical simulations and uncertainty (Rockafellar, 2001), used to evaluate and improve the performance of the design by accounting for uncertainty and variability in the design process, (Ng and Willcox, 2014). There are two main approaches for optimisation under uncertainty (OUU) the first approach is a robust design, (Putko et al., 2002),that is concern to find a design that is insensitive to small changes in the uncertain quantities of structural parameters geometry, and the second approach is reliability-based design, (Qu and Haftka, 2004) which seeks to obtain optimisation solution where designs with a small probability of failure.

4.8.1 Robust design optimisation

A robust design optimisation is an approach that aims to minimise the sensitivity of system performance on uncertainties in input design variables that arising out either in the manufacturing or users environment (Fowlkes and Creveling, 1995). In this thesis we consider aleatory uncertainty caused by uncertainties in geometrical dimensions due to manufacturing tolerances. Uncertainties are handled in a probabilistic way, where the design variables have a variability followed normal distribution, see Figure 4.31 which reveals the concept of robust optimization. It can be noted that the uncertainty in design variables leads to the variability of the response f which is needed to be quantified and minimized. Choosing variable setting x_2 instead of x_1 will yield a narrower response distribution and thus a more robust design. The optimal robust design is chosen typically based on a trade-off between optimising the mean performance of the system and minimising the variance of performance due to uncertainties (Lonn, 2008).

The robust optimization formulation is aimed to:

$$\begin{aligned} & \text{find} \quad x \quad \text{that satisfies} \\ \textit{minimising} \quad & \{E(f(x,y), \sigma(f(x,y)\} \\ \textit{subjectto} \quad & \sigma(f,x) \leq \sigma_1 \end{aligned} \tag{4.68}$$

where $E(f)$ is the mean value (expected value) of the performance function and $\sigma(f)$ is the standard deviation the performance function. σ_1 is the maximum limit of the allowable standard deviation.

4.9 Background of Uncertainty

The measurement of uncertainty is a fundamental process used for evaluating the quality of the product(Measurand). Measurand refers to the quantity being measured (Farrance and Frenkel, 2012).

Different measurement of evaluating uncertainty has been conducted following the guide to the expression of uncertainty in measurement (GUM) which was performed to provides a framework and complete guidance and references for estimating uncertainty (BIPM et al., 2008).

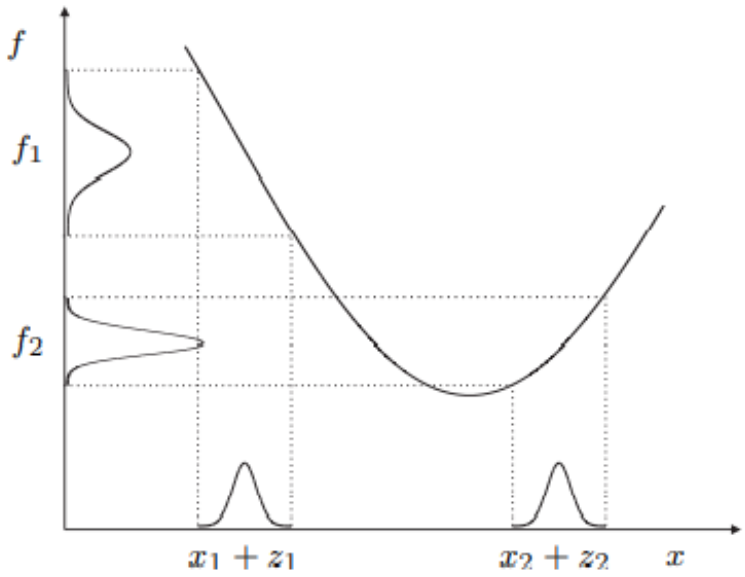

Figure 4.31: Principle of Robust Design Optimisation (Bonte, 2007)

The methodology of the GUM can be broken down into the following steps:

1. Definition of the measurand and input sources. This step is to identify the variables of input sources that directly or indirectly impact the estimation of the measurement. As an example equation 4.69 which involves a measurand y as a function of four inputs sources $x_1, \ldots, x_4$.

$$y = f(x_1, x_2, x_3, x_4) \tag{4.69}$$

2. Modelling a model needs to be carried out at this step in order to predict the results based on the input sources. The modelling step relates the input sources to the output and also capture how the inputs influence the measurements, hence, a strength model allows good prediction of uncertainty.

3. Estimation of the uncertainties of input sources. In this step uncertainties for all the input sources need to be estimated, based on GUM there are two types to evaluate quantities uncertainties (Bell, 2001; Watanabe et al., 2013):

3.1. **Type A** In this type the uncertainty is evaluated from series of repeated observations, the source of the uncertainties can be calculated using statistical analysis in terms of the standard deviation of a set of n repeated measurements (Jornada et al., 2010). For example: x represents a set of data, for example repeated readings of an instrument: $x_1, \ldots, x_n$ and n is the number of observations The standard deviation of the probability distribution with the reading x can be expressed as:

$$s(x) = \sqrt{\frac{1}{n-1}\sum_{i=1}^{n}(x_i - x)^2} \tag{4.70}$$

The reputability of a set of n measurements of the quantity x cause uncertainty $u(x)$ of the quantity x which can be represented by $u(x)$

$$u(x) = \frac{s(x)}{\sqrt{n}} \tag{4.71}$$

3.2. **Type B** In this type, the uncertainty is obtained by non-statistical procedures. The estimation of uncertainties of the Type B input sources is needed to be carried out carefully based on analysis of observations or in an accurate scientific judgment, using all collective data about the measurement procedure.

4.9.1 Probabilistic description of uncertainty

The fundamental theory of uncertainty is described by (Zacks, 2012), X represents a vector of random variables $x_1, x_2 \ldots, x_n$ which can be completely assigned by a cumulative distribution function (CDF) or a probability density function (PDF), denoted by PX(x) and pX(x) see Figure 4.32.

the probability of X between x_1 to x_2 is denoted by the area under the curve . Thus, the probability density function can be calculated from :

$$Pr[x_1 < X \leq x_2] = \int_{x_1}^{x_2} p(x) = P_x(x_2) - P_x(x_1) \tag{4.72}$$

The random variables X considered in the current work are supposed to follow a normal (Gaussian) distribution, described by a mean value $\mu(x)$ and a standard

deviation $\sigma(x)$ for estimating the expected value $E(X)$, variance $Var(X)$ of the random variable are given by Equations (A.3), (A.4) and (A.5) respectively.

$$E(X) = \mu(x) = \int_{-\infty}^{\infty} xp(x)dx \tag{4.73}$$

$$Var(X) = \sigma^2 x = \int_{-\infty}^{\infty} (x - \mu x)^2 p(x)dx \tag{4.74}$$

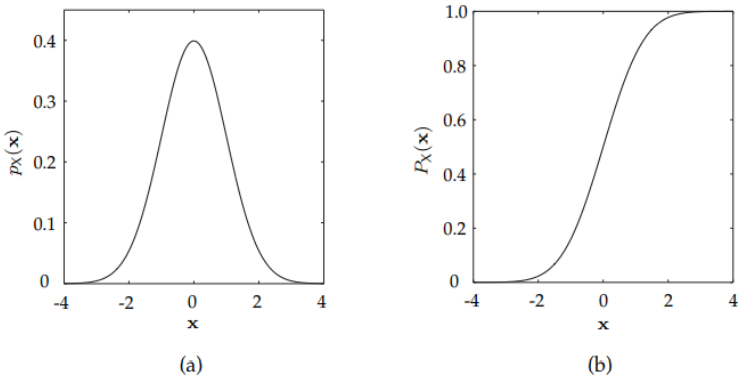

Figure 4.32: (a) Probability Density Function (PDF) and (b) Cumulative Distribution Function (CDF) of a Gaussian distribution(Zacks, 2012)

4.9.2 Propagation of uncertainties

The framework of GUM is based on the law of propagation of uncertainties (LPU) , which is derived from a set of approximations to simplify the calculations and it is valid for a wide range of models. For example for a set of N variables $x_1,\ldots,x_n$ the measurand y can be described in terms of the variables as presented in Equation 4.75 and the uncertainty of y can be expressed in a first-order Taylor series.

$$y = f(x_1, \ldots, x_n) \tag{4.75}$$

$$u_y^2 = \sum_{i=1}^{N} (\frac{\partial f}{\partial x_i})^2 u_{x_i}^2 + 2 \sum_{i=1}^{N-1} \sum_{j=i+1}^{N} (\frac{\partial f}{\partial x_i})(\frac{\partial f}{\partial x_j}) cov(x_i, x_j) \tag{4.76}$$

The second term of equation 4.76 can be neglected under the assumption of no correlation between the input variables. Thus , Equation 4.76 can be simplified to:

$$u_y^2 = \sum_{i=1}^{N} (\frac{\partial f}{\partial x_i})^2 u_{x_i}^2 \tag{4.77}$$

Equation 4.77 is valid for only one standard deviation that means about 86.7 % can be covered during the measurements. The model output relates the inputs sources in a nonlinear relationship and the truncation of Taylor's series expansion up to first-order terms cannot correct the error propagation. GUM method has several limitations (Lepek, 2003; Herrador and González, 2004; Couto et al., 2013):

1. GUM method is valid only when the model is linear, thus when the model is a nonlinear relationship estimation will not be accurate due to the truncation of Taylor's series expansion up to first-order terms cannot correct the error propagation.

2. GUM methods require the input sources in the same manner; thus GUM method is not valid when one or more of the input sources are much larger than the others, or when the distributions of the input quantities are not symmetric.

To overcome these limitations, three solutions have been adopted involving propagation of distributions of the probability distributions of the input quantities which are analytical integration, numerical integration and numerical simulation of Monte Carlo methods which is used in the current thesis.

4.9.3 Monte Carlo Simulation

Monte Carlo Simulation (MCS) is an alternative to the GUM approach particularly in cases where the GUM approach fails. MCS provided reliable, robust and fast results for different measurements models as compared to the GUM method. The MCS method can be used to estimate non-linear models. depending on the quality and reliability of the available information different methods can be used for accounting for uncertainties. In such methods, the Monte Carlo method, is

used in which the input data is characterised as random variables and use repeated random sampling to compute their effects on the data of interest. In case of the probability density functions of the input data are sufficiently accurate and sufficiently large samples are taken then a reasonable estimate of the probability distribution of the data of interest can be computed. The inputs data are assumed to follow a normal distribution and the spread of random numbers is predetermined by its specified mean and its specified standard deviation. For each input, the MCS procedure generates a numeric value drawn at random from its respective PDF (Farrance and Frenkel, 2014). Figure 4.33 shows a probability density function based on Gaussian distribution for $\mu = 0$ and $\sigma = 0.5, 1$ and 1.5. The Gaussian density function is given by :

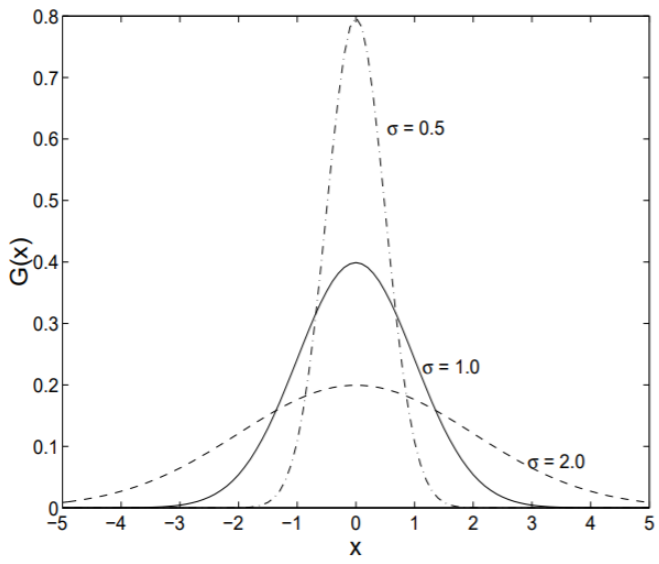

Figure 4.33: Gaussian distribution(Murthy, 2001)

4.10 Uncertainty Quantification (UQ)

Uncertainty Quantification (UQ) studies the effects of uncertainties in input sources on the output (objectives). For a set of input variable distributions, UQ finds probability distributions for the outputs.

Firstly, input sources are identified. These are: width of the channel (W_c), the height of the channel (H_c), the substrate thickness (H_b) and space between channels (W_w). Here we assume these variables as normally distributed random variables.

The system for this purpose CFD model is adopted and described in section.

The CFD model is then used to obtain the solution for the design points (DOE) points. The alternative model is validated with actual results from the CFD model ans is called surrogate model. This surrogate model predicts the outputs of Monte Carlo simulations for approximately (10^5) runs.

We then run Monte Carlo numerical simulations to propagate the distribution. For each sample, the function is evaluated in thousands of iterations across the whole range of input. Covering the entire input range allows the determination of the PDF of outputs (Bodla et al., 2013).

The expected mean μ and standard deviation σ are then calculated for the output PDF.

$$\mu_{fi} = \frac{1}{N}\sum_{j=1}^{N} f_i^j \tag{4.78}$$

$$\sigma_{fi}^2 = \frac{1}{N}\sum_{j=1}^{N}(f_i^j - \mu_{fi})^2 \tag{4.79}$$

4.11 Robust design optimisation method

The robust design optimisation procedures seek to minimise the objective functions, depicted in 4.78. The uncertainty with the response surface and a confidence region, we then solve the optimisation problem . Given the probabilistic models $f_1(\mathbf{x})$ and $f_2(\mathbf{x})$,

$$\begin{aligned} &\underset{\mathbf{x}\in\Omega_0}{\text{minimize}} \quad \mu_{\omega(\mathbf{x})} =: \omega\mu_{f_1(\mathbf{x})} + (1-\omega)\mu'_{f_2(\mathbf{x})} \\ &\text{subject to} \quad \sigma_{f_1(\mathbf{x})} < \sigma_1, \quad \sigma_{f_2(\mathbf{x})} < \sigma_2. \end{aligned} \tag{4.80}$$

with $\omega \in [0, 1]$.

4.12 Summary

This chapter provided a mathematical model and differential equations that can be used in the numerical simulation of the PCR process. In addition, significant information on CFD and the main steps of solving a simulation model is provided in this chapter. The boundary conditions such as inlet, outlet, walls, symmetry and coupling a conjugate heat transfer problem are presented. The validation of the numerical results of fluid flow and heat transfer achieved for the prototype serpentine PCR have been validated against previous experimental and numerical work. In the optimisation section of the PCR systems design, Optimal Latin Hypercube (OLH) approach is used to create the design of experiment (DOE) points, by using a permutation genetic algorithm, whereas RBF and ANN approximations are used to build the surrogate models (Meta-models) for Δp vs T_{dev}, Δp vs Q_t and T_{dev} vs Q_t thought the design space. An optimisation methodology is presented to create the Pareto front of non-dominated solutions for Δp vs T_{dev}, Δp vs Q_t and T_{dev} vs Q_t which enables designers to explore a sufficient compromise between the objectives. Moreover, the concept of robust design optimisation is presented in this chapter.The next chapter applies the CFD and optimisation methodology in this chapter to PCR systems. Chapter 7 applies the CFD methodology and robust optimisation in this chapter to PCR system.

Chapter 5

Computational Fluid Dynamics Analysis and Optimisation of Polymerase Chain Reaction Thermal Flow Systems

5.1 Introduction

In this Chapter a novel Computational Fluid Dynamics-enabled multi-objective optimisation methodology for Polymerase Chain Reaction flow systems is proposed and used to explore the effect of geometry, material and flow variables on the temperature uniformity, pressure drop and heating power requirements, in a prototype three-zone thermal flow system. A conjugate heat transfer model for the three-dimensional flow and heat transfer is developed and solved numerically using COMSOL Multiphysics® and the solutions obtained demonstrate how the design variables affect each of the three performance parameters.

This present work is motivated by the thermo-flow design and optimisation of fluidic channels used in PCR systems. They are used widely in rapid diagnostic systems for bacterial species leading to e.g. infectious diseases, or for the rapid and accurate detection of bacterial species causing micro-biologically induced corrosion in oil and gas production systems.

This Chapter is organised as follows. Section5.2 describes the numerical methods and the specification of the conjugate heat transfer problem. Section5.3 presents the validation of the numerical model and a series of numerical results which demonstrate the dependence of the thermal flow systems on key parameters. Section5.4 presents a single and multi-objective optimisation formulation for PCR flows and a series of CFD and optimisation results which demonstrate the potential to manipulate designs to achieve the competing objectives. Finally, conclusions are drawn in Section5.5.

5.2 Numerical Methods

The problem of the microfluidic channel and heating arrangements, together with modelling and numerical methods are described in this section.

5.2.1 Problem Description and Configuration

The serpentine microfluidic channel, shown in Figure 4.14, passing through denaturation ($95°C$), annealing ($56°C$) and extension ($72°C$) zones is used as a prototypical CFPCR thermal flow problem. This is based on those considered previously by (Hashimoto et al., 2004; Chen et al., 2008; Chen et al., 2013) but with a glass, rather than a PDMS, substrate material to increase thermal conductivity and temperature uniformity. In addition, the cover material (H_p) used here is PMMA, which can provide good thermal insulation as well as the practical advantages of good optical access and a low cost. A schematic diagram of the microfluidic channel geometry is presented in Figure 4.15 where W_c, H_c, W_w, H_b and L are the microchannel width, height, wall thickness (the space between the channels), the bottom height and the total length respectively.

There are three individual copper blocks with cartridge heaters placed underneath the glass chip with a constant distance between them of $S = 1mm$, the length of the heaters being $9mm$ underneath the denaturation and annealing zones and $40mm$ underneath the extension zone. The height and length of each heater are $H_h = 2mm$ and L_h=$9mm$. The length of the denaturation, annealing

and extension zones are chosen to achieve the typical residence time ratios of $1:1:4$ respectively (Chen et al., 2008).

5.2.2 Conjugate Heat Transfer Model

A conjugate heat transfer model of the steady, single-phase, laminar flow problem shown in Figure 4.15 was developed using the following simplifying assumptions employed by previous studies (Chen et al., 2008; Moschou et al., 2014; Aziz et al., 2016; Chiu et al., 2017). The liquid is water, with temperature-dependent density, thermal conductivity and viscosity, and the effects of radiation and buoyancy are neglected within the computational domain. There is no internal heat generation.

The Reynolds number (Re), is given by:

$$Re = \frac{\rho_f V_{ch} D_h}{\mu_f}, \tag{5.1}$$

where ρ_f and μ_f are the density and viscosity of the fluid respectively, V_{ch} is the channel inlet velocity and D_h the channel hydraulic diameter defined by:

$$D_h = \frac{2W_c H_c}{W_c + H_c}. \tag{5.2}$$

For CFPCR flows, $V_{ch} \sim 1mm/s$, $D_h \sim 10^{-4}$ m and a water density of $10^3 kg/m^3$ and dynamic viscosity $10^{-3} Pa \cdot s$, leads to $Re \sim O(10^{-1})$, i.e. laminar flow conditions.

The flow is modelled using the governing continuity and Navier-Stokes equations (White and Corfield, 2006):

$$\nabla \cdot (\rho_f \mathbf{u}) = 0, \tag{5.3}$$

and

$$\rho_f(T_f)\,(\mathbf{u} \cdot \nabla)\,\mathbf{u} = \nabla \cdot \left[\mu_f\,(T_f)\left(\nabla \mathbf{u} + (\nabla \mathbf{u})^T\right) - p\mathbf{I} - \frac{2}{3}\mu_f\,(T_f)\,(\nabla \cdot \mathbf{u})\mathbf{I}\right], \tag{5.4}$$

where $\mathbf{u}$ and p are respectively the fluid velocity vector and pressure.

The heat transfer is a combination of conduction in the solid domain and convection in the fluid, coupled through conjugate heat transfer boundary conditions

at the solid-fluid interface (Davaji, 2016). The energy equation for the convective heat transfer in the fluid is given by

$$\rho_f(T_f)C_{pf}\left(T_f\right)\mathbf{u}\cdot\nabla T_f = \nabla\cdot\left(k_f\nabla T_f\right)+\dot{Q}_{gen}, \tag{5.5}$$

while the energy equation for conductive heat transfer in the solid is

$$\nabla\cdot\left(k_s\nabla T_s\right)=0, \tag{5.6}$$

where C_{pf}, k_f and k_s represent the specific heat and thermal conductivities of the fluid and solid respectively. $\dot{Q}_{gen}$ denotes the internal heat generation (W/m^3) which is taken to be 0.

The thermo-physical properties of the water ($\rho_f(T_f)$, $\mu_f(T_f)$, $C_{pf}(T_f)$ and k_f) depend on the temperature and are given by (Bergman et al., 2011):

$$\rho_f = 838.466+1.4T-0.003T^2+3.72\times10^{-7}T^3, \tag{5.7}$$

$$\begin{aligned}\mu_f =& 1.38-0.0212T-1.36\times10^{-4}T^2-4.64\times10^{-7}T^3\\ &+8.9\times10^{-10}T^4-9.08^{-13}T^5+3.846\times10^{-16}T^6,\end{aligned} \tag{5.8}$$

$$C_{pf} = 12010.147-80.407T+0.3099T^2-5.382\times10^{-4}T^3+3.625\times10^{-7}T^4, \tag{5.9}$$

$$k_f = -0.869+0.00895T-1.584\times10^{-4}T^2-7.975\times10^{-9}T^3, \tag{5.10}$$

where T is in Kelvin. The thermal conductivity of copper is $k_s = 400W/(m\cdot K)$ and the target temperatures in the denaturation, annealing and extension zones are ($95°C$, $55°C$ and $72°C$) respectively.

5.2.2.1 Boundary Conditions

The computational domain and boundary conditions are shown in Figure 4.15. At the walls, no-slip velocity boundary conditions $\mathbf{u}=\mathbf{u}_s=0$ are applied. The inlet velocity V_{ch} is set to achieve a typical Reynolds number of 0.7 and the inlet temperature is fixed at $T_{f,in}=20°C$, with an ambient pressure condition, $p=p_0$, imposed at the outlet.

The conductive heat transfer in the solid is coupled to the convective heat transfer in the fluid through the following conjugate heat transfer boundary conditions at the solid-liquid interface (Davaji, 2016), Γ: (i) continuity in temperature, $T_{(s,\Gamma)}$=$T_{(f,\Gamma)}$ and (ii) continuity of heat flux given by Fourierâ€™s law (Qu and Mudawar, 2002):

$$-k_s \frac{\partial T_s}{\partial n}|_\Gamma = k_f \frac{\partial T_f}{\partial n}|_\Gamma \tag{5.11}$$

The upper surface of the domain includes the effect of natural convection via a heat transfer coefficient of $15W/\left(m^2 \cdot K\right)$ (Chen et al., 2008; Chen et al., 2015). All the outer surface boundary conditions are considered to be adiabatic except at the bottom of the copper heaters where temperatures are set to $96.7°C$, $73°C$ and $55.7°C$ respectively for the denaturation, extension and annealing zones.

The governing equations are solved subject to the boundary conditions using COMSOL Multiphysics 5.4 ®.

5.2.3 Performance Metrics

Three performance metrics are calculated for each flow. The temperature uniformity in the zones is calculated by quantifying deviations from the target temperature, T_{target}, via

$$T_{dev} = \sqrt{\frac{\iiint \left(T_{f_{i,j,k}} - T_{target}\right)^2 dV}{\iiint dV}}. \tag{5.12}$$

The hydraulic performance is measured by calculating the pressure difference along the channel

$$\Delta p = p_{in} - p_{out}. \tag{5.13}$$

Heating power, Q, in each zone Q_d, Q_e and Q_a was obtained at the bottom of the heater surfaces using $\mathbf{n} \cdot (k\nabla T) = q/A_h$ where $\mathbf{n}$ denotes the outward normal vector of the domain and A_h is the surface area of the heater. The total heating power is calculated by:

$$Q_t = Q_d + Q_a + Q_e, \tag{5.14}$$

where Q_t, Q_d, Q_a and Q_e represent the total heat power in watts (W), heat transfer to denaturation zone, and heat extracted from annealing zone and heat transfer to the extension zone respectively.

5.3 Numerical Results

5.3.1 Numerical Validation

The effect of grid density has been examined in section 4.6.6 by obtaining numerical solutions on a series of structured Finite Element grids of increasing refinement in Table 4.1. The fifth grid size with number of elements equal to 877552 was selected based on a trade off between computational time and solution accuracy. The numerical model was then validated by comparing with experimental results of Duryodhan et al. (2016) and numerical results of Chen et al. (2008), see Figures 4.17–4.18 and their discussion in section 4.6.6 for more detail.

5.3.2 One-dimensional (1-D) thermal modelling

Several previous studies of heat transfer in micro-channel structures have employed simplified analyses successfully. For small channels with $D_h \sim 50\mu m$, convective heat transfer can often be neglected (Gui and Ren, 2006) and for flows which are fully developed thermally, 1-D models may also be useful. The thermal entrance length for laminar flow can be estimated by (Holman, 2009)

$$L_{th} = 0.05 RePr D_h \tag{5.15}$$

where Pr is the Prandtl number given by

$$Pr = \frac{C_p \mu}{k}. \tag{5.16}$$

For the cases considered here $L_{th} \sim 20\mu$m so the thermal entrance length can be neglected. By applying the energy balance approach described in (Bergman et al., 2011; Cengel, 2014) the average flow temperature, $T_{f,avg}$, for the constant wall temperature, T_w, is given by

$$T_{f,avg}(x) = T_w - (T_w - T_{in}) \times \exp\left(\frac{-h.P.x}{\dot{m} C_{pf}}\right) \tag{5.17}$$

where x is the distance along the channel, T_{in} is the fluid inlet temperature, $\dot{m}$ is the mass flow rate, $h^{'}$ is a heat transfer coefficient, P is the perimeter of the microchannel and C_{pf} is the fluid heat capacity. The Nusselt number for fully

developed laminar flow inside a channel heated at constant wall temperature can be calculated based on correlation proposed by Shah (Shah, 1978)

$$Nu = 7.541(1 - 2.61\epsilon + 4.97\epsilon^2 - 5.119\epsilon^3 + 2.702\epsilon^4 - 0.548\epsilon^5) \tag{5.18}$$

where $\epsilon = W_c/H_c$. Two different values of $h^{'}$ are used in the solution (3.57). Model 1 obtains $h^{'} = h$ from:

$$Nu = hD_h/k \tag{5.19}$$

while the model 2 uses this value of h within an effective heat transfer coefficient $h^{'}$ proposed by (Xu et al., 2012; Ranmode et al., 2019) :

$$h^{'} = [1/h + H_b/k_s]^{-1} \tag{5.20}$$

that accounts for the effects of substrate thickness. Predictions of the 1-D models (3.57) are compared with those of the 3-D conjugate heat transfer model in Figure 5.1, for the thermal conditions specified in the denaturation zone. Figure 5.1(a) shows that for the case with V_{ch}=4mm/s and zero substrate thickness, $H_b = 0\mu m$, the agreement is excellent. However for cases with larger values of H_b, the discrepancy between the models is more significant due to the thermal resistance of the substrate, although the effective heat transfer coefficient presented in Equation (5.20) does improve predictions for the thicker substrate. More generally, it is found that the 1-D model works well provided the conductive thermal resistance, defined by $R_{th} = H_b/k_s$, is small. This cannot be neglected for cases considered below, with larger substrate thicknesses, and for which full 3-D simulations are required.

5.3.3 Effect of substrate material

The effect of the substrate material on the temperature profile is considered next, for flow in a channel with dimensions: $H_c = 150\mu m$, $W_c = 500\mu m$, $H_b = 850\mu m$, $W_w = 50\mu m$, $H_h = 2000\mu m$, $H_{PMMA} = 1500\mu m$ and $S = 1mm$. Figure 5.2 shows the effect of the material on the fluid temperature profile at the low inlet flow velocity $V_{ch} = 0.1mm/s$. The fluid temperatures in these cases are reasonably uniform for all materials, with the fluid temperature for glass and silicone chips

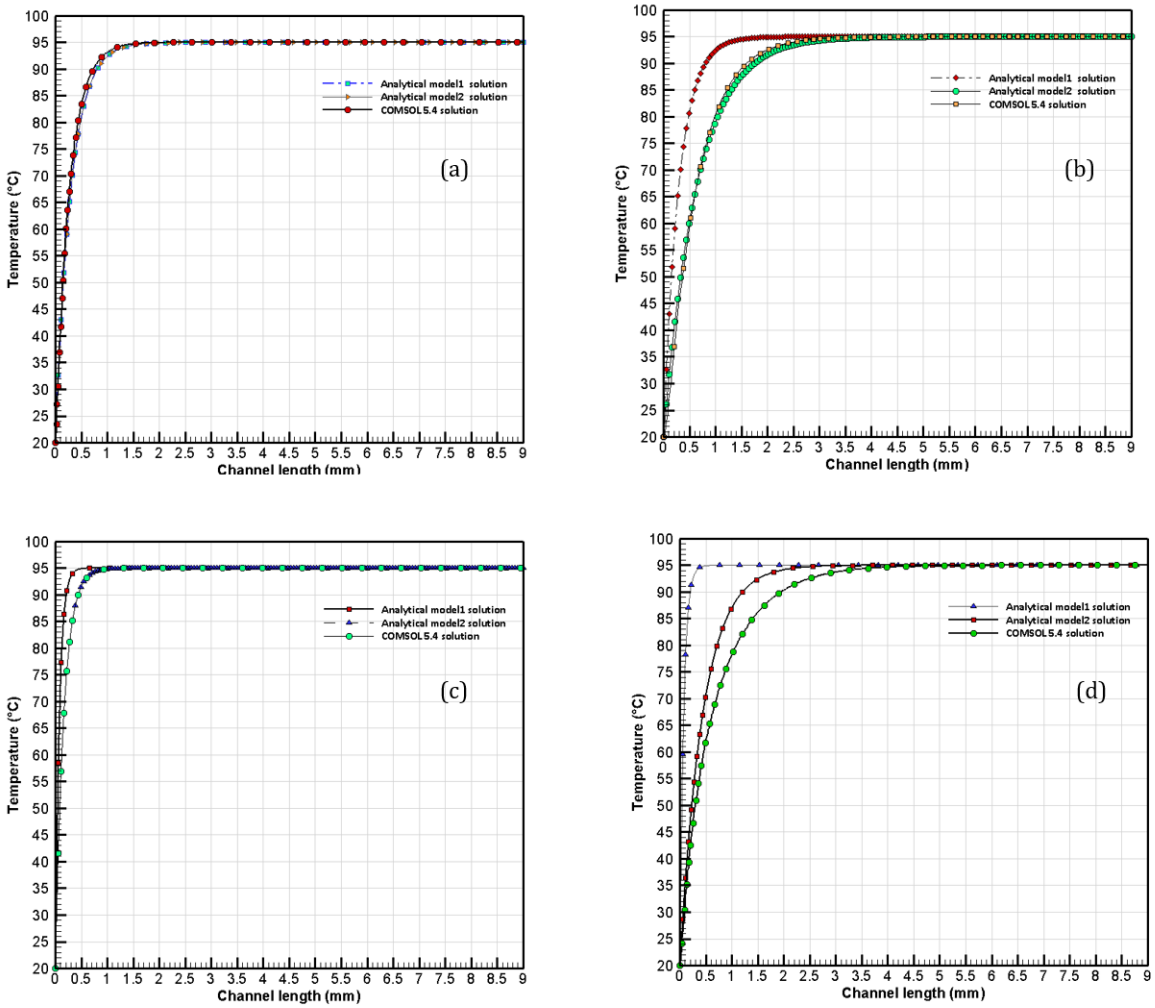

Figure 5.1: Comparison of 1-D and CFD predictions of centreline temperature in the CFPCR denaturation zone with (a) V_{ch}=4mm/s, H_b=0 μm; (b) V_{ch}=4mm/s, H_b=200μm; (c) V_{ch}=1mm/s, H_b=200μm; (d) V_{ch}=1mm/s, H_b=850μm

being closest to the target temperatures in the zones while that for the polyimide chip is furthest from the target profile. The size of the deviations from the target temperature profiles generally decreases as the thermal conductivity of the chip material increases due to the smaller thermal resistance between the heated substrate and the flowing liquid. As noted (Chen et al., 2013), this can however

lead to greater thermal interference between zones.

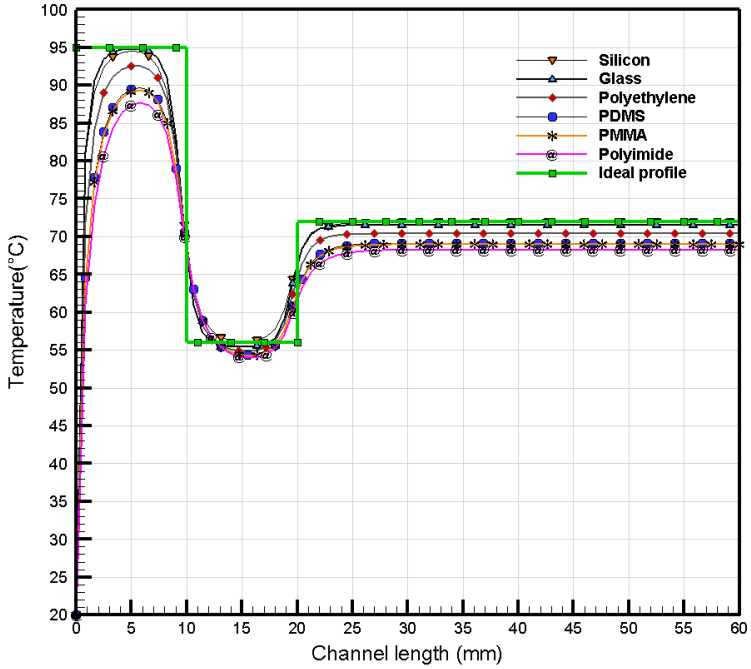

Figure 5.2: Temperature profile along the centerline of CFPCR zones at $V_{ch} = 0.1mm/s$.

Figure 5.3 shows the effect of increasing the inlet velocity to $V_{ch} = 1mm/s$. This leads to greater discrepancies from the target temperatures in each zone, since convective heat transfer becomes more significant at the higher speed. Once again, the deviations from the target temperature profile decrease as thermal conductivity increases. Figure 5.4 summarises the effect of material and inlet flow velocity on the deviations from the target temperatures, and quantifies the monotonic increases in T_{dev} as V_{ch} increases and thermal conductivity decreases, due to the increased convection and thermal resistance respectively.

It is instructive to calculate two dimensionless parameters for the present problems. The first, the Peclet number,quantifies the relative importance of con-

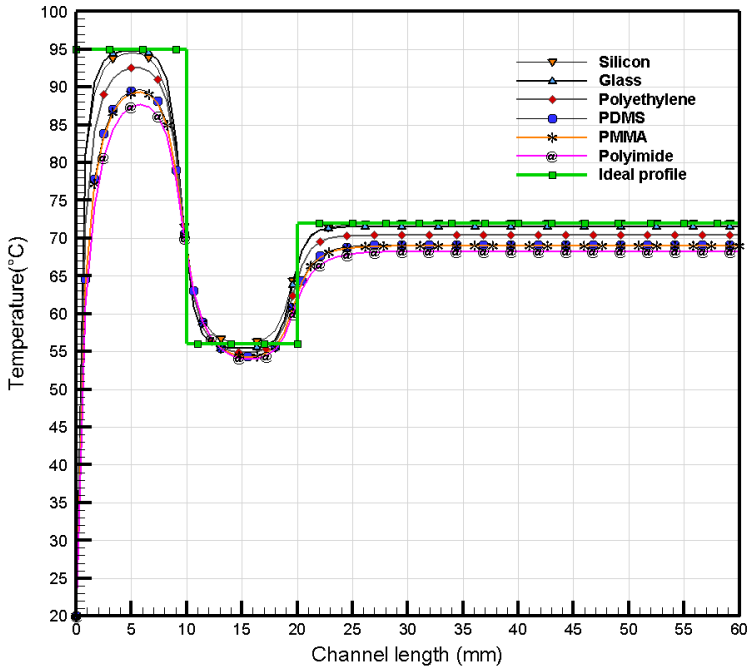

Figure 5.3: Temperature profile along the centerline of CFPCR zones at $V_{ch} = 1mm/s$.

vection compared to conduction in the liquid and is defined by (Lin et al., 2014):

$$P_e = V_{ch}.D_h/\alpha \tag{5.21}$$

where α is the thermal diffusivity of the liquid. The second assesses the importance of axial conduction compared to convection in micro-scale systems and is defined by (Maranzana et al., 2004):

$$M = \frac{q_{cond}}{q_{conv}} = \frac{(k_s.H_b)}{(\rho_f.C_{pf}.H_c.V_{ch})} \tag{5.22}$$

Values are given in Table 5.1 for examples of the cases considered here.

Since $Pe > 1$ convection is influential in all cases and temperature variations along the channel result from the competition between convection, which acts to increase them, and conduction, which acts to reduce them. Lower axial conduction for the particular case of PMMA at V_{ch}=1mm/s may explain why its

Material	T_{dev} (°C)			P_e			M		
	V_{ch1}	V_{ch2}	V_{ch3}	V_{ch1}	V_{ch2}	V_{ch3}	V_{ch1}	V_{ch2}	V_{ch3}
Polyimide	44.522	73.888	94.613	1.442	8.850	14.978	0.0034	5.81×10^{-4}	3.49×10^{-4}
PMMA	40.336	63.988	84.747	1.439	8.794	14.858	0.0044	7.35×10^{-4}	4.41×10^{-4}
PDMS	39.448	62.881	82.573	1.439	8.783	14.834	0.00463	7.74×10^{-4}	5.36×10^{-4}
Polyethylene	29.665	57.753	61.778	1.434	8.679	14.583	0.0088	0.00148	8.82×10^{-4}
Glass	19.366	38.309	47.790	1.430	8.597	14.359	0.0324	0.0054	0.0032
Silicon	18.152	20.799	22.922	1.428	8.575	14.295	3.0129	0.502	0.301

Table 5.1: The effect of chip material and inlet velocity on T_{dev}, Pe and M for $V_{ch1} = 1mm/s$, $V_{ch2} = 6mm/s$, $V_{ch3} = 10mm/s$, for $H_b = 850\mu m$.

$T_{dev} = 40.336$ is greater than $T_{dev} = 38.309$ for glass at the much higher velocity V_{ch}=6mm/s.

In view of its good thermal and optical properties, all results below use glass as the substrate material. Figure 5.5 and Table 5.1 show how the temperature variation T_{dev} in glass chips is affected by channel inlet velocity V_{ch} and demonstrates clearly how the temperature profile throughout the three PCR zones is very different from the target profile at the higher speeds. Also Figure 5.6 displays the temperature contours variation in the $x-y$ plane taken in the middle of the channel. This Figure shows that how the inlet velocity affects the temperature of the fluid. As expected for all cases the fluid inlet temperature is $20°C$ which increases gradually along the channel due to the local heat transfer coefficient which is higher near the channel entrance where the boundary layer thickness is very small. It can be noted from Figure 5.6 (a) that the convective potential is very low, this gives rise to more pronounced diffusive effects leading to a break up of the boundary layer causing the flow to be similar to isothermal flow. Figures 5.6 $(b-d)$ reveal that increasing the inlet velocity leads to increasing momentum and thermal diffusion in the axial direction causing the isotherm line along the denaturation moving farther downstream which affects the temperature uniformity in the next zone.

The same trend is also noted in Figure 5.7, however, using PDMS channel which has low thermal conductivity so low temperature-variation is only achieved at very low inlet speeds (low momentum effect). This occurs because the low thermal conductivity of PDMS leads low diffusive effects that become more pronounced with increasing momentum effect due to increasing fluid velocity. So the

worst case scenario can be seen in figure 5.7 *d* which combines both low thermal conductivity (i.e. low diffusive effects) of PDMS and high fluid speed, i.e. high momentum.

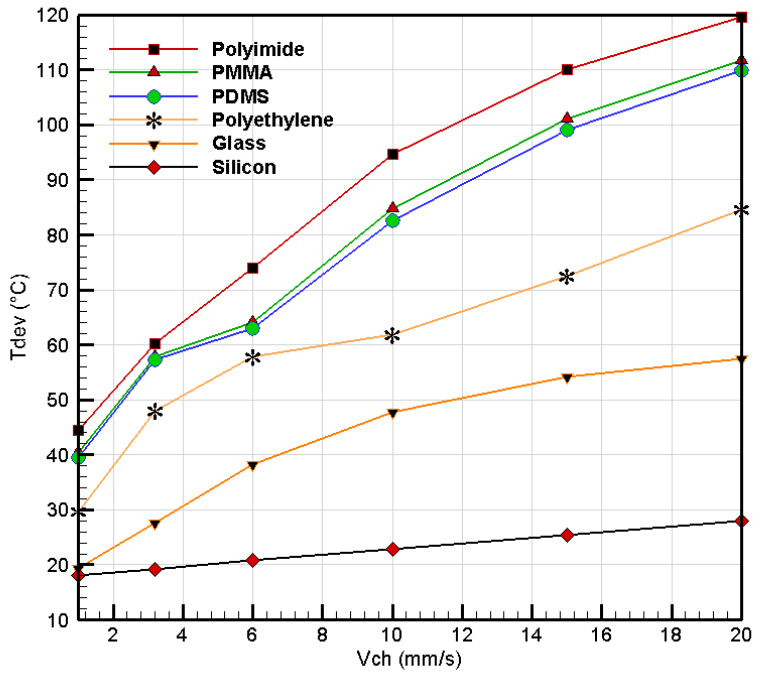

Figure 5.4: The effect of material type on the PCR performance responses in terms of T_{dev} at different inlet velocity $V_{ch} = (1 - 20)mm/s$.

The effect on heating power is considered next. Figure 5.8 and Table 5.2 show that the heating power consumption increases as the velocity increases and that the comparatively high thermal conductivity of silicon leads to at least an order of magnitude larger heating power requirement.

The results show that T_{dev} is influenced by the competition between convection and axial conduction that results from the material type, flow rate and channel size. In practice, there are other competing objectives which need to be considered, such as the need to minimise the pressure drop and heating power consumption. The next section extends the analysis to formulate and solve multi-objective optimisation problems relevant to PCR systems.

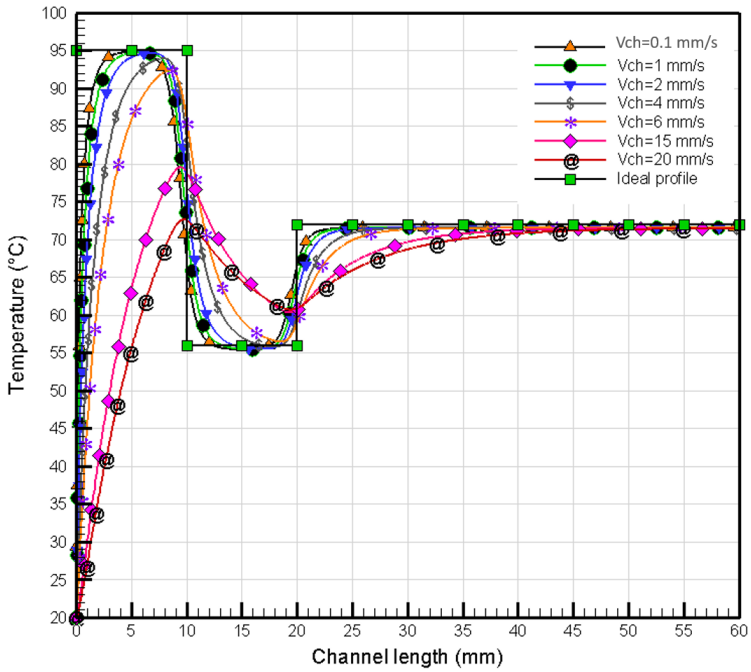

Figure 5.5: Temperature profile along the centerline of CFPCR zones at different velocities using a glass substrate.

Material	$Q_t(W)$				
	$k_s(W/m.K)$	V_{ch1}	V_{ch2}	V_{ch3}	V_{ch4}
Polyimide	0.15	0.054	0.105	0.146	0.183
PMMA	0.19	0.058	0.109	0.157	0.203
PDMS	0.2	0.059	0.111	0.160	0.207
Polyethylene	0.38	0.071	0.164	0.195	0.246
Glass	1.4	0.122	0.283	0.393	0.475
Silicon	130	5.293	5.384	5.476	5.607

Table 5.2: The effect of chip material on heating power required for $V_{ch1} = 1mm/s$, $V_{ch2} = 6mm/s$, $V_{ch3} = 10mm/s$, $V_{ch4} = 15mm/s$.

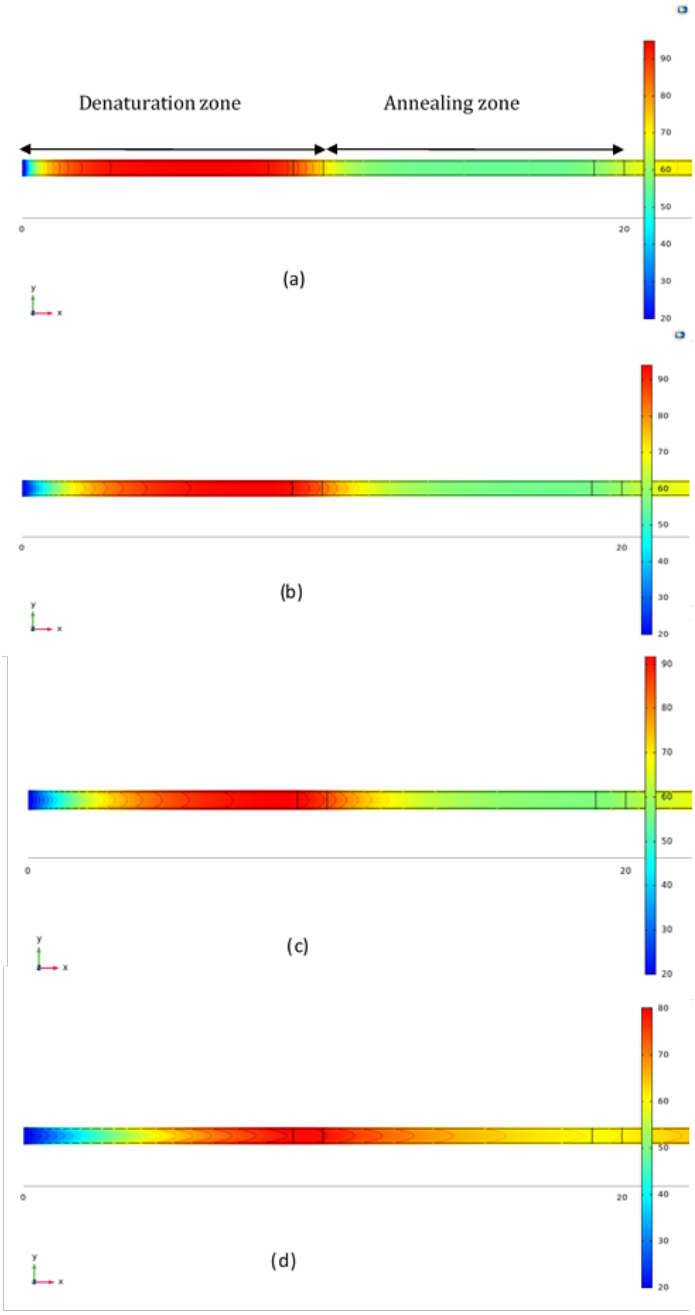

Figure 5.6: Temperature contour variation using a glass substrate.

5.4 Optimisation

As surrogate-enabled, multi-objective optimisation methodology (Haftka et al., 2016) is developed to explore the compromises that can be struck between tem-

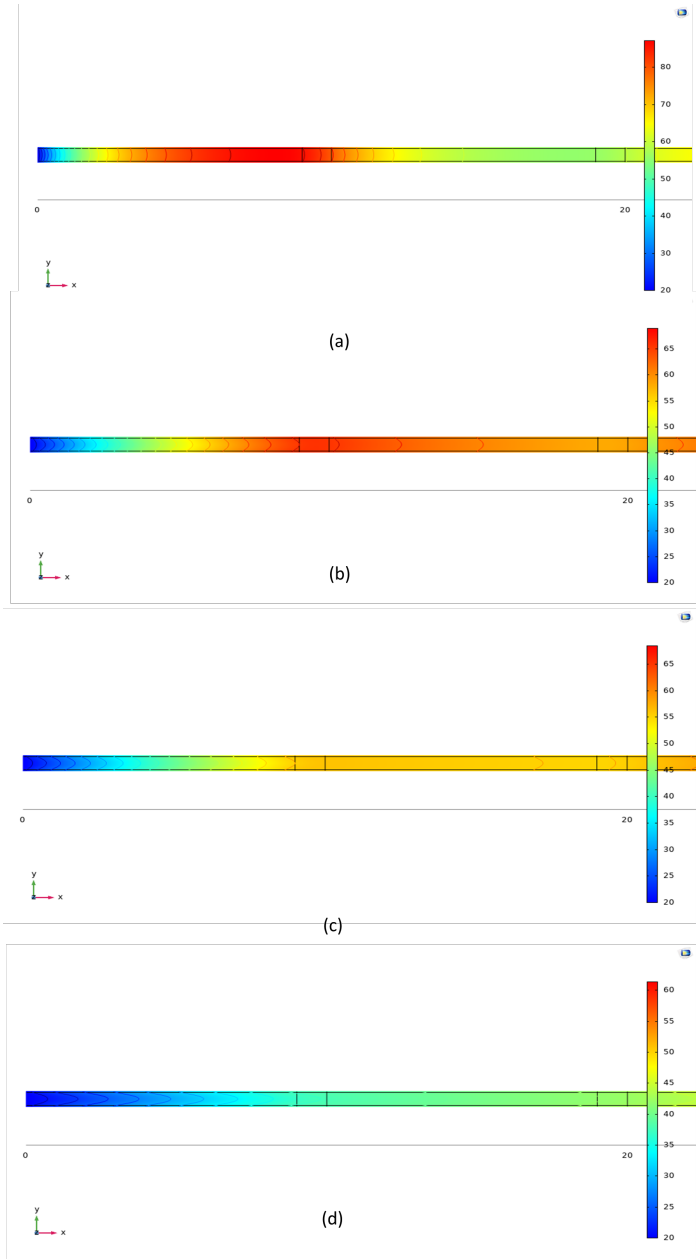

Figure 5.7: Temperature contour variation using a PDMS substrate.

perature uniformity throughout the three zones and the pressure drop and heating power required. Its key steps are:

1. Formulate the optimisation problem: specify the objective functions and constraints.

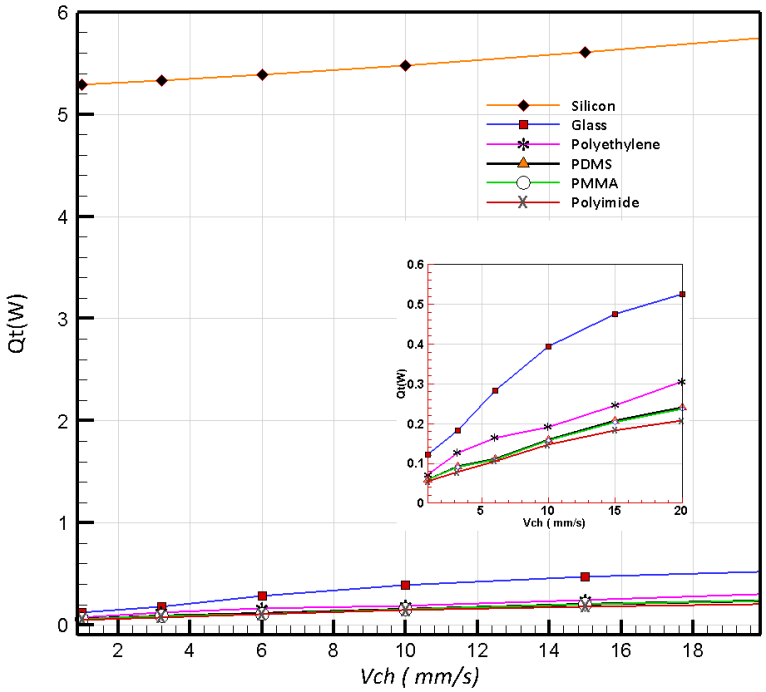

Figure 5.8: The effect of material type and inlet velocity V_{ch} on the heating power requirement.

2. Design space parameterisation: specify the design variables and design space.

3. Design of experiments (DoE): generate a relatively small number of well-scattered design points throughout the design space.

4. CFD solutions: obtain CFD solutions of the conjugate heat transfer problem at each of the DoE points and extract values of the objective functions from them.

5. Surrogate modelling: build and validate accurate surrogate models for each objective function throughout the design space using an appropriate surrogate modelling method.

6. Multi-objective optimisation: embed the surrogate models within an appropriate multi-objective optimisation algorithm and generate Pareto surfaces

showing optimal compromises between each objective function and validate their accuracy against the CFD solutions at selected Pareto points.

5.4.1 Problem Formulation

The prototype three-zone PCR system is optimised according to the competing objectives of minimising each of the temperature deviation, T_{dev}, pressure drop, Δp, and heating power, Q_t, defined in section 2.3. The influence of the four design variables W_c, H_c, H_b and W_w is explored at a constant Reynolds number $Re = 0.7$, and with constant $T_{f,in} = 20°C$, $S = 1mm$, $H_h = 2mm$, $H_p = 1.5mm$ and $L = 60mm$. Temperatures at the bottom of the copper heaters over the denaturation, extension and annealing zones are set at $96.7°C$, $73°C$ and $55.76°C$ respectively. The multi-objective optimisation problem considered here is the minimisation of each of $\{T_{dev}, \Delta p, Q_t\}$ within the design space:

$$
\begin{aligned}
150\mu m \leq W_c \leq 500\mu m,\\
50\mu m \leq H_c \leq 150\mu m,\\
400\mu m \leq H_b \leq 800\mu m,\\
70\mu m \leq W_w \leq 800\mu m.
\end{aligned}
$$

5.4.2 Effect of channel size

Table 5.3 shows typical results of varying the channel dimensions, W_c and H_c, on the pressure drop Δp and temperature deviation T_{dev}. Pressure drop Δp is effectively independent of H_b and W_w and depends only on the W_c and H_c through a strong dependence on channel cross-sectional area, $W_c \times H_c$. In contrast, T_{dev} also depends on H_b through its influence on the substrate thermal resistance. As H_b increases, conduction into the liquid decreases leading to larger temperature variations.

5.4.3 Design of experiments (DOE) and CFD solutions

After choosing the range of the design variables, design of experiments (DOE) points were generated and distributed within design space see Figure 5.9 using an Optimal Latin Hypercube Sampling technique (Narayanan et al., 2007). CFD

Case no.	W_c(mm)	H_c (mm)	H_b(mm)	$\Delta p(Pa)$	$T_{dev}(K)$
1	0.5	0.15	0.8	50.27	26.04
3	0.15	0.15	0.8	147.59	25.74
4	0.15	0.05	0.8	1416.10	20.44
5	0.5	0.15	0.4	49.92	19.71
6	0.5	0.05	0.4	986.33	16.66
7	0.15	0.15	0.4	146.67	19.34
8	0.15	0.05	0.4	1413.30	15.30

Table 5.3: Effect of channel size on T_{dev} and Δp for the case of $Re = 0.7$, $T_f = 20°C$, $W_w = 0.07$mm.

simulations were then run at these design points to generate the $\mathbf{y} = (T_{dev}, \Delta p, Q_t)$ data set for use within the surrogate models.

5.4.4 Surrogate Modelling

Two surrogate modelling approaches are used. The first is based on cubic Radial Basis Functions (RBFs) where the surrogate model y_k (k^{th} component of $\mathbf{y}$ with $k = 1, 2, 3$) for the output variable $\mathbf{y}$ at a design point $\mathbf{x} = (W_c, H_c, H_b, W_w)$ is given by

$$y_k(\mathbf{x}) = \sum_{i=1}^{N} \lambda_i \phi\left(\|\mathbf{x} - \mathbf{x}_i\|\right), \quad \phi\left(\|\mathbf{x} - \mathbf{x}_i\|\right) = \beta\|\mathbf{x} - \mathbf{x}_i\|^3, \tag{5.23}$$

with $\mathbf{x}_i$ being the i^{th} DoE point ($1 \leq i \leq N$), taken from $N = 560$ CFD simulations. $\|\cdot\|$ denotes the l^2 norm, λ_i are RBF parameters. β is a calibration parameter for the cubic RBF function. For each surrogate model β is determined using a relatively simple Leave-One-Out (LOO) calibration, where each sample point is left out of the RBF function and then used to predict the value at the omitted DoE point. The Root Mean Square Error (RMSE) of the discrepancies between the predicted and actual DoE points is then minimised with respect to the β parameter over a suitable interval (González Niño et al., 2019).

The second approach uses fully connected Neural Networks (NNs) available within Tensor Flow, using N_{train}=176 of these randomly selected for the training

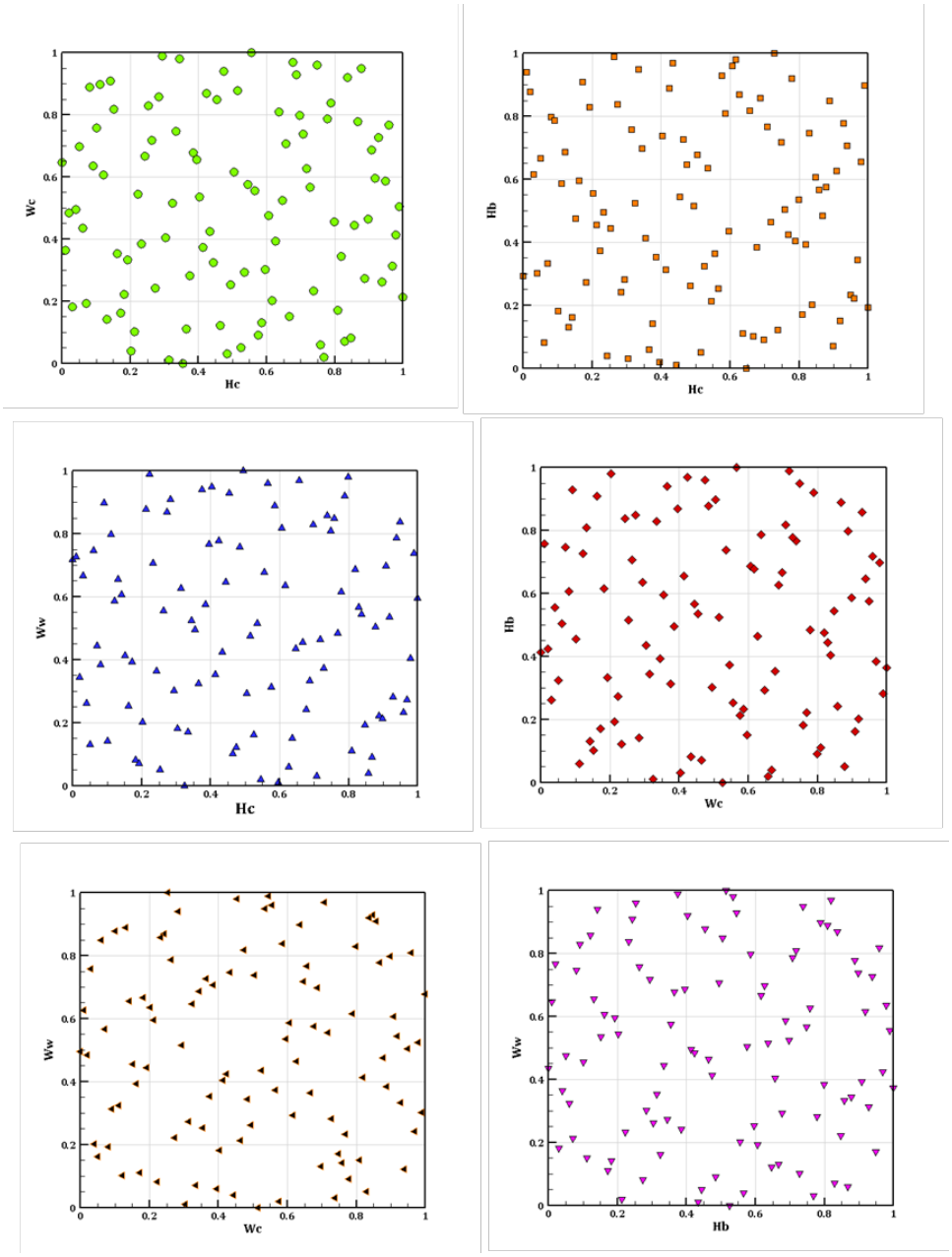

Figure 5.9: Design of Experiments.

data set and the remaining N_{tests}=50 used as the test data set. A Stochastic Gradient Descent (SGD) method is used to minimise the cost function:

$$cost = \sum_{i=1}^{N_{train}} \|\mathbf{y}_i^{predict} - \bar{\mathbf{y}}_i^{train}\|/N_{train}. \tag{5.24}$$

The calculations are terminated after 5×10^4 iterations to avoid over-fitting when the error

$$err = \sum_{i=1}^{N_{train}} \|\mathbf{y}_i^{predict} - \bar{\mathbf{y}}_i^{test}\|/N_{test} \tag{5.25}$$

does not decrease as shown in Figure 5.10.

In (5.24) and (5.25), $\bar{\mathbf{y}}$ is the normalised data set given by

$$\bar{y}_k = \frac{y_k - y_{k,min}}{y_{k,max} - y_{k,min}}, \quad (k = 1, 2, 3) \tag{5.26}$$

with y_k being the k^{th} component of $\mathbf{y}$, and $y_{k,min}$ ($y_{k,max}$) being the minimum (maximum) of all the N data points for the k^{th} component.

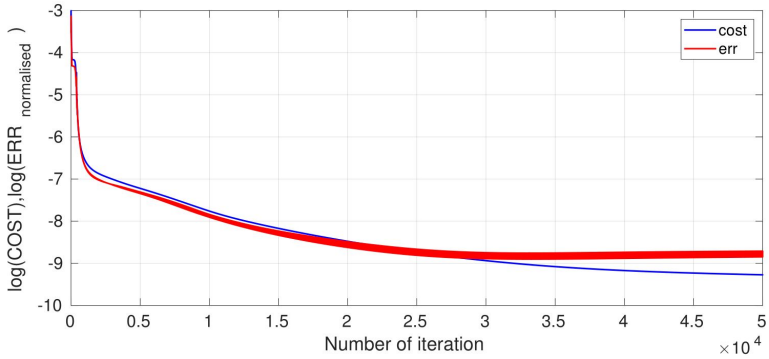

Figure 5.10: Convergence of the cost function evaluated on the training data and error measured on the test data set.

The training procedure random process is performed 10 times for the same NN before the effect of using different topologies is explored. The three best NNs that can reduce the error in the testing dataset to around 0.3% are shown in Figure 5.11.

A reliable method of determining the best NN is to let them predict another unseen data set. Therefore these three NNs are tested on 50 additional CFD data points, and the relative error is shown in Table 5.4. From these we can conclude that the one-layer NN with 100 neurons is the most accurate, and will be used in all NN results presented below.

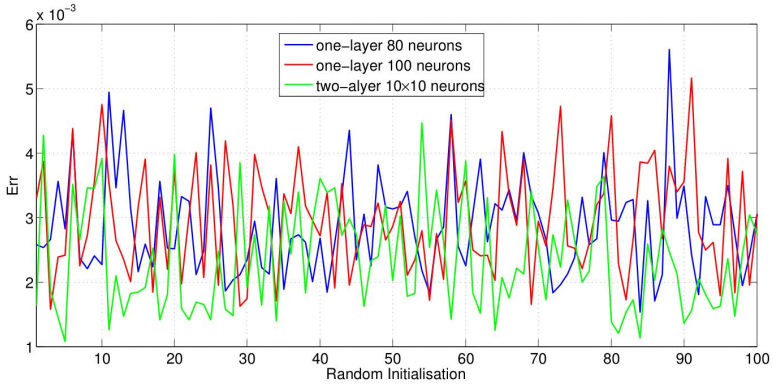

Figure 5.11: Final error of running the same NN 100 times, which is initialized randomly.

One-layer NN with 80 neurons	one-layer NN with 100 neurons	Two-layer NN with 10×10 neurons
3.5773×10^{-3}	2.0128×10^{-3}	2.4820×10^{-3}

Table 5.4: Error testing on 50 additional data points.

5.4.5 Single-Objective optimisation

Optimising each of the objectives in isolation is relatively straightforward and valuable insight can be obtained from examining the surrogate models of each individual objective. Figure 5.15 shows examples of surrogate model surfaces for T_{dev}, which indicate that minimising T_{dev} requires the smallest W_c, H_c and H_b values. Similar insights can be gained by examining the surrogate models for the other objectives. The global minima for each individual objective are shown in Table 5.5: for example, the first row shows the design point corresponding to the global minimum for the objective T_{dev}, together with the other two objectives at this point. Note that the minimum value of T_{dev} corresponds to comparatively large values of Δp and Q_t, whereas the minimum Δp corresponds to comparatively large T_{dev} and Q_t. This indicates that it is interesting to explore the trade-off between the objective functions through a multi-objective analysis.

In the previous sub-sections, single objective optimisation was presented to find the best PCR design for different objective functions. In this section, multi-

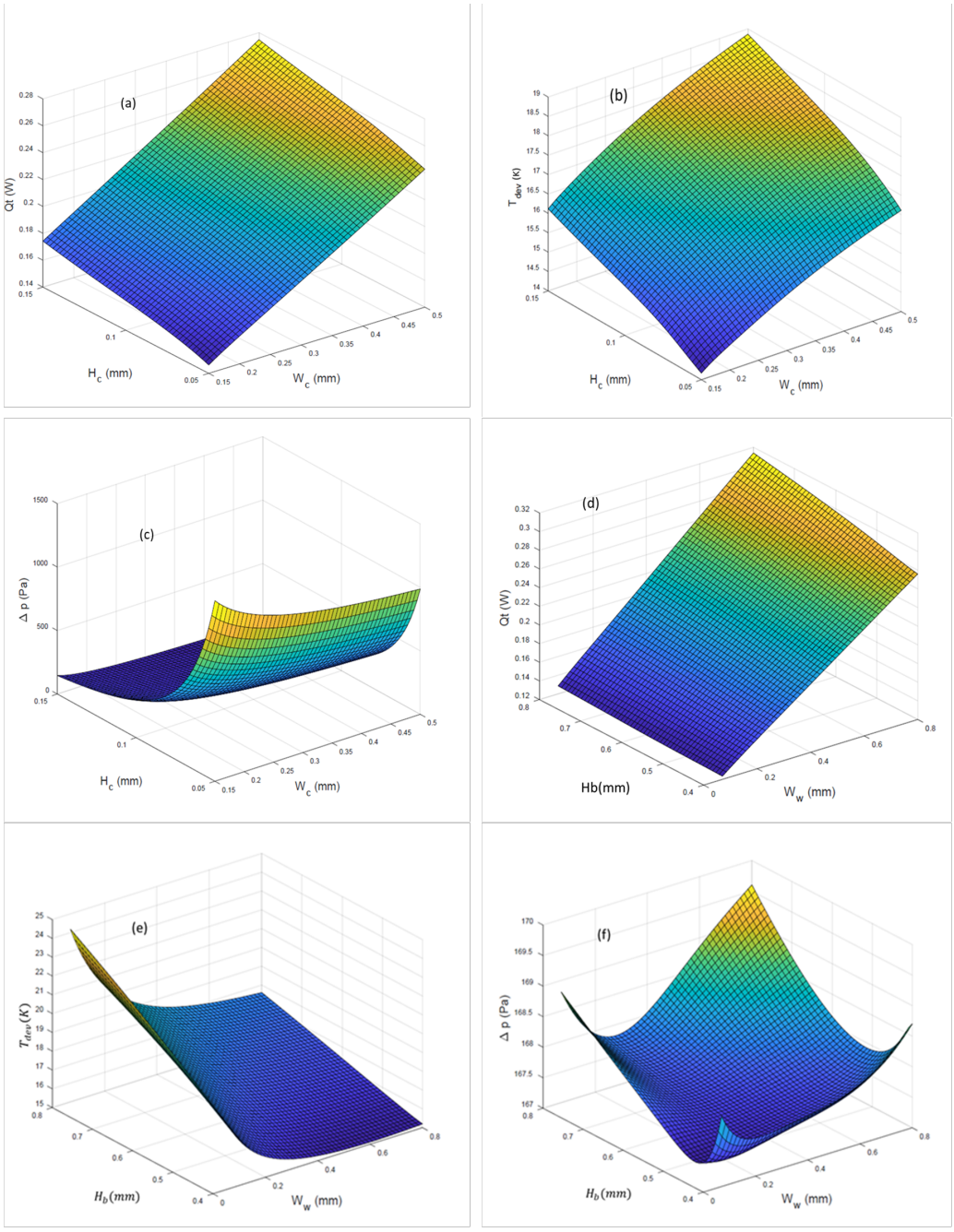

Figure 5.12: Typical surrogate model surfaces of T_{dev} as a function of (a) H_c vs W_c (with $H_b = 0.6$, $W_w = 0.435$), (b) H_c vs W_c (with $H_b = 0.6$, $W_w = 0.435$, (c) H_c vs W_c (with $H_b = 0.6$, $W_w = 0.435$), (d) H_b vs W_w (with $H_c = 0.1$, $W_c = 0.325$), (e) H_b vs W_w (with $H_c = 0.1$, $W_c = 0.325$), (f) H_b vs W_w (with $H_c = 0.1$, $W_c = 0.325$.)

Table 5.5: Single objective optimisation.

Objective	Global min.	W_c (mm)	H_c (mm)	H_b (mm)	W_w (mm)	T_{dev} (K)	$\Delta p(Pa)$	$Q_t(W)$
$T_{dev}(K)$	12.864	0.150	0.050	0.400	0.727	-	1426.464	0.192
$\Delta p(Pa)$	49.782	0.500	0.150	0.799	0.799	19.684	-	0.381
$Q_t(W)$	0.063	0.150	0.050	0.400	0.070	15.307	1413.317	-

objective optimisation will be presented to identify if there is a best compromise between different objectives such Δp vs T_{dev}, Δp vs Q_t and T_{dev} vs Q_t.

5.4.6 Multi-Objective Pareto Analysis

The RBF and NN methods were used to create Pareto curves of non-dominated solutions for Δp vs T_{dev}, Δp vs Q_t and T_{dev} vs Q_t. The RBF method uses the Multi-Objective Genetic Algorithm (MOGA) solver in MATLAB, whereas the NN methods use the SciPy.optimization module By using written and developed by Dr yonxing in Python based on a simple weighting between the competing objectives (this was part of the collaboration in writing my paper). The Pareto curves from the RBF and NN meta-modelling are all very similar to each other - the Pareto curves for Δp vs T_{dev} are shown in Figure 5.13 and its accuracy is confirmed by the further validation with the CFD predictions at points P1-P7 shown in Table 5.6. This provides a basis for finding an appropriate balance between these competing objectives. It shows, for example, that reducing T_{dev} from 14 to 13 would require a four-fold increase of Δp, from 250 to $1000Pa$, while reducing Δp below $100Pa$ comes at the price of a sharp rise in T_{dev}.

Figure 5.14 compares the temperature profile from a design point on the Pareto curve ($H_c = 50\mu m$, $W_c = 152\mu m$, $H_b = 403\mu m$, $W_w = 667\mu m$, $H_h = 2000\mu m$, $H_{PMMA} = 1500\mu m$ and $S = 1mm$) with that from a non-optimised Design of Experiments point ($H_c = 150\mu m$, $W_c = 500\mu m$, $H_b = 800\mu m$, $W_w = 70\mu m$, $H_h = 2000\mu m$, $H_{PMMA} = 1500\mu m$ and $S = 1mm$). It can be seen that the temperature profile from the optimised solution is much closer to the target temperature profile than for the non-optimised one.

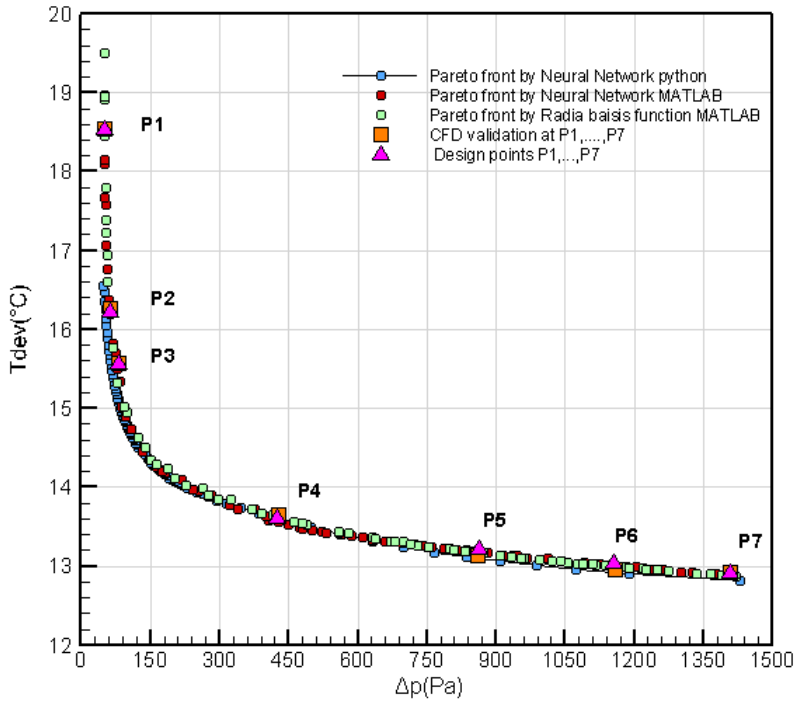

Figure 5.13: Pareto curves of Δp vs T_{dev}, obtained using RBF and NN surrogate modelling.

Figure 5.15 shows the other two-dimensional Pareto curves for the competing objectives Δp vs Q_t and T_{dev} vs Q_t, obtained using the one-layer NN with 100 neurons available in TensorFlow, combined with the SciPy.optimization module. Figure 5.15(a) shows that Q_t can be reduced significantly without a major pressure drop penalty, but that reducing it below 0.06 does require a significantly larger Δp. Figure 5.15(b) shows that there is a reasonably linear, negative correlation between T_{dev} vs Q_t for $T_{dev} > 13$ but that Q_t increases sharply for lower values of T_{dev}. Finally, Figure 5.16(a) extends the Pareto analysis to consider all three competing objectives, T_{dev}, Δp and Q_t simultaneously. The non-linearities make it difficult to fit all the Pareto points onto a smooth surface, however it is possible to create smooth Pareto surfaces over subsets of the design space, see Figure 5.16(b). These surfaces provide a scientific basis for achieving an appropri-

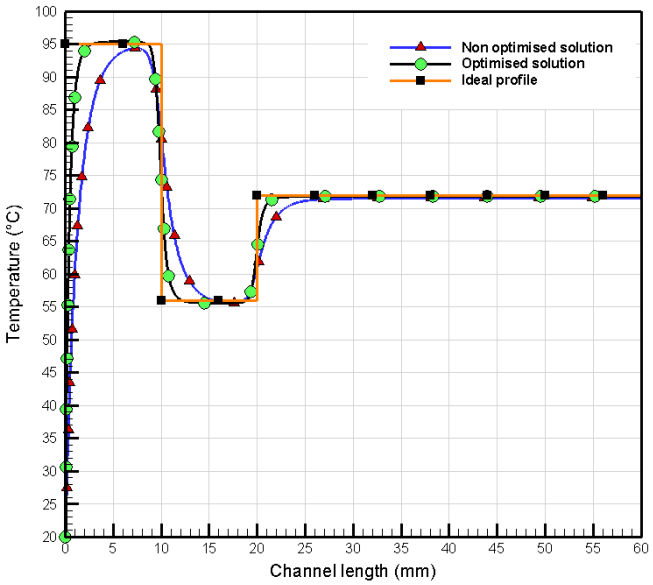

Figure 5.14: A comparison of temperature profiles in PCR fluidic channel from an optimised and a non-optimised solution.

ate balance between these three competing objectives, based on practical design requirements.

points	Geometrical dimensions(mm)				Δp (pa)		T_{dev} (K)		$error\%$	
	H_b	H_c	W_c	W_w	$Pareto$	CFD	$Pareto$	CFD	Δp	T_{dev}
P1	0.624	0.149	0.467	0.557	51.679	51.528	18.526	18.534	0.294	0.040
P2	0.441	0.145	0.363	0.636	63.903	63.552	16.215	16.272	0.552	0.347
P3	0.453	0.149	0.246	0.637	80.166	80.445	15.555	15.570	0.346	0.094
P4	0.404	0.083	0.152	0.688	426.179	427.880	13.603	13.642	0.397	0.284
P5	0.402	0.061	0.150	0.696	862.899	859.140	13.201	13.131	0.437	0.536
P6	0.402	0.054	0.150	0.696	1155.840	1157.20	13.030	12.965	0.117	0.508
P7	0.402	0.050	0.150	0.717	1408.68	1407.5	12.897	12.922	0.083	0.192

Table 5.6: PCR design performance at seven operating conditions points located on the Pareto front together with CFD validation as shown in Figure .

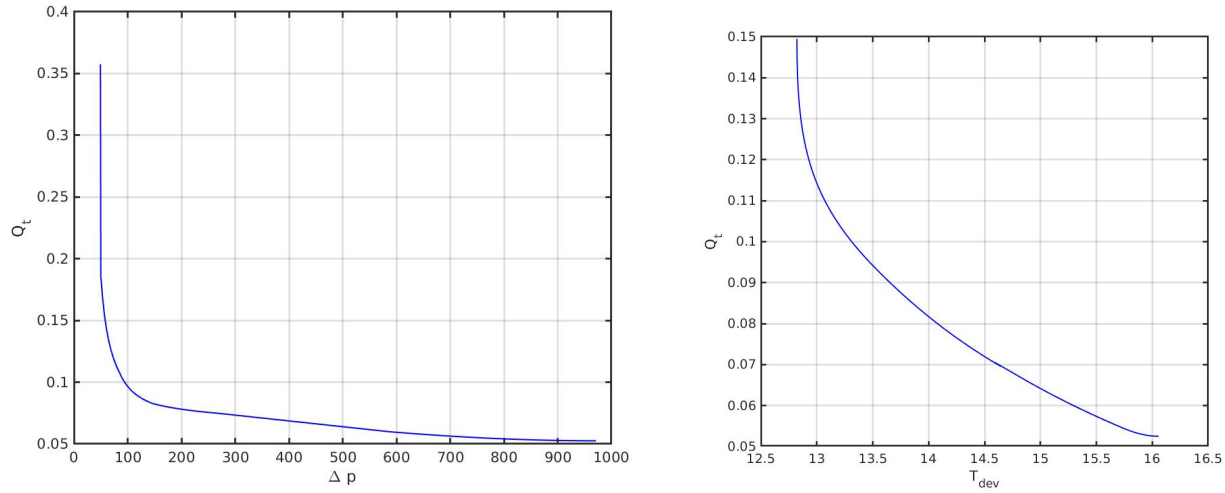

(a) Δp vs Q_t.

(b) T_{dev} vs Q_t.

Figure 5.15: Pareto curves of the competing objectives.

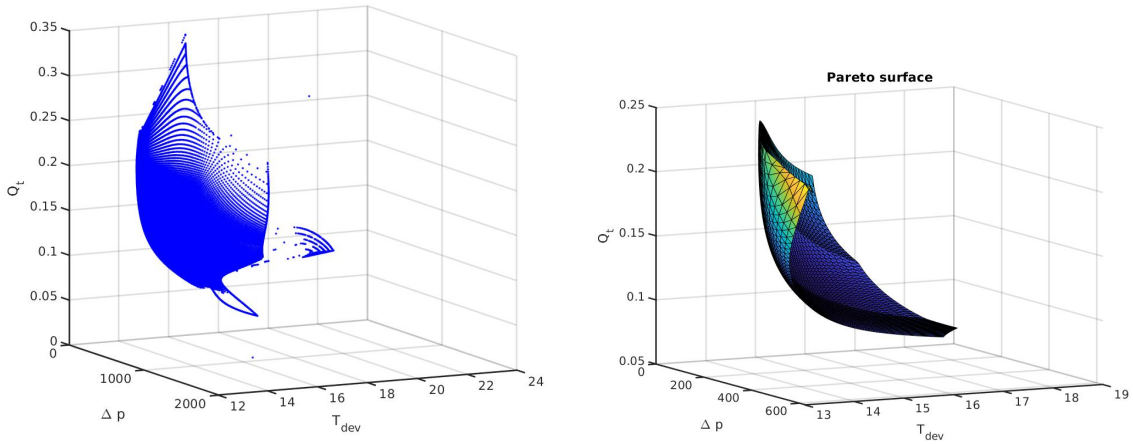

(a) Pareto set as discrete points.

(b) Part of the Pareto set fitted to a smooth surface.

Figure 5.16: Three dimensional Pareto set.

5.5 Summary

The present Chapter proposes a novel Computational Fluid Dynamics (CFD)-enabled optimisation methodology which enables the trade-offs between competing objectives of temperature uniformity, pressure drop and heating power consumption to be explored. This allows designers to maximise the proportion of PCR liquid that experiences the target temperature range for the required time period in each zone, to preserve the structural integrity of the CFPCR chip or to minimise the time taken or overall power consumption (heating and hydraulic) throughout thermal cycling. In the next Chapter the quantification of uncertainty of design variables towards optimum robust design will discussed.

Chapter 6

Robust Design Optimisation of PCR Systems

6.1 Introduction

The deterministic optimisation described in Chapter 5 is unable to account for uncertainties in PCR system dimensions, arising out of manufacturing tolerances, as well as variations in operating conditions. causing unreliable design due to the fluctuation existing in input parameters or environment. Robust Design Optimisation methods enable the effect of uncertainties to be accounted for systematically.

Robust design optimization (RDO) is an effective approach for accounting for uncertainties in input variables on the resultant output design objectives. The target of this chapter is to present a Robust design of PCR systems that aims to obtain a solution in which the system is the most insensitive to input variations.

6.2 Description of the model

A schematic diagram of the microfluidic channel geometry is presented in Figure 4.15 where W_c, H_c, W_w, H_b and L are the microchannel width, height, wall thickness (the space between the channels), the bottom height and the total length respectively.

There are three individual copper blocks with cartridge heaters placed underneath the glass chip with a constant distance between them of $S = 1mm$, the length of the heaters being $9mm$ underneath the denaturation and annealing zones and $40mm$ underneath the extension zone. The height and length of each heater are $H_h = 2mm$ and L_h=$9mm$. The length of the denaturation, annealing and extension zones are chosen to achieve the typical residence time ratios of $1 : 1 : 4$ respectively (Chen et al., 2008). See Table 6.3 for more details about boundary condition used for deterministic and robustness design.

6.2.1 Conjugate Heat Transfer Model

A conjugate heat transfer model of the steady, single-phase, laminar flow problem shown in Figure 4.15 is developed using a number of assumptions described in Chapter The flow is modelled using the governing continuity and Navier-Stokes equations.

6.3 Geometrical uncertainties in CFPCR flows

Robust design is to optimise the mean and minimize the variability that results from uncertainty represented by noise factors (Zang et al., 2005).

The robustness design optimisation is a type of sensitivity analysis used determine the response variation and identifying what parameters cause the variation.

The work in this chapter is based on the first proposed design under uncertainty in microchannel PCR systems. A number of assumption are used in advance:

1. Each design variable is used to generate a random variable that follows a Gaussian distribution.

2. The default standard deviation equals 5%or 10% of the mean value (Zhang and Jaluria, 2020).

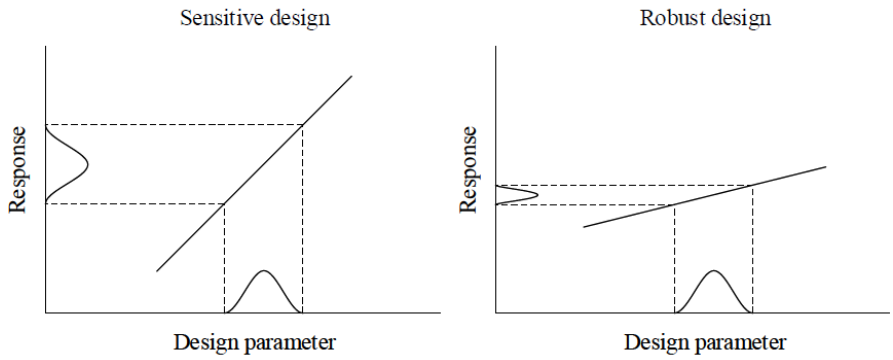

Figure 6.1: An illustrative example of the difference between a sensitive design and a robust design

3. From the 3-sigma rule, about 68%, 95%, and 99.7% of the values drawn from the distribution are within one sigma, two sigma, and three sigma away from the mean.

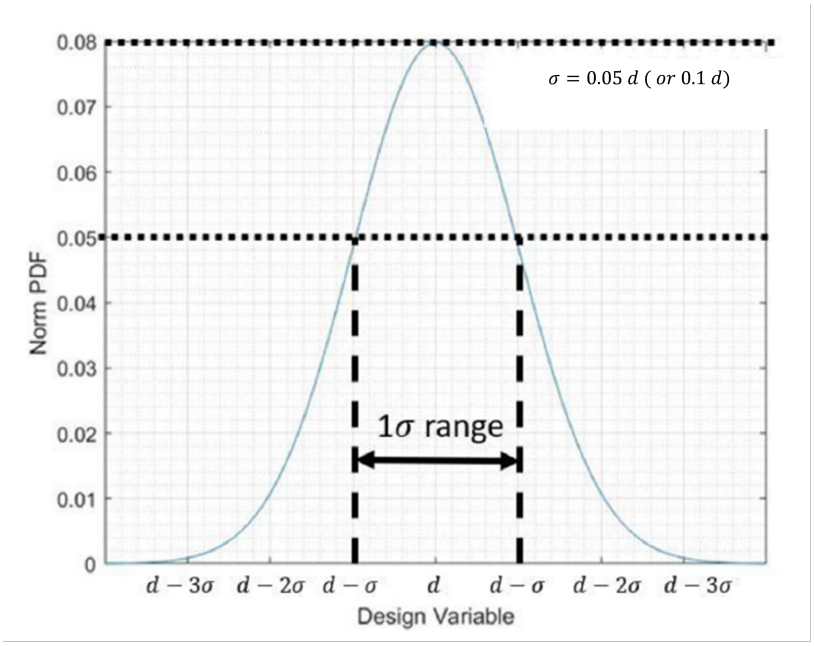

Figure 6.2: The design variable distributions.

Let $\mu \in \mathbb{R}$ and $\sigma^2 > 0$ and let

$$X \sim \mathcal{N}(\mu,\, \sigma^2)\,.$$

Then Suppose X has a finite expected value $E(X)$ and finite variance $\sigma^2 = V(x)$

$$\begin{aligned}\mathbf{E}[X] &= \frac{1}{\sqrt{(2\pi\sigma^2)}}\int_{-\infty}^{\infty} xe^{-(x-\mu)^2)/(2\sigma^2)}dx \\ &= \frac{1}{\sqrt{(2\pi\sigma^2)}}\int_{-\infty}^{\infty}(x+\mu)e^{-(x)^2)/(2\sigma^2)}dx \\ &= \mu + \frac{1}{\sqrt{(2\pi\sigma^2)}}\int_{-\infty}^{\infty} xe^{-(x)^2)/(2\sigma^2)}dx = \mu \end{aligned} \tag{6.1}$$

similarly , the variance can be simplified to:

$$\mathbf{Var}[X] = \mathbf{E}[X^2] - \mu^2 = \cdots = \sigma^2 \tag{6.2}$$

Also $\sigma = \sqrt{\mathbf{Var}[X]}$ is the standard deviation of X.

6.3.1 Validation of probabilistic solution

In order to validate the code of MATLAB used in this thesis based on Monte Carlo (MCS), the code is validated with a case study solved by (Couto et al., 2013) which was Measurement of Brinell hardness test. This test was carried out by exerting a load on a hard material in spherical shape placed over the surface of the test sample as depicted in the schematic diagram

The sphere will penetrate through the sample during the test leaving an indented mark upon unloading. The diameter of this mark is inversely proportional to the hardness of the material of the sample. The first in the solution is to identify the input sources for this case which were : Load (F), Indenter diameter (D) and Diameter of the mark (d). the second step is to prepare the model associated with input sources and relates them with output. The model used for the Brinell hardness (HB) is depicted in Equation 6.3

$$HB = \frac{0.204F}{\pi D(D - \sqrt{D^2 - d^2})} \tag{6.3}$$

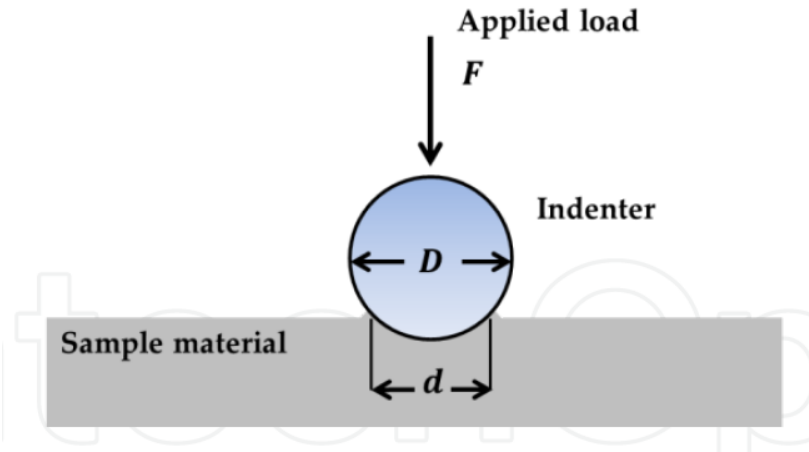

Figure 6.3: Schematic representation of a Brinell hardness test (Couto et al., 2013)

Input sources	Type	PDF	PDF parameters
Load (F)	B	Gaussian	$\mu = 29400N, \sigma = 294N$
Indenter diameter (D)	B	Gaussian	$\mu = 10mm, \sigma = 0.005mm$
Diameter of the mark (d)	A	Gaussian	$\mu = 3mm, \sigma = 0.035mm$

Table 6.1: Input sources and associated PDFs with their respective parameters for the estimation of uncertainty of a Brinell hardness test.

the third step is to obtain information about the uncertain sources. **Load (F)** the applied load was fixed at 29400 N, and the provided certificate of the machine demonstrates an expanded uncertainty of 2%, with k = 2 and a coverage probability of 95%. Thus, Gaussian distribution can be used to represents the results. Gaussian PDF is used with mean 29400 N and standard deviation of $U/k = (0.02 \times 29400N)/2 = 294N$. The same procedure is done for the **Indenter diameter (D)** and **Diameter of the mark (d)** using the certificate of measurement of them. Table 6.1 summarised the input sources and associated PDFs .

The results of PDF for the Brinell hardness values are obtained for $M = 2\times10^5$ trials and compared with obtained results by (Couto et al., 2013) which are shown in Figures 6.4 and 6.5. Also Monte Carlo simulation results for $M = 2\times10^5$ trials

are shown in Table 6.2. The comparison showed good agreements between the current results and the results determined by (Couto et al., 2013) .

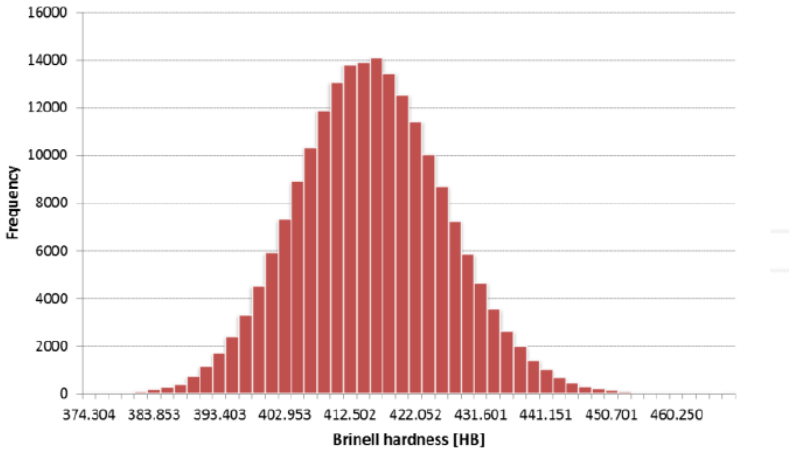

Figure 6.4: PDF for the Brinell hardness estimated by Monte Carlo simulation obtained by current study obtained by (Couto et al., 2013)

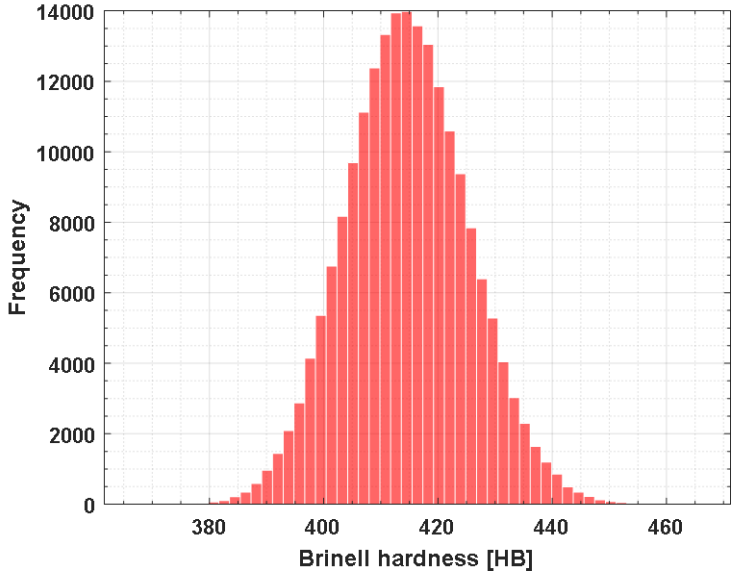

Figure 6.5: PDF for the Brinell hardness estimated by Monte Carlo simulation obtained by current study

Parameter	Value((Couto et al., 2013))	Value (current study)
Mean (μ)	$415HB$	$414.67HB$
Standard deviation (σ)	$11HB$	$10.73HB$

Table 6.2: Statistical parameters obtained for the Monte Carlo simulation of the Brinell hardness measurement model.

6.4 Uncertainty Quantification for PCR systems(UQ)

Uncertainty Quantification (UQ) is a process used to assess the impact of the uncertain input sources on the output (objectives). For a given set of distributions for the inputs, UQ seeks to determine probability distributions for the outputs. The Uncertainty Quantification for PCR systems under consideration in the current thesis is conducted following the same procedures described in the previous section.

1. The first step is to identifies the input sources, in this thesis, the input parameters considered for UQ analysis are as follows: width of the channel (W_c), the height of the channel (H_c) , the substrate thickness (H_b) and space between channels (W_w). These variables are assumed to be normally distributed random variables. The corresponding variation in the input sources are depicted in the Table 6.3 including uncertain and deterministic design parameters.

2. The second step is to model the system for this purpose CFD model is adopted and described in section. This model is used only to obtain the solution for the design points (DOE) points and the alternative model is named surrogate model which is validated with actual results obtained by the CFD model. Then this surrogate model is used to predict the output points of Monte Carlo simulation about (10^5) runs.

3. The third step is to run Monte Carlo numerical simulation to propagate the distribution. For each drawn sample, the function is evaluated for thousands of iterations in order to cover the entire range of the input PDF. When the entire variation of the input variable is covered, the PDF of outputs can be determined (Bodla et al., 2013).

Type	Input	condition	Distribution	σ_{in}
Geometrical boundary	H_c	uncertain	NORM	$0.05 - 0.1$
Geometrical boundary	W_c	uncertain	NORM	$0.05 - 0.1$
Geometrical boundary	W_w	uncertain	NORM	$0.05 - 0.1$
Operating boundary	Re	constant	0.7	-
Operating boundary	T_{in}	constant	$20°C$	-
Operating boundary	T_d	constant	$96.7°C$	-
Operating boundary	T_a	constant	$55.76°C$	-
Operating boundary	T_e	constant	$73°C$	-
Operating boundary	h	constant	$15(W/m.K)$	-

Table 6.3: Input sources and boundaries of PCR system.

4. The fourth step is to determine expected μ and σ calculated for the PDF for the output. The output functions (objective) in RDO include the mean μ and standard deviation σ of stochastic responses (Chatterjee et al., 2019) which are presented in Equation 6.4 and Equation 6.5. Table 6.4 shows μ and σ calculated for the PDF for the output at six evaluations points.

$$\mu_{fi} = \frac{1}{N}\sum_{j=1}^{N} f_i^j \tag{6.4}$$

$$\sigma_{fi}^2 = \frac{1}{N}\sum_{j=1}^{N}(f_i^j - \mu_{fi})^2 \tag{6.5}$$

Figure 6.6 shows the effect of sensitivity and data uncertainty of input variables that are randomly distributed (follow Gaussian distribution) on the output data. Figure 6.6 (a) and (b) reveals a good agreement between the predicted output data obtained from the Neural network surrogate model based on DOE points and the actual data computed from the CFD model. This is because the input variation was zero so μ_{f1} which represents Δp is equal to the predicted one , also μ_{f_2} which represents T_{dev} is equal the predicted one. Figure 6.6 (c) and Figure 6.6 (d) show the variation effect of four design variables $(W_{ch}, H_{ch}, H_b, W_w)$ on the objectives. These variables were randomly distributed based on Gaussian distribution ($\sigma = 0.05$), and the predicted output from Monte Carlo simulations.

H_c	W_c	H_b	W_w	σ_{in}	f_1	$\mu_{1(N.N)}$	$\mu_{1(MLSM)}$	σ_{out1}	f_2	$\mu_{1(N.N)}$	$\mu_{2(MLSM)}$	σ_{out2}
0	0	0.5	0.5	0.0	0.998	0.998	0.998	2E-15	0.0916	0.091	0.091	0
0	1	0.5	0.5	0.0	0.069	0.069	0.069	1E-16	0.246	0.246	0.246	6E-16
1	0	0.5	0.5	0.0	0.679	0.679	0.679	1E-15	0.283	0.283	0.283	6E-16
1	1	0.5	0.5	0.0	0	1.06E-10	1E-07	0	0.454	0.454	0.454	1E-15
0.5	0.5	0	0	0.0	0.086	0.086	0.086	5.5E-17	0.394	0.394	0.393	5E-16
0.5	0.5	0	1	0.0	0.086	0.086	0.086	1E-16	0.160	0.160	0.160	0
0	0	0.5	0.5	0.05	0.998	1.033	1.000	0.284	0.091	0.122	0.090	0.116
0	1	0.5	0.5	0.05	0.069	0.073	0.080	0.021	0.246	0.245	0.244	0.111
1	0	0.5	0.5	0.05	0.679	0.725	0.684	0.240	0.283	0.312	0.282	0.125
1	1	0.5	0.5	0.05	0	0.0005	0.014	0.003	0.454	0.486	0.452	0.114
0.5	0.5	0	0	0.05	0.086	0.088	0.086	0.015	0.394	0.4196	0.393	0.102
0.5	0.5	0	1	0.05	0.086	0.087	0.083	0.015	0.160	0.214	0.161	0.153

Table 6.4: Uncertainty quantification of inlet variables (σ_{in}) on output in terms of $f_1 = \Delta p$ and $f_2 = T_{dev}$ where μ_1 represents the average of the PDF output for estimated the Δp and μ_2 represents the average of the PDF output for estimated the T_{dev}

.

It can be noted that small variations between the predicted outputs and the actual output values. These variations increased as the input variation increased see Figures 6.6 (e) and (f) for input variation ($\sigma = 0.1$). Also, it can be seen from Figures 6.6 (c) and (e) the least variation between predicted and actual data was at points 4 while the least variation between the predicted and actual T_{dev} was at point 2 see Figures 6.6 (d) and (f). This indicates that it is interesting to investigate the optimisation of robust design. The MLSM model is valid only at a deterministic approach in which the design variables are not taken the noise effect. It could be developed to include the noise effect and this out of the scope of this study. The uncertainty design approach was based on a Neural network approximate model.

6.5 Optimisation

There are two main approaches to optimisation under uncertainty , design for reliability and design for robustness (robust design optimisation) which is considered in this thesis. The optimisation often aims to minimise objectives function

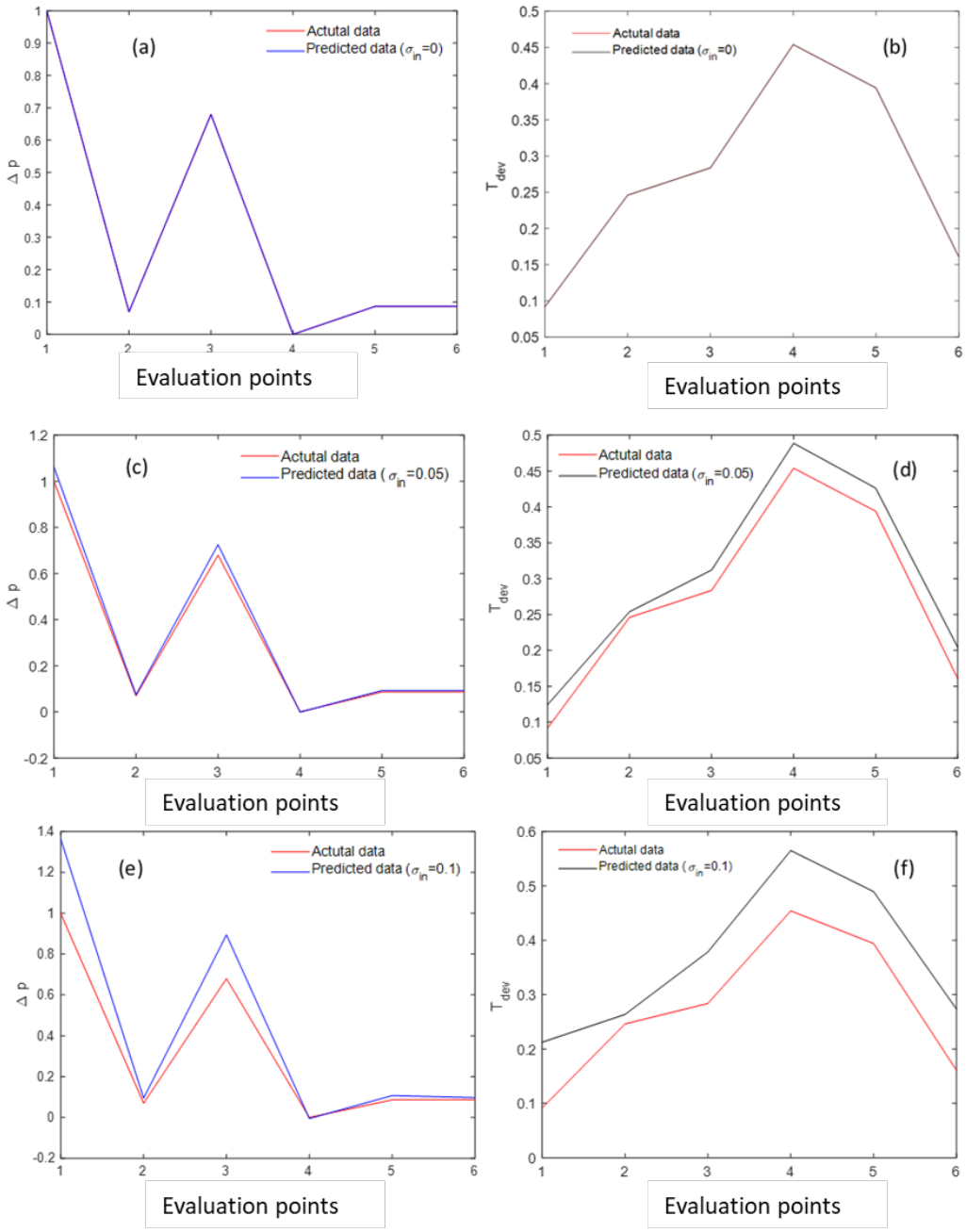

Figure 6.6: Uncertainty effect of inlet variables (σ_{in}) on output in terms of Δp and T_{dev} at six evaluation points.

within the design domain.

Robust design is often conducted to optimise the mean and minimize the variation that results from uncertainty represented by the noise factor. The process of robust design optimisation (RDO) is to search the surrogate model to locate a design point at which the objective (output) has minimum sensitivity to the uncertain variation of input parameters (Zang et al., 2005). The variability of input variable cause noise effect of the output for example in the current thesis the deterministic target is either Δp or T_{dev} which are corrupted to μ and σ (noise) due to the uncertainty in the input parameters (W_c,H_c,H_b and W_w). These uncertain parameters can not be controlled but their effect (σ) can be adjusted (Park et al., 2006). In this chapter surrogate model-based robust optimization is used based on previous studies employed by(Jin et al., 2003) , (Nejadseyfi et al., 2019) and the proposed method (Shin et al., 2016). The flow chart of robust design optimisation used in this thesis is depicted in Figure 6.7

Its key steps are :

1. Formulate the optimisation problem: specify the objective functions and constraints.

2. Design space parameterisation: specify the design variables and design space.

3. Design of experiments (DoE): This step is to generate a set of design experiments (DOE) relatively small number of well-scattered design points throughout the design space considering both design and noise input variables. Also, the DOE points domain is improved and extended to include sub-domain outside the boundaries to overcome the issue of extrapolation.

4. CFD solutions: obtain CFD solutions of the conjugate heat transfer problem at each of the DoE points and extract values of the objective functions from them.

5. In this step, create a surrogate model using N.N.

6. Choose evaluation points from the design points.

7. Identify the uncertainty for each evaluation points.
8. Use Monte Carlo simulation to propagate the standard deviation and to estimate the output of the distribution from the surrogate model.
9. Compute the output in terms of mean and standard deviation.
10. Create a surrogate model from the obtained results to predicts the output means and standard deviation (Vu et al. 2017)
11. Embed the surrogate models within an appropriate optimisation algorithm (ga or fmincon) to minimise the output (mean) with constraints of standard deviation. For multi-objective optimisation: the surrogate models embedded within an appropriate multi-objective optimisation algorithm Pareto front was generated showing optimal compromises between each objective function.

6.5.1 Problem Formulation of robust design optimization

In this design the input variables W_c, H_c, H_b and W_w are specified as uncertain variable with a given σ and mean value for each variables. Then Monte Carlo Simulation (MCS) is used to propagate the uncertainty by generating random points for each design evaluation about 10^5 considering σ of each point. The output functions (objective) in RDO include the mean μ and standard deviation σ of stochastic responses (Chatterjee et al., 2019) Consequently, the objectives function in RDO can be expressed in terms of the mean and standard deviation of stochastic responses (Jin et al., 2003; Chatterjee et al., 2019):

$$f(\mathbf{x}) = \tilde{\mathbf{f}}(\mu_{\mathbf{r}}(\mathbf{x})\sigma_{\mathbf{r}}(\mathbf{x})) \tag{6.6}$$

while the nonlinear constraints are formulated as:

$$g(\mathbf{x}) = \tilde{g}(\mu_c(\mathbf{x}), \sigma_c(\mathbf{x})) \tag{6.7}$$

where μ_r and μ_c represent the means of the response of the objective and constraints. While σ_r and σ are their standard deviations. design. Thus the robust optimisation problem of Δp can be defined as:

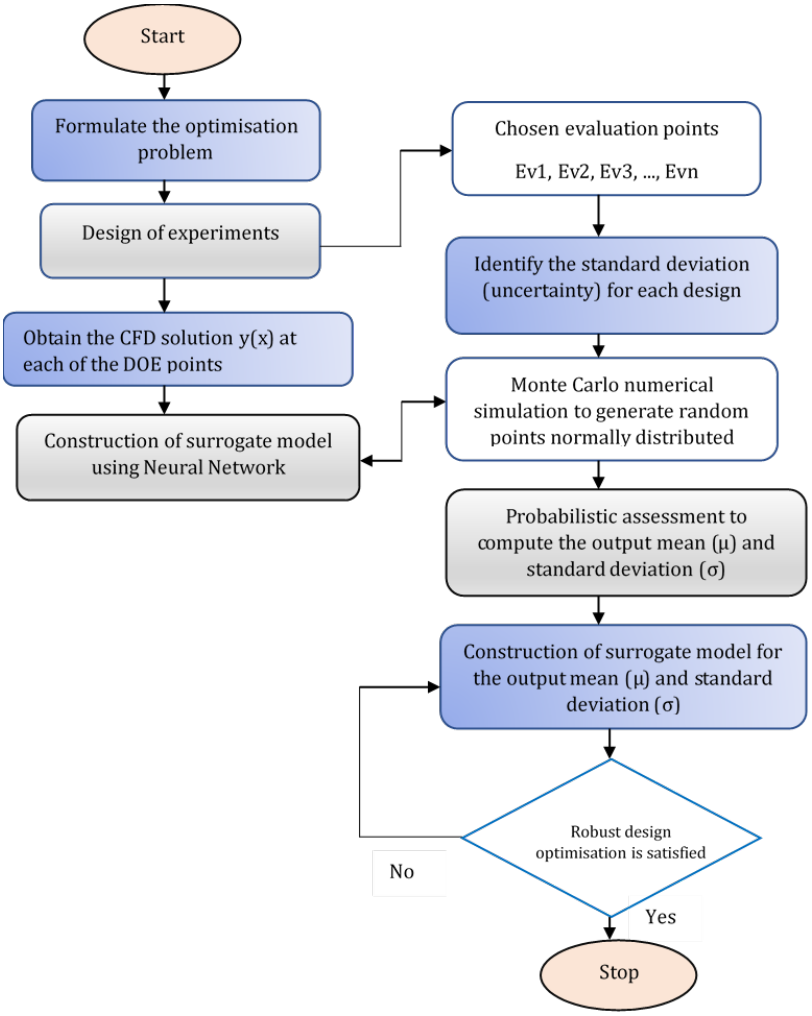

Figure 6.7: Robust optimization steps

$$\textbf{Minimise} \quad \Delta p$$
$$\textbf{such that } \sigma(\Delta p) < \epsilon_1$$

The robust optimisation problem of $\sigma(T_{dev})$ can be defined as:

$$\textbf{Minimise} \quad T_{dev}$$
$$\text{such that } \sigma(T_{dev}) < \epsilon_2$$

where ϵ_1 and ϵ_2 are chosen to verify minimum σ with respect to minimum objective.

6.5.2 Design of experiments (DOE) and CFD solutions

After choosing the range of the design variables a matrix of 300 design of experiments (DOE) points were generated using an Optimal Latin Hypercube Sampling technique (Narayanan et al., 2007).

$$DOE = \begin{bmatrix} \mathbf{x_{i,1}} & \mathbf{x_{i,2}} & \mathbf{x_{i,3}} & \mathbf{x_{i,4}} \\ \vdots & \vdots & \vdots & \vdots \\ \mathbf{x_{n,1}} & \mathbf{x_{n,2}} & \mathbf{x_{n,3}} & \mathbf{x_{n,4}} \end{bmatrix} \tag{6.8}$$

where $\mathbf{x_{i,1}}, \mathbf{x_{i,2}}, \mathbf{x_{i,3}}, \mathbf{x_{i,4}}$ represents the four design variables (W_{ch}, H_{ch}, W_w, H_b) are considered in this study. n represents the number of generated points.

CFD simulations were then run at these design points to generate the $\mathbf{y} = (T_{dev}, \Delta p, Q_t)$ data set for use within the surrogate models. The design points

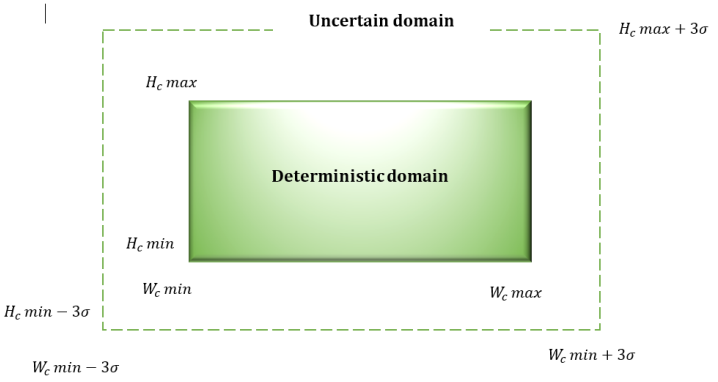

Figure 6.8: Extended DOE domain to include effects of uncertainty.

and their corresponding output obtained from CFD are normalised to $[0, 1]$ by

$$\frac{x_i - x_i^{min}}{x_i^{max} - x_i^{min}}, \quad \frac{y_i - y_i^{min}}{y_i^{max} - y_i^{min}}, \quad i = 1, 2 \tag{6.9}$$

6.5.3 Surrogate Modelling

As elucidated in chapter 4, different tools can be used to find the surrogate models, in the current chapter two surrogate modelling approaches are used. The first is

based on Moving Least Squares(MLSM) approach which explined in Chapter 4 and the second is based on the Artificial neural network (ANN).

6.5.3.1 Artificial neural network

The surrogate modelling approach is created using fully connected Neural Networks (NNs) available within the MATLAB toolbox. MATLAB toolbox of artificial neural network has an efficient tool used to fit the relation between input data and target. The process of learning the ANN can be broken down into steps.

1- select data (MATLAB toolbox allow the user to select data).

2- create and train a network.

3- evaluate its performance using mean square error and regression analysis.

Different types of functions of training the network are available in MATLAB among them Levenberg-Marquardt back-propagation algorithm (trainlm) which is taken as the default training function in the BP neural network. Although this algorithm typically demands more memory it has been adopted in the current work due to it has certain superiority in the learning of BP network, (Zhao et al., 2010) and it need less time.

1. **Training** These are presented to the network during training, and the network is adjusted according to its error.

2. **validation** These are used to measure network generalization, and to halt training when generalization stops improving.

3. **Testing** These have no effect on training and so provide an independent measure of network performance during and after training. A set of available data is divided to train data about 70 % and 15 % for validation and 15 % for testing data. Levenberg-Marquardt back-propagation algorithm (trainlm) N_{train}=420 of these randomly selected for the training data set and the remaining N_{tests}=90 used as the validation data set and N_{tests}=90 used for test data set . A Bayesian Regularization scheme is adopted to minimise the MSE function:

$$MSE = \sum_{i=1}^{N_{train}} (\|\mathbf{y}_i^{predict} - \mathbf{y}_i^{true}\|)^2 / N_{train}. \tag{6.10}$$

Where $\mathbf{y}_i^{predict}$ is the output determined by the network for the ith pattern and $\mathbf{y}_i^{true}$ is the corresponding output that is given in the training dataset (target). Mean Squared Error (MSE) is the average squared difference between outputs and targets. Lower values of MSE are desirable and zero means no error.

Figure 6.9 shows training errors, validation errors and testing errors to find validation error in the training process. The best validation performance was 0.0061816 occurred at iteration 72, and the network at this iteration was returned. It can be seen in Figure 6.9 the mean squared error of the network starting at a large value and decreasing to a smaller value, which means that network learning is improving.Three lines are plotted include training ,validation and test lines. The input and target vectors were randomly divided into three sets. 70 % of the vectors were used for training the network. 15% of those were used for validating how well the network was generalized. Training vectors continues as long as training reduces the network error on validation vectors. After generalization stop improving the training stops automatically by Levenberg-Marquardt back-propagation algorithm, as indicated by an increase in the mean square error of the validation samples. In order to avoid the problem of over-fitting, which plagues many optimisation and learning algorithms. Finally, the last 15 % of the vectors provide an independent test of network generalization about data that the network has never seen.

Regression R values measure the correlation between outputs and targets. An R-value of 1 means a close relationship, 0 means a random relationship (Khan et al., 2014). The coefficient of determination (R^2) can be evaluated as:

$$R^2 = 1 - \frac{\sum_{i=1}^{N_{train}} (\|\mathbf{y}_i^{predict} - \mathbf{y}_i^{true}\|)^2}{\sum_{i=1}^{N_{train}} (\|\mathbf{y}_i^{true} - \bar{\mathbf{y}}_i\|)^2}. \tag{6.11}$$

where $\bar{\mathbf{y}}_i = \frac{\sum_{i=1}^{N_{train}} \mathbf{y}_i^{true}}{N_t rain}$.

Figure 6.10 reveals regression plots for the output with respect to training, validating and testing data. The value of the correlation coefficient (R) for each phase was calculated. The R-value was around 0.999 for the total response in the model.

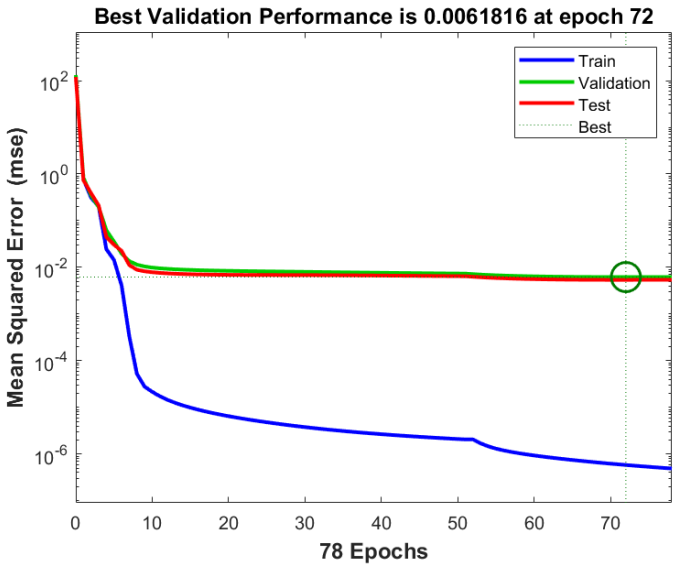

Figure 6.9: Best validation performance.

6.5.4 Single-Objective Optimisation

Optimisation of a single objective at deterministic parameters was conducted in Chapter 5 by optimising each of the objectives in isolation . This process was obtained from examining the surrogate models of each individual objective. The figure 6.11 shows examples of surrogate model surfaces for T_{dev}. The global minimum for each individual objective are shown in Table 6.5.

Besides the deterministic optimization described above, a probabilistic optimization is carried out. For this purpose, each surrogate model was examining to find the robust design points that satisfied the minimum variation of surrogate model output with taking into account uncertainties in the geometric parameters. Also constraints the standard deviation of the predicted objective function to a prescribed value, thus resulting in a robust design. Thus the robust optimisation problem of Δp can be defined as:

$$\textbf{Minimise} \quad \Delta p$$
$$\textbf{such that } \sigma(\Delta p) < \epsilon_1$$

The robust optimisation problem of (T_{dev}) can be defined as:

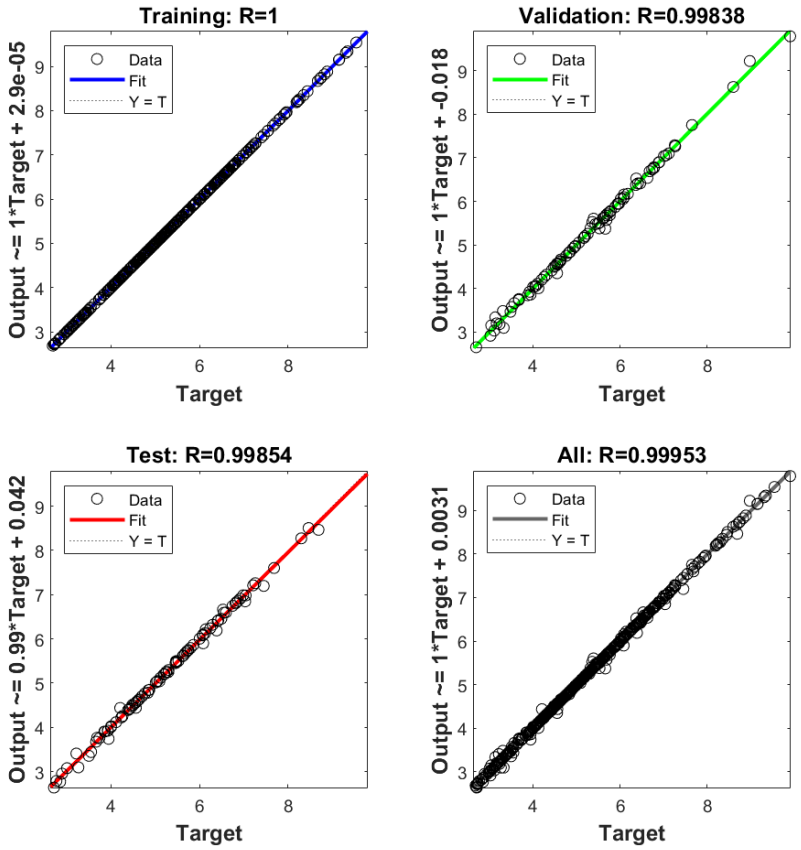

Figure 6.10: Regression plots for training, testing and validation phases and the total response in the ANN model.

$$\textbf{Minimise} \quad T_{dev}$$
$$\text{such that } \sigma(T_{dev}) < \epsilon_2$$

where ϵ_1 and ϵ_2 are chosen to verify minimum σ with respect to minimum objective.

The robust design for each individual objective are shown in Tables 6.6 and 6.7 respectively.

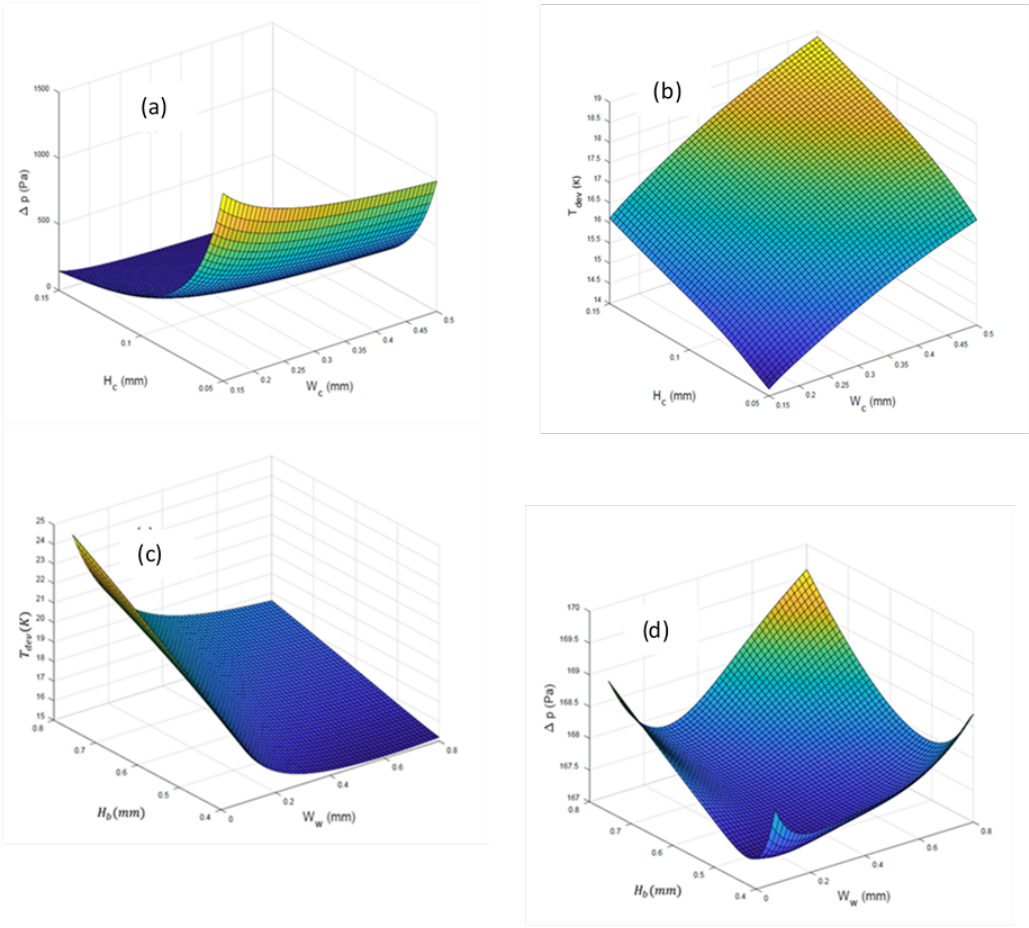

Figure 6.11: Typical surrogate model surfaces of T_{dev} as a function of (a) H_c vs W_c (with $H_b = 0.6$, $W_w = 0.435$), (b) H_c vs W_c (with $H_b = 0.6$, $W_w = 0.435$, (c) H_c vs W_c (with $H_b = 0.6$, $W_w = 0.435$), (d) H_b vs W_w (with $H_c = 0.1$, $W_c = 0.325$).)

6.5.5 Multi-Objective Pareto Analysis

In the previous sub-sections, single-objective optimisation was carried out to find the robust design objective less effective by input variation. In this section, Multi-objective robust design is presented to provide a compromise between the objectives. In order to determine a solution that is the robust, feasible and optimal design. Thus, a trade off between a feasible, optimal, and robust design is required. three scenarios are used in the literature based on designer need :

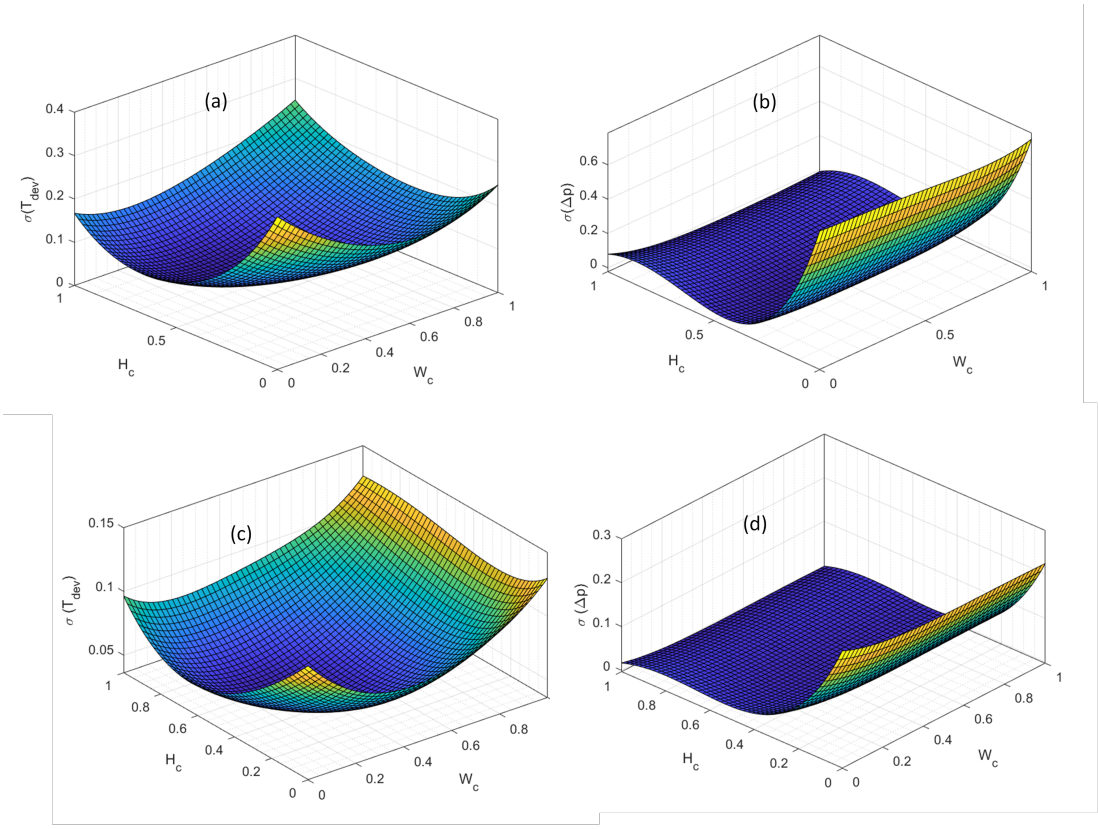

Figure 6.12: Typical surrogate model surfaces of $\sigma(\Delta p)$ and $\sigma(T_{dev}$ as a function of H_c vs W_c at ($\sigma_{in} = 0.05$ and 0.1).

the first technique is the **importance between optimal design and robust design is equal**. while the second approach is **Optimal design is primary and robust design is secondary** In this approach the problem is solved for optimal design first then the final solution is obtained from the Pareto optimal set based on the robustness design. The third **optimal design criteria is Robust design is primary and optimal design is secondary** in this approach the final solution is chosen from the most robust solutions based on the values of the objective functions (Wang et al., 2012). In the current work the second approach was adopted . The NN method was used to create Pareto curves of non-dominated deterministic solutions for Δp vs T_{dev}, and compromise solutions of robustness design expressed by Pareto curves at ($\sigma_{in} = 0.05$) and ($\sigma_{in} = 0.1$). for Δp vs T_{dev},

Objective	Target	W_c(mm)	H_c (mm)	H_b(mm)	W_w (mm)	$T_{dev}(K)$	$\Delta p(Pa)$
Globalmin.	minimise T_{dev}	0.150	0.050	0.400	0.727	12.864	1426.464
Globalmin.	minimise Δp	0.500	0.150	0.799	0.799	19.684	49.782

Table 6.5: Single objective optimisation.

Objective	Target	W_c(mm)	H_c (mm)	H_b(mm)	W_w (mm)	$T_{dev}(K)$	$\Delta p(Pa)$
Robustness.	minimise $\sigma(T_{dev})$	0.275	0.106	0.551	0.583	14.958	158.96
Robustness.	minimise $\sigma(\Delta p)$	0.4045	0.1407	0.7129	0.1818	22.939	64.935

Table 6.6: Robustness design at 5% i.e $\sigma = 0.05$

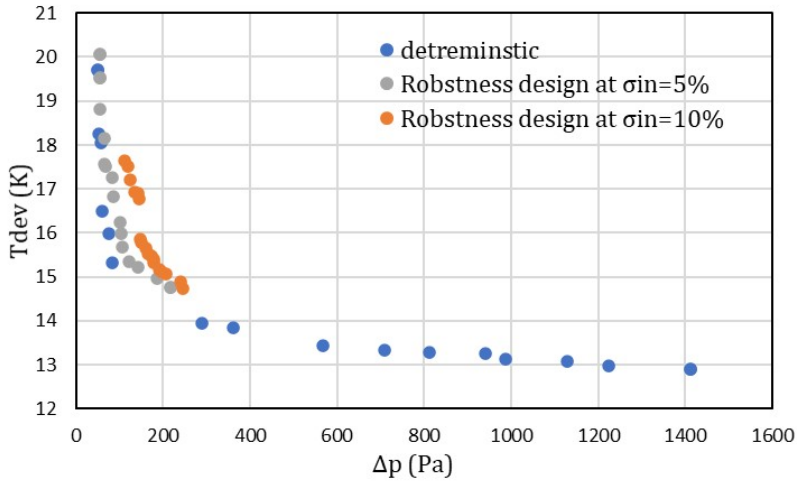

Figure 6.13: Typical surrogate model surfaces of $\sigma(\Delta p)$ as a function of H_c vs W_c.

6.6 Conclusion

A three dimensional numerical model of microchannel PCR was developed and validated for deterministic optimisation. The deterministic optimisation was concentrated in obtaining the global optimal design and global Pareto-optimal frontier, representing the best possible compromise solution between the objectives. However, in practice, the design requirements could be interested in obtaining robust solutions. This solution is, less sensitive to small changes in input variables. for this purpose an uncertainty analysis is carried out to demonstrate the effect of uncertainties of input variables on the output objectives. The proposed N.N approach are compared with MLSM and with true values of CFD response

Objective	Target	W_c(mm)	H_c (mm)	H_b(mm)	W_w (mm)	$T_{dev}(K)$	$\Delta p(Pa)$
Robustness.	minimise $\sigma(T_{dev})$	0.1500	0.1500	0.4651	0.2592	15.801	144.458
Robustness.	minimise $\sigma(\Delta p)$	0.4764	0.1117	0.6390	0.4333	19.789	107.489

Table 6.7: Robustness design at 10% i.e $\sigma = 0.1$.

at $\sigma_{in} = 0$ which shows good agreements. The probabilistic design was examined for each of the design variables considering the uncertainty in the input variables. These sensitivities were $0.05 - 0.1$ the critical parameters affect the output,i.e at which the output quantities are highly sensitive which were identified as W_c and H_c. For robust design optimisation (RDO) the results show that the competing is between the output deviations $\sigma(T_{dev})$ and $\sigma(\Delta p)$ and also the robustness design points are not the same as deterministic optimum points. A Pareto front of robust design optimisation (RDO) optimization approach was created to provide a compromise solutions for the designer depend on the uncertainty quantification ($\sigma = 0$, $\sigma = 0.05$ and $\sigma = 0.1$). The Pareto front of multi-objective solutions demonstrate that the robust optimisation Pareto front is slightly shifted from that of the deterministic solution, and this shift increases with increasing uncertainty in the input design variables. Hence in the presence of uncertainty the deterministic Pareto front is not useful and its solution is restricted.

Chapter 7

Discussion and Conclusions

7.1 Introduction

This thesis is concerned with the thermo-flow design and robust optimisation of fluidic channels used in Polymerase Chain Reaction (PCR) systems which have revolutionised biological research (Cui and Wang, 2019). Recently these have been applied in rapid diagnostic systems for bacterial species leading to e.g. infectious diseases, or for the rapid and accurate detection of bacterial species causing micro-biologically induced corrosion in oil and gas production systems. The main focus of this PhD was to explore the effect of geometry, material and flow variables on the temperature uniformity, pressure drop and heating power requirements in a prototype PCR thermal system. Optimisation of geometrical and operating design variables was used to form practical design recommendations. A robust optimisation approach was also developed to predict the uncertainty in the design configuration of PCR systems. As explained in Chapters 1 and 2 early PCR systems used time-consuming devices involving wells where the whole chip is heated up and cooled down during each thermal stage. These were superseded by Continuous Flow PCR (CFPCR) devices, introduced first by (Kopp et al., 1998), based on single-phase flow in a serpentine fluidic channel of rectangular cross-section with three temperature stages in a glass substrate supported by three independent copper block heaters. Controlling the residence times in the denaturation, annealing and extension zones is crucial since insufficient dwell times in each thermal state can seriously degrade DNA amplification efficiency.

The literature review of PCR systems shows that little attention has been paid to the critical analysis of the thermal flow in PCR systems. The literature review demonstrates that there remains ample scope for CFPCR device optimisation

The need for effective design presents a complex multi-objective optimisation problem with several competing objectives, constraints and design variables. Key objectives include the minimisation of total processing time and heating power requirements, and the maximisation of temperature uniformity and DNA amplification efficiency. There are also important structural constraints on the pressure drop that can be supported by a PCR chip, while the drive towards device miniaturisation constrains the spacing between fluidic channels. These are all influenced by design variables such as flow speeds, fluid and chip thermal properties, the heating arrangements used, fluidic channel and chip dimensions, their channel shape and the distances between the thermal zones. The present study proposes a novel Computational Fluid Dynamics (CFD)-enabled optimisation methodology which enables the trade-offs between competing objectives of temperature uniformity, pressure drop and heating power consumption to be explored. This allows designers to maximise the proportion of PCR liquid that experiences the target temperature range for the required time period in each zone, to preserve the structural integrity of the CFPCR chip or to minimise the time is taken or overall power consumption (heating and hydraulic) throughout thermal cycling.

7.2 Discussion

The discussion of this study is divided into two-four parts: a one dimensional PCR model, a three dimensional PCR model, optimisation of PCR and robust optimisation of PCR.

7.2.1 Three-dimensional heat transfer model of PCR systems

A fully coupled conjugate heat transfer model for the three-dimensional flow and heat transfer was developed and solved numerically using COMSOL Multiphysics

V5.4 ®. The effect of grid density was examined by obtaining numerical solutions on a series of structured Finite Element grids of increasing refinement, confirming the grid Independence of the results.

The numerical model was first compared with the experimental results (Duryodhan et al., 2016) for thermal flow in diverging channels. The comparison showed that the agreement between the experimental and numerical results was generally very good. The next comparison was with the numerical results of (Chen et al., 2008) where $H_c = 150\mu m$, $W_c = 50\mu m$, $S = 1mm$, $V_{ch} = 6mm/s$ and $T_{f,in} = 72°C$. Once again the numerical predictions of the temperature profile along the three temperature zones, the comparison results, were in very good agreement with the published results.

7.2.2 One dimensional model

Predictions of the 1-D model (3.57) were compared with those of the 3-D conjugate heat transfer model, for the thermal conditions specified in the denaturation zone. The results showed that for the case with V_{ch}=4mm/s and zero substrate thickness, $H_b = 0\mu m$, the agreement is excellent. However, for cases with larger values of H_b, the discrepancy between the models is much more significant due to the thermal resistance of the substrate. More generally, it is found that the 1-D model works well provided the conductive thermal resistance, defined by $R_{th} = H_b/k_s$, is small. This cannot be neglected for cases considered below, with larger substrate thicknesses, and for which full 3-D simulations are required.

7.2.3 Effect of system parameters

Effect of substrate material The effect of substrate material on the temperature profile was examined, for flow in a channel with dimensions: $H_c = 150\mu m$, $W_c = 500\mu m$, $H_b = 850\mu m$, $W_w = 50\mu m$, $H_h = 2000\mu m$, $H_{PMMA} = 1500\mu m$ and $S = 1mm$ (i.e one topology). The effects of the different materials (Polyimide, PMMA, PDMS, Polyethylene, Glass and Silicon) on the fluid temperature profile were examined at the low inlet flow velocity $V_{ch} = 0.1mm/s$. The obtained results showed that fluid temperatures in these cases are reasonably uniform for all materials, with the fluid temperature for glass and silicon chips being closest to

the target temperatures in the zones while that for the polyimide chip is furthest from the target profile. The size of the deviations from the target temperature profiles generally decreases as the thermal conductivity of the chip material increases due to the smaller thermal resistance between the heated substrate and the flowing liquid.

Effect of inlet velocity The effect of increasing the inlet velocity V_{ch} on the temperature profile was examined using glass as the substrate material. The results showed how the temperature variation T_{dev} in glass chips is affected by channel inlet velocity V_{ch} and showed the deviations from the target temperature increase as the inlet flow velocity increases and showed that the temperature profile throughout the three PCR zones is very different from the target profile at the higher speeds due to convective heat transfer becomes more significant at the higher speed. This was confirmed by examining the value of the Peclet number P_e which indicates the relative importance of convection to conduction.

The effects of the different materials Polyimide, PMMA, PDMS, Polyethylene, Glass and Silicon at different velocity on the temperature profile was examined. Firstly, the effect of increasing the inlet velocity to $V_{ch} = 1mm/s$. This leads to greater discrepancies from the target temperatures in each zone since convective heat transfer becomes more significant at a higher speed. Then, the deviations from the target temperature profile decrease as thermal conductivity increases. The effect of material and inlet flow velocity on the deviations from the target temperatures, and quantifies the monotonic increases in T_{dev} as V_{ch} increases and thermal conductivity decreases, due to the increased convection and thermal resistance respectively. Since $Pe > 1$ convection is influential in all cases and temperature variations along with the channel result from the competition between convection, which acts to increase them, and conduction, which acts to reduce them. Lower axial conduction for the particular case of PMMA at V_{ch}=1mm/s may explain why its $T_{dev} = 40.336$ is greater than $T_{dev} = 38.309$ for glass at the much higher velocity V_{ch}=6mm/s.

Heating power consumption The effects of geometrical and operating parameters on heating power were considered and the investigation results showed that the heating power consumption increases as the velocity increases and that

the comparatively high thermal conductivity of silicon leads to at least an order of magnitude larger heating power requirement.

The results showed that T_{dev} is influenced by the competition between convection and axial conduction that results from the material type, flow rate and channel size. In practice, there are also other competing objectives that need to be considered, such as the need to minimise the pressure drop as well as the heating power consumption. This motivated the development and application of optimisation methods in this thesis.

7.2.4 Optimisation

The PCR microchannel system was parametrised into four design variables which are channel width W_c, channel height H_c, substrate thicknessH_b and spacing between channelsW_w.

The optimisation was conducted to explore the geometrical parameters so the effect of channel size on the pressure drop Δp and temperature deviation T_{dev} was examined by varying the channel dimensions, W_c, H_c,H_b and W_w. The results showed that the Pressure drop Δp is effectively independent of H_b and W_w and depends only on the W_c and H_c through a strong dependence on channel cross-sectional area, $W_c \times H_c$. In contrast, T_{dev} also depends on H_b through its influence on the substrate thermal resistance. As H_b increases, conduction into the liquid decreases leading to larger temperature variations. These findings were matched with surrogate model surfaces.

7.2.5 Single objective optimisation

Each objective was optimised in isolation, this was obtained by examining the surrogate models of each individual objective. It was noted that the minimum value of T_{dev} corresponds to comparatively large values of Δp and Q_t, whereas the minimum Δp corresponds to comparatively large T_{dev} and Q_t. This demonstrates that it is interesting to explore the trade-off between the objective functions through a multi-objective analysis.

7.2.6 Multi-Objective Pareto Analysis

The RBF and NN methods were used to create Pareto curves of non-dominated solutions for Δp vs T_{dev}, Δp vs Q_t and T_{dev} vs Q_t. The RBF method uses the Multi-Objective Genetic Algorithm (MOGA) solver in MATLAB, whereas the NN methods use the SciPy.optimization module in Python based on a simple weighting between the competing objectives. The Pareto curves from the RBF and NN meta-modelling were all very similar to each other. The accuracy of Pareto front was confirmed by the further validation with the CFD predictions. The Pareto curves from the RBF and NN meta-modelling were all very similar to each other - the Pareto curves for Δp vs T_{dev} provide a basis for finding an appropriate balance between these competing objectives. It showed, for example, that reducing T_{dev} from 14 to 13 would require a four-fold increase of Δp, from 250 to $1000Pa$, while reducing Δp below $100Pa$ comes at the price of a sharp rise in T_{dev}.

7.3 Robust design optimisation

After exploring the deterministic optimization, probabilistic optimization was conducted using robust optimisation based on the surrogate modelling. The uncertainty quantification UQ was used to predict the design variables that minimise the objective function and restricting the standard deviation of these objectives to a prescribed value. This takes into account uncertainties in the geometric variables, thus resulting in a robust design. In this design the input variables W_c, H_c, H_b and W_w were specified as uncertain variable with a given σ and mean value for each variables. Then Monte Carlo Simulation (MCS) was used to propagate the uncertainty by randomly generating points for each design evaluation about 10^5 considering σ of each point. The output functions (objective) in RDO include the mean μ and standard deviation σ of stochastic responses. in the early stage of this design, six design points were are specified as the uncertain variable with a given σ and mean value for each variable then Monte Carlo Simulation (MCS) was used to propagate the uncertainty approximately (10^5) and the output of the objective functions are evaluated at these points using surrogate model (ANN).

The results of the evaluated points in terms of mean μ and standard deviation σ for the output are depicted in Figure6.6. It can be noted from Figures 6.6(c) and (e) that point 4 has minimum sensitive variation and to uncertainty and minimum μ but is has a high variation for uncertainty for T_{dev} Figures 6.6. Also,o it can be noted from Figures 6.6 (d) and (f) that the minimum T_{dev} can be specified at point 1 but design the point 2 has a minimum variation that means the minimum robust point tends to be shifted from point 1 to point 2. The robust design of T_{dev} is the trade-off between point 1 and point 2. The example above was just to clarify the process of robust design. The probabilistic design was examined for each of the design variables considering the uncertainty in the input variables. These sensitivities were $0.05 - 0.1$ the critical parameters affect the output, i.e at which the output quantities are highly sensitive which was identified as W_c and H_c. For robust design optimisation (RDO) the results show that the competing is between the output deviations $\sigma(T_{dev})$ and $\sigma(\Delta p)$ and also the robust design points are not the same of deterministic optimum points. A Pareto front of robust design optimisation (RDO) optimization approach was created to provide a compromise solutions for the designer depend on the uncertainty quantification ($\sigma = 0$, $\sigma = 0.05$ and $\sigma = 0.1$).

7.4 Conclusion

This thesis proposes the first CFD-enabled optimisation methodology for thermal flow in PCR systems, accounting for temperature uniformity, pressure losses and heating power requirements. Results have shown that temperature variations in the PCR liquid along zones are determined by the competition between convection and conduction in the vertical and axial directions, with the former acting to exacerbate temperature variations and the latter to reduce them. The temperature variations are a nonlinear function of flow rate, channel size, substrate material thermal properties and substrate dimensions. Generally, reducing both the flow rate, which reduces convection, and substrate thermal resistance, $R_{th} = H_b/k_s$, which increases conduction into the liquid, decreases temperature deviations along a channel. The values of the Peclet and axial conduction numbers can provide further, valuable insight into the relative importance of convection

and conduction and their influence on temperature uniformity. The dependence of pressure drop and heating power on design variables is much simpler. The former only depends on the channel sizes, W_c and H_c, and increases rapidly as channel cross-sectional area $W_c \times H_c$ decreases, whereas heating power requirements depend mainly on the substrate thermal conductivity, with results showing those for silicon being an order of magnitude larger than for the other materials considered. If obtaining high levels of temperature uniformity is the key consideration then it is possible to choose a substrate with high conductivity, small substrate thickness and small channel area. However, since there are often important structural constraints on the pressure drop that can be supported by a PCR chip, then it would be necessary to choose a larger channel area to reduce pressure drop. This study has shown that a multi-objective optimisation methodology can provide the information designers need to make these decisions in a scientifically rigorous manner. Pareto curves from the multi-objective optimisation methodology demonstrate clearly the compromises that can be struck between temperature uniformity, pressure drop and heating power throughout the three zones. For example, these have quantified the price that must be paid in terms of increased pressure drop and heating power in order to get high-temperature uniformity in the zones. , Besides the deterministic optimisation discussed above in which the input variables are assumed to be deterministic, A framework was developed for probabilistic optimisation in which the uncertain inputs was evaluated using UQ and Monte Carlo numerical simulation. The critical input parameters at which the objective (output) are more sensitive were determined and they were (W_c) and (H_c).

7.5 Recommendations for Future Works

From the achievements of the present thesis, the major extended works for the future study are recommended and outlined as follows:

1. The present thesis was focused on numerical analysis and optimisation of PCR systems using single-phase liquid-water. The experimental work has

been severely restricted by COVID and has had to have much less prominence. Experimental work validation of the numerical results of this thesis should be considered in future work.

2. The investigation of the operating boundary conditions was conducted in this work. However further analysis and optimisation need to be carried based on changing the operating boundary conditions.

3. The proposed optimisation framework of robust design optimisation can be extended to include reliability-based optimisation in future work.

4. The robust optimisation was conducted using Monte Carlo numerical simulation, however, this method needs a large number of iteration so for future work using Polynomial Chaos Expansion (PCE) and Gaussian process model would need.

5. The proposed optimisation framework is generic and can be extended to account for other practical objectives, such as the DNA amplification achieved throughout the PCR zones.

6. The optimisation work can be extended to explore the performance of alternative PCR microfluidic system design topologies to be carried out to establish robust optimisation with high accuracy and less time.

7. The move towards droplet-based PCR is very important and numerical and experimental work of PCR based droplet should be investigated.

8. Considering the uncertainty in the input variables along the channel leads to fluctuation in the design product. However, if we consider this variable according to linear variation, it could result in convergent or divergent channel, this can be considered in future work.

Appendix A

Examples of FEM implementation

In order to to fully understand the numerical methodology of approximating PDE's solutions, it is important to start with a simple problems that can be solved easily and then it can be extended to more complex problems. For this purpose a basic problem under is considered here which is to solve the conduction heat transfer from homogeneous metal wire of length L with a constant cross section area A as in Pepper and Heinrich (2017). The left end is assumed to expose to a prescribed heat flux, q, and the right end is held at a constant temperature $T = T_L$, and over length of the rod insulation material is mounted the rod as shown in Figure A.1.

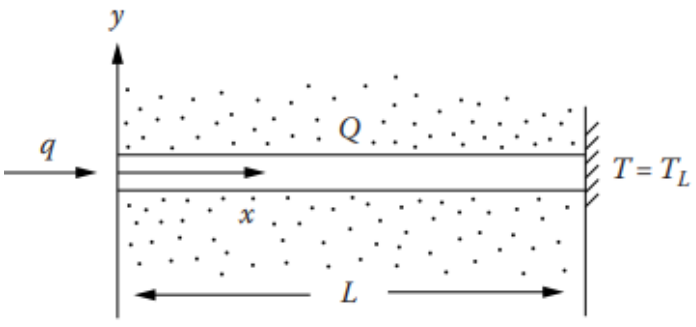

Figure A.1: Conduction of heat in a rod of length L(Pepper and Heinrich, 2017)

The differential equation that governs the distribution of temperature across the rod can be represented by Fourier's law as:

$$-k\frac{\partial T}{\partial x} - k\frac{\partial^2 T}{\partial x^2} = Q, \quad 0 < x < L \tag{A.1}$$

where x represents the length coordinate k represents the thermal conductivity of the material (assumed constant) Q represents the internal heat generation per unit volume. The boundary conditions associated with the problem are:

$$-k\frac{\partial T}{\partial x} - k\frac{\partial^2 T}{\partial x^2} = Q, \quad atx = 0 \tag{A.2}$$

$$T = T_L, \quad at \quad x = L \tag{A.3}$$

The exact solution to Equation A.1 with boundary conditions A.2 for constant Q , is:

$$T(x) = T_L + \frac{q}{k}(L - x) + \frac{Q}{2k}(L^2 - x^2) \tag{A.4}$$

The approximate solution of temperature distribution of of Equation A.1 can be reached using appropriate shape functions of the independent variable x, denoted by $\phi(x)$, and corresponding unknown parameters α_j. $T(x)$ can be denoted over the whole domain $0 \leq x \leq l$, as:

$$T(x) = \alpha_1\phi_1(x) + \alpha_2\phi_2(x) + \ldots + \alpha_n\phi_n(x) \tag{A.5}$$

where $\phi(x)$ is named shape function. Equation A.5 can be expressed in summation form as:

$$T(x) = \sum_{i=1}^{n+1} \alpha\phi_i(x) \tag{A.6}$$

The residual error can be defined as:

$$R(T, x) = -k\frac{\partial^2 T}{\partial x^2} - Q \quad , 0 < x < L \tag{A.7}$$

where T is the approximation to the true solution.

The idea of the weighted residuals method is based on multiply the residual by a weighting function and force the integral of the weighted expression to vanish, that is

$$\int_0^L W(x)R(T,x)dx = 0 \tag{A.8}$$

Here $W(x)$ is the weighting function. Using different weighting functions and and replacing each of them in Equation A.8, then a set of linear equations can be created in the unknown parameters α which can be used to find an approximation of T in the form of the finite series given in Equation A.6. The type of the selected weighting function depends on the type of chosen method of weighted residual. In this example the weights are set equal to the shape functions $\phi(x)$, based on the Galerkin procedure as:

$$W_i(x) = \phi_i(x) \tag{A.9}$$

and since the number of unknown parameters α_j is equal to the number of shape functions ϕ_j , a system of linear algebraic equations with the same number of equations as unknowns will be generated. The left-hand side integrals in Equation A.8 can be determined using shape functions $\phi(x)$ as weights $W(x)$. Hence, the Galerkin procedure gives:

$$\int_0^L \phi(x)\Big[- k\frac{d^2T}{dx^2} - Q\Big]dx \tag{A.10}$$

Integration by parts can be applied to the second derivative term in Equation A.10, that is give:

$$\int_0^L \phi(x)\Big[- k\frac{d^2T}{dx^2}\Big]dx = \int_0^L \phi(x)k\frac{d\phi}{dx}\frac{dT}{dx}dx - k\phi\frac{dt}{dx}\Big|_0^L \tag{A.11}$$

Thus Equation A.10 can be expressed as :

$$\int_0^L k\frac{d\phi}{dx}\frac{dT}{dx}dx - \int_0^L \phi\, Q\, dx - k\phi\frac{dT}{dx}\Big|_0^L = 0 \tag{A.12}$$

Applying equation A.6 for each weighting function $\phi(x)$ Equation A.12 can be expressed as:

$$\sum_{j=1}^{n+1} k\Big[\int_0^L \frac{d\phi_i}{dx}\frac{d\phi_j}{dx}dx\Big]\alpha_j - \int_0^L \phi_i\, Q\, dx + k + \phi_i\Big[- k\frac{dT}{dx}\Big]\Big|_{x=0}^{x=L} = 0 \tag{A.13}$$

The variation of $\phi(x)$ between nodes over each element is assumed linear,thus, the dependent variable T can be expressed using Equation over one element with two nodes.

$$T(x) = \phi_i(x)\alpha_i + \phi_{i+1}\alpha_{i+1} \quad x_i \leq x \leq x_{i+1} \tag{A.14}$$

Here $\phi(x_i) = 1$ and $\phi(x_{i+1}) = 0$ and vice versa $\phi_{i+1}(x_i) = 0$ and $\phi_{i+1}(x_i + 1) = 1$

$$\begin{aligned}
\sum_{j=1}^{2} k\left[\int_0^{L/2} \frac{d\phi_1}{dx}\frac{d\phi_j}{dx}dx\right]\alpha_j - \int_0^{L/2} \phi_1(x)\, Q\, dx - k\phi_1(x)\frac{dT}{dx}\Big|_{x=0}^{x=L/2} &= 0 \\
\sum_{j=1}^{2} k\left[\int_0^{L/2} \frac{d\phi_2}{dx}\frac{d\phi_j}{dx}dx\right]\alpha_j - \int_0^{L/2} \phi_2(x)\, Q\, dx - k\phi_2(x)\frac{dT}{dx}\Big|_{x=0}^{x=L/2} &= 0
\end{aligned} \tag{A.15}$$

$$k\left[\int_0^{L/2} \frac{d}{dx}\phi\right]\left[\frac{d}{dx}\right]dx\alpha - Q\int_0^{L/2} \phi^T dx - \begin{bmatrix} q \\ 0 \end{bmatrix} = 0 \tag{A.16}$$

BY replacing $\phi = \begin{bmatrix} 1 - \frac{2x}{L} & \frac{2x}{L} \end{bmatrix}$ and $\frac{d}{dx}\phi = \begin{bmatrix} -\frac{2}{L} & \frac{2}{L} \end{bmatrix}$ and integrating Equation A.16 to get :

$$\frac{2k}{L}\begin{bmatrix} 1 & -1 \\ -1 & 1 \end{bmatrix}\begin{bmatrix} \alpha_1 \\ \alpha_2 \end{bmatrix} - \frac{QL}{4} - \frac{1}{1} - \begin{bmatrix} q \\ 0 \end{bmatrix} = \begin{bmatrix} 0 \\ 0 \end{bmatrix} \tag{A.17}$$

Similar procedure can be applied for element 2 to obtain :

$$\frac{2k}{L}\begin{bmatrix} 1 & -1 \\ -1 & 1 \end{bmatrix}\begin{bmatrix} \alpha_1 \\ \alpha_2 \end{bmatrix} - \frac{QL}{4} - \frac{1}{1} - \begin{bmatrix} 0 \\ 0 \end{bmatrix} = \begin{bmatrix} 0 \\ 0 \end{bmatrix} \tag{A.18}$$

Then assembly process is started in which Equations A.17 and A.19 are combined together since they have the weighting function $\phi_2(x)$ to get :

$$\frac{2k}{L}\begin{bmatrix} 1 & -1 & 0 \\ -1 & 2 & -1 \\ 0 & -1 & 1 \end{bmatrix}\begin{bmatrix} \alpha_1 \\ \alpha_2 \\ \alpha_3 \end{bmatrix} = \begin{bmatrix} q \\ 0 \\ 0 \end{bmatrix} + \frac{QL}{4}\begin{bmatrix} 1 \\ 2 \\ 1 \end{bmatrix} \tag{A.19}$$

$\alpha_3 = T_L$ is given hence, two equations with two unknowns α_1 α_2 can be solved to get:

$$\begin{aligned}
\alpha_1 &= \frac{qL}{k} + \frac{QL^2}{2k} + T_L \\
\alpha_2 &= \frac{qL}{2k} + \frac{3QL^2}{8k} + T_L
\end{aligned} \tag{A.20}$$

In the next example the Partial differential equation represents steady advection-diffusion phenomena can be described as:

$$u\frac{\partial T}{\partial x} - k\frac{\partial^2 T}{\partial x^2} = Q \quad , 0 < x < L \tag{A.21}$$

$$u\frac{\partial T}{\partial x} - k\frac{\partial^2 T}{\partial x^2} = f(x, y, z) \tag{A.22}$$

where (x, y, z) are the independent variables while T , u and f are dependent variables. An ordinary differential equation is a differential equation expressed in terms of the derivatives of one independent variable (Zill, 2012). Thus , in one dimensional the above partial differential equation is converted to ordinary differential equation expresses steady advection-diffusion phenomena which is solved in this section to explain the basic concept steps of finite element analysis.

$$u\frac{dT}{dx} - k\frac{d^2 T}{dx^2} = f \tag{A.23}$$

Here u and k denote the known which are constant velocity and diffusivity, respectively also f represents the known source function. While T is the scalar dependent variable unknown.

The finite element solution procedure described above is adopted to solve Equation A.23 , thus , the domain is divided to a number of element as shown in Figure A.2

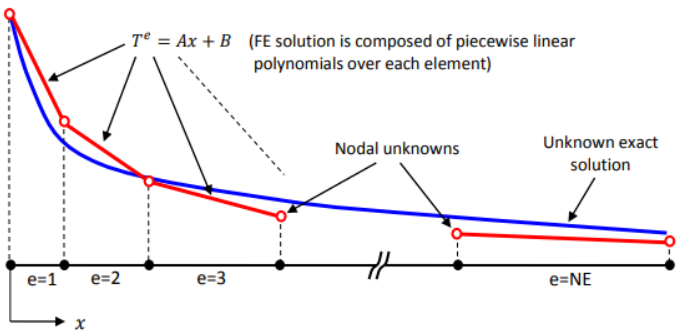

Figure A.2: Typical first order continuous approximate solution over a 1D domain with linear elements

It can be noted from Figure A.2, the approximations over the elements are linear. The overall solution is C^0 continuous, i.e. the solution itself is continuous at element interfaces, but not its first derivative.

In order to find FE approximate solutions over each element, the unknown values, shown with red circles in Figure need to be computed at the nodes of the mesh. For this task linear algebraic equations need to be obtained. The differential equation presented in equation A.23, together with appropriate boundary conditions, is known as the strong form of the problem. The weighted residual is type numerical solution method in FE approach that enables use of the weak form of the problem. The weak form can be obtained by different method for example Method of Weighted Residuals (MWR) of differential equation is used to obtain the weak form, as:

$$R(x) = u\frac{dT}{dx} - k\frac{d^2T}{dx^2} - f \tag{A.24}$$

This Residual needs to be minimised as much as possible in order to obtain accurate results. In weighted residual technique , this minimisation is ac hived by using the following weighted integral method:

$$\int_\Omega w(x)R(x)d\Omega = 0 \tag{A.25}$$

$$\int_\Omega \left(wu\frac{dT}{dx} - wk\frac{d^2T}{dx^2} - wf\right)dx = 0 \tag{A.26}$$

where Ω is the computational domain. Due to equation A.24 includes second order differential equation and approximations over elements are only first order, thus special care need to be paid for this point. Integration by parts is applied to the second order derivatives in the second part of equation A.26. It can be noted the differentiation order of the unknown is reduced T from 2 to 1 and the differentiation order of the weight function is increased from 0 to 1.

$$\int_\Omega -wk\frac{d^2T}{dx}dx = \int_\Omega k\frac{dw}{dx}\frac{dT}{dx}dx - \int_\Gamma wk\frac{dT}{dx}n_x d\Gamma \tag{A.27}$$

where Γ is the boundary of the domain with its unit outward normal being n_x. By Substituting Equation A.27 into A.26, the following expression is obtained

$$\int_{\Omega}\left(wu\frac{dT}{dx}+k\frac{dw}{dx}+k\frac{dw}{dx}\frac{dT}{dx}\right)dx=\int_{\Omega}wfdx+\int_{\Gamma}wk\frac{dT}{dx}n_xd\Gamma \tag{A.28}$$

Note that the second term on RHS includes $k\frac{dT}{dx}$, which is equal to heat flux with a minus sign in front. Heat flux is a kind of natural (or Neumann) boundary condition (NBC) and automatic inclusion of NBC in the system is an advantage of FEM. The next step is to write the equations in terms of approximations over nodes.

$$T^h(x)=\sum_{j=1}^{n}T_jS_j \tag{A.29}$$

where T^h is the desired approximate solution , n is the number of nodes in the domain, $T_j's$ are the nodal unknowns and $S_j's$ are the user selected shape functions. The desired approximate solution A.29can be substitute into weak form Equation A.28 to get:

$$\int_{\Omega}\left[wu\Big(\sum_{j=1}^{NN}T_j\frac{dS_j}{dx}\Big)+k\frac{dw}{dx}\Big((\sum_{j=1}\frac{dS_j}{dx}\Big)\right]dx=\int_{\Omega}wfdx-\int_{\Gamma}wq_nd\Gamma \tag{A.30}$$

One of the most important aspects in an FEM is the selection of weight functions. In Galerkin FEM, the weight functions are selected to be the same as shape functions. Since there are n shape functions, there are n different selections for weight function and this leads to n different equations that can be used to solve for n nodal unknowns. It is possible to represent these set of equations in matrix form as:

$$[K]U=F+B \tag{A.31}$$

where $[K]$ is the stiffness matrix, is the nodal unknown vector, F is the force vector and B is the so called boundary integral vector, given as follows

$$\begin{aligned}\int_{\Omega}\left(S_ju\frac{dS_j}{dx}+k\frac{dS_i}{dx}\frac{dS_j}{dx}\right)dx\\ F_i=\int_{\Omega}S_ifdx\\ Bi=\int_{\Gamma}S_iq_nd\Gamma\end{aligned} \tag{A.32}$$

Values of NN nodal unknowns are found by solving this system of equations. Then the global system can be formed by assembling each element refer to Sert (2020).

Bibliography

Al–Hashmi, S., Heggs, P. and Dixon-Hardy, D., 2015. Design, fabrication and test a new hybrid parabolic dish concentrator with stirling engine & pcm-storage in oman.

Al–Neama, A.F., Kapur, N., Summers, J. and Thompson, H.M., 2017. An experimental and numerical investigation of the use of liquid flow in serpentine microchannels for microelectronics cooling. *Applied Thermal Engineering*, **116**, pp.709–723.

Al–Neama, A.F.M., 2018. *Serpentine minichannel liquid-cooled heat sinks for electronics cooling applications*. PhD thesis. University of Leeds.

Acar, E., 2010. Optimizing the shape parameters of radial basis functions: an application to automobile crashworthiness. *Proceedings of the Institution of Mechanical Engineers, Part D: Journal of Automobile Engineering*, **224**(12), pp.1541–1553.

Afework, B., Hanania, J., Stenhouse, K. and Donev, J., 2020. *Thermal conductivity* [Online]. Calgary: University of Calgary. Available from: https://energyeducation.ca/encyclopedia/Thermal_conductivity [Accessed 13 January 2021].

Agarwal, G., Kazior, T., Kenny, T. and Weinstein, D., 2017. Modeling and analysis for thermal management in gallium nitride HEMTs using microfluidic cooling. *Journal of Electronic Packaging*, **139**(1).

Agrawal, A. and Lal, B., 2009. Rapid detection and quantification of bisulfite reductase genes in oil field samples using real-time PCR. *FEMS Microbiology Ecology*, **69**(2), pp.301–312.

Agrawal, N. and Ugaz, V.M., 2007. A buoyancy-driven compact thermocycler for rapid pcr. *Clinics in laboratory medicine*, **27**(1), pp.215–223.

Ahrberg, C.D., Manz, A. and Chung, B.G., 2016. Polymerase chain reaction in microfluidic devices. *Lab on a Chip*, **16**(20), pp.3866–3884.

Ahsan, A., 2011. *Convection and conduction heat transfer*. BoD–Books on Demand.

Allen, J.W., Kenward, M. and Dorfman, K.D., 2009. Coupled flow and reaction during natural convection pcr. *Microfluidics and Nanofluidics*, **6**(1), pp.121–130.

Almeida, J.P., Oliveira, J.F. and Pinto, A.A., 2015. *Operational research: io 2013-xvi congress of apdio, bragança, portugal, june 3-5, 2013*. Vol. 4. Springer.

Arpaci, V.S., 1966. Conduction heat transfer. *1966, 550 &. ADDISON-WESLEY PUBLISHING CO., READING, MASS.*

Aziz, I., Jamshaid, R., Zaidiand, T. and Akhtar, I., 2016. Numerical simulation of heat transfer to optimize DNA amplification in polymerase chain reaction. *2016 13th international bhurban conference on applied sciences and technology (ibcast)*. IEEE, pp.456–462.

Azmi, A.Z., 2010. *Finite element solution of heat conduction problem*. PhD thesis. Universiti Teknologi Malaysia.

Baco, S.B., Oprime, P.C., Campanini, L. and Ganga, G.M.D., 2019. Design of experiments used in computer trials: a supportive method for product development. *Pesquisa Operacional*, **39**(2), pp.295–316.

Batchelor, C.K. and Batchelor, G., 2000. *An introduction to fluid dynamics*. Cambridge university press.

Bates, S., Sienz, J. and Toropov, V., 2004. Formulation of the optimal latin hypercube design of experiments using a permutation genetic algorithm. *45th aiaa/asme/asce/ahs/asc structures, structural dynamics & materials conference*, p.2011.

Belgrader, P., Devaney, J.M., Del Rio, S.A., Turner, K.A., Weaver, K.R. and Marino, M.A., 1996. Automated polymerase chain reaction product sample preparation for capillary electrophoresis analysis. *Journal of Chromatography B: Biomedical Sciences and Applications*, **683**(1), pp.109–114.

Bell, S.A., 2001. A beginner's guide to uncertainty of measurement.

Bergman, T.L., Incropera, F.P., DeWitt, D.P. and Lavine, A.S., 2011. *Fundamentals of heat and mass transfer*. John Wiley & Sons.

BIPM, I., IFCC, I. and Iupac, I., 2008. Evaluation of measurement data-supplement 1 to the'guide to the expression of uncertainty in measurement. *Propagation of Distributions Using a Monte Carlo Method*.

Blazek, J., 2015. *Computational fluid dynamics: principles and applications*. Butterworth-Heinemann.

Bodla, K.K., Murthy, J.Y. and Garimella, S.V., 2013. Optimization under uncertainty applied to heat sink design. *Journal of Heat Transfer*, **135**(1).

Bonte, M.H.A., 2007. *Optimisation strategies for metal forming processes*.

Cao, Q., Kim, M.-C. and Klapperich, C., 2011. Plastic microfluidic chip for continuous-flow polymerase chain reaction: simulations and experiments. *Biotechnology Journal*, **6**(2), pp.177–184.

Cavazzuti, M., 2012. *Optimization methods: from theory to design scientific and technological aspects in mechanics*. Springer Science & Business Media.

Cavazzuti, M., 2013. Deterministic optimization. *Optimization methods*. Springer, pp.77–102.

Cengel, Y. and Heat, T.M., 2003. *A practical approach*. New York, NY, USA: McGraw-Hill.

Cengel, Y., 2014. *Heat and mass transfer: fundamentals and applications*. 5th ed. New York: McGraw-Hill Higher Education.

Cengel, Y., Cimbala, J. and Solutions, C.C., 2004. Mechanics: fundamentals and applications cengel... *MECHANICS*, **11**, p.22.

Cengel, Y.A. and Ghajar, A.J., 2007. *Heat and mass transfer*.

Çengel, Y.A., Turner, R.H., Cimbala, J.M. and Kanoglu, M., 2008. *Fundamentals of thermal-fluid sciences*. Vol. 703. McGraw-Hill New York.

Chatterjee, T., Chakraborty, S. and Chowdhury, R., 2019. A critical review of surrogate assisted robust design optimization. *Archives of Computational Methods in Engineering*, **26**(1), pp.245–274.

Chen, J., Chen, D., Yuan, T. and Chen, X., 2011. Microfluidic pcr chips. *Nano Biomed Eng*, **3**(4), pp.203–210.

Chen, J.J. and Li, K.T., 2018. Analysis of pcr kinetics inside a microfluidic dna amplification system. *Micromachines*, **9**(2), p.48.

Chen, J.J., Liao, M.H., Li, K.T. and Shen, C.M., 2015. One-heater flow-through polymerase chain reaction device by heat pipes cooling. *Biomicrofluidics*, **9**(1), p.014107.

Chen, J.J., Shen, C.M. and Ko, Y.W., 2013. Analytical study of a microfludic DNA amplification chip using water cooling effect. *Biomedical Microdevices*, **15**(2), pp.261–278.

Chen, P.-C., Fan, W., Hoo, T.-K., Chan, L.C.Z. and Wang, Z., 2012. Simulation guided-design of a microfluidic thermal reactor for polymerase chain reaction. *Chemical Engineering Research and Design*, **90**(5), pp.591–599.

Chen, P.-C., Nikitopoulos, D.E., Soper, S.A. and Murphy, M.C., 2008. Temperature distribution effects on micro-cfpcr performance. *Biomedical Microdevices*, **10**(2), pp.141–152.

Chen, X., Liu, J., Pang, Y., Chen, J., Chi, L. and Gong, C., 2020. Developing a new mesh quality evaluation method based on convolutional neural network. *Engineering Applications of Computational Fluid Mechanics*, **14**(1), pp.391–400.

Chiou, J., Matsudaira, P., Sonin, A. and Ehrlich, D., 2001. A closed-cycle capillary polymerase chain reaction machine. *Analytical Chemistry*, **73**(9), pp.2018–2021.

Chiu, D.T., deMello, A.J., Di Carlo, D., Doyle, P.S., Hansen, C., Maceiczyk, R.M. and Wootton, R.C., 2017. Small but perfectly formed? successes, challenges, and opportunities for microfluidics in the chemical and biological sciences. *Chem*, **2**(2), pp.201–223.

Chunsun, Z., Jinliang, X., Jianqin, W. and Hanping, W., 2006. Continuous-flow polymerase chain reaction microfluidics based on polytetrafluoethylene capillary. *Chinese Journal of Analytical Chemistry*, **34**(8), pp.1197–1203.

Couto, P.R.G., Damasceno, J.C. and de Oliveira, S., 2013. Monte carlo simulations applied to uncertainty in measurement. In: W. Chan, ed. *Theory and applications of monte carlo simulations*. Rijeka, Croatia: InTech. Chap. 2, pp.27–51.

Crews, N., Wittwer, C. and Gale, B., 2008. Continuous-flow thermal gradient pcr. *Biomedical mMcrodevices*, **10**(2), pp.187–195.

Cui, P. and Wang, S., 2019. Application of microfluidic chip technology in pharmaceutical analysis: a review. *Journal of Pharmaceutical Analysis*, **9**(4), pp.238–247.

Daniel, J., Iqbal, S., Millington, R., Moore, D., Lowe, C., Leslie, D., Lee, M. and Pearce, M., 1998. Silicon microchambers for dna amplification. *Sensors and Actuators A: Physical*, **71**(1-2), pp.81–88.

Date, A.W., 2005. *Introduction to computational fluid dynamics*. Cambridge: Cambridge University Press.

Davaji, B., 2016. Thermal microfluidic devices; design, fabrication and applications.

Demello, A.J., 2006. Control and detection of chemical reactions in microfluidic systems. *Nature*, **442**(7101), pp.394–402.

Domingo, D., Malmierca-Vallet, I., Sime, L., Voss, J. and Capron, E., 2020. Using ice cores and gaussian process emulation to recover changes in the greenland ice sheet during the last interglacial. *Journal of Geophysical Research: Earth Surface*, **125**(5), e2019JF005237.

Duryodhan, V., Singh, A., Singh, S.G. and Agrawal, A., 2016. A simple and novel way of maintaining constant wall temperature in microdevices. *Scientific Reports*, **6**, p.18230.

Dyn, N., Levin, D. and Rippa, S., 1986. Numerical procedures for surface fitting of scattered data by radial functions. *SIAM Journal on Scientific and Statistical Computing*, **7**(2), pp.639–659.

Etikan, I. and Bala, K., 2017. Sampling and sampling methods. *Biometrics & Biostatistics International Journal*, **5**(6), p.00149.

Fabritius, B. and Tabor, G., 2016. Improving the quality of finite volume meshes through genetic optimisation. *Engineering with Computers*, **32**(3), pp.425–440.

Farrance, I. and Frenkel, R., 2012. Uncertainty of measurement: a review of the rules for calculating uncertainty components through functional relationships. *The Clinical Biochemist Reviews*, **33**(2), p.49.

Farrance, I. and Frenkel, R., 2014. Uncertainty in measurement: a review of monte carlo simulation using microsoft excel for the calculation of uncertainties through functional relationships, including uncertainties in empirically derived constants. *The Clinical Biochemist Reviews*, **35**(1), p.37.

Forrester, A., Sobester, A. and Keane, A., 2008. *Engineering design via surrogate modelling: a practical guide*. John Wiley & Sons.

Fowlkes, W.Y. and Creveling, C.M., 1995. *Engineering methods for robust product design: using taguchi methods in technology and product development*. Addison-Wesley.

Frei, W., 2016. Keeping track of element order in multiphysics models. *COMSOL Blog, Burlington, MA, accessed Mar*, **1**, p.2019.

Frey, O., Bonneick, S., Hierlemann, A. and Lichtenberg, J., 2007. Autonomous microfluidic multi-channel chip for real-time pcr with integrated liquid handling. *Biomedical Microdevices*, **9**(5), pp.711–718.

Garrido-Merchán, E.C. and Hernández-Lobato, D., 2020. Dealing with categorical and integer-valued variables in bayesian optimization with gaussian processes. *Neurocomputing*, **380**, pp.20–35.

Gen, M. and Cheng, R., 1999. *Genetic algorithms and engineering optimization*. Vol. 7. John Wiley & Sons.

Gevrey, M., Dimopoulos, I. and Lek, S., 2003. Review and comparison of methods to study the contribution of variables in artificial neural network models. *Ecological Modelling*, **160**(3), pp.249–264.

Gilkeson, C., Toropov, V., Thompson, H., Wilson, M., Foxley, N. and Gaskell, P., 2014. Dealing with numerical noise in cfd-based design optimization. *Computers & Fluids*, **94**, pp.84–97.

Gnanavelu, A.B., 2010. *A geometry independent integrated method to predict erosion wear rates in a slurry environment*. PhD thesis. University of Leeds.

González Niño, C., Kapur, N., King, M.-F., Boer, G. de, Blacker, A.J., Bourne, R. and Thompson, H., 2019. Computational fluid dynamic enabled design optimisation of miniaturised continuous oscillatory baffled reactors in chemical processing. *International Journal of Computational Fluid Dynamics*, pp.1–15.

Gui, L. and Ren, C.L., 2006. Numeric simulation of heat transfer and electrokinetic flow in an electroosmosis-based continuous flow pcr chip. *Analytical Chemistry*, **78**(17), pp.6215–6222.

Gur, S., Danielson, T., Xiong, Q., Hin, C., Pannala, S., Frantziskonis, G., Savara, A. and Daw, C.S., 2016. Wavelet-based surrogate time series for multiscale simulation of heterogeneous catalysis. *Chemical Engineering Science*, **144**, pp.165–175.

Gutmann, H.-M., 2001. A radial basis function method for global optimization. *Journal of Global Optimization*, **19**(3), pp.201–227.

Haftka, R.T., Villanueva, D. and Chaudhuri, A., 2016. Parallel surrogate-assisted global optimization with expensive functions–a survey. *Structural and Multidisciplinary Optimization*, **54**(1), pp.3–13.

Hall, M. and Allinson, D., 2010. Heat and mass transport processes in building materials. *Materials for energy efficiency and thermal comfort in buildings*. Elsevier, pp.3–53.

Hamad, H.S., Kapur, N., Khatir, Z., Querin, O., Thompson, H. and Wilson, M., 2021. Cfd-enabled optimization of polymerase chain reaction thermal flow systems. *Advances in heat transfer and thermal engineering*. Springer, pp.409–416.

Hardt, S. and Schönfeld, F., 2007. *Microfluidic technologies for miniaturized analysis systems*. Springer Science & Business Media.

Hashimoto, M., Chen, P.-C., Mitchell, M.W., Nikitopoulos, D.E., Soper, S.A. and Murphy, M.C., 2004. Rapid PCR in a continuous flow device. *Lab on a Chip*, **4**(6), pp.638–645.

He, T., Wang, C., Urisu, T., Nagahiro, T., Tero, R. and Xia, R., 2010. The pdms-based microfluidic channel fabricated by synchrotron radiation stimulated etching. *Optics Express*, **18**(9), pp.9733–9738.

Helton, J.C. and Davis, F.J., 2000. *Sampling-based methods for uncertainty and sensitivity analysis*. (Technical report). Sandia National Labs., Albuquerque, NM (US); Sandia National Labs â€¦.

Herrador, M.Á. and González, A.G., 2004. Evaluation of measurement uncertainty in analytical assays by means of monte-carlo simulation. *Talanta*, **64**(2), pp.415–422.

Hetsroni, G., Mosyak, A. and Segal, Z., 2001. Nonuniform temperature distribution in electronic devices cooled by flow in parallel microchannels. *IEEE Transactions on Components and Packaging Technologies*, **24**(1), pp.16–23.

Hirsch, C., 2007. *Numerical computation of internal and external flows: the fundamentals of computational fluid dynamics*. Elsevier.

Holman, J.P., 2008. *Heat transfer (si units) sie*. Burlington, USA: Tata McGraw-Hill Education.

Holman, J., 2009. *Heat transfer*. 10th ed. New York: McGraw-Hill.

Holmgren, G., Andersson, P., Jakobsson, A. and Frigyesi, A., 2019. Artificial neural networks improve and simplify intensive care mortality prognostication: a national cohort study of 217,289 first-time intensive care unit admissions. *Journal of Intensive Care*, **7**(1), p.44.

Hu, H.H., 2012. Computational fluid dynamics. *Fluid mechanics*. Elsevier, pp.421–472.

Hughes, T.J., Franca, L.P. and Balestra, M., 1986. A new finite element formulation for computational fluid dynamics: v. circumventing the babuška-brezzi condition: a stable petrov-galerkin formulation of the stokes problem accommodating equal-order interpolations. *Computer Methods in Applied Mechanics and Engineering*, **59**(1), pp.85–99.

Ibrahim, A. and Alfa, A., 2017. Optimization techniques for design problems in selected areas in wsns: a tutorial. *Sensors*, **17**(8), p.1761.

Iman, R.L. and Conover, W., 1980. Small sample sensitivity analysis techniques for computer models. with an application to risk assessment. *Communications in Statistics-Theory and Methods*, **9**(17), pp.1749–1842.

Innis, M.A., Gelfand, D.H. and Sninsky, J.J., 1999. *Pcr applications: protocols for functional genomics*. Academic Press.

Jin, R., Du, X. and Chen, W., 2003. The use of metamodeling techniques for optimization under uncertainty. *Structural and Multidisciplinary Optimization*, **25**(2), pp.99–116.

Jornada, D.H. da, Caten, C. ten and Pizzolato, M., 2010. Guidance documents on measurement uncertainty: an overview and critical analysis. *NCSLI Measure*, **5**(1), pp.68–76.

Jung, S., Pyeon, J.-H., Lee, H.-S., Park, M., Yoon, I. and Rho, J., 2020. Construction cost estimation using a case-based reasoning hybrid genetic algorithm based on local search method. *Sustainability*, **12**(19), p.7920.

Kandlikar, S., Garimella, S., Li, D., Colin, S. and King, M.R., 2005. *Heat transfer and fluid flow in minichannels and microchannels*. elsevier.

Karayiannis, T. and Mahmoud, M., 2017. Flow boiling in microchannels: fundamentals and applications. *Applied Thermal Engineering*, **115**, pp.1372–1397.

Khan, M.A., Huque, S. and Mohammad, A., 2014. A neural network model for estimating global solar radiation on horizontal surface. *2013 international conference on electrical information and communication technology (eict)*. IEEE, pp.1–4.

Khandurina, J., McKnight, T.E., Jacobson, S.C., Waters, L.C., Foote, R.S. and Ramsey, J.M., 2000. Integrated system for rapid pcr-based dna analysis in microfluidic devices. *Analytical Chemistry*, **72**(13), pp.2995–3000.

Khatir, Z. and Thompson, H., 2019. Cfd-enabled design optimisation of industrial flows-theory and practice. *International Journal of Computational Fluid Dynamics*, **33**(6-7), pp.235–236.

Kim, H., Park, N. and Hahn, J.H., 2016. Parallel-processing continuous-flow device for optimization-free polymerase chain reaction. *Analytical and Bioanalytical Chemistry*, **408**(24), pp.6751–6758.

Kodzius, R., Xiao, K., Wu, J., Yi, X., Gong, X., Foulds, I.G. and Wen, W., 2012. Inhibitory effect of common microfluidic materials on PCR outcome. *Sensors and Actuators B: Chemical*, **161**(1), pp.349–358.

Kopp, M.U., De Mello, A.J. and Manz, A., 1998. Chemical amplification: continuous-flow PCR on a chip. *Science*, **280**(5366), pp.1046–1048.

Kotinis, M. and Kulkarni, A., 2012. Multi-objective shape optimization of transonic airfoil sections using swarm intelligence and surrogate models. *Structural and Multidisciplinary Optimization*, **45**(5), pp.747–758.

Kumar, S., Thorsen, T. and Das, S.K., 2008. Thermal modeling for design optimization of a microfluidic device for continuous flow polymerase chain reaction (pcr). *Heat transfer summer conference*. Vol. 48494, pp.323–330.

Kurganov, A. and Tadmor, E., 2000. New high–resolution central schemes for nonlinear conservation laws and convection–diffusion equations. *Journal of Computational Physics*, **160**(1), pp.241–282.

Lee, J., Lee, M., Kulla, E. and Tripathi, A., 2017. The effect of dilution on the dispersion with respect to microfluidic channel geometries. *International Journal of Heat and Mass Transfer*, **104**, pp.813–818.

Lepek, A., 2003. A computer program for a general case evaluation of the expanded uncertainty. *Accreditation and Quality Assurance*, **8**(6), pp.296–299.

Lewis, R.W., Nithiarasu, P. and Seetharamu, K.N., 2004. *Fundamentals of the finite element method for heat and fluid flow*. John Wiley & Sons.

Lin, J.-R., Wu, C.-M., Liou, T.-M. and Huang, C.-Y., 2014. The study of axial heat conduction with various hydraulic diameters of microchannel. *Procedia Engineering*, **79**, pp.273–278.

Lonn, D., 2008. *Robust design: accounting for uncertainties in engineering*. PhD thesis. Linkoping University Electronic Press.

Loweth, E., De Boer, G. and Toropov, V., 2011. Practical recommendations on the use of moving least squares metamodel building. *Proceedings of the thirteenth international conference on civil, structural and environmental engineering, chania, crete, greece.*

Madenci, E. and Guven, I., 2015. *The finite element method and applications in engineering using ansys®*. Springer.

Makarynskyy, O., Makarynska, D., Rayson, M. and Langtry, S., 2015. Combining deterministic modelling with artificial neural networks for suspended sediment estimates. *Applied Soft Computing*, **35**, pp.247–256.

Maranzana, G., Perry, I. and Maillet, D., 2004. Mini-and micro-channels: influence of axial conduction in the walls. *International Journal of Heat and Mass Transfer*, **47**(17-18), pp.3993–4004.

Mardle, S., Pascoe, S. et al., 1999. An overview of genetic algorithms for the solution of optimisation problems. *Computers in Higher Education Economics Review*, **13**(1), pp.16–20.

McKaya, M., Beckmana, R. and Conoverb, W., 1979. Comparison of three methods for selecting values of input variables in the analysis of output from a computer code. *Technometrics*, **21**(2), pp.239–245.

Mehendale, S., Jacobi, A. and Shah, R., 1999. Meso-and micro-scale frontiers of compact heat exchangers. *Applied optical measurements*. Springer, pp.139–158.

Miao, G., Zhang, L., Zhang, J., Ge, S., Xia, N., Qian, S., Yu, D. and Qiu, X., 2020. Free convective pcr: from principle study to commercial applicationsâ€"a critical review. *Analytica Chimica Acta*, **1108**, pp.177–197.

Minasny, B. and McBratney, A.B., 2006. A conditioned latin hypercube method for sampling in the presence of ancillary information. *Computers & Geosciences*, **32**(9), pp.1378–1388.

Miralles, V., Huerre, A., Malloggi, F. and Jullien, M.-C., 2013. A review of heating and temperature control in microfluidic systems: techniques and applications. *Diagnostics*, **3**(1), pp.33–67.

Mohammed, A., Adeniyi, A.A. and Hassan, A.B., 2012. Modelling of serpentine continuous flow polymerase chain reaction microfluidics. *IJEST*, **4**, pp.1183–1189.

Mohr, S., Zhang, Y.-H., MacAskill, A., Day, P., Barber, R.W., Goddard, N., Emerson, D. and Fielden, P., 2007. Numerical and experimental study of a droplet-based pcr chip. *Microfluidics and Nanofluidics*, **3**(5), p.611.

Moschou, D., Vourdas, N., Kokkoris, G., Papadakis, G., Parthenios, J., Chatzandroulis, S. and Tserepi, A., 2014. All-plastic, low-power, disposable, continuous-flow PCR chip with integrated microheaters for rapid DNA amplification. *Sensors and Actuators B: Chemical*, **199**, pp.470–478.

Murthy, K., 2001. Monte carlo: basics. *arXiv preprint cond-mat/0104215*.

Narayanan, A., Toropov, V., Wood, A. and Campean, I., 2007. Simultaneous model building and validation with uniform designs of experiments. *Engineering Optimization*, **39**(5), pp.497–512.

Nejadseyfi, O., Geijselaers, H.J. and Boogaard, A.H. van den, 2019. Evaluation and assessment of non-normal output during robust optimization. *Structural and Multidisciplinary Optimization*, **59**(6), pp.2063–2076.

Ng, L.W. and Willcox, K.E., 2014. Multifidelity approaches for optimization under uncertainty. *International Journal for Numerical Methods in Engineering*, **100**(10), pp.746–772.

Nikishkov, G., 2004. *Introduction to the finite element method*. Aizuwakamatsu, Japan: University of Aizu, pp.1–70.

Nisisako, T., Torii, T. and Higuchi, T., 2002. Droplet formation in a microchannel network. *Lab on a Chip*, **2**(1), pp.24–26.

Northrup, M.A., 1993. Dna amplification with a microfabricated reaction chamber. *Technical digest of 7th intl. conf. on solid-state sensors and actuators*, pp.924–926.

O'connor, S.D. and Dantsker, E., 2002. *Microfluidic devices for heat transfer*. Google Patents.

Oh, H.W., 2012. *Applied computational fluid dynamics*. BoD–Books on Demand.

Park, G.-J., Lee, T.-H., Lee, K.H. and Hwang, K.-H., 2006. Robust design: an overview. *AIAA Journal*, **44**(1), pp.181–191.

Park, J. and Park, H., 2017. Thermal cycling characteristics of a 3d-printed serpentine microchannel for DNA amplification by polymerase chain reaction. *Sensors and Actuators A: Physical*, **268**, pp.183–187.

Patankar, S., 1980. Numerical heat transfer and fluid flow: crc press.

Patera, A.T., 1984. A spectral element method for fluid dynamics: laminar flow in a channel expansion. *Journal of Computational Physics*, **54**(3), pp.468–488.

Peiró, J. and Sherwin, S., 2005. Finite difference, finite element and finite volume methods for partial differential equations. *Handbook of materials modeling*. Springer, pp.2415–2446.

Pepper, D.W. and Heinrich, J.C., 2017. *The finite element method: basic concepts and applications with matlab, maple, and comsol*. CRC press.

Petrini, M., 2012. Improvements to the backpropagation algorithm. *Annals of the University of PetrosÌ§ani. Economics*, **12**, pp.185–192.

Polder, D. and Van Hove, M., 1971. Theory of radiative heat transfer between closely spaced bodies. *Physical Review B*, **4**(10), p.3303.

Pragati, K., Sharma, H. et al., 2012. Concept of computational fluid dynamics (cfd) and its applications in food processing equipment design. *Journal of Food Processing and Technology*, **3**(1).

Putko, M.M., Taylor III, A.C., Newman, P.A. and Green, L.L., 2002. Approach for input uncertainty propagation and robust design in cfd using sensitivity derivatives. *Journal of Fluids Engineering*, **124**(1), pp.60–69.

Qiu, X., Mauk, M.G., Chen, D., Liu, C. and Bau, H.H., 2010. A large volume, portable, real-time pcr reactor. *Lab on a Chip*, **10**(22), pp.3170–3177.

Qu, W. and Mudawar, I., 2002. Analysis of three-dimensional heat transfer in micro-channel heat sinks. *International Journal of heat and mass transfer*, **45**(19), pp.3973–3985.

Qu, X. and Haftka, R., 2004. Reliability-based design optimization using probabilistic sufficiency factor. *Structural and Multidisciplinary Optimization*, **27**(5), pp.314–325.

Ranmode, V., Singh, M. and Bhattacharya, J., 2019. Analytical formulation of effective heat transfer coefficient and extension of lumped capacitance method to simplify the analysis of packed bed storage systems. *Solar Energy*, **183**, pp.606–618.

Rapp, B.E., 2016. *Microfluidics: modeling, mechanics and mathematics*. William Andrew.

Razavi, S., Tolson, B.A. and Burn, D.H., 2012. Review of surrogate modeling in water resources. *Water Resources Research*, **48**(7).

Rockafellar, R.T., 2001. *Optimization under uncertainty, lecture notes*. Citeseer.

Rumelhart, D.E., Hinton, G.E. and Williams, R.J., 1985. *Learning internal representations by error propagation*. (Technical report). California Univ San Diego La Jolla Inst for Cognitive Science.

Rumelhart, D.E., Hinton, G.E. and Williams, R.J., 1986. Learning representations by back-propagating errors. *Nature*, **323**(6088), pp.533–536.

Sadler, D.J., Changrani, R., Roberts, P., Chou, C.-F. and Zenhausern, F., 2003. Thermal management of biomems: temperature control for ceramic-based pcr and dna detection devices. *IEEE Transactions on Components and Packaging Technologies*, **26**(2), pp.309–316.

Salvi, D., Boldor, D., Ortego, J., Aita, G. and Sabliov, C., 2010. Numerical modeling of continuous flow microwave heating: a critical comparison of comsol and ansys. *Journal of Microwave Power and Electromagnetic Energy*, **44**(4), pp.187–197.

Schaerli, Y., Wootton, R.C., Robinson, T., Stein, V., Dunsby, C., Neil, M.A., French, P.M., DeMello, A.J., Abell, C. and Hollfelder, F., 2009. Continuous-flow polymerase chain reaction of single-copy dna in microfluidic microdroplets. *Analytical Chemistry*, **81**(1), pp.302–306.

Schneegaß, I., Bräutigam, R. and Köhler, J.M., 2001. Miniaturized flow-through pcr with different template types in a silicon chip thermocycler. *Lab on a Chip*, **1**(1), pp.42–49.

Serani, A., Pellegrini, R., Wackers, J., Jeanson, C.-E., Queutey, P., Visonneau, M. and Diez, M., 2019. Adaptive multi-fidelity sampling for cfd-based optimisation via radial basis function metamodels. *International Journal of Computational Fluid Dynamics*, **33**(6-7), pp.237–255.

Sert, C., 2020. *Me 582 finite element analysis in thermofluids* [Online]. Middle East Technical University. Available from: http://users.metu.edu.tr/csert/teaching_notes.htm [Accessed 1 June 2020].

Shah, R., 1978. A correlation for laminar hydrodynamic entry length solutions for circular and noncircular ducts.

Shapiro, A., 2003. Monte carlo sampling methods. *Handbooks in Operations Research and Management Science*, **10**, pp.353–425.

Shin, S., Hoang, T.-T., Le, T.-H. and Lee, M.-Y., 2016. A new robust design method using neural network. *Journal of Nanoelectronics and Optoelectronics*, **11**(1), pp.68–78.

Shu, C., Ding, H. and Yeo, K., 2004. Solution of partial differential equations by a global radial basis function-based differential quadrature method. *Engineering Analysis with Boundary Elements*, **28**(10), pp.1217–1226.

Singh, J. and Ekaputri, M., 2006. Pcr thermal management in an integrated lab on chip. *Journal of physics: conference series*. Vol. 34, 1. IOP Publishing, p.222.

Sivanandam, S. and Deepa, S., 2008. Genetic algorithms. *Introduction to genetic algorithms*. Springer, pp.15–37.

Slotnick, J., Khodadoust, A., Alonso, J., Darmofal, D., Gropp, W., Lurie, E. and Mavriplis, D., 2014. CFD vision 2030 study: a path to revolutionary computational aerosciences.

Sonker, M., Sahore, V. and Woolley, A.T., 2017. Recent advances in microfluidic sample preparation and separation techniques for molecular biomarker analysis: a critical review. *Analytica Chimica Acta*, **986**, pp.1–11.

Squires, T.M. and Quake, S.R., 2005. Microfluidics: fluid physics at the nanoliter scale. *Reviews of Modern Physics*, **77**(3), p.977.

Stroock, A.D., Dertinger, S.K., Ajdari, A., Mezic, I., Stone, H.A. and Whitesides, G.M., 2002. Chaotic mixer for microchannels. *Science*, **295**(5555), pp.647–651.

Swidzinski, J., Keramat, M. and Chang, K., 1999. A novel approach to efficient yield estimation for microwave integrated circuits. *42nd midwest symposium on circuits and systems (cat. no. 99ch36356)*. Vol. 1. IEEE, pp.367–370.

Tachibana, H., Saito, M., Tsuji, K., Yamanaka, K., Tamiya, E. et al., 2015. Self-propelled continuous-flow pcr in capillary-driven microfluidic device: microfluidic behavior and dna amplification. *Sensors and Actuators B: Chemical*, **206**, pp.303–310.

Tarn, M.D., Sikora, S.N., Porter, G.C., Oâ€™Sullivan, D., Adams, M., Whale, T.F., Harrison, A.D., Vergara-Temprado, J., Wilson, T.W., Shim, J.-u. et al., 2018. The study of atmospheric ice-nucleating particles via microfluidically generated droplets. *Microfluidics and Nanofluidics*, **22**(5), p.52.

Thomas, S., Orozco, R.L. and Ameel, T., 2014. Thermal gradient continuous-flow PCR: a guide to design. *Microfluidics and Nanofluidics*, **17**(6), pp.1039–1051.

Tissot, J.-Y. and Prieur, C., 2015. A randomized orthogonal array-based procedure for the estimation of first-and second-order sobol'indices. *Journal of Statistical Computation and Simulation*, **85**(7), pp.1358–1381.

Tsuda, S., Jaffery, H., Doran, D., Hezwani, M., Robbins, P.J., Yoshida, M. and Cronin, L., 2015. Customizable 3d printed 'plug and play' millifluidic devices for programmable fluidics. *PLoS One*, **10**(11), e0141640.

Tu, J., Yeoh, G.H. and Liu, C., 2018. *Computational fluid dynamics: a practical approach*. Burlington, USA: Butterworth-Heinemann.

Tuckerman, D.B. and Pease, R.F.W., 1981. High-performance heat sinking for vlsi. *IEEE Electron Device Letters*, **2**(5), pp.126–129.

Urquhart, M., Ljungskog, E. and Sebben, S., 2020. Surrogate-based optimisation using adaptively scaled radial basis functions. *Applied Soft Computing*, **88**, p.106050.

Versteeg, H.K. and Malalasekera, W., 2007. *An introduction to computational fluid dynamics: the finite volume method*. Pearson Education.

Viana, F.A., Haftka, R.T. and Steffen, V., 2009. Multiple surrogates: how cross-validation errors can help us to obtain the best predictor. *Structural and Multidisciplinary Optimization*, **39**(4), pp.439–457.

Vicente, F.A., Plazl, I., Ventura, S.P. and Znidarsic-Plazl, P., 2020. Separation and purification of biomacromolecules based on microfluidics. *Green Chemistry*, **22**(14), pp.4391–4410.

Al-Waaly, A., 2015. *The effect of heat transfer on temperature measurement and itâ€™s applications to study microchannel heat sinks*. PhD thesis. University of Glasgow.

Walczak, S. and Cerpa, N., 1999. Heuristic principles for the design of artificial neural networks. *Information and Software Technology*, **41**(2), pp.107–117.

Wang, G.G. and Shan, S., 2006. Review of metamodeling techniques in support of engineering design optimization. *Journal of mechanical design*, **129**(4), pp.370–380.

Wang, J.-X., Wu, J.-L. and Xiao, H., 2017. Physics-informed machine learning approach for reconstructing reynolds stress modeling discrepancies based on dns data. *Physical review fluids*, **2**(3), p.034603.

Wang, W., Caro, S., Bennis, F. and Augusto, O.B., 2012. Toward the use of pareto performance solutions and pareto robustness solutions for multi-objective robust optimization problems. *Engineering systems design and analysis*. Vol. 44861. American Society of Mechanical Engineers, pp.541–550.

Watanabe, K., Miyagi, Z., Dolah, R. and Takahasi, K., 2013. Evaluation of uncertainty method with interaction in paper permeability tester. *Proceedings of the seventh international symposium on mechanics*. Gyeongsang National University.

White, F.M., 2009. *University of rhode island. fluid mechanics*. McGraw Hill Publishers.

White, F.M. and Corfield, I., 2006. *Viscous fluid flow*. Vol. 3. McGraw-Hill New York.

Whitesides, G.M., 2006. The origins and the future of microfluidics. *Nature*, **442**(7101), pp.368–373.

Woolley, A.T., Hadley, D., Landre, P., deMello, A.J., Mathies, R.A. and Northrup, M.A., 1996. Functional integration of pcr amplification and capillary electrophoresis in a microfabricated dna analysis device. *Analytical Chemistry*, **68**(23), pp.4081–4086.

Xu, B., Li, P.-W. and Chan, C.L., 2012. Extending the validity of lumped capacitance method for large biot number in thermal storage application. *Solar Energy*, **86**(6), pp.1709–1724.

Yang, J., Liu, Y., Rauch, C.B., Stevens, R.L., Liu, R.H., Lenigk, R. and Grodzinski, P., 2002. High sensitivity pcr assay in plastic micro reactors. *Lab on a Chip*, **2**(4), pp.179–187.

Yunus, A.C., 2010. *Fluid mechanics: fundamentals and applications (si units).* Tata McGraw Hill Education Private Limited.

Zacks, S., 2012. *Introduction to reliability analysis: probability models and statistical methods*. Springer Science & Business Media.

Zang, C., Friswell, M. and Mottershead, J., 2005. A review of robust optimal design and its application in dynamics. *Computers & Structures*, **83**(4-5), pp.315–326.

Zhang, C. and Xing, D., 2007. Miniaturized pcr chips for nucleic acid amplification and analysis: latest advances and future trends. *Nucleic Acids Research*, **35**(13), pp.4223–4237.

Zhang, C. and Xing, D., 2009. Parallel dna amplification by convective polymerase chain reaction with various annealing temperatures on a thermal gradient device. *Analytical Biochemistry*, **387**(1), pp.102–112.

Zhang, C., Xu, J., Ma, W. and Zheng, W., 2006. Pcr microfluidic devices for dna amplification. *Biotechnology Advances*, **24**(3), pp.243–284.

Zhang, H., Che, F., Lin, T. and Zhao, W., 2019. *Modeling, analysis, design, and tests for electronics packaging beyond moore*. Woodhead Publishing.

Zhang, Q., Wang, W., Zhang, H. and Wang, Y., 2002. Temperature analysis of continuous-flow micro-pcr based on fea. *Sensors and Actuators B: Chemical*, **82**(1), pp.75–81.

Zhang, X. and Jaluria, Y., 2020. Reliability-based optimization and design limits of microchannel cooling systems. *International Journal of Heat and Mass Transfer*, **149**, p.119202.

Zhang, Y. and Jiang, H.-R., 2016. A review on continuous-flow microfluidic PCR in droplets: advances, challenges and future. *Analytica Chimica Acta*, **914**, pp.7–16.

Zhang, Y. and Ozdemir, P., 2009. Microfluidic DNA amplificationâ€"a review. *Analytica Chimica Acta*, **638**(2), pp.115–125.

Zhao, Z., Xin, H., Ren, Y. and Guo, X., 2010. Application and comparison of bp neural network algorithm in matlab. *2010 international conference on measuring technology and mechatronics automation*. Vol. 1. IEEE, pp.590–593.

Zhu, X., Modi, H., Ayala, A. and Kilbane, J., 2006. Rapid detection and quantification of microbes related to microbiologically influenced corrosion using quantitative polymerase chain reaction. *Corrosion*, **62**(11), pp.950–955.

Zill, D.G., 2012. *A first course in differential equations with modeling applications*. Cengage Learning.